# Investigations on dehydration and rehydration processes in the $CaSO_4$ – $H_2O$ system at controlled time, temperature and humidity conditions

Inaugural - Dissertation

zur

Erlangung des Doktorgrades

der Mathematisch-Naturwissenschaftlichen Fakultät

der Universität zu Köln

vorgelegt von

Laura Maria Ritterbach

aus Neuss

Berichterstatter: Prof. Dr. Petra Becker-Bohatý
(Gutachter)

Prof. Dr. Sandro Jahn

Tag der mündlichen Prüfung: 11.06.2021

# Abstract

This thesis takes as its primary focus to reinvestigate the dehydration of gypsum ($CaSO_4 \cdot 2\,H_2O$) at moderate to low temperatures with defined $H_2O$ partial pressures, and to provide a systematic examination of $T-$ and $p_{H_2O}$-induced rehydration of hemihydrate (mineral bassanite, $CaSO_4 \cdot 0.5\,H_2O$). Therefore, isothermal and isohumid powder XRD and Raman spectroscopic measurements were conducted. The isothermal treatment of gypsum over time ranges up to 60 h at temperatures $\leq 150\,°C$ and relative humidities $\leq 5.5\%$ (averagely), yielded the formation of hemihydrate and $\gamma$-anhydrite ($\gamma$-$CaSO_4$). The process-dependence on particle sizes was evident. $\beta$-anhydrite ($\beta$-$CaSO_4$, mineral anhydrite) was not found as dehydration product of these measurement series but formed over time ranges up to six months at 60 °C/11% RH and 80 °C/30% RH. Rehydration of hemihydrate to gypsum was investigated at temperatures $\leq 40\,°C$ and relative humidities $\leq 95\%$. The great influence of applied sample humidities on the hydration rate became apparent. Fraction of conversion vs. time ($\alpha - t$) plots were derived by quantitative phase analysis by the Rietveld method of several isothermal/isohumid powder XRD measurements. If suitable, isokinetic and isoconversional kinetic analysis was performed and the applicability discussed. The dehydration process of gypsum to hemihydrate was found to differ with surrounding $T$ and $p_{H_2O}$ values. The greater part of the data could be fitted with the nucleation-controlled Johnson-Mehl-Avrami-Erefe'ev-Kolmogorov equation and the autocatalytic Prout-Tompkins model. The hydration process of hemihydrate seems more complex. Exemplary, a time-dependent hydration curve measured at 35 °C and 91% relative humidity was fitted with the power law and the 3D diffusion equation according to Ginstling-Brounshtein. Implication of the present findings for de- and rehydration reactions of calcium sulfate phases in the Atacama Desert, Chile, are debated.

# Zusammenfassung

In dieser Arbeit liegt der Fokus auf einer systematischen Untersuchung des $CaSO_4$ – $H_2O$ Systems in Abhängigkeit der Parameter Temperatur, Wasserdampfpartialdruck und Zeit. Calciumsulfatphasen sind wichtige Roh- und Baustoffe und finden vielfältige Verwendung vom Trockenmörtel bis hin zum Additiv in Kosmetikprodukten. Gips ($CaSO_4 \cdot 2\,H_2O$) und Anhydrit ($CaSO_4$) sind zudem häufige natürlich vorkommende Sulfatminerale. Das Halbhydrat Bassanit (als synthetische Phase of Hemihydrat genannt, $CaSO_4 \cdot 0.5\,H_2O$) wird ebenfalls in der Natur gebildet, ist jedoch aufgrund seiner Metastabilität viel seltener aufzufinden als Gips und Anhydrit. Aufgrund der industriellen und geologischen Relevanz sind De- und Rehydrierungsreaktionen von Calciumsulfatphasen Gegenstand vieler früheren und aktuellen Studien. Trotz des Wissens um den Einfluss des Wasserdampfpartialdrucks wurde dieser oftmals außer Acht gelassen. Für die vorliegende Dissertation wurde die Dehydrierung des Gipses bei moderaten bis tiefen Temperaturen mit definierten $H_2O$ Partialdrücken untersucht. Die Bedingungen der $p_{H_2O}$-induzierten Hemihydrat-Rehydrierung wurden ebenfalls studiert. Als Untersuchungsmethoden wurden *in situ* Röntgenpulverdiffraktometrie und Ramanspektroskopie eingesetzt.

Die isotherme Behandlung von Gips $\leq 150\,°C$ und $\leq 5{,}5\%$ relativer Feuchtigkeit bedingte die Bildung von Hemihydrat und $\gamma$-Anhydrit ($\gamma$-$CaSO_4$) innerhalb von 60 h. Die Abhängigkeit des Prozesses von Partikelgrößen wurde deutlich. $\beta$-Anhydrit ($\beta$-$CaSO_4$, strukturell äquivalent zum Mineral Anhydrit) war kein Dehydrierungsproduct dieser Messreihen, wurde aber innerhalb von sechs Monaten und Bedingugen von $60\,°C/11\%$ RH and $80\,°C/30\%$ RH nachgewiesen. Die Rehydrierung von Hemihydrat konnte bei Temperaturen von $\leq 40\,°C$ und relativen Feuchten von $\leq 95\%$ verfolgt werden. Der dominante Einfluss des Wasserdampfpartialdruckes auf die Hydrierungsrate wurde hierbei ersichtlich. Für einige isotherme/isohumide Röntgenpulverdiffraktions-Messreihen wurden Umsatz-vs.-Zeit- ($\alpha - t$) Kurven mithilfe von quantitativer Phasenanalyse durch die Rietveld Methode erstellt. Die Kurven wurden für isokinetische und isokonversionale kinetische Auswertungen und Diskussionen genutzt, sofern dies anwendbar war. Dabei wurde die Änderung des Gips–Hemihydrat–Dehydrierungsprozesses von den Parametern Temperatur und Wasserdampfpartialdruck deutlich.

Ein Großteil der Daten konnte jedoch mit den kinetischen Modellen nach Johnson-Mehl-Avrami-Erefe'ev-Kolmogorov (Keimbildungs- und Wachstums Modell) und Prout-Tompkins (autokatalytisches Modell ) angepasst werden. Die geschwindigkeitsbestimmenden Prozesse der Rehydrierung von Hemihydrat scheinen komplexer zu sein. Eine bei 35 °C und 91% relativer Feuchte gemessene Umsatz-vs.-Zeit-Kurve wurde exemplarisch für die kinetische Modellanpassung ausgesucht. Die Kurve konnte mit einer Kombination aus einem Potenzgesetz und der 3D Diffusionsgleichung nach Ginstling-Brounshtein beschrieben werden. Da die vorliegende Arbeit auf einem Teilprojekt des Sonderforschungsbereichs 1211 "Earth Evolution at the Dry Limit" basiert, werden die Möglichkeiten von De- und Rehydrierungsreaktionen von Calciumsulftaphasen in der Atacamawüste in Chile, unter Berücksichtigung der dortigen Temperatur- und Luftfeuchtebedingungen, diskutiert.

# Table of Contents

# List of Figures

# List of Tables

# List of Abbreviations

**DH** Calcium sulfate dihydrate, $CaSO_4 \cdot 2\,H_2O$

**HH** Calcium sulfate hemihydrate, $CaSO_4 \cdot 0.5\,H_2O$

**SH** Calcium sulfate subhydrate, $CaSO_4 \cdot n\,H_2O$ $(0.5 \leq n \leq 0.8)$

**AH** Calcium sulfate, $CaSO_4$

**AI** $\alpha$-Anhydrite, $\alpha$-$CaSO_4$

**AII** $\beta$-Anhydrite, $\beta$-$CaSO_4$

**AIII** $\gamma$-Anhydrite, $\gamma$-$CaSO_4$

**RH** Relative humidity

**ICSD** Inorganic Crystal Structure Database

**CRC** Collaborative Research Center

**TA** Thermal analysis

**TG** Thermogravimetry

**DTG** Differential thermogravimetry

**DTA** Differential thermal analysis

**JMAEK (model)** Johnson-Mehl-Avrami-Erefe'ev-Kolmogorov (model)

**CNT** Classical nucleation theory

**XRD** X-Ray diffraction

# Chapter 1

# Introduction

Investigating the $CaSO_4$ – $H_2O$ system with focus on systematic parameter control is of great interest. Calcium sulfate phases are important working materials, as well as abundant natural occurring sulfates on earth (and mars). This industrial and geological prevalence motivated and motivates manifold examinations. In the past, especially dehydration reactions of calcium sulfate dihydrate ($CaSO_4 \cdot 2\,H_2O$), gypsum, were extensively studied. The main points of interest concern the products of dehydration. Four principal phases are reported: Hemihydrate ($CaSO_4 \cdot 0.5\,H_2O$), $\gamma$-anhydrite ($\gamma$-$CaSO_4$), $\beta$-anhydrite ($\beta$-$CaSO_4$), and $\alpha$-anhydrite ($\alpha$-$CaSO_4$). $\alpha$-Anhydrite is the high-temperature phase that is stable between 1200 °C and 1400 °C. $\beta$-Anhydrite, which is the structural equivalent to the mineral anhydrite, is usually produced at temperatures $\geq$ 250 °C. Hemihydrate and $\gamma$-anhydrite are metastable, low-temperature dehydration products that are structurally similar to each other. $\gamma$-Anhydrite is commonly understood as dehydrated, undistorted hemihydrate. In contrast to gypsum–hemihydrate, hemihydrate–$\beta$-anhydrite and gypsum–$\beta$-anhydrite conversions, the hemihydrate–$\gamma$-anhydrite transformation does not require distinct structural changes. Hemihydrate is structurally identical to bassanite. In the form of 'Plaster of Paris', the phase is utilized as building or technical material due to its fast rehydration capacity to gypsum. Many investigations studied the specific setting behaviour in slurries. Usually, hemihydrate is distinguished in an $\alpha$ and a $\beta$-phase. The modifications do not exhibit discriminable crystal structures but differ in their hydration behavior and technical production.

The exact formation temperatures of hemihydrate and $\gamma$- and $\beta$-anhydrite, strongly depends on the applied heating protocol, sample characteristics, measurement time, and partial pressure of water. Equation 1-1 shows the two-step dehydrational process of gypsum in the solid state.

$$CaSO_4 \cdot 2\,H_2O\,(s) \xrightarrow[\text{step 1}]{p_{H_2O1}, T_1, t_1} CaSO_4 \cdot 0.5\,H_2O\,(s) + 1.5\,H_2O\,(g) \xrightarrow[\text{step 2}]{p_{H_2O2}, T_2, t_2} \gamma-/\beta\text{-}CaSO_4\,(s) + 2\,H_2O\,(g) \tag{1-1}$$

with $t$ = time, $T$ = temperature and $p_{H_2O}$ = water vapor-pressure. Under isothermal and isohumid measurement conditions, $p_{H_2O1} = p_{H_2O2}, T_1 = T_2$, and $t_2 > t_1$ follows. If non-isothermal and non-isohumid conditions are applied, $p_{H_2O_1} > p_{H_2O_2}$ and $T_2 > T_1$ with disregard of $t_2$ and $t_1$ is evident.

The rehydrational processes of hemihydrate and $\gamma$-/$\beta$-anhydrite are given by Expressions 1-2 and 1-3, respectively.

$$\mathrm{CaSO_4 \cdot 0.5\,H_2O\,(s) + 1.5\,H_2O\,(g) \xrightarrow{p_{H_2O},\,T,\,t} CaSO_4 \cdot 2\,H_2O\,(s)} \tag{1-2}$$

$$\mathrm{\gamma - /\beta - CaSO_4\,(s) + 2\,H_2O\,(g) \xrightarrow{p_{H_2O},\,T,\,t} CaSO_4 \cdot 2\,H_2O\,(s)} \tag{1-3}$$

Despite the known $p_{\mathrm{H_2O}}$ influence on de- and rehydration processes of $\mathrm{CaSO_4 \cdot}n\mathrm{H_2O}, 0 \leq n \leq 2$ phases, comparably few studies provide detailed information on that matter. Moreover, the hydration of hemihydrate has primarily been investigated in aqueous suspensions due to the importance of the setting process. Due to the kinetic checks, $\beta$-anhydrite hydration in water has been the subject of very few studies. Basic information on hemihydrate and $\beta$-anhydrite hydration promoted by $p_{\mathrm{H_2O}}$ has not been provided yet.

Further, the underlying project of the present thesis substantiates a concrete geological significance. This work bases on a subproject of the Collaborative Research Center (CRC) 1211 "Earth Evolution at the Dry Limit". The CRC was launched to investigate the mutual relationships of Earth surface processes and the evolution of life in arid to hyper-arid environments such as the Atacama Desert in Chile. Therefore, diverse aspects of biological activity, past and present climatic conditions, and transformations of the desert landscapes are studied. Regarding Atacama soils, surfaces and subsurfaces, gypsum and anhydrite are abundant constituents. A couple of geomorphological features (*e.g.* gypsum wedges) affecting soil-dynamic processes are assumed to result from de- and rehydration processes of these minerals. It is further believed that the prevailing temperature and humidity conditions can promote these reactions on diurnal or seasonal time scales. This supposition in conjunction with the above mentioned material scientific aspects establishes the need for an experimental investigation under controlled time, temperature, and humidity conditions.

# Chapter 2

# The $CaSO_4$ – $H_2O$ system

This Chapter focuses on calcium sulfate and its hydrates. Different aspects of the $CaSO_4$ – $H_2O$ system are covered, including the crystalline phases, solubility behavior, nucleation and growth theories, natural abundances, and technical relevance. Special attention is given to the review of examinations with focus on de- and rehydration reactions of calcium sulfate phases (Section 2-3).

## 2-1 Crystalline phases

The $CaSO_4$ – $H_2O$ system contains several distinct crystalline phases. Here, the structures existent at ambient pressure conditions are contemplated. To date, nine phases are established as there are three natural occurring phases, gypsum, bassanite, and anhydrite, and a set of synthetic calcium sulfate phases that are obtained during laboratory experiments and/or industrial processing of gypsum.

### 2-1-1 Calcium sulfate minerals

The two hydrous minerals are gypsum (dihydrate, DH, $CaSO_4 \cdot 2\,H_2O$) and bassanite (hemihydrate, HH, $CaSO_4 \cdot 0.5\,H_2O$). Both are monoclinic structures with the space groups $I2/a$ and $I2$, respectively. The anhydrous mineral anhydrite (AH, $CaSO_4$) crystallizes in the orthorhombic system with the space group *Amma*. Gypsum and anhydrite are thermodynamically stable under ambient temperature, humidity, and pressure conditions, whereas bassanite is a metastable mineral and less abundant in nature than gypsum and anhydrite (Van Driessche et al., 2017; Freyer and Voigt, 2003; Mirwald, 2008).

### 2-1-2 $CaSO_4$ modifications

Three anhydrous calcium sulfate modifications can be distinguished, including a trigonal (space group $P31c$) high-temperature phase, a hexagonal (space group $P6_222$) low-temperature phase, and the mineral anhydrite, respectively its synthetic structural equivalent. As (hydrated) calcium sulfates are subject of industrial and scientific interests, various publications are dedicated to the $CaSO_4 - H_2O$ system and two classifications for differentiation between the three anhydrous calcium sulfates evolved.

In industry, the high-temperature phase is termed AI and evolves through gypsum calcination (thermal treatment at elevated temperatures) at 1200 °C. It decomposes to CaO, $SO_2$ and $O_2$ at 1350 °C - 1400 °C (Flörke, 1952a). As it is metastable, AI is not relevant as a working material and will recrystallize to the orthorhombic $CaSO_4$ modification (synthetic anhydrite) at ambient conditions (Grahmann, 1920; Gutt and Smith, 1967; Hanic et al., 1985). Synthetic anhydrite is named AII or insoluble anhydrite (gypsum calcination at 300 °C - 900 °C) and the low-temperature anhydrite polymorph is referred to as AIII or soluble anhydrite (bassanite calcination at 100 °C). AIII is metastable and readily rehydrates to bassanite under ambient temperature and humidity conditions (Carbone et al., 2008; Chang et al., 1996; Palacio et al., 2014). Here, the temperature information refers to the temperatures applied during the industrial process as given by Bundesverband der Gipsindustrie e.V. (2013).

Studies with focus on the crystallographic and material scientific aspects of calcium sulfate phases usually use the designation $\alpha$-anhydrite/$\alpha$-AH, $\beta$-anhydrite/$\beta$-AH, and $\gamma$-anhydrite/$\gamma$-AH instead of AI, AII and AIII, respectively, but the lines are blurred and several authors use both designations for clarity.

The formation temperatures of $\beta$- and $\gamma$-anhydrite during laboratory experiments differ from those applied in the technical process and strongly depend on a variety of parameters including the specific experimental set-up and measurement protocol, grain sizes, sample masses, temperature, time, and water-vapor pressures. Some publications, in which gypsum was treated thermally for several hours without $p_{H_2O}$-control, mention threshold temperatures of 100 °C - 130 °C concerning $\gamma$-anhydrite formation (Khalil and Gad, 1972; Ball and Norwood, 1969) and 250 °C - 350 °C for $\beta$-anhydrite evolution (*e.g.* Seufert et al., 2009; Khasanov et al., 2015; Abriel et al., 1990).

### 2-1-3 $CaSO_4 \cdot 0.5\,H_2O$ modifications

Depending on the treatment, gypsum dehydrates to $\alpha$- or $\beta$-hemihydrate (Lewry and Williamson, 1994; Singh and Middendorf, 2007). In industry, $\alpha$-hemihydrate is produced by wet method (Singh and Middendorf, 2007). This includes dehydration of gypsum in acidic water suspensions or hydrothermally with added electrolytes. Also, a production using autoclaves at 100 °C to 150 °C is common. $\beta$-Hemihydrate is obtained by calcinating gypsum (Follner et al., 2002; Wirsching, 2000).

In the laboratory, $\alpha$-hemihydrate is produced by treating gypsum in acid or salt solutions at elevated temperatures or through heating the dihydrate at high water-vapor pressures. In contrast, $\beta$-hemihydrate is only gained through heating gypsum at low water-vapor pressures (Singh and Middendorf, 2007). The dehydration of gypsum to $\alpha$- and $\beta$-hemihydrate in the condensed state has been described as topotactic. The dehydration of single gypsum crystals to $\alpha$-hemihydrate evolves via retention of the crystallographic $c$-axis (Bobrov et al., 1987). The formation of $\beta$-hemihydrate proceeds with the original $b$- or $c$-axis of gypsum becoming the new $c$-axis of hemihydrate (Heide, 1969). The discrimination of hemihydrates according to their production methods is widely accepted and applied, yet some authors define $\alpha$- and $\beta$-hemihydrate in a different manner.

$\alpha$- and $\beta$-Hemihydrate differ in their morphologies as the $\alpha$-modification is well-formed with idiomorphic crystallites (typical aggregates of hexagonal columns) in opposition to $\beta$-hemihydrate. They also vary in solubility, effects in thermal analysis, heat of solution, specific surface, and physical properties of technical end products. For example, the setting behavior of the less reactive $\alpha$-modification is reduced compared to the $\beta$-form but results in an overall denser, stronger plaster (Korovyakov et al., 2004; Freyer and Voigt, 2003; Kogel et al., 2006). Whether their crystal structures are identical to each other (and the mineral bassanite) or not, has been discussed in the literature. For example, Kuzel and Hauner (1987) and Oetzel et al. (2000b) found both forms to be monoclinic, as the mineral. Contrary, Bushuev et al. (1983), Follner et al. (2002), and Christensen et al. (2008, 2010) published a monoclinic and a trigonal crystal structure. Schmidt et al. (2011) state that there is no true difference between the hemihydrate structures and ascribe the findings of mentioned authors presumably to the "hemihydrate typical" broadening of reflections. Considering the structure solution history of the mineral bassanite which presumably was affected by merohedric twinning and, therefore, pseudo-hexagonal symmetry (Section 2-2-1), it could be possible that structure discrimination of $\alpha$- and $\beta$-hemihydrate is affected by the similar issues.

Information on the crystal structure of the $\beta$-modification is consistent. It is in accordance with the structure of the natural phase bassanite (Ballirano and Melis, 2009c) and, as it is gained solely through heating gypsum at low water-vapor pressures and without chemical additives, it is the only relevant hemihydrate phase for the dehydration and rehydration processes contemplated in this work.

Comparable to $\gamma$- and $\beta$-anhydrite formation from gypsum, the transformation temperature of gypsum to hemihydrate depends strongly on sample and experimental parameters. When gypsum is heated at ambient (environmental $p_{H_2O}$) conditions, the $\beta$-hemihydrate formation threshold temperature was found to be 45 °C (Seufert et al., 2009). The upper limit of hemihydrate evolution is around 200 °C (Powell, 1958; Wirsching, 2000). During laboratory experiments of several minutes to several hours, many studies find the temperature of $\beta$-hemihydrate evolution to be set between 80 °C - 120 °C (*e.g.* Prasad et al., 2005; Chang et al., 1999; Sarma et al., 1998; Harrison, 2012; Robertson and Bish, 2007; Ballirano and Melis, 2009c; Abriel et al., 1990).

### 2-1-4 Calcium sulfate subhydrates

Synthetic calcium sulfate phases that feature 0.5 to 0.8 $H_2O$ molecules per formula unit are collectively termed subhydrates. Their occurrences are witnessed at distinct synthesis conditions, primarily referring to environmental water-vapor pressures (Ballirano et al., 2001). The subhydrates include the following phases: $CaSO_4 \cdot 0.6\,H_2O$ (space group $I2$), $CaSO_4 \cdot 0.625\,H_2O$ (space group $P3_121$), $CaSO_4 \cdot 0.67\,H_2O$ (space group $I2$), and $CaSO_4 \cdot 0.8\,H_2O$ (space group $P3_121$). All subhydrates, as well as $\gamma$-anhydrite, exhibit structural similarities as they derive from the bassanite structure type. Whether the formation of subhydrates with differing amounts of water molecules, *e.g.* $CaSO_4 \cdot n\,H_2O$ with $0.5 \leq n \leq 1$, is possible, remains to be scrutinized.

All mentioned calcium sulfate phases, their common designations, chemical formula, space groups, synthesis conditions in the laboratory and references are presented in Table 2-1. If applicable, Inorganic Crystal Structure Database (ICSD) codes are also given (FIZ Karlsruhe, 2020). For the subhydrates, the synthesis conditions refer to the production methods described in the corresponding publications. For $\alpha$-, $\beta$-, $\gamma$-anhydrite and the hemihydrates, the synthesis conditions refer to the widely accepted laboratory production of the respective phases by heating gypsum (without $p_{H_2O}$-control). Methods of producing dihydrate and synthetic anhydrite by solution/precipitation processes are not included here but in Section 2-4.

**Table 2-1:** Overview of crystalline calcium sulfate phases (without high-pressure phases). RH = relative humidity.

| Phase name | Mineral name | Formula | Symmetry | Synthesis conditions | References/ICSD code |
|---|---|---|---|---|---|
| Dihydrate, DH | Gypsum | $CaSO_4 \cdot 2\,H_2O$ | $I2/a$ (standard setting $C2/c$) | | Wooster (1936)/15982, Atoji and Rundle (1958)/27875, Cole and Lancucki (1974)/2058, Pedersen and Semmingsen (1982)/27221, Schofield et al. (2000)/81650, Boeyens and Ichharam (2002)/409581, De la Torre et al. (2004)/151692, Fernandez-Martinez et al. (2006)/409581, Khasanov et al. (2008)/246242, Comodi et al. (2008)/161622 |
| ($\alpha$-/$\beta$-)Hemihydrate, ($\alpha$-/$\beta$-)HH | Bassanite | $CaSO_4 \cdot 0.5\,H_2O$ | $I2$ (standard setting $C2$) | $\alpha$-HH: heating gypsum in acid or salt solutions or at high $p_{H_2O}$, $\beta$-HH: heating gypsum at low $p_{H_2O}$ at *e.g.* 80 °C - 120 °C for minutes to hours | Bushuev (1982), Bushuev et al. (1983), Bezou et al. (1995)/79528, Weiss and Braeu (2009)/380286, Ballirano et al. (2001)/92947, Schmidt et al. (2011)/262106 |
| Subhydrate 0.6, SH 0.6 | | $CaSO_4 \cdot 0.6\,H_2O$ | $C2$ | preparation of bassanite at 25 °C/95 % RH | Bezou et al. (1995)/69061 |
| Subhydrate 0.625, SH 0.625 | | $CaSO_4 \cdot 0.625\,H_2O$ | $P3_221$ | preparation of bassanite at 25 °C/75 % RH | Schmidt et al. (2011)/262107 |
| Subhydrate 0.67, SH 0.67 | | $CaSO_4 \cdot 0.67\,H_2O$ | $B2$ (standard setting $C2$) | hydrothermal synthesis in water from 2 g gypsum | Bushuev (1982)/20803 |
| Subhydrate 0.8, SH 0.8 | | $CaSO_4 \cdot 0.8\,H_2O$ | $P3_121$ | treatment of 0.01 mol. $CaCl_2$ solution and saturated $H_2SO_4$ acid for several days | Abriel (1983)/37170 |
| $\gamma$-Anhydrite, $\gamma$-AH, AIII, soluble anhydrite | | $CaSO_4$ | $P6_222$ | heating gypsum at low temperatures (*e.g.* > 100 °C - 130 °C for several hours) | Flörke (1952a)/24470, Lager et al. (1984)/159702, Christensen et al. (2008)/86316 |
| $\beta$-Anhydrite, $\beta$-AH, AII, insoluble anhydrite, synthetic anhydrite | Anhydrite | $CaSO_4$ | $Amma$ (standard setting $Cmcm$) | heating gypsum at high temperatures (*e.g.* > 250 °C - 350 °C for several hours) | Hoehne (1962)/28546, Cheng and Zussman (1963)/15876, Hawthorne and Ferguson (1975)/40043, Morikawa et al. (1975)/1956, Kirfel and Will (1980)/16382, Hartman (1989), Antao (2011)/183916 |
| $\alpha$-Anhydrite, AI | | $CaSO_4$ | $P31c$ | heating gypsum > 1200 °C and < 1400 °C | Hanic et al. (1985) |

## 2-2 Crystal structures

In the following, the structural networks of (hydrated) calcium sulfates regarding common and distinguishable features are presented. The influence of $H_2O$ molecules on the arrangement and packing density of $Ca-SO_4$ chains is shown.

### 2-2-1 Structures of gypsum, bassanite and anhydrite

The three minerals are characterized by chains of alternating $Ca^{2+}$ and $[SO_4]^{2-}$ ions with typical Ca··S atomic distances of 3.15 Å. The distance between two $Ca-SO_4$ chains is approximately 3.5 Å. The chains form a network by arranging Ca and S positions in adjacent chains opposite each other. Resulting from this structural alignment, $Ca^{2+}$ are surrounded by four oxygen neighbours of the same chain with a Ca-O distance of 2.55 Å and by another two to four oxygen atoms of the vicinal chain with Ca-O ≈ 2.35 Å - 2.4 Å. If water molecules are abundant, they complete the $Ca^{2+}$ coordination with $Ca-OH_2$ ≈ 2.4 Å - 2.5 Å. (Pattrick, 2001)

Crystallographic information on gypsum, bassanite, and anhydrite and the respective references are given in Table 2-2.

In the gypsum structure, calcium ions are linked to four (same chain) plus two (adjacent chain) oxygen atoms and additionally to two $H_2O$ molecules, resulting in each calcium ion being coordinated by eight oxygen atoms, as displayed in Figure 2-1 (Wooster, 1936). In three dimensions, the structures consists of zigzag double layers of $Ca-SO_4$ chains along the crystallographic [101] direction (body-centered lattice) that are flanked by layers of water molecules on either side (Figure 2-2). Adjacent layers are held together by weak hydrogen bonds that cause the excellent cleavage of gypsum along (00l) planes (Grattan-Bellew, 1975). The pronounced folding of layers can be attributed to further hydrogen bonding to second following layers (Chang et al., 1999; Cole and Lancucki, 1974).

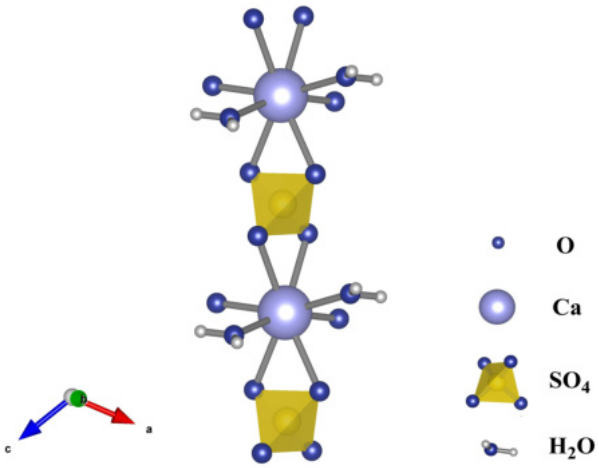


**Figure 2-1:** Section of the $Ca-SO_4$ chain in the gypsum structure. Structure data is taken from Schofield et al. (2000).

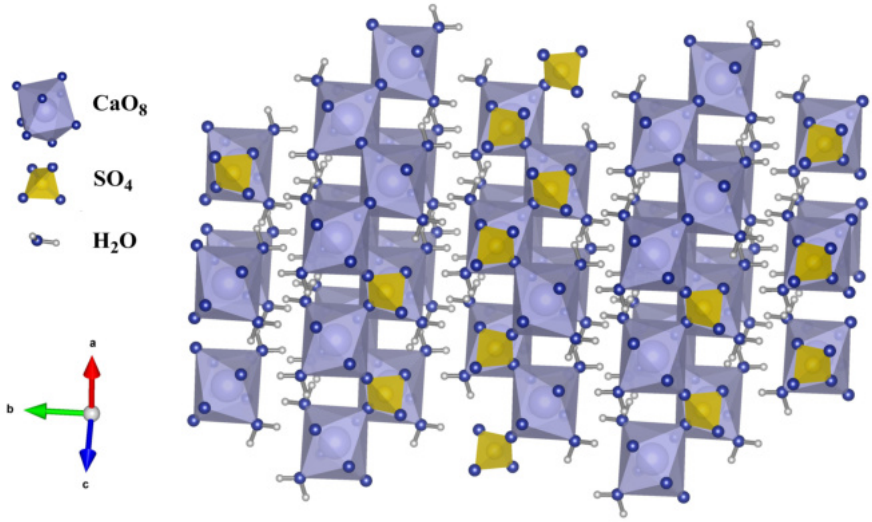


**Figure 2-2:** Projection of gypsum (space group *I*2/c) displaying the alternating sheets of $Ca-SO_4$ double chains and $H_2O$. Structure data is taken from Schofield et al. (2000).

Bassanite (Figure 2-3) is characterized by $Ca-SO_4$ chains forming a channel structure along the crystallographic [001] direction, whereby one channel is made up by six chains. Together with their voids, the channels build a host–guest network with the channels as hosts for the small water molecules as guests (Voigtländer et al., 2003). This feature enables the phase to hold differing amounts of water molecules without major structural reorganization explaining the evolution of subhydrates and $\gamma$-anhydrite as 'dehydrated bassanite' (Hand, 1997).

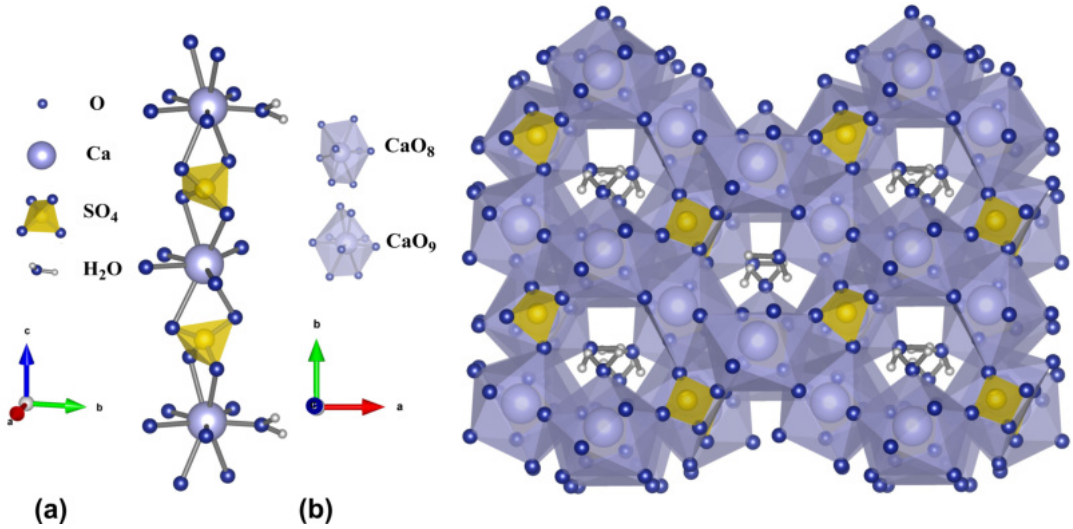


**Figure 2-3:** Crystal structure of bassanite. **(a)** $Ca-SO_4$ chain element showing the eight-fold (4 oxygen atoms of the same chain + 4 oxygen atoms of the adjacent chain) and nine-fold (additional $H_2O$) coordination of calcium. **(b)** Pseudo-trigonal bassanite framework viewed along the $H_2O$-filled $Ca-SO_4$ channels. Structure data taken from Bezou et al. (1995).

In bassanite, calcium is eight-fold, and when water atoms are introduced, nine-fold coordinated (Bushuev, 1982). The structural framework is pseudo-trigonal, as the presence of $H_2O$ molecules enforces a symmetry lowering distortion that ultimately causes a monoclinic symmetry (Ballirano et al., 2001; Weiss and Braeu, 2009). According to Weiss and Braeu (2009), the highest possible applicable symmetry, ignoring minor distortions, would be $P6_422$ (aristotype). Using a Bärnighausen tree, the authors reduced the symmetry in three steps to the monoclinic space group $C2$ (hettotype, Figure 2-4). The translationengleiche subgroups t2 and t3 require an orientation change of the unit cell keeping all translations but belong to a lower crystal class, whereas the isomorphic subgroup i2 belongs to the same or enantiomorphic space group type with fewer translations forcing an unit cell enlargement (special kind of klassengleiche subgroups, Wondratschek et al., 2004).

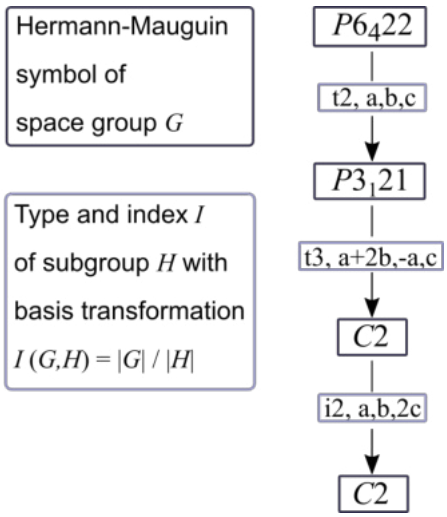


**Figure 2-4:** Symmetry reduction for bassanite from hexagonal to monoclinic according to Weiss and Braeu (2009).

The pseudo-trigonal structure and/or twinning of bassanite has caused earlier publications to find a trigonal or even hexagonal symmetry, *e.g.* Flörke (1952b), Bushuev (1982), Abriel (1983), Lager et al. (1984), Caspari (1936), and Gallitelli (1933). Figure 2-5 shows the positions of $H_2O$ in the channels along the $c$-axis and perpendicular to the $a-b$-plane. The molecules cause a monoclinic distortion of the hexagonal channel framework.

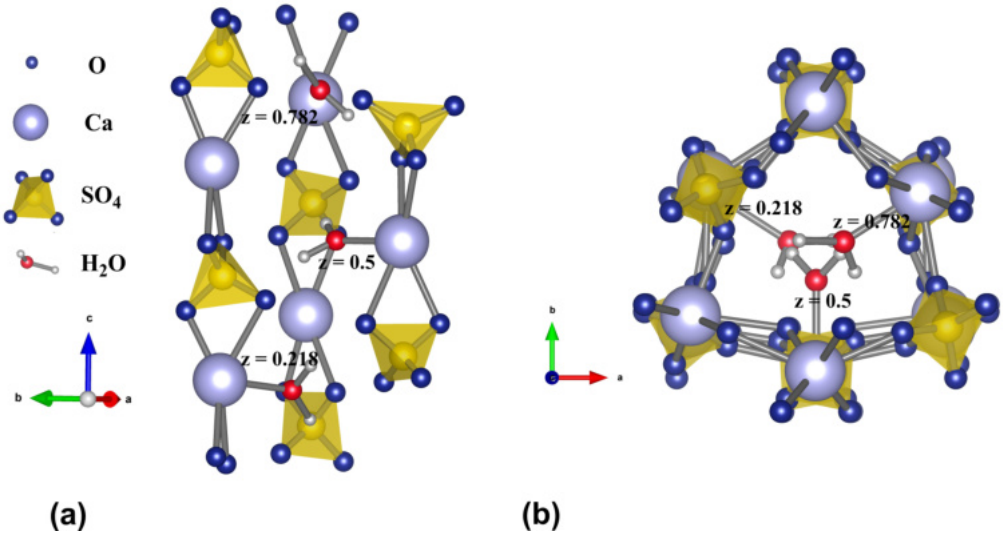


**Figure 2-5:** Positions of $H_2O$ molecules in bassanite **(a)** along and **(b)** orthogonal to [001]. For better overview, the oxygen atoms belonging to $H_2O$ molecules are colored red and fractional $z$-coordinates are given. Structure data taken from Bezou et al. (1995).

The anhydrous calcium sulfate mineral, anhydrite, consists of edge-sharing $CaO_8$ polyhedra and $SO_4$ tetrahedra that form alternating $Ca-SO_4$ chains parallel to the $c$-axis. A fragment of the chain is shown in Figure 2-6. Along the $b$-axis, chains link by sharing polyhedra corners (Hawthorne and Ferguson, 1975). In three dimensions, this generates a densely packed orthorhombic framework. The crystal structure of anhydrite is displayed in Figure 2-7. As mentioned in Section 2-1-2, the synthetic phase $\beta$-anhydrite is structurally equivalent to the mineral.

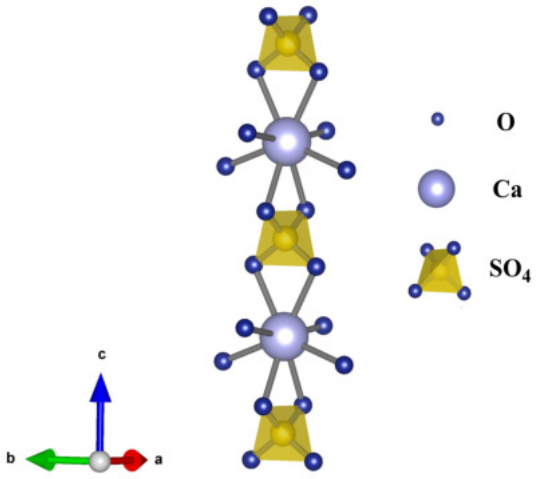


**Figure 2-6:** Section of the $Ca-SO_4$ chain in the anhydrite structure. Structure data taken from Hawthorne and Ferguson (1975).

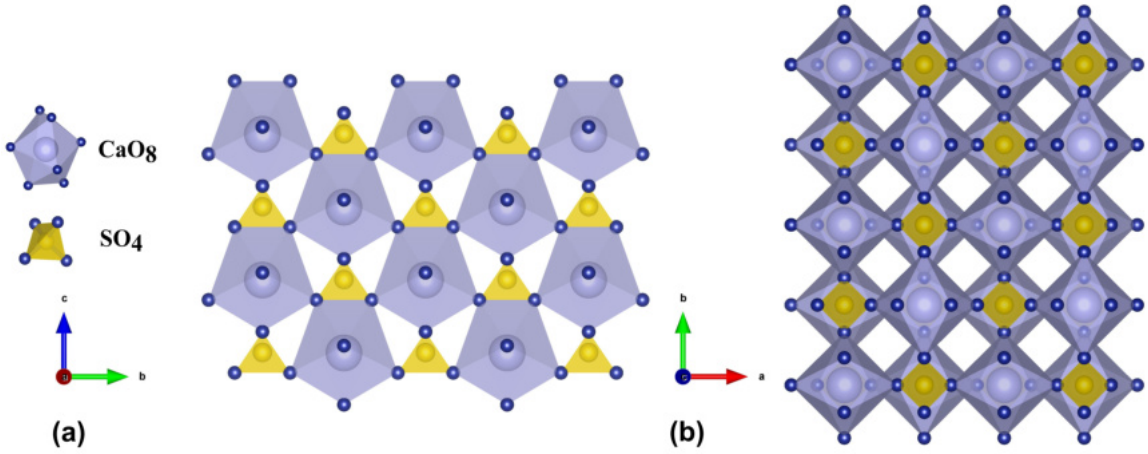


**Figure 2-7:** Crystal structure of anhydrite. **(a)** Structure displayed perpendicular to [010] showing edge-sharing $CaO_8$ polyhedra and $SO_4$ tetrahedra. **(b)** Corner-linked polyhedra and tetrahedra perpendicular to [001]. Structure data taken from Hawthorne and Ferguson (1975).

All calcium sulfate minerals share the common motif of $Ca–SO_4$ chains but the varying amounts of water molecules require distinct structural arrangements. Their transitions are related to changes in composition: The heat-induced transformation of a hydrated to a less or not hydrated calcium sulfate is described by the breakdown of a single solid phase into a solid and a gaseous product and therefore a decomposition reaction (Nic et al., 2005, p. 257). Vice versa, the rehydration reaction demands water availability (liquid or gaseous) for nucleation and growth of the new salt hydrate (Thanh et al., 2014).

**Table 2-2:** Structural parameters of calcium sulfate minerals. $a, b, c, \alpha, \beta, \gamma$ = lattice parameters, $V$ = cell volume, $Z$ = formula unit.

| | **Gypsum** | **Bassanite** | **Anhydrite** |
|---|---|---|---|
| **Symmetry** | $I2/a$ | $I2$ | $A$mma |
| ***a*/Å** | 5.673 | 12.019 | 6.993 |
| ***b*/Å** | 15.105 | 6.930 | 6.995 |
| ***c*/Å** | 6.491 | 12.669 | 6.245 |
| $\alpha$/ ° | 90 | 90 | 90 |
| $\beta$/ ° | 118.512 | 90.235 | 90 |
| $\gamma$/ ° | 90 | 90 | 90 |
| ***V*/Å$^3$** | 488.91 | 1055.33 | 305.48 |
| ***Z*** | 4 | 12 | 4 |
| **Reference** | Schofield et al. (2000) | Bezou et al. (1995) | Hawthorne and Ferguson (1975) |

### 2-2-2 Structures of $\gamma$-anhydrite and the subhydrates

The crystal structure of $\gamma$-anhydrite can be interpreted as dehydrated bassanite (Figure 2-8). The channel framework of calcium sulfate chains along the $c$-axis remains intact but, due to the missing water molecules, the structure undergoes ordering and exhibits hexagonal symmetry. The empty channels have a diameter of 6.968 Å which equals lattice parameters $a$ and $b$ (Christensen et al., 2008). The filled channels in bassanite have diameters ranging between 6.71 Å for the Ca ·· Ca, and 7.14 Å for the S ·· S distance (Bezou et al., 1995). The extensive vacancies inside the channels of $\gamma$-anhydrite is energetically unfavorable and causes the thermodynamic instability at ambient conditions and associated rehydration to bassanite (Allmann, 1994).

Information on structural parameters of $\gamma$-anhydrite and the subhydrate phases is given in Table 2-3.

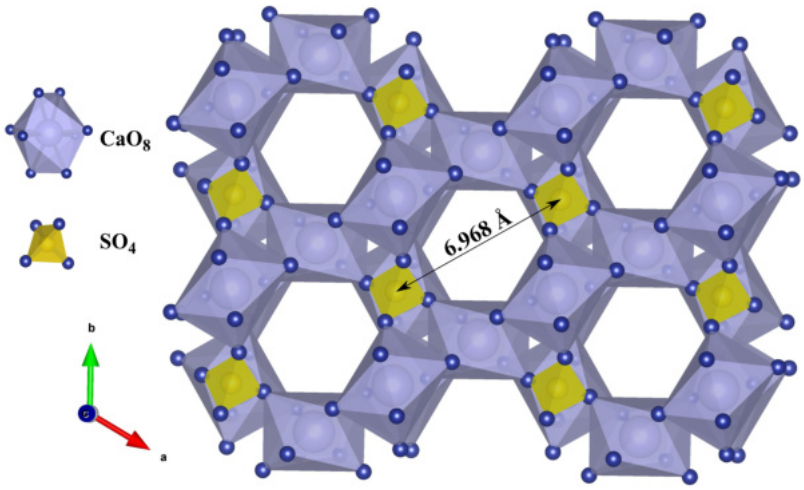


**Figure 2-8:** Crystal structure of $\gamma$-anhydrite showing the undistorted, hexagonal channel framework along the [001] direction. Structure data taken from (Christensen et al., 2008).

Like the evolution of $\gamma$-anhydrite, the occurence of subhydrates can be deduced to the host–guest channel structure of bassanite and its ability to host various amounts of water molecules without undergoing severe structural changes (Flörke, 1952b). Here, the phases registered in the ICSD are presented.

Figure 2-9 shows the structures of the phases subhydrate 0.6 (SH 0.6), subhydrate 0.625 (SH 0.625), subhydrate 0.67 (SH 0.67), and subhydrate 0.8 (SH 0.8) perpendicular to their channels. The nature of water channel occupation of bassanite-type crystal structures is and has been of great interest throughout the years. If all possible water positions inside the channels were occupied, the formation of a calcium sulfate monohydrate ($CaSO_4 \cdot H_2O$) with only $CaO_9$ polyhedra would result, exceeding the theoretical steric hindrance limit of 0.66 water molecules per formula unit (Bezou et al., 1995).

The phases SH 0.6 and SH 0.625 were characterized by Bezou et al. (1995) and Schmidt et al. (2011), respectively. In the case of SH 0.6, the water molecules enter the coordination of Ca in two out of six chains that build the channels. They are grouped by two adjacent molecules with strong hydrogen bonding (Bezou et al., 1995). In SH 0.625, four different types of channels exist. In three of these channel types, each four $H_2O$ molecules are systematically translated mutually. The fourth channel present is similar to these in bassanite.

The subhydrates SH 0.67 and SH 0.8 were investigated by Bushuev (1982) and Abriel (1983), respectively. Both structures reach or exceed the steric limit of 0.66 water molecules. In the first case, two of three and in the second case, four of five possible $H_2O$ positions are occupied. The authors addressed the steric hindrance and notice a mutual repulsion of water molecules leading to arrangements that benefit the maximization of $H_2O$ - $H_2O$ distances. This led them to conclude that the monohydrate formation is unlikely. The authors mention how bassanite is the most stable subhydrate structure, lacking steric hindrance and possessing ordered distribution of vacancies and $H_2O$ positions, as every second possible position is occupied.

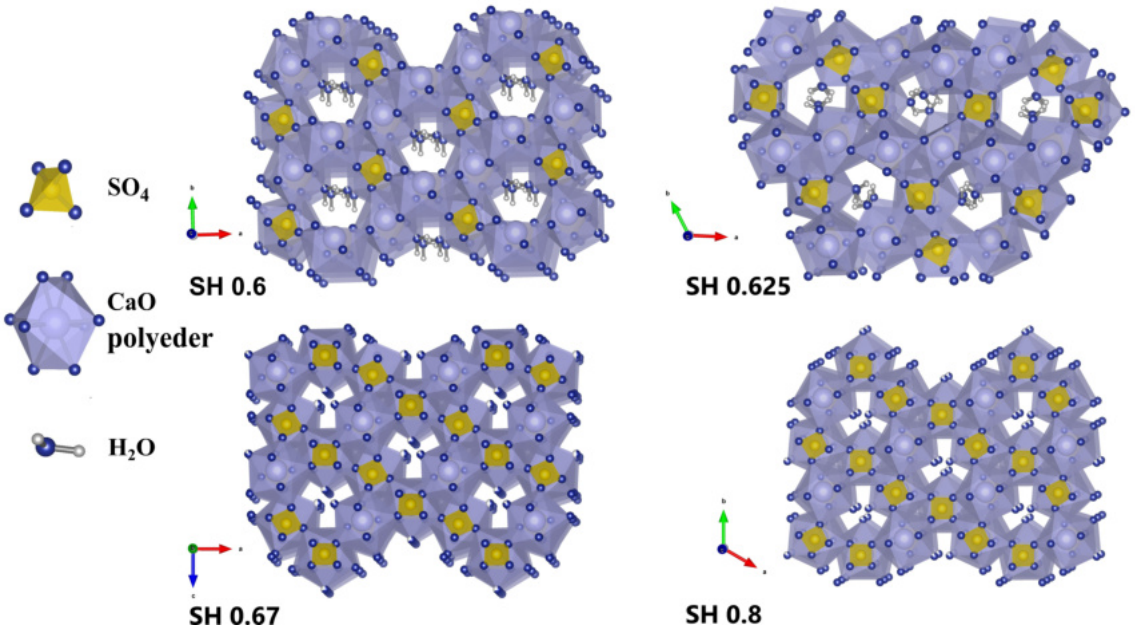


**Figure 2-9:** Crystal structures of subhydrate 0.6 (SH 0.6), subhydrate 0.625 (SH 0.625), subhydrate 0.67 (SH 0.67) and subhydrate 0.8 (SH 0.8) showing the differing $H_2O$ arrangements between the $Ca-SO_4$ chains. Hydrogen positions of SH 0.67 and SH 0.8 are not available. Structure data taken from Bezou et al. (1995); Schmidt et al. (2011); Bushuev (1982); Abriel (1983).

Figures 2-10 to 2-15 display the subhydrates along and perpendicular to their channel structure with regard to $H_2O$ positions and alignment. To provide better overview, oxygen atoms of $H_2O$ are colored red and calcium coordination polyhedra are not depicted as eight or nine vertex figures, but in such a way as to ensure the visibility of $H_2O$.

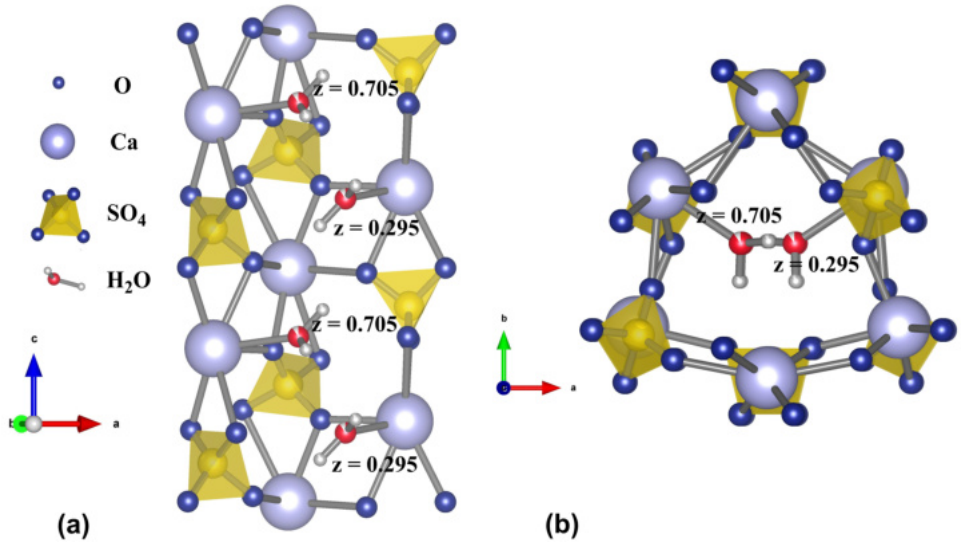


**Figure 2-10:** Crystal structure of subhydrate 0.6: Occupation of calcium sulfate channels with $H_2O$ molecules **(a)** along and **(b)** perpendicular to the channel structure. Fractional $z$-coordinates of oxygen atoms of $H_2O$ molecules are given. Structure data taken from Bezou et al. (1995)

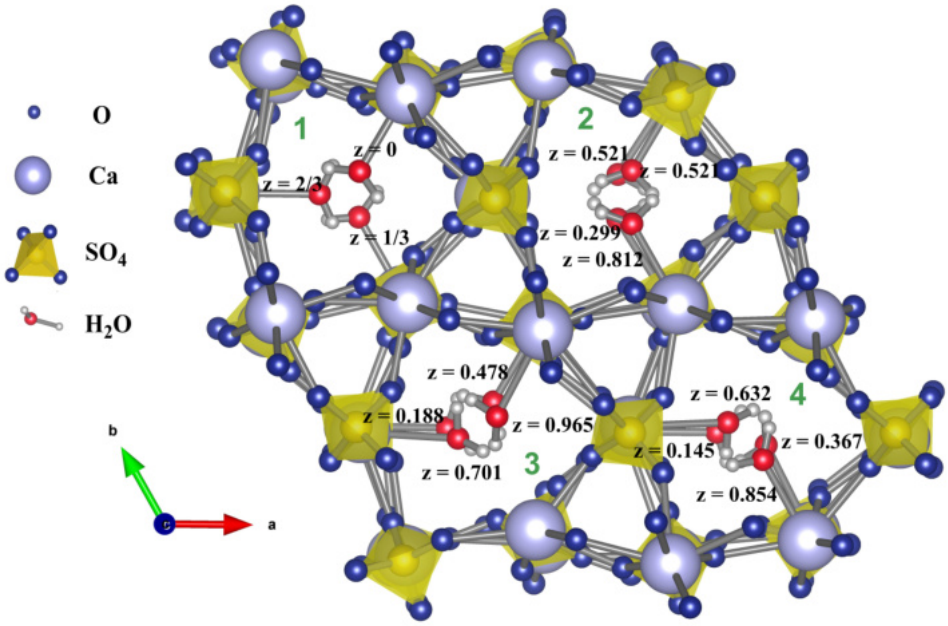


**Figure 2-11:** Crystal structure of subhydrate 0.625: Occupation of four different calcium sulfate channels with $H_2O$ molecules perpendicular to the channel structure. The channels are numbered in green for better overview. Channel 1 resembles those in bassanite. Fractional $z$-coordinates of oxygen atoms of $H_2O$ molecules are given. Structure data taken from Schmidt et al. (2011).

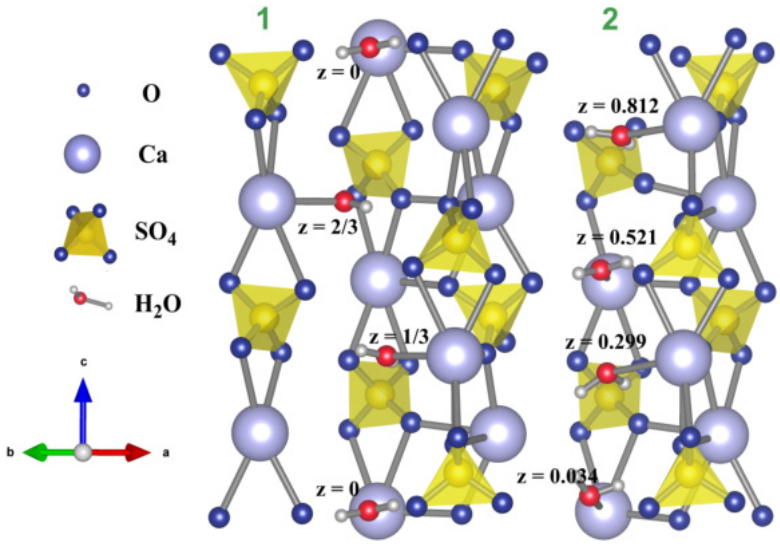


**Figure 2-12:** Crystal structure of subhydrate 0.625: Occupation of calcium sulfate channels with $H_2O$ molecules along channels 1 and 2 (Figure 2-11). Fractional $z$-coordinates of oxygen atoms of $H_2O$ molecules are given. Structure data taken from Schmidt et al. (2011).

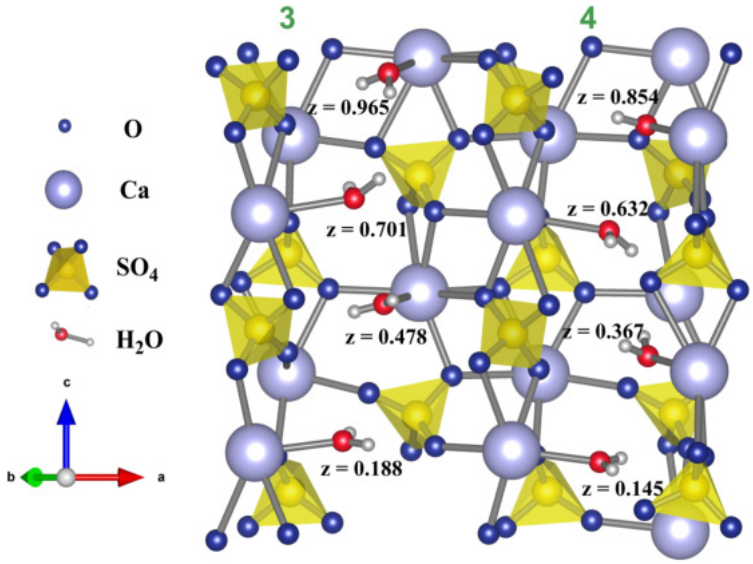


**Figure 2-13:** Crystal structure of subhydrate 0.625: Occupation of calcium sulfate channels with $H_2O$ molecules along channels 3 and 4 (Figure 2-11). Fractional $z$-coordinates of oxygen atoms of $H_2O$ molecules are given. Structure data taken from Schmidt et al. (2011).

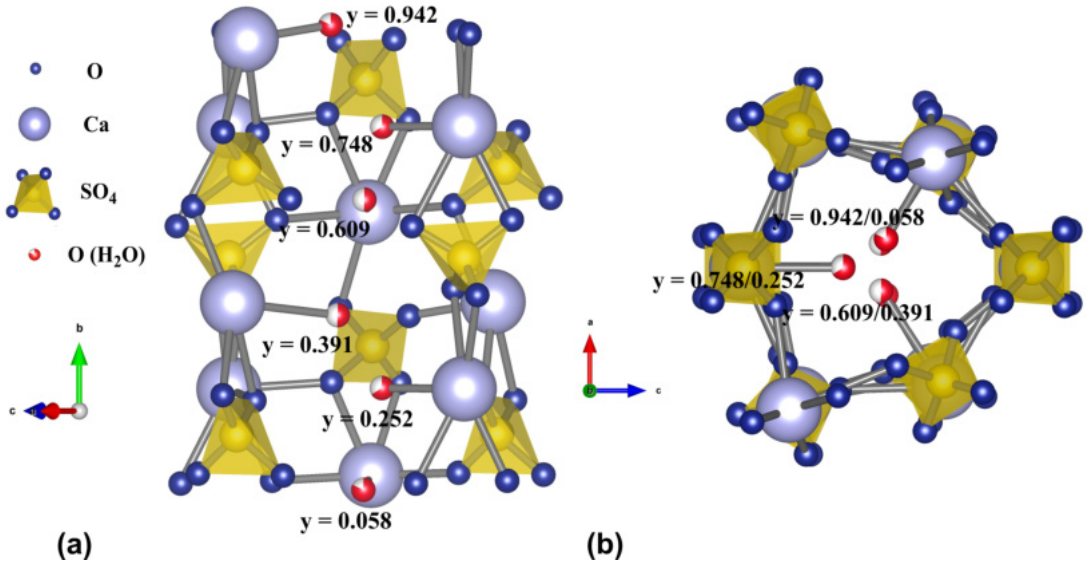


**Figure 2-14:** Crystal structure of subhydrate 0.67: Occupation of calcium sulfate channels with water molecules **(a)** along and **(b)** perpendicular to the channel structure. Fractional $y$-coordinates of oxygen atoms of $H_2O$ molecules are given. Structure data taken from Bushuev (1982).

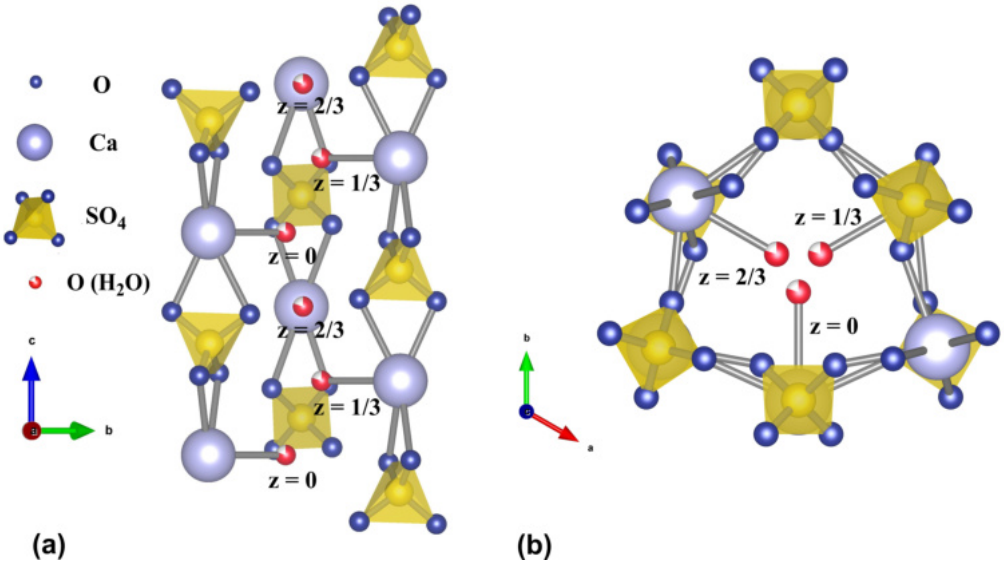


**Figure 2-15:** Crystal structure of subhydrate 0.8: Occupation of calcium sulfate channels with $H_2O$ molecules **(a)** along and **(b)** perpendicular to the channel structure. Fractional $z$-coordinates of oxygen atoms of $H_2O$ molecules are given. Structure data taken from Abriel (1983).

**Table 2-3:** Structural parameters of $\gamma$-anhydrite and calcium sulfate subhydrates. $a, b, c, \alpha, \beta, \gamma$ = lattice parameters, $V$ = cell volume, $Z$ = formula unit, SH = Subhydrate.

| | $\gamma$-Anhydrite | SH 0.6 | SH 0.625 | SH 0.67 | SH 0.8 |
|---|---|---|---|---|---|
| **Symmetry** | $P6_222$ | $C2$ | $P3_221$ | $B2$ | $P3_121$ |
| ***a*/Å** | 6.968 | 11.999 | 13.869 | 12.028 | 6.986 |
| ***b*/Å** | 6.968 | 6.925 | 13.869 | 12.674 | 6.968 |
| ***c*/Å** | 6.360 | 6.3766 | 12.718 | 6.927 | 6.410 |
| $\alpha$/° | 90 | 90 | 90 | 90 | 90 |
| $\beta$/° | 90 | 90 | 90 | 90.21 | 90 |
| $\gamma$/° | 120 | 90 | 120 | 90 | 120 |
| ***V*/Å$^3$** | 264.97 | 529.89 | 2118.7 | 1055.96 | 269.53 |
| ***Z*** | 3 | 6 | 24 | 12 | 3 |
| **Reference** | Christensen et al. (2008) | Bezou et al. (1995) | Schmidt et al. (2011) | Bushuev (1982) | Abriel (1983) |

Concurrently, the structures of $\gamma$-anhydrite and calcium sulfate subhydrates demonstrate the flexibility of the bassanite-type channel structure but also indicate that solely the occupation of every other possible position is energetically favorable at ambient temperature and humidity conditions.

The correct water occupation of channels had been the subject of controversial discussions. For many years, the phases hemihydrate and $\gamma$-anhydrite were considered to be structurally identical. The $H_2O$ molecules in hemihydrate were believed to have zeolithic character and the system was regarded as bivariant. Considering temperature and water vapor-pressure, the water content could then vary continuously without changes in the crystal structure (Preturlan et al., 2019). Some studies described such a bivariant system with 0 to 0.67 $H_2O$ molecules per formula unit, *e.g.* Gardet et al. (1976). Meanwhile, the crystallographic differences between hemihydrate and $\gamma$-anhydrite are free of doubt and several authors and structure databases acknowledged the presented subhydrates as distinct polymorphs (*e.g.* Schmidt et al., 2011).

## 2-3 Dehydrational and rehydrational phase transformations

Dehydration and rehydration processes in the $CaSO_4 - H_2O$ system have been studied for decades. Its supposed simplicity, the great relevance of calcium sulfates as industrial materials, and their geological role motivated many investigations focusing on diverse aspects of the transformational processes. The extensive scope of literature throughout the years allows for detailed insight in these processes but also causes contradiction. Latter can presumably be deduced to the varying experimental set-ups, controlled parameters, and sample properties. Calcium sulfates need to be scrutinized very carefully with regard to internal and external parameters as the last decades of research prove. To assess the information on dehydration and rehydration processes and, consecutively, design further experiments, it is important to reflect the existing information with attention on the measurement circumstances. This review is, however, not exhaustive due to the great extent the system was investigated.

### 2-3-1 Dehydration processes

The vast majority of studies concerning calcium sulfate transformations in the solid state concentrates on the dehydration of gypsum to hemihydrate or $\gamma$-anhydrite. Seldom, dehydration is contemplated until $\beta$-anhydrite. At first, the existence and differences of solid phases were debated. Eventually, the focus shifted to the process and its kinetics under defined miscellaneous conditions. The investigations were primarily executed by thermal analytical, diffraction and spectroscopic methods. In the following, selected information from studies throughout the years are presented. The findings of several examinations concerning gypsum or hemihydrate dehydration experiments are compiled in Table 2-4.

Lavoisier's examinations in 1765 are one of the first scientific examinations on calcium sulfates. His gypsum calcination experiments yielding differences in the behavior of structurally bound water laid the foundation for following investigations on gypsum dehydration (Wirsching, 2000). In 1887, Le Châtelier took up Lavoisier's approach and conducted dihydrate heating experiments, in which he observed a two-step dehydration process by tracing heat effects caused by temperature standstills. The loss of 1.5 water molecules occurred at 128 °C and the consecutive loss of 0.5 water molecules at 163 °C yielded complete dehydration (quoted by Groves, 1958, p. 108). Le Châtelier was also the first to recognize that the widely used building material 'Plaster of Paris' is equivalent to calcium sulfate hemihydrate and how its setting leads to gypsum formation (Posnjak, 1938). The role of hemihydrate as industrial material is further contemplated in Section 2-7.

In 1903, Van't Hoff et al. conducted one of the first extensive studies on the $CaSO_4 - H_2O$ system. During their investigations on phase equilibria in contact with water, they identified the four solid phases anhydrite, gypsum, hemihydrate, and - the compound provoking subsequent discussions - 'soluble anhydrite'. Due to some experimental mistakes during the study (Charola et al., 2006), reinvestigations of solid calcium sulfate phases were carried out by Ramsdell and Partridge (1929). The authors came, *inter alia*, to the conclusion that Van't Hoff's soluble anhydrite is not a distinct calcium sulfate but structurally identical to hemihydrate. According to them, their study confirmed the results by Linck and Jung (1924) who described the nature of hemihydrate as zeolitic (in reference to the release and uptake of water molecules without changes in the crystal structure). A few years later, Caspari (1936) also reported that calcium sulfate hemihydrate and its dehydration product show identical X-ray diffraction patterns. In contrast to those findings, Feitknecht (1931), Onorato (1932) and Gallitelli (1933) stated that the hemihydrate and the so-called soluble anhydrite are indeed different in their crystal structures as they recognized minor differences in the diffraction patterns. Even more so, Feitknecht (1931) believed that Linck and Jung (1924) did measure a partially rehydrated instead of the supposed dehydrated sample. Similarly, Weiser et al. (1936) concluded that water molecules occupy fixed positions in the lattice and attributed differing results of other studies to measurement and experimental circumstances.

This result disparity starts and foreshadows the long-term dissent about the structural differences of hemihydrate and $\gamma$-anhydrite and the character of the $H_2O$ bonds. Many investigations later, the disagreements had been put to an end and the results by Weiser et al. (1936) and fellow colleagues were acknowledged with the wide acceptance of 0.5 $H_2O$ per formula unit in hemihydrate and its structural difference to the "soluble" $\gamma$-anhydrite.

A connoting study on the $CaSO_4 - H_2O$ system was done by Posnjak (1938). His investigations included dehydrating selenite single crystals by contemplating differential heating curves. The two-step dehydration process was always observed but the heating rate and coarseness strongly influenced the temperature of the heating curve maxima. Posnjak also confirmed Van't Hoff's statement in regard to four solid phases. As he acknowledged the evidence for the enantiomorphic inversion of anhydrite to the high-temperature phase, he suggested to use the commonly followed way of differentiating polymorphic modifications by labeling the anhydrous calcium sulfates $\alpha$-, $\beta$-, $\gamma$-anhydrite.

Regarding dehydration reactions under controlled water-vapor pressures, it was Weiser et al. (1936) who already pointed out the need for atmosphere control during decomposition reactions. Several years later, McAdie (1964) also adressed the lack of systematic water-vapor pressure control. He carried out kinetic experiments by measuring the weight loss of polycrystalline gypsum particles between 100 °C and 140 °C at $p_{H_2O}$ ranging from 0 hPa to (nearly) 1013 hPa. His elucidation of the reaction kinetics as throughout linear was criticized by later studies (*e.g.* Ball and Norwood, 1969). However, the influence of water-vapor pressure on dehydration stages (gypsum–hemihydrate and hemihydrate–$\gamma$-anhydrite) became evident.

Thermal analytical (TA) methods including thermogravimetry (TG), differential thermogravimetry (DTG), differential thermal analysis (DTA) and differential scanning calorimetry (DSC) were particularly widely applied to study gypsum dehydration reactions. Among these, TG was most frequently used to identify the thermal formation conditions of calcium sulfate phases, as Keattch (1967) reflected. He mentions how previous work showed that not a two- but a single-step dehydration process is observed when small sample sizes are heated dynamically in static air atmospheres. To achieve a two-step process, he applied a combination of isothermal and non-isothermal treatment. Isothermal dehydration at 90 °C to 93 °C yielded weight loss that equals -1.5 water molecules and subsequent heating to 160 °C caused further dehydration. His results were obtained without controlling $p_{H_2O}$ and with a combination of dynamic and static heating, lacking systematic parameter control. Cautiously interpreted from a today's point of view, Keattch's brief article might be understood as an example how the industrial relevance of gypsum plaster products created the fast need of information about the calcium sulfate–water system. However, the differing sample and measurement parameters of alike investigations rather created a patchwork of results.

In 1969, Ball and Norwood strongly criticized the results obtained by studies that were not aware of the need for atmosphere control. They studied reaction kinetics of synthetic gypsum dehydration and chose temperatures between 80 °C - 152 °C and water-vapor pressures between 0.001 Pa - 6000 Pa. Their dehydration products were $\beta$-hemihydrate and $\gamma$-anhydrite. Over the range of 115 °C - 152 °C and all water-vapor pressures, they only observed $\gamma$-anhydrite as dehydration product. At lower temperatures, hemihydrate is produced and stabilized by higher water-vapor pressures. However, their results are not consistent throughout the temperature and pressure regime as it is incongruent that hemihydrate is stable at circa 84 °C and a $p_{H_2O}$ of 2400 Pa but would decompose further to $\gamma$-anhydrite at the same $p_{H_2O}$ and a lower temperature. Concerning the reaction kinetics, they found the rate-controlling steps (nucleation control, boundary control, diffusion of water) to vary with temperature and water-vapor pressure.

In a consecutive study about hemihydrate dehydration (115 °C to 140 °C, $p_{H_2O}$ = 0 Pa to 5600 Pa), Ball and Urie (1970) constitute a diffusion-controlled mechanism for the emergence of $\gamma$-anhydrite.

A different approach to control the surrounding atmosphere was taken by Molony and Ridge (1968). To avoid most influences, they conducted measurements at 85 °C *in vacuo* so that the dehydration process was only controlled by the educt–product interface and water diffusion. They found the interface progression to control the rate. Taylor and Baines (1970) also did not control the water-vapor pressure but the surrounding air pressure from 1.3 hPa - 1016 hPa at 100 °C and discovered that the fastest reaction rate would be at air pressures between 930 Pa and 2400 Pa which suggests, according to them, that the optimization of the reaction rate would occur at lesser $p_{H_2O}$ values. Both studies chose alternatives to control the water-vapor pressure to study dehydration kinetics but since calcium sulfate transformation processes are defined by the loss of $H_2O$ molecules, understanding the effect of water-vapor pressure is of great interest.

Due to hemihydrate having two forms, Kuntze (1965) looked at the influence of water-vapor on the evolution of $\alpha$- and $\beta$-hemihydrate. He observed $\beta$-hemihydrate to always be the dehydration product in the $p_{H_2O}$ range of 164 hPa - 1013 hPa at temperatures from 0 °C - 200 °C using a heating rate of 6 °C min$^{-1}$. Under these circumstances, he found the gypsum–$\beta$-hemihydrate conversion to proceed at 150 °C. The discrimination between the two hemihydrates was done by evaluating peak positions during DTA. From the displacement of the second peak position, indicating $\gamma$-anhydrite evolution, he figured that for each temperature a threshold water-vapor pressure exists, above which $\gamma$-anhydrite cannot be formed.

Deeper focusing on the kinetic processes of gypsum dehydration were, *inter alia*, Borisenko (1965), Khalil (1982), and Vakhlu et al. (1985). Vakhlu et al. mutually compared the results of the first mentioned authors and with earlier studies conducted by McAdie (1964), Molony and Ridge (1968), Heide (1969), Ball and Norwood (1969), Murat and Comel (1971), and Negro and Stafferi (1972). The authors elaborated how the formal kinetic approaches/findings are inconsistent with each other. Once again, the different experimental conditions (*e.g.* disregard of water-vapor pressure control, non-isothermal vs. isothermal conditions) are most likely to impede corroborating findings. A decade later, Deutsch et al. (1994) carried out isothermal experiments and tested 15 equations to find the best fitting model. However, no model fitted all samples which they mainly deduce to differences in crystallite characteristics.

Putnis et al. (1990) studied gypsum dehydration at negligible water-vapor pressure from 50 °C - 106 °C by combining *in situ* infrared (IR) spectroscopy and TG. As one of the first groups, they used two techniques to investigate the dehydration mechanism and to revise subhydrate evolution during dehydration. Concerning appearances of dehydration products, they did not observe subhydrates and confirmed hemihydrate and $\gamma$-anhydrite which is in accordance with other dehydration studies. As dehydration mechanism, they observed nucleation to drive the reaction. However, their TA experiment failed to prove the two-step dehydration as the loss of water appeared to be continuous.

Abriel et al. (1990) conducted a neutron and X-ray diffraction (XRD) experiment (22 °C - 350 °C) with which he confirmed subhydrates during gypsum dehydration. He states that although vacuum was applied, local $H_2O$ steam pressures generated by the decomposing gypsum cause evolving dehydration products to develop overfull tunnels. Considering the dehydration mechanism, he notes a topotactic one as at least one-dimensional structural chain elements should be preserved.

Badens et al. (1998), who did experiments with controlled transformation-rate thermal analysis (CTRA) at constant pressure of water-vapor (1 Pa, 500 Pa and 900 Pa), found the final dehydration products to vary with applied water-vapor pressures. In accordance with Abriel et al. (1990) they propose a topotactic transformation under the circumstances of their experiment.

The (comparatively) present state of investigations on gypsum dehydration can possibly be represented by studies like Prasad et al. (2001), Chio et al. (2004), Prasad et al. (2005), Carbone et al. (2008), Ballirano and Melis (2009b), Ballirano and Melis (2009a), Berthold et al. (2011), Lou et al. (2011), and Schmid et al. (2020). These authors predominantly used *in situ* powder XRD or spectroscopy without $p_{H_2O}$-control to study the dehydration reactions. Berthold et al. (2011), constructed a coupled DTA-$\mu$XRD$^2$ set-up to follow the non-isothermal dehydration process up to $\beta$-anhydrite evolution. Carbone et al. (2008) focused on the gypsum dehydration at a reduced air pressure of 100 Pa and temperatures ranging from 40 °C - 80 °C. The dehydration study by Lou et al. (2011) was only conducted with gypsum obtained by flue gas desulfurization (FGD). Although FGD gypsum is structurally identical to natural gypsum and known for a long time, the relevance rose due to the increase in power plants and $SO_2$ emissions since the 2000's (Lu et al., 2010) in East Asia. Some of these studies are relevant to the present work and their findings are compared the present results in Chapter 6.

**Table 2-4:** Dehydration experiments in the solid state - Overview. DH = Dihydrate, $CaSO_4 \cdot 2\,H_2O$, HH = Hemihydrate, $CaSO_4 \cdot 0.5\,H_2O$, AH = Anhydrite, $CaSO_4$, SH 0.8 = Subhydrate, $CaSO_4 \cdot 0.8\,H_2O$, RH = Relative humidity, *as far as specified.

| Reference | Method/Experimental conditions | Dehydration temperature/Products* | Activation Energy $\mathbf{E_a}$* | Kinetic information* |
|---|---|---|---|---|
| Le Châtelier (1887) | DH dehydration by heating to 200 °C, analysis by temperature halts | 128 °C (DH → HH); 163 °C (HH → γ-AH) | | |
| McAdie (1964) | Isothermal and non-isothermal, isohumid DH dehydration at jacket temperatures (JT) of 100 °C - 139 °C and $p_{H_2O}$ = 0 hPa - 1013 hPa, analysis by TG | 97.1 °C (DH → HH, 100 °C JT, 0 hPa); 119.2 °C (DH → HH, 139 °C JT, 0 hPa); no dehydration at 100 °C JT, 1013 hPa; 123 °C (DH → HH, 139 °C JT, 1013 Pa); 99.1 °C (HH → γ-AH, 100 °C JT, 0 Pa); 126.3 °C (HH → γ-AH, 139 °C JT, 0 Pa); 99.3 °C (HH → γ-AH, 100 °C JT, 133 hPa); 126.7 °C (HH → γ-AH, 139 °C JT, 133 hPa) | 109 kJ mol$^{-1}$ (DH → HH, 100 °C - 139 °C JT, 0 hPa); 201 kJ mol$^{-1}$ (DH → HH, 100 °C - 139 °C, 133 hPa); 87.5 kJ mol$^{-1}$ (HH → γ-AH, 100 °C - 139 °C JT, 0 hPa); 121 kJ mol$^{-1}$ (HH → γ-AH, 100 °C - 139 °C JT, 133 hPa) | Water-vapor causes initial acceleration and subsequent retardation of the dehydration rate. **Formal kinetics:** Linear, zero-order process $\alpha = kt$ [1] |
| Kuntze (1965) | Isohumid DH dehydration at temperatures up to 500 °C and $p_{H_2O}$ = 0 hPa - 1013 hPa, analysis by DTA [2] | 110 °C (DH → HH, 0 hPa); 145 °C γ-AH (0 hPa); 120 °C HH (1013 hPa); 187 °C (HH → γ-AH, 1013 hPa) | | |
| Keattch (1967) | Isothermal DH dehydration at 90 °C - 93 °C, analysis by TG [3] | HH → γ-AH within 2 h | | |
| Molony and Ridge (1968) | Isothermal DH dehydration *in vacuo* at 85 °C | DH → γ-AH after 24 h conversion of 94 % | | Kinetics controlled by interface advance. **Formal kinetics:** Contracting volume (diminishing sphere) appears rate controlling, $A - B(1-\alpha)^{1/3} = kt$ with constants $A, B$ |
| Ball and Norwood (1969) | Isothermal and isohumid DH dehydration at 80 °C - 152 °C and $p_{H_2O}$ = 0 hPa - 60 hPa | < 115 °C (DH → HH); > 115 °C (HH → γ-AH) | Minimum - maximum $E_a$ values: 41 kJ mol$^{-1}$ (DH → γ-AH, 22 hPa, diffusion control); 246 kJ mol$^{-1}$ (DH → HH, 6 hPa, nucleation control) | > 110 °C: Diffusion controlled, **formal kinetics**: $\alpha^2 = kt$; < 110 °C, complex kinetics affected by water-vapor, including *e.g.* nucleation and boundary control processes at $p_{H_2O}$ = 1 hPa, **formal kinetics**: $2(-\ln(1-\alpha))^{2/3} = kt$ (JMAEK [4]), $1-(1-\alpha)^{0.5} = kt$ (contracting area/disc), $(1-\alpha)\ln(1-\alpha) + \alpha = kt$ (2D diffusion) |
| Heide (1969) | Analysis by $\mu$TG | | 130 kJ mol$^{-1}$ (DH → HH) | Nucleation control of reaction rate, **formal kinetics**: $(-\ln(a-\alpha))^{1/n} = kt$ |

Continued on next page

continued.

| Reference | Method/experimental conditions | Dehydration temperature/products* | Activation energy $E_a$* | Kinetic information* |
|---|---|---|---|---|
| Ball and Urie (1970) | Isothermal and isohumid HH dehydration at 115 °C - 152 °C and $p_{H_2O}$ = 0 hPa - 53 hPa, analysis by TG | $\gamma$-AH was obtained at all temperature and $p_{H_2O}$ values | Minimum - maximum $E_a$ values: 27 kJ mol$^{-1}$ (0 hPa) - 205 kJ mol$^{-1}$ (53 hPa) | Diffusion-controlled mechanism (1D, 2D) |
| Murat and Comel (1971) | Non-isothermal DH dehydration, analysis by $\mu$DTA/DTA | | Differing values for overall three stages of DH $\rightarrow$ $\gamma$-AH: 288 kJ mol$^{-1}$ - 577 kJ mol$^{-1}$ (nucleation), 105 kJ mol$^{-1}$ - 251 kJ mol$^{-1}$(nuclei propagation), 59 kJ mol$^{-1}$ - 63 kJ mol$^{-1}$ (diffusion of water), probably all $\gamma$-AH | Three types of controlling kinetics: Nucleation/nucleation growth/diffusion |
| Clifton (1971) | Non-isothermal DH dehydration at 25 °C - 500 °C and $p_{N_2}$ = 1 hPa - 1013 hPa, analysis by DTA/TG/DSC | 150 °C (DH $\rightarrow$ HH); 197 °C (DH $\rightarrow$ $\gamma$-AH); 375 °C (DH $\rightarrow$ $\beta$-AH) | | |
| Khalil and Gad (1972) | Isothermal DH dehydration at 90 °C, analysis by DTA | HH formation after 3 h - 4 days | | |
| Negro and Stafferi (1972) | Non-isothermal $\mu$DTA | $\gamma$-AH | 75 kJ mol$^{-1}$ - 79 kJ mol$^{-1}$ (HH $\rightarrow$ $\gamma$-AH) | **Formal kinetics:** $(-\ln(1-\alpha))^n = kt$ (JMAK with $n = 2$) |
| Gardet et al. (1976) | Isothermal and isohumid DH dehydration at 54 °C to 85 °C and dynamic vacuum to $p_{H_2O}$ = 43 hPa, analysis by TG | Dehydration to $\gamma$-AH all temperatures and all partial pressures | 155 kJ mol$^{-1}$ (dynamic vacuum), 251 kJ mol$^{-1}$ (43 hPa) | Reaction rates decrease monotonically with water-vapor pressure. **Formal kinetics:** $\ln(\alpha/(1-\alpha)) + C = kt$ (Prout - Tompkins [5]) and $1-(1-\alpha)^{1/n} = kt$ (contracting area/volume) |
| Paulik et al. (1992) | Non-isothermal DH dehydration up to 400 °C, analysis by TG/DTG [6]/DTA | 115 °C - 125 °C (DH $\rightarrow$ HH); 120 °C - 200 °C (HH $\rightarrow$ $\gamma$-AH) | | |
| Vakhlu et al. (1985) | Non-isothermal DH dehydration, analysis by TG/DTA/DTG | 127.7 °C to 127.8 °C (DH $\rightarrow$ HH), 153 °C to 156 °C (DH $\rightarrow$ $\gamma$-AH) | 113 kJ mol$^{-1}$ (DH $\rightarrow$ $\gamma$-AH) | Best fit was yielded with nucleation control. **Formal kinetics:** $(-ln(1-\alpha))^{0.5} = kt$ (JMAEK) |
| Putnis et al. (1990) | Isothermal DH dehydration at 50 °C - 106 °C at negligible $p_{H_2O}$, analysis by IR [7] spectroscopy and TG | $\gamma$-AH at all temperatures | No changes in $E_a$ values as function of the degree of dehydration were detected: 90.3 kJ mol$^{-1}$ | Nucleation control appeared to be rate-controlling. |
| Abriel et al. (1990) | Non-isothermal DH dehydration at 22 °C - 350 °C, analysis by *in situ* neutron diffraction and XRD | > 57 °C (DH $\rightarrow$ SH 0.8/$\gamma$-AH), > 252 °C (DH $\rightarrow$ $\beta$-AH) | | |

Continued on next page

continued.

| Reference | Method/experimental conditions | Dehydration temperature/products* | Activation energy $E_a$* | Kinetic information* |
|---|---|---|---|---|
| Deutsch et al. (1994) | Isothermal (40 °C to 90 °C) and non-isothermal DH and HH dehydration, analysis by TG, DTA | Isothermal: Differing results depending on sample, *e.g.* at 90 °C $\gamma$-AH formation after 8 h, non-isothermal: 100 °C - 130 °C (DH → HH) | | Differences in DH - HH (accelatory) and HH - $\gamma$-AH (deccelatory) kinetics. **Formal kinetics:** No kinetic model fitted all the samples. Best fits: Reaction order (DH - HH), $\alpha^n = kt$ (Power law, HH - $\gamma$-AH) |
| Strydom et al. (1995) | Non-isothermal DH dehydration up to 450 °C, analysis by TG/DSC [8] | Dehydration proceeds > 60 °C, mainly at 95 °C - 170 °C (DH → HH/$\gamma$-AH) | Three parts of dehydration with different $E_a$ values: 392.5 kJ mol$^{-1}$ ± 100 kJ mol$^{-1}$; 100.5 kJ mol$^{-1}$ ± 1.2 kJ mol$^{-1}$; 95 kJ mol$^{-1}$ ± 15 kJ mol$^{-1}$ | Three types of **formal kinetics:** for $\alpha < 0.1$: 3D diffusion acc. to Jander; for $0.1 < \alpha < 0.7$: First order reaction with autocatalytic activation acc. to Prout - Tompkins; $0.7 > \alpha$: Diffusion control acc. to Šesták - Berggren |
| Hudson-Lamb et al. (1996) | Non-isothermal DH dehydration up to 450 °C, analysis by TG/DSC | Dehydration proceeds > 60 °C, > 165 °C mainly $\gamma$-AH formation | Minimum - Maximum $E_a$ values: 88 kJ mol$^{-1}$ ± 18 kJ mol$^{-1}$, 137.2 kJ mol$^{-1}$ ± 24.5 kJ mol$^{-1}$ | Differing types of **formal kinetics** depending on sample and conversion fraction, including 3D diffusion acc. to Jander/nucleation acc. to JMAEK/-first order reaction |
| Sarma et al. (1998) | Non-isothermal DH dehydration up to 277 °C at circa 60 % RH, analysis by *in situ* Raman spectroscopy | 115 °C (DH → HH), 175 °C (HH → $\gamma$-AH) | 92.25 kJ mol$^{-1}$ (DH → HH); 32.94 kJ mol$^{-1}$ (HH → $\gamma$-AH) | |
| Badens et al. (1998) | Non-isothermal DH dehydration up to 647 °C at $p_{H_2O}$ = 0.01 hPa, 5 hPa, 9 hPa, analysis by CRTA[9] | 80 °C (DH → HH, 9 hPa), 108 °C (HH → $\gamma$-AH, 9 hPa) | | |
| Chang et al. (1999) | Non-isothermal DH dehydration from 25 °C to 300 °C and stagnant RH of circa 50 % at 25 °C, analysis by *in situ* Raman spectroscopy | 118 °C - 142 °C (DH → HH); 92 °C - 122 °C (HH → $\gamma$-AH) | | |
| Oetzel et al. (2000b) | Isothermal, non-isothermal, isohumid DH dehydration from 20 °C to 200 °C and up to $p_{H_2O}$ = 1000 hPa, analysis by *in situ* XRD | Isothermal: 86 °C (DH → HH, 10 hPa, several minutes); non-isothermal: 190 °C - 200 °C (DH → HH, $p_{H_2O}$ = 10 hPa), non-isothermal: 100 °C (DH → $\gamma$-AH, ambient $p_{H_2O}$) | | |
| Prasad et al. (2001) | Non-isothermal DH dehydration at 27 °C - 177 °C, analysis by *in situ* Raman spectroscopy | > 97 °C: HH formation with preceding $\gamma$-AH; > 360 °C $\beta$-AH formation | 32.5 kJ mol$^{-1}$ (HH → $\beta$-AH) | |

Continued on next page

continued.

| Reference | Method/experimental conditions | Dehydration temperature/products* | Activation energy $E_a$* | Kinetic information* |
|---|---|---|---|---|
| Fatu (2001) | Non-isothermal DH dehydration up to 165 °C, analysis by TG/DTA | | Minimum - Maximum $E_a$ values: 117 kJ mol$^{-1}$ (loss of water), 283 kJ mol$^{-1}$ (nuclei interaction with texture) | |
| Chio et al. (2004) | Non-isothermal DH dehydration from 18 °C to 100 °C, analysis by *in situ* $\mu$Raman spectrometry | At 100 °C $\gamma$-AH formation (no intermediate HH) | | |
| Prasad et al. (2005) | Non-isothermal DH dehydration at 27 °C - 157 °C, analysis by *in situ* FTIR [10] | At 117 °C $\gamma$-AH formation (no intermediate HH) | | |
| Ballirano and Melis (2009b) | Isothermal DH dehydration at 75 °C - 130 °C, 50 % RH at room temperature, analysis by *in situ* XRD | 95 °C - 120 °C (DH $\rightarrow$ HH, 8 h); > 125 °C (HH $\rightarrow$ $\gamma$-AH, 8 h) | 109 kJ mol$^{-1}$ (DH $\rightarrow$ $\gamma$-AH) | No change of dehydration mechanism considering HH and $\gamma$-AH evolution. **Formal kinetics:** Nucleation control (JMAEK) |
| Ballirano and Melis (2009a) | Isothermal HH dehydration from 105 °C to 150 °C, 50 % RH at room temperature, analysis by *in situ* XRD | 115 °C - 135 °C (HH $\rightarrow$ $\gamma$-AH) | 73.5 kJ mol$^{-1}$ independent of kinetic model | **Formal kinetics:** Nucleation control yielded best fit (JMAEK) |
| Berthold et al. (2011) | Non-isothermal DH dehydration up to 450 °C, analysis by $\mu$XRD/DTA | 100 °C - 150 °C (DH $\rightarrow$ HH); 350 °C - 400 °C (HH $\rightarrow$ $\gamma$-AH) | | |
| Lou et al. (2011) | Isothermal (70 °C - 95 °C) and non-isothermal (95 °C - 170 °C) DH dehydration at negligible and autogeneous $p_{H_2O}$, analysis by TG/DSC | Dehydration to $\gamma$-AH at all temperatures, one-step process (negl. $p_{H_2O}$) vs. two-step process (autogen. $p_{H_2O}$) | 111 kJ mol$^{-1}$ - 194 kJ mol$^{-1}$ (DH $\rightarrow$ HH); 72 kJ mol$^{-1}$ - 136 kJ mol$^{-1}$ (DH $\rightarrow$ $\gamma$-AH) | DH to HH transformation is mainly nucleation and nuclei growth controlled (autog. $p_{H_2O}$); HH to $\gamma$-AH is controlled by phase boundary mechanisms (neg. $p_{H_2O}$) |
| Schmid et al. (2020) | Non-isothermal DH dehydration from 30 °C to 1300 °C, analysis by *in situ/ex situ* Raman spectroscopy | > 80 °C HH formation; > 110 °C $\gamma$-AH formation; > 180 °C traces of $\beta$-AH formation | | |

[1] $\alpha$ = conversion fraction, $k$ = rate constant (Chapter 4).
[2] DTA = differential thermal analysis.
[3] TG = thermogravimetry.
[4] JMAEK (model) = kinetic reaction model according to authors Johnson, Mehl, Avrami, Erefe'ev, Kolmogorov (Chapter 4-1).
[5] Prout-Tompkins (model) = kinetic reaction model according to authors Prout and Tompkins (Chapter 4-1).
[6] DTG = differential thermogravimetry.
[7] IR = infrared spectroscopy.
[8] DSC = differential scanning calorimetry.
[9] CRTA = constant rate thermal analysis.
[10] FTIR = Fourier-Transform infrared spectroscopy.

This tabular overview emphasizes result ambiguity as well as similarities. The dehydration process is described by a two-step process (DH → HH → $\gamma$-AH), except in those cases where the chosen heating rate prevents detection of hemihydrate. During dehydration, subhydrate evolution is not witnessed except in one study. The formation of $\beta$-anhydrite is only witnessed if temperatures are increased (circa >> 150 °C). As most studies prefer dynamic heating, isothermal $\beta$-anhydrite formation at lower temperatures is not focused on. Evidently, the dehydration kinetics depend on the study design. To understand the influence of single parameters on process kinetics, it appears necessary to control as many other parameters as possible to yield comparable data sets.

### 2-3-2 Rehydration processes

Compared to the dehydration reactions of calcium sulfate hydrates, rehydration reactions are subject of fewer studies. Investigations regarding water-vapor invoked rehydration of hemihydrate or $\gamma$-/$\beta$-anhydrite in the solid state are not available (to the best of my knowledge). An overview of rehydration experiments is given in Table 2-5.

Several studies are dedicated to the hydration of hemihydrate in suspension due to the great industrial interest in the setting process and its alteration. Hansen (1930) carried out experiments based on the heat evolution of a hemihydrate–water mixture which he assumed to be identical to the rate of setting. He mentions Lavoisier (1765), De Marignac (1873), and Le Châtelier (1887) as some of the first to study hemihydrate setting. Latter described that the contact of hemihydrate with water results in supersaturation of gypsum that eventually leads to gypsum crystallization whereby radiating growths form a strong interlocked mass. By combining Le Châtelier's theory with the assumptions by Cavazzi (1913), Neville and Jones (1929), Budnikoff (1928), and Traube (1919), Hansen (1930) proposed a three-step hydration process. It concluded the formation of a gel or adsorption complex, dissolution of the adsorption complex, and gypsum crystallization from the supersaturated solution. This theory of a gel-type intermediate state had been refuted by later publications (Weiser and Moreland, 1932). Hansen (1930) further discussed the observation that the rate-controlling process appeared to be the precipitation of gypsum and how the addition of salts can accelerate or retard it. Latter relation was corroborated by various authors since then (*e.g.* Cunningham et al., 1952). Presently, it is widely accepted that the hydration process in suspensions evolves via (rapid) dissolution of hemihydrate and (rapid) reprecipitation of dihydrate as it is less soluble than the hemihydrate (Singh and Middendorf, 2007; Isern and Messing, 2016; Gartner and Gaidis, 1989).

Southard (1940) found evidence for different forms of hemihydrate which he termed stable and metastable and which can be interpreted as $\alpha$- and $\beta$-hemihydrate. His experiments pioneeringly showed the discrepancies of the two polymorphs concerning their hydration behavior (differing exothermic peaks) which subsequently became a discrimination criterion.

In the early sixties, several studies took a closer look at reaction kinetics of hemihydrate rehydration in slurries, *e.g.* Ridge and Surkevicius (1962), Ridge (1965), Taplin (1965), and Schiller (1962). For example, Ridge and Surkevicius (1962) conducted isothermal (20.5 °C) and adiabatic experiments with different samples to study rehydration kinetics.

They noticed in all cases a pronounced self-acceleration of rehydration reactions and similarities between isothermal and adiabatic measurements. Ridge (1964) consequently mentions a dependence of the rates of growth and dissolution on the crystal's surface areas which he incorporated in a formal kinetic approach. Similarly, Schiller (1962) and Polak (1960) published kinetic models to describe experimental observations. All models mandate spherical particles. Taplin (1965) criticized the assumption of uniform spheres and the poor fits it yielded. Later publications on hemihydrate rehydration kinetics are, for example, the study by Fujii and Kondo (1986) and the comparative report by Hand (1994), who did not draw any final conclusions regarding the reaction kinetics and mechansim.

More recently, Saha et al. (2012) conducted time-resolved cryogenic transmission electron microscopy (cryoTEM) experiments to shed more light on the early stages of hemihydrate hydration from solution which is discussed in further detail in Section 2-5. Gurgul et al. (2019) used *in situ* powder XRD experiments (with time-resolved synchrotron radiation) to reinvestigate kinetics and mechanisms of hemihydrate hydration in a slurry and found the models by contributors Johnson, Mehl, Avrami, Erefe'ev and Kolmogorov (JMAEK) and Gualtieri (Gualtieri, 2001), which are both nucleation and growth based models, to fit the best.

Regarding $\beta$-anhydrite hydration, Gill (1918) proved the rehydration of natural anhydrite and dead-burnt gypsum plaster ($\beta$-anhydrite evolved from $\alpha$-anhydrite) within six years. The latter rehydrated to a greater extent, presumably due to the finer particle size. Farnsworth (1925) also performed anhydrite hydration experiments and succeeded by grinding the mineral to fine particles of several microns and observed rehydration to gypsum when exposed to excess of water (three weeks for particles of 7 µm). Her results, therefore, corroborate the influence of particle size. Murat et al. (1987) mention the influence of preparation temperature on the rehydration process. They consider the setting to be a dissolution–nucleation growth process and mentions that nucleation appeared to be the crucial step in their experiments. Sievert et al. (2005) conducted rehydration experiments with natural anhydrite (circa 4 % gypsum) in a ball mill at 10 °C and 20 °C and 40 °C and noticed that the gypsum amount formed was lower at 40 °C, than at 10 °C and 20 °C which could be deduced to the equilibrium temperature being close to 40 °C. Additionally, they found an anti-proportional relationship between the amount of formed gypsum and specific surface area of the hydrating anhydrite, which is is not consistent with the results obtained by Farnsworth (1925) and Murat et al. (1987).

**Table 2-5:** Rehydration experiments - Overview. HH = Hemihydrate, $CaSO_4 \cdot \frac{1}{2} H_2O$, AH = Anhydrite, $CaSO_4$, *as far as specified.

| Reference | Method/Experimental conditions | Gypsum recrystallization* information | Kinetic information* |
|---|---|---|---|
| Farnsworth (1925) | Isothermal $\beta$-AH hydration in a slurry at room temperature | Gypsum formation depends on crystal size and hydration time | |
| Conley and Bundy (1958) | $\beta$-AH hydration in a slurry at temperatures between 0 °C - 42 °C | Gypsum formation depends on additives | |
| Ridge and Surkevicius (1962); Ridge (1964) | Isothermal/adiabatic HH hydration in a slurry at 20.5 °C, examination with chemical analysis | | Self-accelerating process in adiabatic and isothermal conditions. Rates of dissolution and growth proportional to surface area. **Formal kinetics:** Ridge model[1] |
| Schiller (1962) | Adiabatic HH hydration in a slurry at room temperature, analysis by temperature rise | | Kinetics controlled by slurry density, rate of growth constant, new phase, difference of solubility, shape of new phase, effective number of nuclei. **Formal kinetics:** Schiller model[2] |
| Taplin (1965) | Isothermal HH hydration in a slurry at 20 °C - 23 °C, analysis by temperature rise | | **Formal kinetics:** Adaption of Schiller and Ridge models to include non spherical particles. |
| Fujii and Kondo (1986) | Isothermal HH hydration at 20 °C, 35 min, analysis by calorimetry (heat of solution) | | **Formal kinetics:** Parabolic law during induction period |
| Murat et al. (1987) | $\beta$-AH hydration in a slurry at 25 °C | | Kinetics depend on temperature of anhydrite production from gypsum, on the mechanical activation by grinding and additives |
| Hand (1994) | Review article: Calculations based on theoretical hydration curves | | Comparison of Schiller and JMAEK models. Evidence was found for all three models, but discussion remained. |
| Sievert et al. (2005) | $\beta$-AH hydration in a ball mill with water at 10 °C, 20 °C and 40 °C | hydration at 40 °C yields less gypsum than at lower temperatures, maximum of specific surface area of hydrating anhydrite and maximum conversion show discrepancy in time | |
| Saha et al. (2012) | Isothermal HH hydration in a supersaturated solution at 25 °C, analysis by time resolved cryoTEM[4] | Acicular gypsum are formed by multistep particle formation model: 1. Amorphous phase, 2. Crystalline product | |
| Gurgul et al. (2019) | Isothermal HH hydration in a slurry at room temperature, analysis by time-resolved synchrotron XRD | $\alpha$- and $\beta$-HH rehydration yields the same setting product. The maximum reaction temperature as proxy for conversion is invalid as it is reached before the reaction is finished | JMAEK and Gualtieri[5] models describe experimental data best. Kinetics differ depending on the hemihydrate type. |

[1] Ridge model = kinetic reaction model of hemihydrate hydration according to the author (Ridge, 1964, Chapter 6-3-5).
[2] Schiller model = kinetic reaction model of hemihydrate hydration according to the author (Schiller, 1962, Chapter 6-3-5).
[3] JMAEK model = kinetic reaction model according to authors Johnson, Mehl, Avrami, Erefe'ev, Kolmogorov (Chapter 4-1).
[4] cryoTEM = transmission electron cryomicroscopy.
[5] Gualtieri model = kinetic reaction model according to the author developed for the crystallization of aluminosilicate zeolites (Gualtieri, 2001).

### 2-3-3 Thermodynamic aspects of the calcium sulfate–water vapor system

Thermodynamic aspects of the $CaSO_4 - H_2O$ system, such as phase equilibria in the solid state depending on temperature and water vapor saturation at atmospheric pressures have been investigated by *e.g.* Kelley et al. (1941), Oetzel et al. (2000a), and Preturlan et al. (2019).

Kelley et al. (1941), who comprehensively addressed thermodynamic properties of gypsum and its dehydration product, gave laboratory data for the hemihydrate–$\gamma$–anhydrite equilibrium ($CaSO_4 \cdot 2\,H_2O$ (s) = $CaSO_4 \cdot 0.5\,H_2O$ (s) + $1.5\,H_2O$ (g)) for several hemihydrate samples, named P, U, W (data by Southard, see Kelley et al., 1941) and LC (data by Lescoeur, *ibid*). The values are plotted in Figure 2-16. The data was tabulated without further specification of samples or experimental set-up.

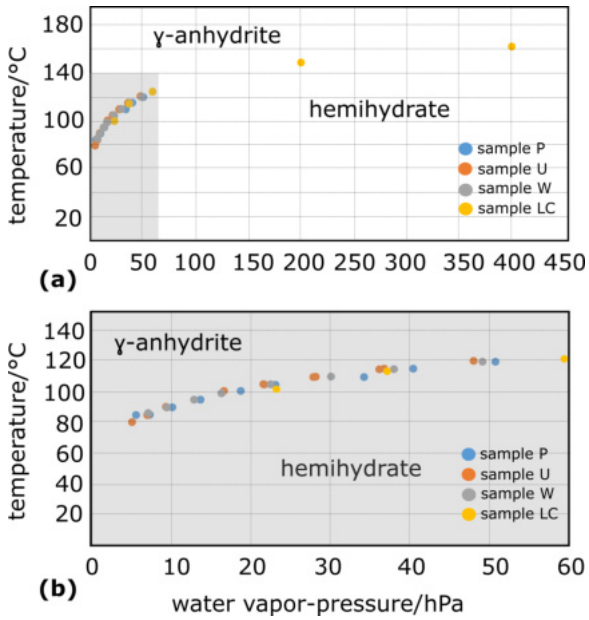


**Figure 2-16: (a)** $p_{H_2O}$–$T$ phase diagram for the equilibrium between hemihydrate and $\gamma$-anhydrite according to data from Kelley et al. (1941, p. 48) based on experiments by Southard (*ibid*, samples P, U, W) and Lescoeur (*ibid*, sample LC). **(b)** Magnification of the shaded area in (a).

Oetzel et al. (2000a) derived a $p_{H_2O}$–$T$ diagram (Figure 2-17 (a)) for the dihydrate, hemihydrate, and $\gamma$-anhydrite stability regions. The different samples were treated isothermally and isohumidly and measuered by *in situ* powder XRD. The conversion points in dependence of temperature and relative humidity (RH) were determined by the first evidence of the new phase in the diffraction pattern. The overall dehydration reactions lasted from several minutes up to two hours. The phase boundary $\gamma$-anhydrite–$\beta$-anhydrite is not contemplated as the authors understood the phase boundary as kinetically and not thermodynamically controlled and not influenced by water-vapor pressure. Moreover, they noted how phase boundaries are universally valid and independent of the gypsum sample that is dehydrated.

Their experimental data sets were not used for further thermodynamic contemplation but fitted algebraically. The dihydrate–hemihydrate boundary was modeled with an exponential equation of the form $40\,°C + 37\,°C\,hPa^{-1} \cdot {p_{H_2O}}^{0.123}$ using the least squares method. The intersect of 40 °C was given and not determined. Similarly, they fitted the hemihydrate–$\gamma$–anhydrite equilibrium with $43\,°C + 31\,°C\,hPa^{-1} \cdot {p_{H_2O}}^{0.23}$ (intersect calculated). The possibility of hemihydrate rehydration to gypsum under the influence of $p_{H_2O}$ was neglected and therefore not examined.

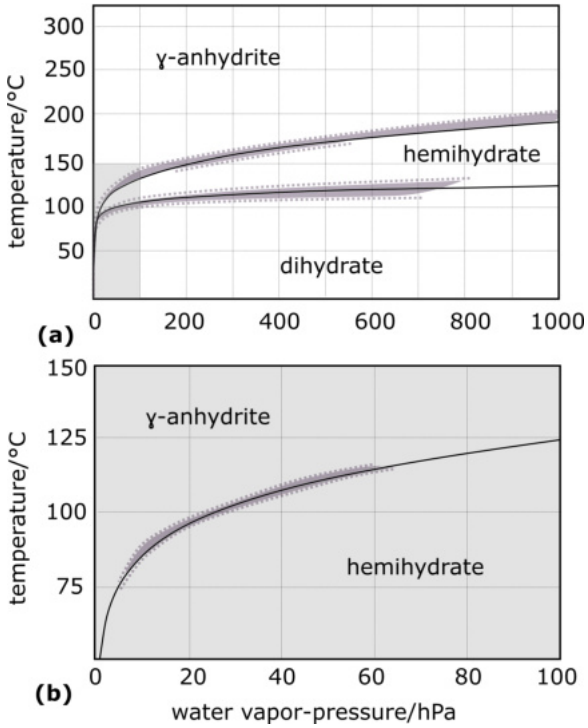


**Figure 2-17: (a)** $p_{H_2O}$–$T$ phase diagram for the equilibrium between gypsum (dihydrate), hemihydrate and $\gamma$–anhydrite adapted from Oetzel et al. (2000a). **(b)** $p_{H_2O}$–$T$ phase diagram for the equilibrium between hemihydrate and $\gamma$–anhydrite adapted from Preturlan et al. (2019). The black lines represent their best data fits and the lilac color outlines the areas of uncertainty due to data scattering. For better comparability of $p_{H_2O}$ and $T$ ranges, corresponding areas are shaded in grey.

In 2019, Preturlan et al. reinvestigated the hemihydrate–$\gamma$-anhydrite equlibrium (Figure 2-17 (b)) by using TA. To ensure that equilibrium is reached, they chose to conduct two measurement protocols, one isohumid protocol where temperature is increased stepwise and one isothermal protocol where the humidity was increased stepwise. Equilibrium values were assumed when the data of both protocols coincided and experiments were conducted for 25 h at $34\,°C \leq T \leq 250\,°C$ and $5\,hPa \leq p_{H_2O} \leq 60\,hPa$. With the obtained values, they proposed an updated version of the $CaSO_4 \cdot 0.5\,H_2O\,(s) = CaSO_4\,(s) \cdot + 0.5\,H_2O\,(g)$ equilibrium and a simplified thermodynamic model on the basis of the Van't Hoff equation.

This equation describes the dependence of a phase equilibrium of a chemical reaction on the temperature at constant ambient pressure (Atkins and de Paula, 2016)

$$\frac{\mathrm{d}}{\mathrm{d}T} \ln K_{eq} = \frac{\Delta_r H^\circ}{RT^2} \tag{2-1}$$

where $K_{eq}$ is the equilibrium constant, $R$ is the ideal gas constant and $\Delta_r H^\circ$ the reaction enthalpy. The equation can further be expressed as

$$\ln K_{eq} = \frac{\Delta_r G^\circ}{RT} = \frac{\Delta_r H^\circ}{RT} + \frac{\Delta_r S^\circ}{R} \tag{2-2}$$

with the changes in Gibbs free energy $\Delta_r G^\circ$, enthalpy $\Delta_r H^\circ$ and entropy $\Delta_r S^\circ$ of the dehydration reaction (Preturlan et al., 2019). As $K_{eq}$ can be obtained by the relation of partial pressure to bulk pressure according to the mass actions law, it can be written as $K_{eq} = K_p = \frac{p_{\mathrm{H_2O}}}{p^\circ}^{0.5}$ and Van't Hoff's equation becomes

$$\ln K_p = \ln \frac{p_{\mathrm{H_2O}}}{p^\circ} = \frac{\Delta_r H^\circ}{RT} + \frac{\Delta_r S^\circ}{R}. \tag{2-3}$$

According to the Van't Hoff approximation (Atkins and de Paula, 2016), which assumes $\Delta_r H^\circ$ and $\Delta_r S^\circ$ to be constant, $\ln K_p$ is a linear function of $\frac{1}{T}$ and by plotting them, $\frac{-\Delta_r H^\circ}{R}$ is obtained by the slope. Likewise, $\frac{\Delta_r S^\circ}{R}$ is yielded by the intercept of the linear fit. The $\ln K_p$ vs. $\frac{1}{T}$ values of Preturlan et al. (2019) were defined by plotting stability points of hemihydrate and $\gamma$-anhydrite onto the $p_{\mathrm{H_2O}}$–$T$ plane and determining equilibrium values with perceiving limits of hemihydrate and $\gamma$-anhydrite stability regions. Their estimation of $\frac{-\Delta_r H^\circ}{R}$ and $\frac{-\Delta_r S^\circ}{R}$ were $35.5\,\mathrm{kJ\,mol^{-1}}$ and $80.0\,\mathrm{J\,mol\,K^{-1}}$, respectively.

Comparing data by Kelley et al. (1941), Oetzel et al. (2000a), and Preturlan et al. (2019), discrepancies concerning the hemihydrate–$\gamma$-anhydrite conversion become evident (Figure 2-18). Only Oetzel et al. (2000a) provided data for the dihydrate-hemihydrate phase equilibrium. Data by Preturlan et al. (2019) suggest $\gamma$-anhydrite stability with a given humidity at lower temperatures than data by Kelley et al. (1941) and Oetzel et al. (2000a). Preturlan et al. (2019) addressed these findings and criticized the lack of error information. Further, they considered the differences to result from the used starting material and its chemical composition as the thermodynamic activity can vary with impurities. This conclusion might explain differences to some extent but does not seem consistent with the findings of Kelley et al. (1941) and Oetzel et al. (2000a), that the sample type is irrelevant. Hence, alternative or additional reasons for data scattering could be found in the different experimental methods and the kinetic control of phase boundaries. This is not addressed by the respective authors.

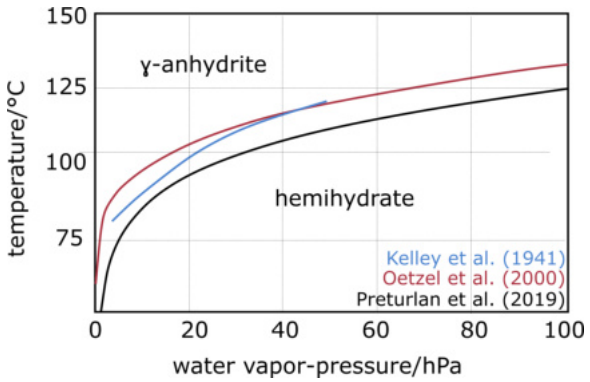


**Figure 2-18:** Comparative $p_{H_2O}$–$T$ phase diagram for the hemihydrate and $\gamma$–anhydrite equilibrium adapted from Preturlan et al. (2019).

In 1971, Clifton constructed a $p_{N_2}$–$T$ diagram (Figure 2-19) by plotting peak temperatures of endothermic and exothermic effects versus the gaseous pressure (1 hPa, 266 hPa, 530 hPa, 800 hPa, 1013 hPa) in the DTA cell. He ran non-isothermal measurements with heating rates between 3 °C min$^{-1}$ - 20 °C min$^{-1}$. Concerning the water-vapor pressure in the specimen tube, he assumed much greater values than the bulk residual pressure but did not give estimations. Therefore, his data can not be compared to that of Oetzel et al. (2000a) and Preturlan et al. (2019).

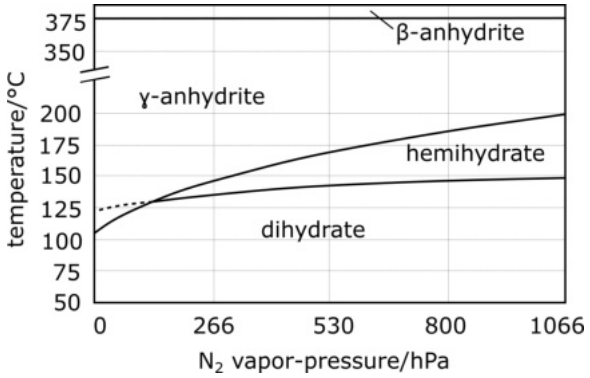


**Figure 2-19:** $p_{N_2}$–$T$ phase diagram for the equilibrium of gypsum, hemihydrate, $\gamma$-anhydrite, and $\beta$-anhydrite adapted from Clifton (1971). The black solid lines represent his best data fits. The black dotted line is not based on measurements but indicates his assumption.

## 2-4 Solubility

As stated in Section 2-1, the terminology of calcium sulfate phases varies. In accordance with many publications on solubilities in the $CaSO_4 - H_2O$ system, $CaSO_4 \cdot 2\,H_2O$ and $\beta$-$CaSO_4$ are followingly referred to as gypsum, respectively anhydrite. $CaSO_4 \cdot 0.5\,H_2O$ is termed hemihydrate and not called by its mineral name.

Like hydration and especially dehydration processes, the solubility of calcium sulfates in solutions with focus on gypsum–anhydrite and gypsum–hemihydrate transition temperatures at atmospheric pressure has been extensively studied over the past decades. The great number of publications can, *inter alia*, be deduced to the long history of controversy about the exact gypsum–anhydrite equilibrium in pure water, which is of particular importance for the geology of evaporites. The aqueous gypsum–hemihydrate transition, which is interesting for applications of technical gypsum products but has lesser relevance for natural phenomena, is subject to notably fewer studies. Both transition temperatures were also examined under the influence of additives.

### 2-4-1 Gypsum–anhydrite transition temperature in water

The first gypsum–anhydrite transition temperature of 63.5 °C was published by Van't Hoff et al. (1903). Later, studies by D'Ans (1968), Posnjak (1938), and Hill (1937) stated a lower value of 42(2) °C based on solubilty experiments and thermodynamic data analysis. This value agrees with the value of Kelley et al. (1941), who conducted thermodynamic calculations. However, Zen (1965) noted that Kelley et al. (1941) used inconsistent input data so that their calculations could not support the earlier findings. Hardie (1967) carried out a comprehensive study using an isothermal reaction approach where extrapolation of data yielded a transition temperature of 58(2) °C. This is in agreement with the value of 55.5(15) °C by Knacke and Gans (1977) and with the temperature modeled by Raju and Atkinson (1990). A more recent experimental study by Kontrec et al. (2002) specifies a temperature value of 40 °C.

In their review article, Freyer and Voigt (2003) provide an extensive literature overview on the $CaSO_4 - H_2O$ solubility diagram and state that the slow crystallization kinetics (of anhydrite below 70 °C) are the reason for the contradictory results of 42 °C - 60 °C for the gypsum–anhydrite equilibrium. This considerably widely scattered data was also contemplated by Charola et al. (2006), Van Driessche et al. (2017), and Serafeimidis and Anagnostou (2015). Latter conducted thermodynamic modeling that yielded an approximate transition temperature of 49 °C.

According to Freyer and Voigt (2003), higher transition temperatures were widely accepted during the past due to the specific studies of Hardie (1967) and Knacke and Gans (1977). However, preference of higher over lower transition values cannot be justified according to their careful evaluation of the respective experimental set-ups. Hardie (1967) extrapolated the temperature on the basis of incomplete conversion runs and also yielded unexpected results.

Knacke and Gans (1977) exploited the fact that a mixed gypsum–anhydrite solution is controlled by the saturation concentration of gypsum and measured the electrical conductivity. At 53 °C and 58 °C, they added dihydrate to aqueous anhydrite solutions that showed nearly constant conductivity. Consequently, gypsum saturation was reached and they noticed a decrease in conductivity and, therefore, saturation at 53 °C (gypsum is stable). At 58 °C, the solution behaved contrary (anhydrite is stable). Thus, they deduced the temperature of 55.5(15) °C as transition temperature. Nonetheless, Freyer and Voigt (2003) pointed out that the illustrated conductivity (proportional to anhydrite concentration in solution) is not stable but increases with time. This contradicts the findings of other experiments of anhydrite dissolution (Hill, 1937; D'Ans, 1933) so that the results of Knacke and Gans (1977) are not preferable over other findings.

The lack of a precise gypsum–anhydrite transition is recapitulated by Van Driessche et al. (2017). The authors refer to Hulett and Allen (1902) who already came to the same conclusion that broad variations of solubility data exist, despite considerate experiments with rather small errors. Concerning thermodynamic modeling approaches, Serafeimidis and Anagnostou (2015) mention the great dependence of thermodynamic models on the selection of starting parameters. In their case, consideration of the pore and crystal sizes - influence on equilibria were shown by Freundlich (1922) - was crucial and can explain deviations from earlier calculations, *e.g.* those by MacDonald (1953).

The dependence of experimental data on the specific set-ups and sample parameters, the kinetic checks of anhydrite precipitation (anhydrite does not precipitate in supersaturated solution for several months) and/or the general acceptance of transition temperatures around $\approx 55$ °C may be the reason for the supposed decrease of reinvestigations in the recent past. Differing databases in speciation programs mirror the difficulties of the experimental approaches. (Ossorio et al., 2014)

### 2-4-2 Gypsum–hemihydrate transition temperature in water

The temperature values for the gypsum–hemihydrate transition given in literature range from roughly 80 °C to 110 °C. Again, Van't Hoff et al. (1903) provided the first value of 106 °C by conducting dilatometric and tensiometric measurements. Posnjak (1938) obtained a value of 97(1)° from solubility experiments which they later confirmed by hemihydrate crystallization from gypsum at 100.5°. These temperatures are circa equal to the values of 98 °C - 100 °C by Partridge and White (1929). Azimi et al. (2007) found the transition temperature to be around 99.2 °C based on solubility modeling.

### 2-4-3 Hemihydrate–anhydrite transition temperature in water

According to Van Driessche et al. (2017), no hemihydrate–anhydrite transition is observable in the temperature range of 50 °C - 1200 °C in aqueous solutions and it is assumed that hemihydrate remains metastable. In the range of 0 °C - 200 °C, hemihydrate is unstable (Kontrec et al., 2002).

Figures 2-20 and 2-21 show abstracted $CaSO_4$ solubility diagrams adapted from Freyer and Voigt (2003) who plotted experimental data sets of different studies. Figures 2-21 (a) and (b) show enlarged sections of Figure 2-20 to illustrate the rather ill-defined stability regions of phases in the $CaSO_4 - H_2O$ system.

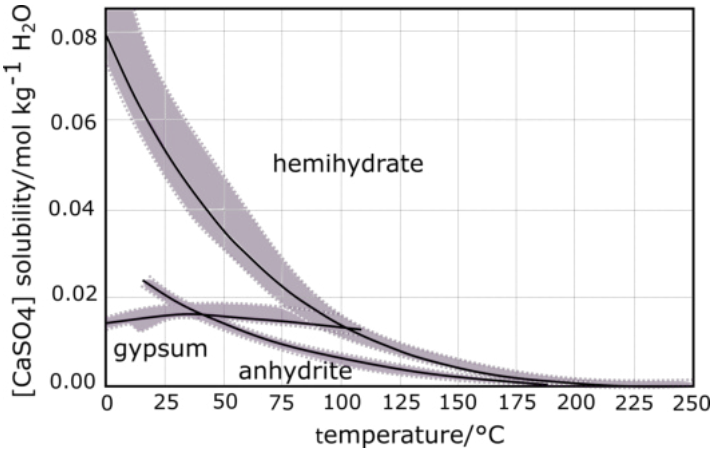


**Figure 2-20:** Solubility diagram adapted from Freyer and Voigt (2003) who plotted data at saturation pressure by D'Ans (1933); D'Ans et al. (1955); Sborgi and Bianchi (1940); Hill (1937); D'Ans (1968); Bock (1961). The black lines represent their best data fits and the lilac color outlines the areas of uncertainty due to data scattering. The curve intersections give the respective transition temperature.

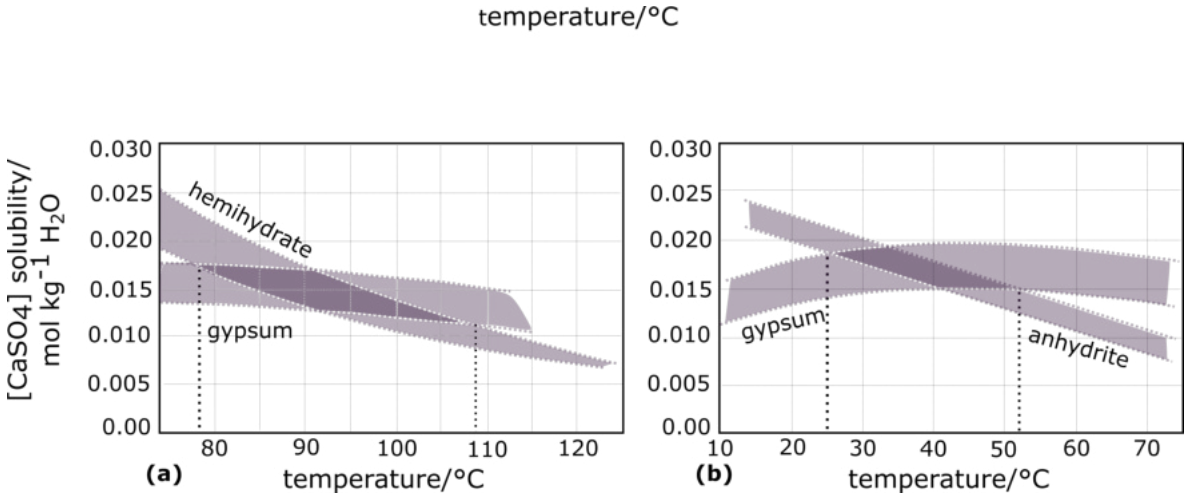


**Figure 2-21:** **(a)** Gypsum–hemihydrate transition: Enlarged part of Figure 2-20. **(b)** Gypsum–anhydrite transition: Enlarged part of Figure 2-20. Diagrams adapted from Freyer and Voigt (2003).

### 2-4-4 Transition temperatures in electrolyte solutions

The contemplation of gypsum and anhydrite solubilities in salt solutions are comprehensive. For example, experiments were conducted in solutions of nitrates (Seidell and Smith, 1904), in nitric acid solution (Zhang and Muhammed, 1989), in sodium sulfate and sodium nitrate solutions (Yeatts and Marshall, 1969), in aqueous sulfuric acids (Zdanovskii and Vlasov, 1968; Clegg et al., 1994; Hardie, 1967), in solutions of magnesium salts (Kruchenko, 1985), and in sodium perchlorate solutions (Kalyanaraman et al., 1973).

Azimi et al. (2007) approached the investigation of calcium sulfate solubility in multi-component solutions by modeling. Despite this variety in electrolyte solutions, the focus lies predominantly on NaCl solutions due to its relevance for natural systems (*e.g.* in the evaporitic precipitation sequence alongside gypsum).

Figure 2-22 shows the solubilities of gypsum and anhydrite in NaCl solutions at 25 °C according to Charola et al. (2006), who assembled data of several studies. The calcium sulfate solubilities increase with NaCl concentration until a maximum is reached for roughly [NaCl] = 2 mol kg$^{-1}$ $H_2O$. Subsequently, both solubilities decrease slightly with ascending NaCl molalities and intercept at [NaCl] ≈ 4 mol kg$^{-1}$ $H_2O$. This behaviour can be explained with $Na^+$ and $Cl^-$ being unlike ions to $Ca_2{}^+$ and $SO_4{}^{2-}$ (Charola et al., 2006). When non-common ions (chlorides and nitrates of sodium, potassium and magnesium) are added, the solubility of calcium sulfate is significantly increased (Freyer and Voigt, 2003). Although result contradictions (Figure 2-22: shaded area) impact the investigations of salt influence on calcium sulfate solubility, this finding is free of doubt (Freyer and Voigt, 2003; Charola et al., 2006; Serafeimidis and Anagnostou, 2015). Complementary, common ions (calcium chloride and calcium nitrate) cause a solubility decrease due to the hydration ability of the electrolyte (Kruchenko, 1985).

It is also widely accepted that a saturated NaCl solution lowers the gypsum–anhydrite and gypsum–hemihydrate transition temperature significantly due to faster equilibration. The water activities shrink with rising salt concentration and cause decreasing transition temperatures. (Charola et al., 2006; Freyer and Voigt, 2003; Raju and Atkinson, 1990)

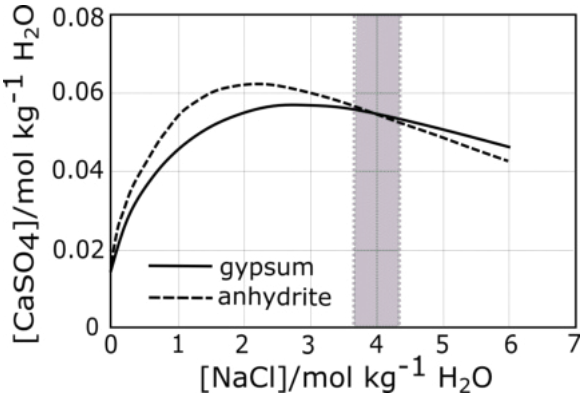


**Figure 2-22:** Solubility diagram of gypsum and anhydrite in dependence of NaCl concentration at 25 °C, adapted from Charola et al. (2006) who fitted data (black lines) of D'Ans et al. (1955); Shternina (1949); Madgin and Swales (1956); Shternina (1957); Bock (1961); Samoilov (1963); Marshall and Slusher (1966); Power et al. (1966); Block and Waters (1968); Yeatts and Marshall (1969). The lilac color outlines the areas of uncertainty.

## 2-5 Nucleation and growth

Understanding nucleation phenomena has been subject to many studies and many mineral systems as it is the key event in crystallization and mineralization. Pioneering work was conducted by Fahrenheit in the early 1700s as he scrutinized the supercooling of water (Kelton and Frenkel, 2016). Driven by the importance of industrial matters and geological questions, the picture of a crystallization process according to the classical nucleation theory (CNT) was drawn during the nineteenth and early twentieth century. However, this theory has been proven erroneous. It is summarized in Appendix A. The following two sections focus on several studies about gypsum, hemihydrate and anhydrite in aqueous suspensions that pay attention to the nucleation and growth processes.

### 2-5-1 Gypsum precipitation

Considering gypsum nucleation kinetics, induction periods and their dependence on temperature, supersaturation, and pH values, findings of authors like Packter (1974), Klepetsanis and Koutsoukos (1989), He et al. (1994), Alimi et al. (2003), Rashad et al. (2004), and Fan et al. (2010) corroborated the conclusion that gypsum formation is reasonably well described by the CNT. However, their results do not base on direct observations of nucleation mechanisms.

More recently, many studies broached the issue of nucleation proceeding via precursor and intermediate phases, questioning the approximations and applicability of the CNT (Smeets et al., 2017; Van Driessche et al., 2017). Calcium sulfate formation pathways at room temperature have been scrutinized with transmission electron microscopy (TEM) by Wang et al. (2012) who witnessed amorphous calcium sulfate and hemihydrate prior to dihydrate formation. Also using TEM, Van Driessche et al. (2012) witnessed amorphous particles turning into nanorods of hemihydrate that eventually aggregate and form gypsum crystals.

Jones (2012) monitored gypsum crystallization due to evaporation by attenuated total reflection Fourier-transform infrared (ATR FTIR) spectroscopy and described the development of a disordered, in the sense of amorphous, solid rearranging to an ordered, crystalline solid. She also proposes that water ability is linked to longevity of the disordered solid. Further, as described above, Saha et al. (2012) used time-resolved cryoTEM and also proposed a multi-step dihydrate crystallization pathway including nano clusters turning into amorphous particles that form acicular crystalline gypsum in less than a minute. As Van Driessche et al. (2017) resume in their review, gypsum formation from solution appears to evolve via some kind of precursor or intermediate phases. According to them, it is problematic to follow nucleation on real time scales as *in situ* methods tend to lack resolution and information and *ex situ* methods may suffer from artifacts of many kind, such as beam influence and sample preparation.

Stawski et al. (2016) designed an *in situ* experiment for which they used fast time-resolved small and wide angle X-ray scattering (SAXS/WAXS) to overcome impasses and formulated another non-classical multi-step crystallization pathway from supersaturated solution that covers four stages. In the first stage, a nanometer-scale species evolves, in the second and third stage, loose domains are formed and aggregation takes place.

Lastly, the aggregated fractal surfaces grow and coalescence into the crystalline phase. The primary species appears to contain $Ca–SO_4$ chains, those structural fragments that all calcium sulfates share, and the aggregations in stage three are composed of $Ca–SO_4$ framework together with disordered water molecules. The layer structure of gypsum is assumed to develop by rearranging of the disordered phase, especially the water molecules, into the ordered gypsum phase. If water supply is limited during the ordering process, Ossorio et al. (2014), Tritschler et al. (2015b), and Tritschler et al. (2015a) showed that bassanite (despite its metastability) or even anhydrite will emerge. (Stawski et al., 2016)

These findings stress the key role of water applicability and, moreover, the plausibility of crystallization from solution via alternative or non-classical reaction pathways, for calcium sulfates - and presumably for various other systems - which may entail multiple steps and types of intermediates that rely on nano particle- or cluster-based mechanisms (Stawski et al., 2020; Cölfen and Antonietti, 2005; Baumgartner et al., 2013; De Yoreo, 2013). This behavior can be viewed as compliance of Ostwald's rule of stages (Ostwald, 1897) that state that a system does not go directly into the most stable but a metastable frame in order to minimize $\Delta G$ of initial and evolving phase (Karthika et al., 2016). Yet, CNT seemingly still provides a good description of nucleation processes in some cases (Smeets et al., 2017).

### 2-5-2 Hemihydrate and anhydrite precipitation

Relatively rarely dealt with is the direct precipitation and nucleation of hemihydrate and anhydrite from solution. Some studies focused on the spontaneous hemihydrate and anhydrite formation and the corresponding temperature and salinity regimes. More concrete research targeted at nucleation mechanisms and pathways is missing (Van Driessche et al., 2017).

As solubility measurements and calculations have shown, the stability regime of anhydrite starts at temperatures above 40 °C to 60 °C, yet primary anhydrite precipitation could not be observed at these temperatures. Up to temperatures of 90 °C, gypsum is the dominant precipitation product and above 90 °C, hemihydrate formation takes place as anhydrite is regarded as kinetically hindered (Freyer and Voigt, 2003, and references therein). Ossorio et al. (2014) conducted an experiment series with focus on (primary) anhydrite precipitation depending on temperature, NaCl salinity and time. Experiments at 60 °C were observed for two years but at all salinities, gypsum was the only primary phase. Within several months, phase transformations were observed and anhydrite eventually appeared at temperatures over 80 °C, leading the authors to the conclusion that anhydrite needs to be regarded as pseudo-primary in evaporitic settings if contact to solution is sufficiently long. Hemihydrate and anhydrite precipitation can be strongly influenced to occur at lower temperatures by highly saline solutions, respectively brines, *e.g.* Dixon et al. (2015). Fan et al. (2010) looked at nucleation kinetics of calcium sulfates in supersaturated and electrolytic solutions and could derive a specific surface energy which is twice as high as that of gypsum and 10 times that of hemihydrate, giving reasoning, according to CNT, that gypsum and hemihydrate form readily and anhydrite does not (Ossorio et al., 2014).

## 2-6 Natural reservoirs

Gypsum represents the most abundant sulfate mineral in nature, followed by anhydrite. In contrast to bassanite, which is found rather rarely on earth, they occur as evaporites and sedimentary deposits that are common throughout much of the geologic record.

As sediments, sulfate minerals are mostly associated with carbonates, such as dolomite and ferruginous clastics like shales, marls, and clays. Gypsum is found in recent sediments and near the surface, whereas anhydrite is commonly present in the subsurface. Interbedding of gypsum and anhydrite is not an unusual phenomenon. In depth, however, anhydrite is the sole mineral phase (Murray, 1964). Paragenesis of gypsum and anhydrite include oxidation of sulfides, action of acid sulfate solution or sulphurous vapors on calcium bearing rocks and formation by dehydration (anhydrite replacing gypsum) or rehydration (gypsification) of the respective mineral phase. (Chang et al., 1996)

As evaporite, gypsum principally forms by direct deposition due to evaporation of a brine after precipitation of calcium carbonate and before halite. It can form in deep basin conditions as well as lagoonal environments and flat or sabkha conditions (*e.g.* Gulf of California). In arid and very arid regions, capillary waters with dissolved gypsum rise to the surface and cause precipitation and the formation of an encrusted layer. Such a desert soil crust is also the so called 'gypsum crust' in the Atacama Desert that. The Atacama Desert and its gypsum crust is briefly discussed in Section 3. The question, whether anhydrite can also form primary and not only secondary, has been the topic of discussions and inspired solubility and precipitation experiments that yielded gypsum–anhydrite equilibrium temperatures of 40 °C - 60 °C in pure water, as reviewed above. In highly saline solution, the boundary shifts to circa 18 °C. Nevertheless, the evolution of anhydrite from gypsum alteration is free of doubt and occurs frequently during gypsum diagenesis. (Chang et al., 1996)

Large gypsum and anhydrite reservoirs can be found in many countries as their deposits are ubiquitous on earth. Important localities include USA, Canada, China, France, UK and Germany (Chang et al., 1996). Germany has territories rich in gypsum and anhydrite that constitute one of the greatest reservoirs in Europe. Both minerals are found together in different rock strata sequences, like the Zechstein, Muschelkalk, and Keuper formations. The largest occurences are located around the southern and western Harz borders. The mineral occurences of Muschelkalk and Keuper belong to the upper and middle triassic deposits and can be found, together with halite deposits, along the northern borders of the Alps and in the Lorraine region in north eastern France (Gmelin, 1957). Triassic-bound gypsum and anhydrite also occur in Keuper strata from the Pyrenees to southern Spain, and in the Piedmont and Tuscany in Italy. In the UK, permian, triassic, and upper jurassic rocks contain gypsum and anhydrite deposits. In France and Spain, tertiary gypsum and anhydrite can also be found. (Chang et al., 1996; Gmelin, 1957)

Bassanite is rare on earth and presumably always a product of alteration. It has been found in few places in dry regions, *e.g.* inside cavities of leucite tephrite blocks from the Vesuvian (Zambonini, 1910), in arid Australian soils (Akpokodje, 1984) and Californian desert basins (Allen and Kramer, 1953). The occurence of bassanite in the Atacama Desert has been confirmed by *e.g.* Schlüter and Malcherek (2007), De Waele et al. (2017), and De Waele et al. (2009). In contrast, bassanite is a very abundant mineral on Mars (Vaniman et al., 2009; Wray et al., 2010; Bishop et al., 2014; Rapin et al., 2016). For example, Vaniman et al. (2018) reported the occurrence of all three calcium sulfates together in sedimentary rocks at Gale crater with varying abundances by *in situ* XRD.

## 2-7 Technical and industrial relevance

Dehydration products of gypsum are the backbone of gypsum-based industries and in general important working materials. Gypsum products are also among the oldest working materials of humanity as the earliest evidence for their usage dates back to 7000 - 9000 BC. Like many other building materials, gypsum products became crucially sophisticated during the industrialization in the nineteenth century and have been refined to high-quality industrial products to date. Currently, industrial research focuses on the energetic and performative challenges of modern-day architecture concerning further improvement of gypsum-based products. The most common and most important product is the technical bassanite equivalent, which is often referred to as Plaster of Paris, calcined gypsum or stucco plaster (Karni et al., 1995; Wirsching, 2000). Predominantly, Plaster of Paris as pure hemihydrate or with admixtures of other calcium sulfates, is used as building material in gypsum boards, gypsum blocks, plasters, fillers, and dry screeds. Gypsum is utilized for medical purposes as plaster bandage and as dental stone. Further use of calcium sulfates is applied in cosmetic products, model assembling of any kind, art, agriculture, food production, and stucco. (Bundesverband der Gipsindustrie e.V., 2013)

The industrial processing of gypsum differs greatly from laboratory gypsum dehydration as mentioned earlier. Figure 2-23 shows the different technical calcium sulfate phases and their production conditions during the industrial calcination process according to data by Bundesverband der Gipsindustrie e.V. (2013), Singh and Middendorf (2007), and Wirsching (2000). The raw material gypsum (either of natural origin or obtained from flue gas desulfuration) is treated at different temperatures and methods to obtain the hemihydrate modifications $\alpha$-HH and $\beta$-HH, which can further be heated to produce $\alpha$-AIII and $\beta$-AIII (both equal $\gamma$-anhydrite according to the designation used in the present work). By heating those or gypsum, AIIs ("hardly soluble"), AIIu ("insoluble") and AIIE ("screed", all equal $\beta$-anhydrite according to the designation used in the present work) are produced. The high-temperature phase AI or $\alpha$-anhydrite is not included as it is not produced commercially. The german union 'Bundesverband der Gipsindustrie' further specifies that Plaster of Paris is formed in rotary drumcalciners at 120 °C - 180 °C up to 24 h. Phase mixtures of $\beta$-$CaSO_4 \cdot 0.5\,H_2O$ and $\beta$-$CaSO_4$ are manufactured at two different temperatures (250 °C and 500 °C).

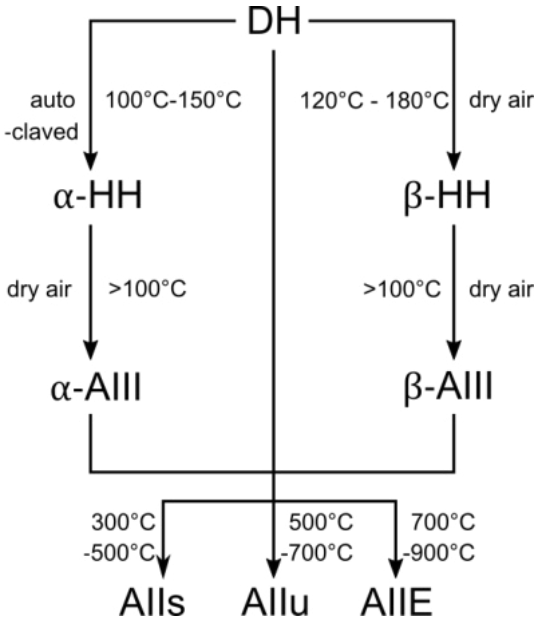


**Figure 2-23:** Commercial phases in the $CaSO_4 - H_2O$ system, compiled with information from Bundesverband der Gipsindustrie e.V. (2013); Singh and Middendorf (2007); Wirsching (2000). DH = Dihydrate, $CaSO_4 \cdot 2\,H_2O$, HH = Hemihydrate, $CaSO_4 \cdot 0.5\,H_2O$, AIII = "soluble" anhydrite, $CaSO_4$, AIIs = "hardly soluble" anhydrite, $CaSO_4$, AIIu = "insoluble" $CaSO_4$, and AIIE = screed, also $CaSO_4$. Both AIII phases are structurally identical to $\gamma$-anhydrite. The $\alpha/\beta$ discrimination solely refers to the preceding hemihydrate. All AII phases are equivalent to $\beta$-anhydrite.

# Chapter 3

# The Atacama Desert

Here, general aspects of the Atacama Desert are briefly reviewed. Predominantly, information on temperature and humidity conditions prevailing in the desert is compiled.

## 3-1 Location and general information

The Atacama is an arid to hyper-arid desert that extends from 18°S to 27°S along the Pacific coast of northern Chile (Figure 3-1, Navarro-González et al., 2003). The driest parts are located between 22°S and 26°S with the hyper-arid core at the coast around 24.5°S (Borgel, 1973). The principal causes of aridity are a combination of the cold Humboldt current creating temperature inversion, the subtropical high-pressure subsidence enforcing adiabatic heating, the Andean (eastern) rain shadow effect,sediment and the great distance to Amazonia-Atlantic moisture sources (Hartley et al., 2005). The Atacama is currently the driest desert on earth (excluding polar regions) and assumed to be one of the oldest deserts exhibiting hyper-aridity (Dunai et al., 2005). Although geological evidence implies less dry conditions throughout time, studies by Alpers and Brimhall (1988) and Sillitoe and McKee (1996) suggest the hyper-aridity to be at least of early Miocene age (linked to the uplift of the Andes mountains). Other studies published a much earlier (ca. 25 Ma) or later (2 Ma) hyper-aridification which is then associated with global and regional cooling (Garreaud et al., 2010).


**Figure 3-1:** Schematic map of the Atacama Desert area (emphasized in grey), adapted from Clarke (2006).

The exact onset of arid to hyper-arid transitions is therefore currently under discussion. However, the exceptional long-term aridity of this region has caused unique conditions such as low erosion rates (Jungers et al., 2013) and mineralogical peculiarities like the accumulation of rare salts, *e.g.* nitrates (Ericksen, 1981). Nitrate-rich soils also occur in other deserts but the occurrence of exploitable nitrate deposits is unique to the Atacama (Ericksen, 1981). The deposits further contain anomalously high concentrations of perchlorates, borates, chromates, and iodates. In general, the Atacama mineralogy is characterized by abundant saline minerals like halite, gypsum, anhydrite, and thenardite, that are present as soils cements, impregnations, veins, and salt flats (Ericksen, 1983). The desert also has a wide variety of copper mineral ores as a result of climate driven supergene Cu enrichment (Marcela et al., 2013). In fact, the region is the prime copper producing province of the world with Chuquicamata as the most important mine (Reich et al., 2009). Among the various Cu-bearing phases of the porphyry deposits is the type locality atacamite. It is an oxychloride with the formula $Ca_2Cl(OH)_3$. High Li concentrations join the list of Atacama features caused by persistent aridity and hyper-aridity (Godfrey and Álvarez-Amado, 2020).

Hyper-aridity affects not only morphological and mineralogical aspects of the Atacama, but also influences the survival of life. In its driest parts, the desert hardly contains any soil bacteria or hypolithic organisms (Navarro-González et al., 2003; Warren-Rhodes et al., 2007). Due to the scarcity of water, flora, and fauna, the Atacama is often thought of as an martian surface analogue on Earth (Grilli Caiola et al., 1993).

The desert's physiography (Figure 3-2) is marked by a coastal range, followed by a central depression and the Precordillera. Prior to the Andean Mountains are sediment-filled basins which is is referred to as Western Cordillera (Valero-Garcés et al., 1999).

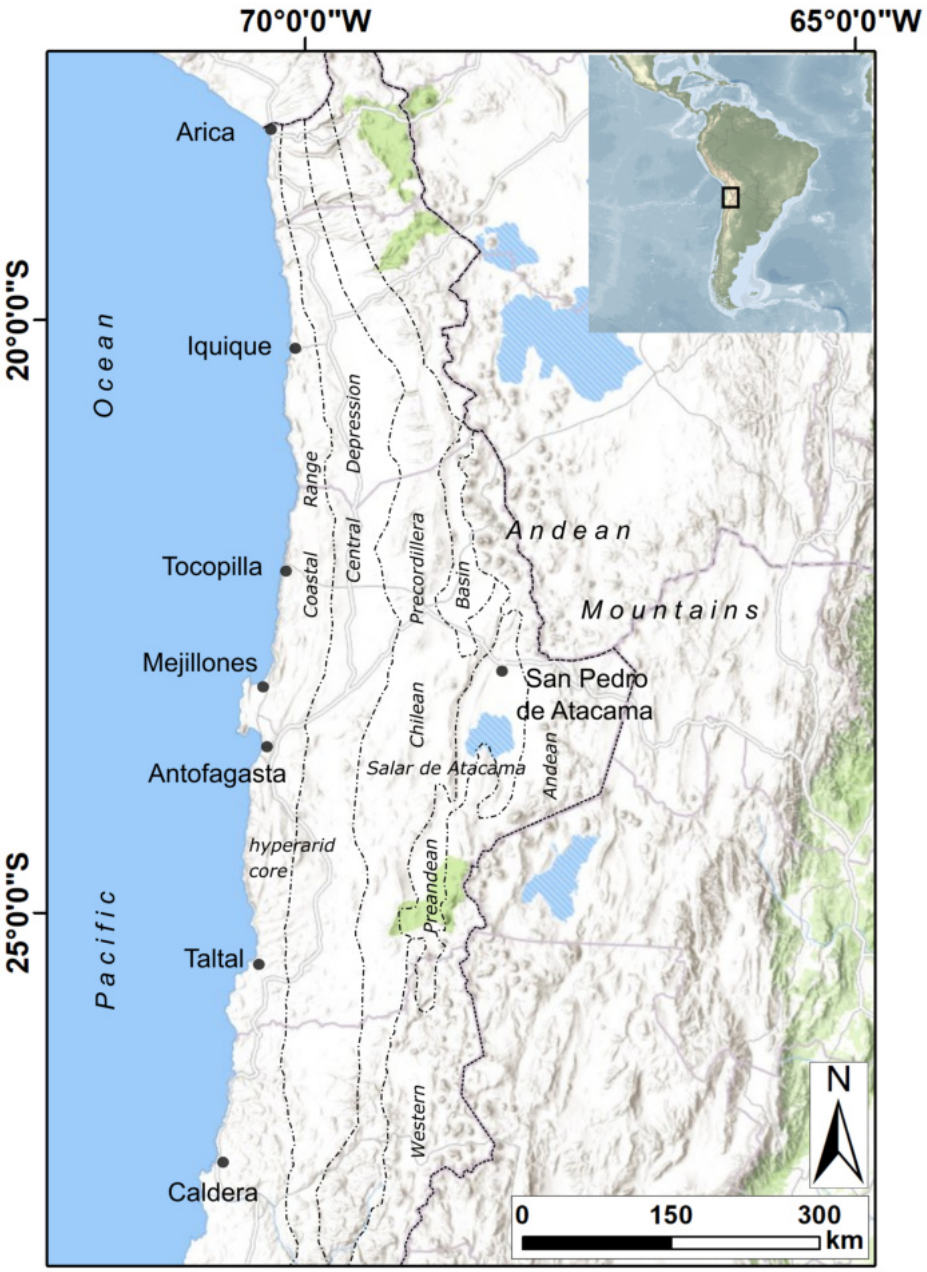


**Figure 3-2:** Physiographic features of the Atacama Desert. The desert is located between the Pacific Ocean to the west and the high Andes to the east. From west to east, the major tectonic units are the Coastal Cordillera, the Central Depression, the Precordillera, and the Western Cordillera (*e.g.* Walk et al., 2020). Map created with ArcGIS 10.5.1.

## 3-2 Temperature and humidity conditions

As mentioned, the juxtaposition of the cold Humboldt current and the Andes mountains results in exceptionally low rainfall for most parts of the desert. Presently, the long-term mean annual precipitation along the coast and the central depression is below 5 mm year$^{-1}$ (measured at 1000 m above sea level, Nicholson, 2011). Precipitation is mainly caused by coastal stratus drizzle and rare rainfall events related to passing cold fronts during the development phase of an El Niño phenomenon (Rutllant et al., 2004; Vargas et al., 2000). However, rainfall does increase radically with distance from the coast and reaches values of 200 mm year$^{-1}$ - 300 mm year$^{-1}$ within 500 km inland. (Nicholson, 2011)

As the overall temperature regime is influenced by the cold Humboldt current, temperatures are relatively low. Mean temperatures are between 10 °C - 20 °C for cold and 20 °C - 30 °C for warm months (Fuentealba et al., 2015). The overall diurnal, annual, and latitudinal temperature changes are rather small with average values of 7.5 °C (annual), 6 °C (diurnal) and 4 °C (difference between 18°S and 30°S). However, northern and southern Atacama climates differentiate slightly. The northern Atacama Desert has mean temperatures of 22 °C during January (warmest month) and 18 °C in August (coldest month) with a diurnal range of 6 °C. The southern part has mean temperatures of 16 °C during January and 12 °C during July which is the coldest month in the south. The diurnal range is 8 °C. (Nicholson, 2011)

Despite generally homogeneous climatic conditions, temperatures are subject to some variability. Regional air temperatures were, for example, monitored by McKay et al. (2003). They report an average air temperature of 16.5 °C, a maximum air temperature of 37.9 °C and a minimum air temperature of −5.7 °C for the period September 1994 – October 1998 in the Yungay area (located in the central depression at 24°4′50″S, 69°5′11″W). Typically, daytime maximum temperatures reached 32 °C. They also mention how the temperature of stones on the desert soil lay 20 °C above air temperatures, enabling maximum ground temperatures close to 60 °C. Temperature information concerning the Atacama region by the World Weather Information Service is only available for the coastal city Iquique (20.2°S, 70.1°W). The mean daily minimum and maximum temperature range between 13.7 °C (July) 18.8 °C (January) and 25.9 °C (July) and 25.9 °C (February), respectively. Their data is based on monthly averages for the thirty year period 1981 - 2010.

In contrast to rainfall events that are scarce and irregular, fog formation is more common and the main water source for endemic desert life (Cáceres et al., 2007). Figure 3-3 gives an impression of fog formation in the Atacama Desert (image by May and Hoffmeister (2018)). Inland, fog evolves generally at slopes and rarely at the coast (once or twice per year). Coastal fog is strongly influenced by the desert's topography and shoreline. These geomorphological features can vary greatly over a short distance and if favorable, so called 'fog oases' are enabled and isolated pockets of vegetation occur. Fog occurs least frequently during winter and more frequently during summer months (Nicholson, 2011).


**Figure 3-3:** Fog evolution in the Atacama Desert (Cerros de Calate) as captured by time lapse images by May and Hoffmeister (2018).

Moisture in the Atacama Desert is highly variable. The relative humidity values reported by McKay et al. (2003) ranged from 8 % - 100 % in air (with high RH values leading to nighttime dew occurrences) and 9 % - 100 % in soil. Mean soil humidity was between 16 % - 40 % and mean air humidity values ranged from 19 % - 45 %. Data by Cáceres et al. (2007), measured along a hyper-arid coast–inland transect (Caloso–Inacesa–Yungay, 23.5°S), corroborated findings by McKay et al. (2003).

To further evaluate Atacama temperature and humidity conditions, data from three permanent weather stations in the Atacama Desert were compiled. The stations were installed by the CRC and provided by Dirk Hoffmann via the CRC 1211 Database Hoffmeister, 2017, 2018a,b). The raw data were assessed with regard to winter and summer temperature and humidity courses. Therefore, soil temperatures, air temperatures, and relative humidity values for the months January (summer) and July (winter) from March 2017 to March 2020 were comprised (figures 3-4, 3-5, 3-6 and 3-7). Raw data marked as incorrect according to database notifications was excluded from analysis. The distribution of temperature and humidity values in figures 3-4, 3-5, 3-6, and 3-7 are displayed as boxplots that combine scatter and central tendency measures: The box extends from the first quartile to the third quartile, meaning that 25% - 75% of the data is in that interquartile range. The line inside the box gives the median, and the light blue square shows the mean. The whiskers extend to the furthest observation within the 1.5 fold of respective interquartile ranges. Data outside that range are classified as outliers and denoted as spheres.

According to Hoffmeister (2017), air temperatures and humidities were obtained with a sensor at 2 m height and without direct irradiation as it is standard practice (instrument HC2S3 by Campbell Scientific). Soil temperatures were measured with an infrared remote temperature sensor at the desert's surface (instrument IR120 by Campbell Scientific). Unfortunately, relative humidity values at surface level were not available. The measurement sites *Cerro Constancia*, *Cerros de Calate*, and *Quebrada Grande* are the respective master stations of three coast–inland transects. The stations are located at 20°4′24.8″S, 69°56′6.0″W; 21°24′10.4″S, 69°50′24.7″W; and 25°5′30.1″S, 70°16′34.0″W, respectively (Hoffmeister, 2017, 2018a,b). They cover the three main focus areas of the CRC 1211 and represent the varying geographical and geomorphological features of the northern, central, and southern parts of the Atacama Desert (Dunai et al., 2020). The transect in the north is characterized by extreme dryness and a thick soil crust in the Coastal Cordillera. The central transect roughly follows the gorge of the Rio Loa where moist Pacific air flows into the central depression due to an opening in the coastal mountain range. The southern transect is marked by a strong coast–inland vegetation gradient from fairly dense to virtually no vegetation (Schween et al., 2020).

Based on data from the northern weather station (*Cerro Constancia*, Figure 3-4, upper panels), mean diurnal air temperature values range from 15.5 °C to 21.5 °C throughout January and, similarly, from 15 °C to 21 °C during July. The overall air temperatures in July reveal wider scattering to warmer but majorly colder temperatures with minima reaching 4 °C. Air temperatures measured at the central station (*Cerros de Calate*, Figure 3-5, upper panels), show a similar behavior. January is characterized by a rather monotone daily temperature profile with mean day temperatures from 13 °C to 20 °C. July temperatures show a greater variance with comparable mean temperatures (15 °C - 20 °C). Again, the same pattern describes the air temperature values of the southern station (*Quebrada Grande*, Figure 3-6, upper panels), at which mean day temperatures are between 13 °C - 22.5 °C (January) and 10 °C - 20 °C (July). Here, minima temperatures reach the freezing point. At all stations, temperature maxima did not exceed 30 °C.

The present data correspond to the literature information on moderate diurnal temperature changes. Figures 3-4 - 3-6 also show that winter temperatures vary significantly stronger than summer temperatures. Moreover, a modest north–south temperature gradient becomes apparent with mean day temperatures decreasing 2 °C - 3 °C from north to south. Relative humidities show great variability with comparably higher mean values in the north in January (≈ 55 % - 80 %, figures 3-4, 3-5, lower left panels), lower mean values in July (≈ 25 % - 40 %, figures 3-4, 3-5, lower right panels), and low mean relative humidities in the south all year round (≈ 10 % - 40 %, Figure 3-6, lower panels). During January, mean relative humidity values are especially low as they do not surpass 25 % (Figure 3-6, lower left panel). The high variability of humidities was also reported in the literature. According to Böhm et al. (2020), water vapor variability largely depends on the sea surface temperature and the internal climate mode El Niño Southern Oscillation.

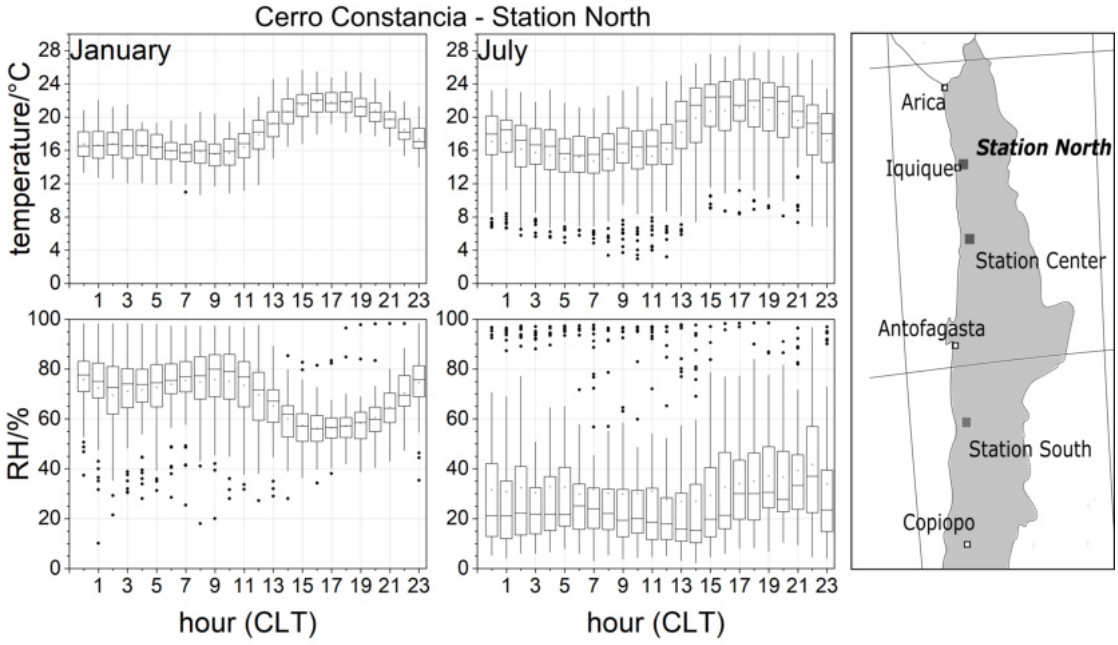


**Figure 3-4:** Selected temperature and relative humidity (RH) values measured at *Cerro Constancia*. CLT = Chile Standard Time. The boxes represent the 25th to the 75th percentile (Interquartile Range, IQR), the whiskers symbolize the range within 1.5 · IQR, the squares shows the mean, the spheres denotes the outliers and the lines indicate the median. The map is modified according to Clarke (2006).

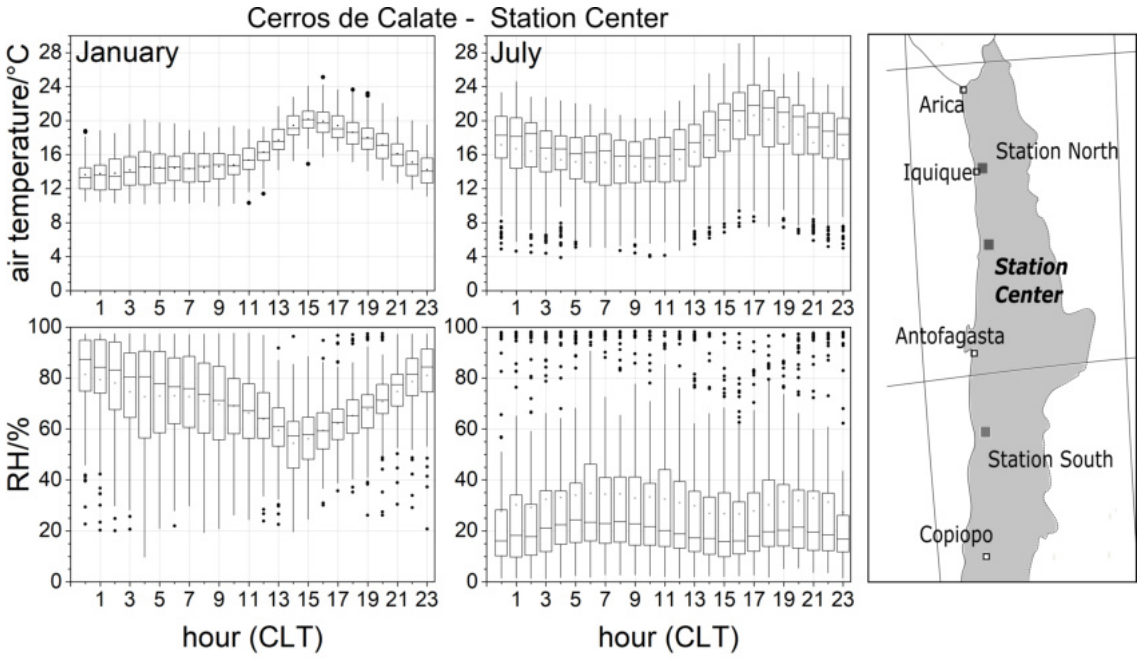


**Figure 3-5:** Selected air temperature and relative humidity (RH) values measured at *Cerros de Calate*. CLT = Chile Standard Time. The data distribution is described in the caption of Figure 3-4. The map is modified according to Clarke (2006).

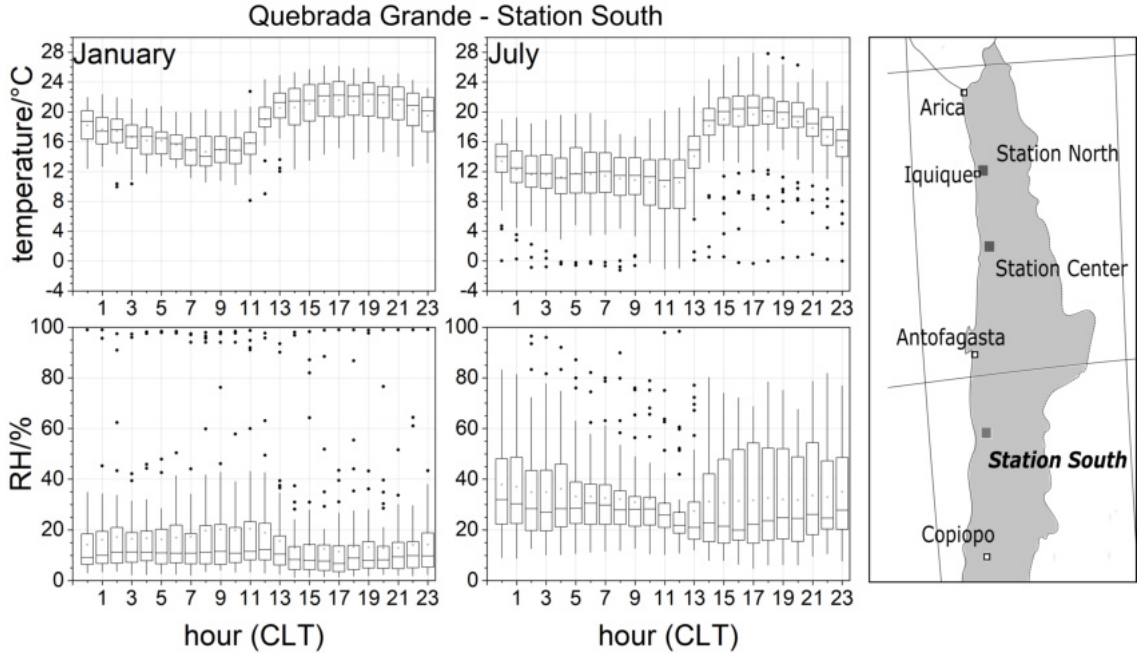


**Figure 3-6:** Selected air temperature and relative humidity values measured at *Quebrada Grande*. CLT = Chile Standard Time. The data distribution is described in the caption of Figure 3-4. The map is modified according to (Clarke, 2006).

Diurnal soil temperature profiles show maximum values between 5 pm and 7 pm. In general, the seasonal difference is evident as temperatures are higher in January than in July. Maximum mean soil temperatures are around 35 °C - 40 °C at the central station during July and January (*Cerros de Calate*, Figure 3-7, middle panels), and around 20 °C - 25 °C (July) and 40 °C (January) at the southern station (*Quebrada Grande*, Figure 3-7, right panels). Here, the January values exhibit comparably great variability towards higher temperatures between 7 and 12 am, possibly due to strong insolation. The northern station, *Cerro Constancia* (Figure 3-7, left panels), has maximum mean temperatures of 35 °C - 38 °C in July and around 48 °C in January.

Overall, the data endorse the findings by McKay et al. (2003), who described soil temperatures that are several degree Celsius higher than air temperatures. Here, maximum mean values range around 40 °C (roughly averaged). The values persist for 1 h - 3 h, mostly during early evenings.

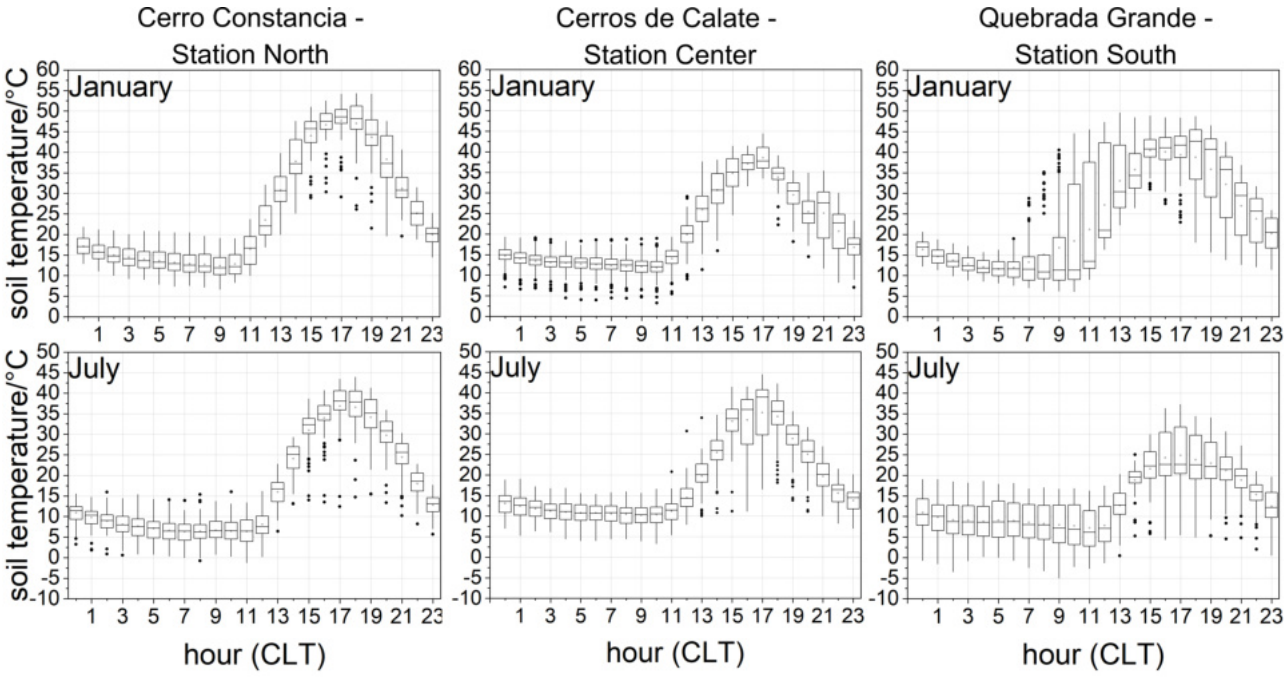


**Figure 3-7:** Selected soil temperatures measured at three weather stations. CLT = Chile Standard Time. The description of data distribution is given in the caption of Figure 3-4.

Absolute mean, maximum, and minimum air temperature, soil temperature, and relative humidity values measured at the weather stations for the time period March 2017 - March 2020 are given in Table 3-1. The maximum soil temperature was measured at the northern station *Cerro Constancia* in February at 5:40 pm (58.2 °C).

**Table 3-1:** Maxima, minima, and mean values of air temperatures, air humidities, and soil temperatures measured at three weather stations in the Atacama Desert from March 2017 to March 2020. Station North = *Cerro Constancia*, Station Center = *Cerros de Calate*, Station South = *Quebrada Grande*.

| | | Air temperature/°C | Rel. humidity/% | Soil temperature/°C |
|---|---|---|---|---|
| **Station North** | **Min** | 2.1 | 1.1 | -3.2 |
| | **Mean** | 17.3 | 48.0 | 20.5 |
| | **Max** | 29.9 | 99.3 | 58.2 (09/28/2018, 5:30 pm) |
| **Station Center** | **Min** | 2.7 | 0.6 | -1.7 |
| | **Mean** | 15.9 | 20.6 | 18.41 |
| | **Max** | 31.2 | 98.3 | 52.2 (03/27/2019, 5:00 pm) |
| **Station South** | **Min** | -2.16 | 0.5 | -6.2 |
| | **Mean** | 16.8 | 19.0 | 18.5 |
| | **Max** | 29.4 | 99.1 | 51.5 (02/13/2019, 5:40 pm) |

## 3-3 Calcium sulfate phases as constituents of Atacama surfaces

The abundance of calcium sulfate minerals in the Atacama is pervasive and has been mentioned and discussed in literature (*e.g.* Ericksen, 1981; Clarke, 2006; Flahaut et al., 2015; Dong et al., 2007; Watson, 1979; Rech et al., 2003; Harris et al., 2016; Voigt et al., 2020).

Gypsum and anhydrite dominate the soils and surfaces of the desert. They are copiously distributed as they have lower solubilities than chlorites or nitrates and are, therefore, more resistant close to the surface (Fernández López et al., 1994). The origins of Ca and S in pedogenic salts vary locally. However, isotopic data by Rech et al. (2003) hints to the adjacent Pacific Ocean and the salt-encrusted playas (salars) as general soil salt sources. Specifically, they mention how marine aerosols strongly influence the gypsum/anhydrite development as far as fog is able to penetrate the inland. Farther from the coast, rock weathering indirectly controls soil salt evolution as the precipitation of charged groundwater forms salars. The surrounding soils enrich in salts by eolian reworking and distribution of the groundwater derived salar salts Rech et al. (2003).

At the surface, pedogenic gypsum and anhydrite can form a crust-like layer which is referred to as gypsum crust. Gypsum crusts, or gypcretes, are significant pedologic and geomorphic features of many arid and hyper-arid areas. They are a type of duricrust which generically describe case-hardened layers above or within a soil (Dixon and McLaren, 2009). The Atacama gypsum crust can predominantly be found on inland slopes of the coastal range and the Central Depression. It is absent from the Precordillean ranges with somewhat more rainfall (Clarke, 2006). The crust is often of microporous, translucent appearance and can host microbial colonies (Wierzchos et al., 2011; Vítek et al., 2013).

Calcium sulfate phases at the surface also appear as powders or larger fragments in or above regolith. As an ultimate desiccation and leaching product, anhydrite can form spheroidal cakes that are adversely referred to as gypsum cakes (Ericksen, 1981).

# Chapter 4

# Solid-state reaction kinetics

The concepts of solid-state reaction kinetics originate from the findings on homogeneous chemical reaction kinetics. Based on the law of mass action that expresses the proportionality of reaction velocity to the quantity of reacting substances, the concepts of reaction rates, rate laws, rate constants, activation energy, and reaction order were introduced and manifested by the end of the nineteenth century (Vyazovkin, 2000). Briefly stated, reaction rates link the speed of reactant–product conversion to time, rate laws relate the reaction rate to concentrations or partial pressures of reactants, and rate constants are indirect measures for reaction velocities as they are rate law-proportionality constants. In fact, they are parameters as they depend on *e.g.* temperature, pressure, and additives. The order of a reaction is determined experimentally and refers to the rate dependence on concentration or partial pressure of the reactant. The term activation energy ($E_a$) was framed by Arrhenius (1889) and specifies the minimum amount of energy that a chemical reaction requires to proceed. It is often depicted as a barrier that must be surmounted. (Bamford and Tipper, 1972; Menzinger and Wolfgang, 1969)

Van't Hoff (1896) showed that the law of mass action or general rate equation formulated by Guldberg and Waage (1879), can be written for a single-step reaction with equally concentrated reactants as

$$\frac{\mathrm{d}C}{\mathrm{d}t} = -kC^n \tag{4-1}$$

with the concentration of each reacting phase $C$, reaction order $n$, and the rate constant $k$. This reaction rate was adopted by Lewis (1905) for a specific solid-state decomposition (autocatalytic thermal decomposition of silver oxide). He replaced the concentration $C$, which is insignificant considering the physical state, with the extent (or fraction) of conversion $\alpha$. This parameter depends on several influencing factors so that $\alpha = f(V, N, s, r, p, t, ...)_{T=const}$ (with $V$ = reacting volume, $N$ = number of nuclei, $s$ = specific surface, $r$ = geometric factor of particles, and $p$ = partial pressure of gaseous products).

The conversion fraction represents relative change in the overall properties and is experimentally measured. By substituting $C$ with $\alpha$, Lewis yielded expression 4-2.

$$\frac{\mathrm{d}\alpha}{\mathrm{d}t} = k\alpha(1-\alpha) \tag{4-2}$$

As stated above, Equations 4-1 and 4-2 are valid for a single-step reaction. Yet, solid-state reactions are often or even predominantly multi-step reactions which was criticized by Ostwald (1894) early on. However, it came into focus several years later. Studies by Macdonald and Hinshelwood (1925), Centnerazwer and Bružs (1926), and Garner and Hailes (1933) proved that single-step reaction kinetics do not ubiquitously apply. This circumstance induced the concept of reaction models. The models act as mathematical remedies to adequately represent the reaction mechanisms, similar to the reaction order concept introduced by Van't Hoff (1896). Therefore, Equation 4-2 can be written as

$$\frac{\mathrm{d}\alpha}{\mathrm{d}t} = kf(\alpha) \tag{4-3}$$

with the mechanistic model $f(\alpha)$ (Vyazovkin, 2000). An overview of widely accepted reaction models (*e.g.* Jacobs and Tompkins, 1955; Young, 1966; Barret et al., 1973; Brown et al., 1980; Šesták, 1984; Schmalzried and Pelton, 1981; Jacobs, 1997) for the solid state is given in Section 4-1.

The quantitative temperature dependence of chemical processes (Arrhenius equation) has been approximated by introducing the idea of a constant $E_a$ value and pre-exponential or frequency factor $A$. Latter refers to the number of times two particles collide pursuant to the collision theory (Arrhenius, 1889). According to Vyazovkin (2000), the studies by Polanyi and Wigner (1928), Bradley (1931), Bradley (1956), Topley (1932), Shannon (1964), and Cordes (1968) introduced the integral form of Equation 4-4 to solid-state reaction kinetics and justified and implemented it's usage. The Arrhenius equation is given by

$$k(T) = A\exp\left(\frac{E_a}{RT}\right) \tag{4-4}$$

where $k$ is the reaction rate coefficient, and $R$ is the gas constant. With Equation 4-4, Equation 4-3 becomes Equation 4-5.

$$\frac{\mathrm{d}\alpha}{\mathrm{d}t} = A\exp\left(\frac{E_a}{RT}\right)\cdot f(\alpha) \tag{4-5}$$

The integral form of Equation 4-5 is given by Equation 4-6.

$$g(\alpha) = A\exp\left(\frac{E_a}{RT}\right)\cdot t \quad \text{with } g(\alpha) = \int_{\alpha}^{0}\frac{\mathrm{d}\alpha}{f(\alpha)} \tag{4-6}$$

Equation 4-5 is generally used to describe the rate of a solid-state reaction. The parameters $A, E_a$, and $f(\alpha)$ are referred to as the kinetic triplet. They are yielded by applying isothermal experimental data to Equations 4-5, respectively 4-6 (Khawam and Flanagan, 2006). The limitation of kinetic models on one side and the complexity of solid-state reactions on the other side led to isoconversional (often misleadingly termed model-free) approaches of analyzing solid-state kinetics (Flynn and Wall, 1966). Isoconversional kinetic analysis is briefly reviewed in Section 4-2.

## 4-1 Isokinetic approaches - Kinetic models

The mathematical description of physicochemical rate processes is a model. They are usually derived by physically sound, mechanistic assumptions, however, some models base on empirical observations. Literature on kinetic models and their application to experimental data designates nucleation and nuclei growth, geometric particle shape, diffusion, and reaction order (in conformity with homogeneous chemical reaction kinetics) as widely used and accepted categories of models. The category names refer to the respective rate-limiting process that controls the reaction. The most common and frequently applied kinetic models are compiled in Table 4-1 and visualized in Figure 4-1 (*e.g.* Perez-Maqueda et al., 2006; Skrdla and Robertson, 2007; Brown and Galwey, 1979; Lee and Dollimore, 1998; Khawam and Flanagan, 2006; Brown and Galwey, 1979). Determining appropriate rate expressions for isothermal data is attained by adapting a theoretical model to the experimental $\alpha$ vs. time (also $\alpha - t$) curve. Commonly, kinetic models are grouped by the shape of the curve as that can be acceleratory (*e.g.* P2, P3, P4 in Figure 4-1), linear (*e.g.* R0 in Figure 4-1), deceleratory (*e.g.* all D, G and R1 - R3 models in Figure 4-1) and sigmoidal (*e.g.* all A models as well as T1 in Figure 4-1). (Khawam and Flanagan, 2006; Brown and Galwey, 1979)

Several authors made suggestions for a general relation that expresses all common reaction mechanisms. Šesták and Berggren (1971) proposed Equation 4-7

$$g(\alpha) = \alpha^m(1-\alpha)^n(-\ln(1-\alpha))^p \tag{4-7}$$

with constants $m$, $n$ and $p$ depending on the reaction mechanism. A simplified version of Equation 4-7 was given by Perez-Maqueda et al. (2006). With $p = 0$ and the introduction of an accommodation constant $c$, Equation 4-8 is yielded.

$$g(\alpha) = c(1-\alpha)^n\alpha \tag{4-8}$$

An alternative algorithm was put forward by Ng (1975)

$$g(\alpha) = \alpha^{1-p}(1-\alpha)^{1-q} \tag{4-9}$$

with $0 < p < 1$ and $0 < q < 1$. These generalized expressions, however, are not expedient for the determination of a reaction mechanism as they have no further meaning. The different derivations and implications of kinetic models are briefly introduced below.

**Table 4-1:** Most common kinetic models in solid-state reaction kinetics after Jacobs (1997), Khawam and Flanagan (2006), Brown et al. (1980), Deutsch et al. (1994), and Galwey and Brown (1999). The corresponding $\alpha - t$ curves are given in Figure 4-1.

| Reaction mechanism/model | Symbol | $f(\alpha) = \frac{1}{k}\frac{\mathrm{d}\alpha}{\mathrm{d}t}$ [1] | $g(\alpha) = kt$ [1] |
|---|---|---|---|
| **Nucleation models** | | | |
| autocatalytic (Prout-Tompkins) | T1 | $\alpha(1-\alpha)$ | $\ln(\alpha/(1-\alpha)) + C$ |
| power law | | $n\alpha^{(n-1)/n}$ | $\alpha^{1/n}$ |
| n = 2 | P2 | $2\alpha^{1/2}$ | $\alpha^{1/2}$ |
| n = 3 | P3 | $3\alpha^{2/3}$ | $\alpha^{1/3}$ |
| n = 4 | P4 | $4\alpha^{3/4}$ | $\alpha^{1/4}$ |
| JMAEK [2] | | $n(1-\alpha)(-\ln(1-\alpha))^{(n-1)/n}$ | $(-\ln(1-\alpha))^{1/n}$ |
| n = 2 | A2 | $2(1-\alpha)(-\ln(1-\alpha))^{1/2}$ | $(-\ln(1-\alpha))^{1/2}$ |
| n = 3 | A3 | $3(1-\alpha)(-\ln(1-\alpha))^{2/3}$ | $(-\ln(1-\alpha))^{1/3}$ |
| n = 4 | A4 | $4(1-\alpha)(-\ln(1-\alpha))^{3/4}$ | $(-\ln(1-\alpha))^{1/4}$ |
| **Geometric models** | | | |
| contracting area | G2 | $2(1-\alpha)^{1/2}$ | $1-(1-\alpha)^{1/2}$ |
| contracting volume | G3 | $3(1-\alpha)^{2/3}$ | $1-(1-\alpha)^{1/3}$ |
| **Diffusion models** | | | |
| 1D diffusion | D1 | $1/(2\alpha)$ | $\alpha^2$ |
| 2D diffusion | D2 | $-(1/\ln(1-\alpha))$ | $(1-\alpha)\ln(1-\alpha)+\alpha$ |
| 3D diffusion (Jander) | D3a | $\frac{3(1-\alpha)^{2/3}}{(2(1-(1-\alpha)^{1/3}}$ | $(1-(1-\alpha)^{1/3})^2$ |
| 3D diffusion (Ginstling-Brounshtein) | D3b | $\frac{3}{2((1-\alpha)^{-1/3}-1)}$ | $1-\frac{2}{3}\alpha-(1-\alpha)^{2/3}$ |
| **Reaction order models** | | | |
| zero order | R0 | 1 | $\alpha$ |
| first order | R1 | $1-\alpha$ | $-\ln(1-\alpha)$ |
| second order | R2 | $(1-\alpha)^2$ | $\frac{1}{1-\alpha}-1$ |
| third order | R3 | $(1-\alpha)^3$ | $\frac{1}{2}(\frac{1}{(1-\alpha)^2}-1)$ |

[1] $k$ = rate constant, $\alpha$ = conversion fraction

[2] JMAEK abbreviates Johnson–Mehl–Avrami–Erefe'ev–Kolmogorov (models).

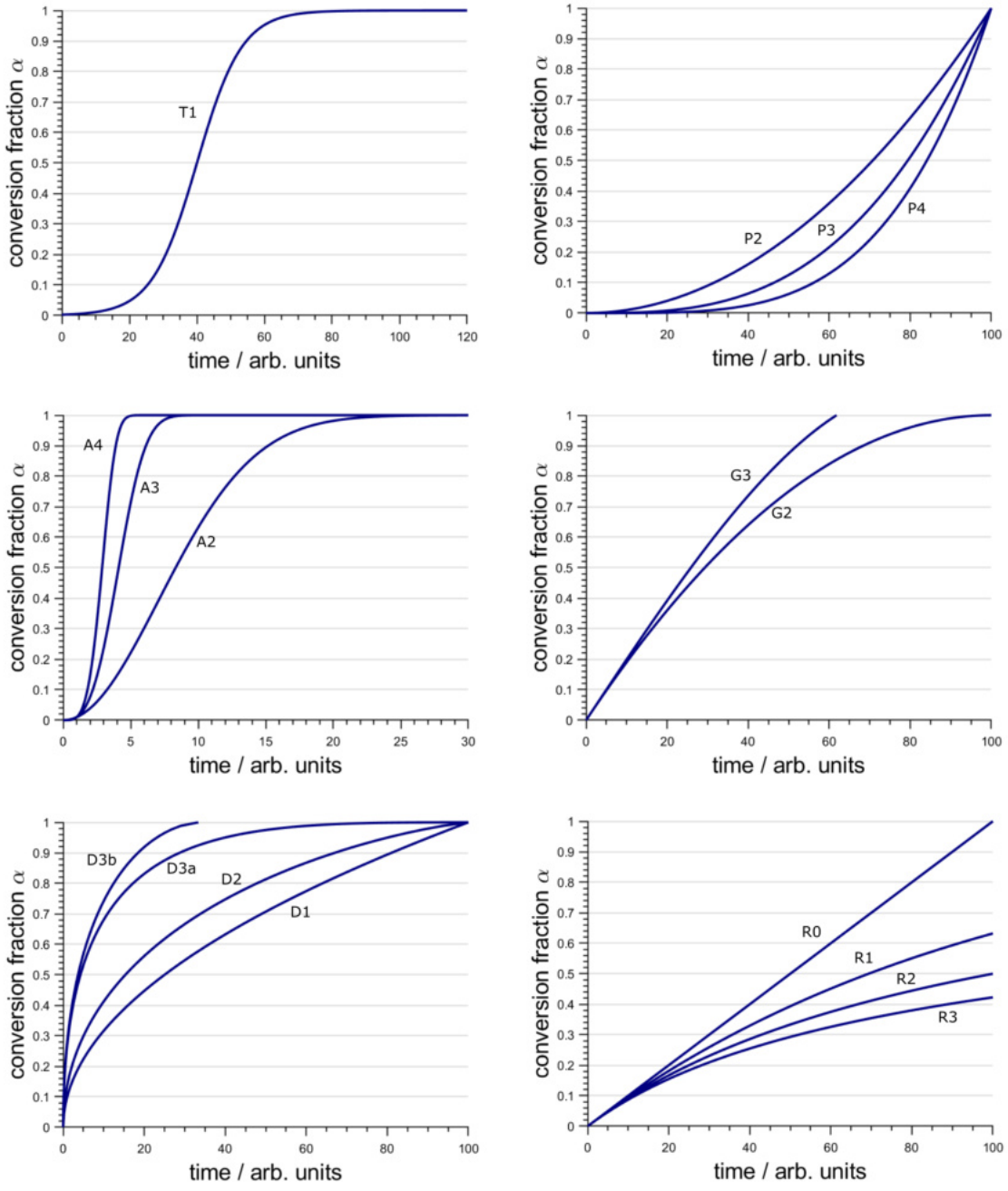


**Figure 4-1:** Visualization of kinetic models as compiled in Table 4-1 as isothermal $\alpha - t$ plots. Data was simulated with a rate constant of $k$ = 0.001 arb. time unit$^{-1}$. For model T1, the rate constant was $k$ = 0.015 arb. time unit$^{-1}$ with integration constant $C = t_{max}$ = 40 (time needed for the maximum rate, inflection point).

**Nucleation models** The concept of nuclei formation and growth impacted the understanding of solid-state reactions profoundly as these reaction mechanisms, *inter alia*, describe decomposition reactions, crystallization processes, and crystallographic transitions (Khawam and Flanagan, 2006, and references therein). The nucleation process is generally described by the simple relation $\mathrm{A(s)} \longrightarrow \mathrm{B(s)} + \mathrm{C(g)}$, where A denotes the solid starting phase, and B and C are the solid, respectively gaseous product phases (Jacobs and Tompkins, 1955). The reaction involves conversion of a small reactant volume to a product and subsequent growth of that product at the contact interface between new and old phase. Nucleation initiation must proceed at the reactants' surfaces where local $E_a$ minima are present. Such regions are preferred reaction onset sites due to diminished lattice stabilization caused by flaws like cracks, dislocations or point defects (Bamford and Tipper, 1972). Several laws of nucleation have been derived. Mathematically, they can be divided into instantaneous nucleation (Equation 4-10), linear single-step nucleation (Equation 4-11), exponential single-step nucleation (Equation 4-12), and multi-step nucleation according to the power law (Equation 4-13, Young, 1966).

$$N = N_0 \tag{4-10}$$

$$N = k_N N_0 t \tag{4-11}$$

$$N = N_0(1 - \exp^{k_N t} \tag{4-12}$$

$$N = Kt^{\beta} \text{ with } K = \frac{N_0(k_i t)^{\beta}}{\beta!} \tag{4-13}$$

with $N$ = number of nuclei present at time $t$, $N_0$ = total number of potential nucleus formation sites, $k_N$ = nucleation rate constant, $\beta$ = successive events of growth nucleus formation with each event having a probability of $k_i$ (Young, 1966; Bamford and Tipper, 1972).

The overall volume of product $V(t)$ at $t$ is then yielded by combination of a nuclei formation rate ($\mathrm{d}N/\mathrm{d}t$) and a nuclei growth law ($F(t)$) as given in Equation 4-14. Integration allows to give rate expressions in the form of $g(\alpha) = kt$, however, as no functional relation between formation and growth terms exists, assumptions about nucleation and growth rates must be made. Subsequently, this obtains i) the power law models, ii) the Johnson-Mehl-Avrami-Erofe'ev-Kolmogorow (JMAEK) models, and iii) the Prout-Tompkins model (autocatalytic model). Throughout formal theories, the assumption of a constant growth rate $F(t) = k_g$ is regarded as a satisfactory simplification.

$$V(t) = \int_0^t \sigma\Big(\int_{t_j}^t F(t)\mathrm{d}t\Big)^{\lambda}\Big(\frac{\mathrm{d}N}{\mathrm{d}t}\Big)_{t=t_j}\mathrm{d}t_j \tag{4-14}$$

with

$$\sigma\Big(\int_{t_j}^t F(t)\mathrm{d}t\Big)^{\lambda} = \sigma(r(t,t_0))^{\lambda} = V(t,t_j) \tag{4-15}$$

where $\sigma$ = shape factor of nuclei, *e.g.* $\frac{4\pi}{3}$ for a sphere, $\lambda$ = growth dimension, $r(t,t_j)$ = radius and $V(t,t_j)$ = volume of growth nucleus formed at time $t_j$ (Bamford and Tipper, 1972).

i) In the case of nucleation obeying the power law, $V(t)$ is directly proportional to $\alpha$ and the power law is yielded (Equation 4-16).

$$\alpha = Ck_N^{\beta}k_g^{\lambda} = (kt)^n \tag{4-16}$$

with $C$ = constant of proportionality and $\beta + \lambda = n$. Random nucleation following the exponential law and $F(t) = k_g$, equals the power law with $n = 4$.

ii) As the nucleation and growth processes do not maintain a continuous increase throughout the whole reaction, constraints are applied in the case of JMAEK kinetic models. The two factors identified for nuclei development restriction are coalescence and ingestion. The restrained nucleation rate can be expressed as a modified exponential law which can not be analytically solved but bypassed by the introduction of an extended conversion fraction $\alpha' = -\ln(1-\alpha) = (kt)^n$. By this, the general expression for JMAEK models is yielded (Equation 4-17, Avrami, 1939, 1940; Erofe'ev, 1946; Johnson, 1939; Kolmogorov, 1937).

$$-\ln(1-\alpha) = (kt)^n \tag{4-17}$$

iii) In solid-state kinetics, the mechanism of autocatalysis refers to the multiplication or branching of nuclei (analogous to homogeneous chain reactions) which is induced by structural changes. Such changes are the formation of dislocations, cracks, and strain at the reaction interface. Further along the reaction, branching will be terminated or curtailed as the converted material increases (Jacobs, 1997). In autocatalytic reactions, the nucleation rate is influenced by existing nuclei catalyzing new nuclei and is modified to include an initiation term, a branching term, and a termination term. Ultimately, Equation 4-18 is reached. This is the Prout–Tompkins model where equal nucleation and branching rate constants are assumed (symmetrical $\alpha - t$ curve).

$$\ln\frac{\alpha}{1-\alpha} = k_b t + C \tag{4-18}$$

where $k_B$ is the branching rate constant and $C$ an integration constant (Prout and Tompkins, 1944). The expression has been modified by *e.g.* Skrdla (2004) to include two different rate constants for branching and nucleation (non-symmetrical $\alpha - t$ curve).

**Geometric models** Here, rapid and dense nucleation is assumed that is followed by progression of all or specific surfaces into the bulk crystallite. The models are distinguished by the geometry of the advancing reaction interface. If nucleation is restricted to specific crystallographic surfaces, the interface can be described as a contracting area (Equation 4-21). Likewise, a contracting volume interface is evident if nucleation occurs on all crystallographic faces (Equation 4-20).

Nucleation on all faces causes the conversion fraction to depend on the particle volume and equals

$$\alpha = \frac{r_0^3 - r^3}{r_0^3} \tag{4-19}$$

where $r$ is the nucleus radius at time $t$ and $r_0$ is the initial radius at time $t_0$. With $r = r_0 - kt$, and $k_v = \frac{k}{r_0}$, $\alpha$ is expressed as

$$\alpha = 1 - (1 - \alpha) = (k_v t)^3 \tag{4-20}$$

(Khawam and Flanagan, 2006). For disc- or plate-like particles, the model depends on $r^2$ and is given by the following equation (Galwey and Brown, 1999).

$$1 - (1 - \alpha) = (k_v t)^2 \tag{4-21}$$

**Diffusion models** In the solid-state, diffusion-limited processes yield reaction rates that are defined by movement and transport of atoms in a crystal structure promoted by point, line, and surface defects. Kinetic expressions are mainly derived by solid–gas interactions and arise from interface advance assumptions, where the rate of product formation decreases proportionally with the increase of product (Jacobs and Tompkins, 1955). In the case of a constant surface area, the kinetic rate solely depends on the product barrier layer and one-dimensional diffusion is obeyed (Equation 4-22). This corresponds to the parabolic rate law as it describes an infinite flat plane without a shape factor (Koga and Criado, 1998).

$$\alpha = (k_G t)^{1/2} \tag{4-22}$$

Two-dimensional diffusion is described by Equation 4-25. The reaction rate bases on a cylindrical particle. Accordingly, the three-dimensional diffusional model assumes spherical solid particles and Equations 4-23 and 4-24 are obtained. In both dimensions, the thickness of the reaction zone $x$ determines $\alpha$. For three-dimensional diffusion, $x$ is related to $\alpha$ with $x = r(1 - (1 - \alpha))^{1/3}$. Following Jander's approach, $x$ depends on $t$ with the parabolic law $x^2 = kt$ (Jander, 1927). By this, Equation 4-23 is obtained.

$$(1 - (1 - \alpha)^{1/3})^2 = k_e t, \quad k_e = \frac{k}{r^2} \tag{4-23}$$

Ginstling and Brounshtein (1950) approached the three-dimensional diffusion model by relating $x$ to $t$ with $x^2\left(0.5 - \frac{x}{3r}\right) = kt$. Then, Equation 4-24 is yielded (Khawam and Flanagan, 2006).

$$1 - \frac{2}{3}\alpha - (1 - \alpha)^{2/3} = kt \tag{4-24}$$

Two-dimensional diffusion links $x$ to $\alpha$ with $x = r(1-(1-\alpha))^{1/2}$. Usually, the approach by Ginstling and Brounshtein is followed, which leads to the expression below.

$$(1-\alpha)\ln(1-\alpha) + \alpha = k_d t, \quad k_d = \frac{4k}{r^2} \tag{4-25}$$

**Reaction order models** These models use reaction rates that are proportional to the unconverted fraction raised to a specific power ($n$). Their accountability to solid-state processes is questioned (Vyazovkin and Wight, 1998). Their general rate equation is given by Expression 4-26 and depending on the value of $n$, integration gives Equations 4-27 - 4-30.

$$\frac{\mathrm{d}\alpha}{\mathrm{d}t} = k(1-\alpha)^n \tag{4-26}$$

$$\alpha = kt \quad \text{for } n = 0 \tag{4-27}$$

$$-\ln(1-\alpha) = kt \quad \text{for } n = 1 \tag{4-28}$$

$$\frac{1}{1-\alpha} - 1 = kt \quad \text{for } n = 2 \tag{4-29}$$

$$\frac{1}{2}((1-\alpha)^{-2} - 1) = kt \quad \text{for } n = 3. \tag{4-30}$$

Model-bound or isokinetic analysis is supplemented by determination of $E_a$ values and $A$. By conducting several isothermal measurements at different temperatures (or a single non-isothermal experiment) and assessing the most appropriate reaction model, Equation 4-4 can be applied in the linear form ($\ln k = \frac{E_a}{R} \cdot \frac{1}{T} + \ln A$). Accordingly, plotting $\ln k$ vs. $\frac{1}{T}$ yields $E_a$ from the slope and $A$ from the intercept. This type of plot is known as Arrhenius plot and widely used throughout all fields of chemical, biological, and material sciences (*e.g.* Flanders et al., 1997; Stanley and Luzio, 1978; Hamada and Takeda, 1994). Due to the problematic prerequisite of describing reactions with a mechanistic model that might be physically unsuitable in the first place, deviations from the linear Arrhenius equation are often the case (Koga, 1994; Truhlar and Kohen, 2001).

## 4-2 Isoconversional approaches

Isoconversional methods do not presume a phenomenological model or constant $E_a$ and $A$ values as conventional model-fitting analysis does. Nevertheless, they are not assumption-free, as the basic concept demands that at any given $\alpha$, the same reactions occur in the same ratio independent of temperature. In reality, this temperature independence might not always be the case (Golikeri and Luss, 1972). Anyhow, isoconversional methods avoid the analytical problem of finding the correct reaction model which can be ambiguous in cases where solid-state reactions are more complex than model-bound assumptions permit (Vyazovkin and Wight, 1997; Vyazovkin, 2000). Varying activation energies can be sufficiently described by isoconversional methods in a wide range of circumstances (Venkatesh et al., 2013).

Isoconversional kinetic analysis therefore involves the evaluation of a dependence of effective $E_a$ values on $\alpha$ and requires a series of experiments at different temperatures (isothermal) or different heating rates (non-isothermal). The cause of differing $E_a$ values can lie in particle size variations or crystal imperfections (true variation) but also arise from the employed kinetic method (artifactual variation, Galwey, 2003; Khawam and Flanagan, 2005).

In the following, the focus is on the analysis of isothermal data, due to the use of isothermal conditions in the present work. In many cases however, isoconversional methods were intended for non-isothermal experiments including different heating rates, altering Equation 4-3 to

$$\frac{\mathrm{d}\alpha}{\mathrm{d}T} = \frac{1}{\beta}\, k(T) f(\alpha) \tag{4-31}$$

where $\beta$ represents the heating rate. With knowledge of the equivalent reaction stages for each heating rate (fixed $\alpha$ values), kinetic analysis can be perfomed (Starink, 1997). The methods can be differential (*e.g.* methods according to Friedman (1964) and Gao and Wang (1986)) or integral. Latter include methods proposed by Kissinger (1957), Augis and Bennett (1978), Akahira and Sunose (1971), Boswell (1980), Flynn and Wall (1966), Ozawa (1965), and Vyazovkin (1997). The isoconversional methods for isothermally acquired data are often adapted from the non-isothermal case. The general isoconversional concept (for isothermal data) is shown graphically in Figure 4-2.

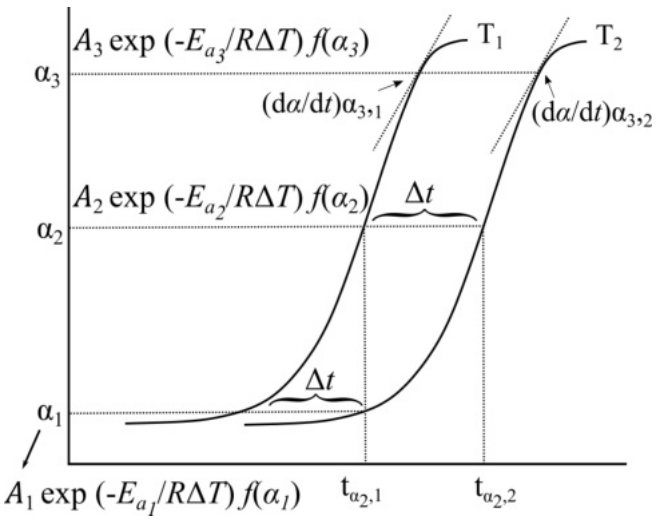


**Figure 4-2:** Representation of isoconversional principles adapated for the isothermal case from Vyazovkin and Sbirrazzuoli (2006): The Arrhenius equation is applied to fixed $\alpha$ values obtained by multiple isothermal measurements to obtain $E_a$ values.

The most common differential method by Friedman (1964) is more often used in its integral form which is then referred to as standard method. The integral method was published by Flynn and Wall (1966) and Ozawa (1965) and is also termed Flynn–Wall–Ozawa method. It takes the natural logarithm of Equation 4-6 which gives Equation 4-32. By plotting $-\ln t$ against $1/T$ at each $\alpha$, activation energies are obtained independent of the mechanistic model.

$$-\ln(t) = \ln\left(\frac{A}{g(\alpha)} - \frac{E_a}{RT}\right) \tag{4-32}$$

If the activation energy varies with $\alpha$, it is usually ascribed to a multi-step reaction mechanism. In fact, it is well applicable to systems where multiple reactions occur. The method fails however, if reactions of widely different type or competitive character with differing products take place (Venkatesh et al., 2013).

Originally, Friedman used the natural logarithm of Equation 4-5 which gives expression 4-33. $E_a$ values are yielded by plotting $\ln \frac{\mathrm{d}\alpha}{\mathrm{d}t}$ vs. $1/T$ at respective $\alpha$ values.

$$\ln\left(\frac{\mathrm{d}\alpha}{\mathrm{d}t}\right) = \ln(Af(\alpha)) - \frac{E_a}{RT} \tag{4-33}$$

A possible verification for the accuracy of both, the integral and differential version of the standard isoconversional method, is to use them on the same data. Corroboration of activation energies indicate independance of $\alpha$ and, therefore, trustworthy or meaningful results (Dowdy, 1987).

Vyazovkin (1997) developed an advanced integral isoconversional method (AIC) for non-isothermally measured data which can also be altered and used for isothermal kinetic analysis. It was primordially designed to increase the accuracy of $E_a$ estimation when the samples actual temperature deviates from the prescribed heating program. The AIC method (non-isothermal case) employs a non-linear algorithm (in contrast to the linear differential and integral methods mentioned above, Equation 4-34).

$$\left|\sum_{i=1}^{n}\sum_{j\neq 1}^{n}\frac{I(E_{a\alpha}, T_{\alpha i})\beta_j}{I(E_{a\alpha}, T_{\alpha j})\beta_i}\right| = \min \tag{4-34}$$

with

$$I(E_a, T_\alpha) = \int_{T_\alpha}^{t_0} \exp\frac{-E_a}{RT}\mathrm{d}T \tag{4-35}$$

where $n$ is the number of experiments carried out at different heating rates $\beta$ and $i, j = 1, 2, ..., n$ are the ordinal numbers of two experiments performed at different temperatures (Vyazovkin, 1997, 2000).

Adopted for the isothermal case, the equations change to Expressions 4-36 and 4-37.

$$\left|\sum_{i=1}^{n}\sum_{j\neq 1}^{n}\frac{I(E_{a\alpha},T_i(t_\alpha))}{I(E_{a\alpha},T_j(t_\alpha))}\right| = \min \tag{4-36}$$

$$I(E_a,T(t)) = \int_{t_{\alpha-\Delta\alpha}}^{t_\alpha} \exp\frac{-E_{a\alpha}}{RT_0}\mathrm{d}t \tag{4-37}$$

with the isothermal temperature $T_0$, $\Delta\alpha = 1/m$ and $m$ = number of $\alpha$ segments chosen for integration. Applied to experimental data, the activation energy represents the parameter that minimizes the algorithm (Pratap et al., 2007; Khawam and Flanagan, 2005).

Kinetic analysis of solid-state reactions is an important and extensive research area with theories and methods that are constantly questioned as knowledge progresses. Numerous studies are occupied with finding the most adequate way of analyzing their respective data kinetically. However, the essential two types of analysis are model-bound or isokinetic and "model-free" or isoconversional. Isokinetic methods fully depend on the reaction model and assume Arrhenius temperature-dependence of rate constants, which must not always be the case (Šimon, 2009). They are not able to divide the contribution of the reaction model and the reaction rate in a doubt-free manner, and the conversion fraction determines the temperature sensitivity of the reaction rate (Pratap et al., 2007). Thus, they are approximate methods. Isoconversional methods are regarded as more precise when it comes to calculating activation energies, however, they are also not assumption-free as stated above. Additionally, they do not help understanding the respective reaction mechanisms as the absence of such is inherent and demanded for these methods to work (Vyazovkin et al., 2011).

# Chapter 5

# Materials and methods

In this chapter, the materials used for all preliminary measurements and dehydration and rehydration experiments in the $CaSO_4$ – $H_2O$ system are declared. Further, the experimental set-ups and procedures are described.

## 5-1 Materials

This Section contains a a listing of the utilized materials. Corresponding links are given in Table B-1. If applied, further treatment of the material is specified.

### 5-1-1 Calcium sulfates

For all dehydration and rehydration experiments, synthetic calcium sulfate dihydrate from Emsure Merck (CAS 10101–41–4, ≤0.01% fractions insoluble in HCl, precipitated for analysis) was used. To rehydrate residual traces of other calcium sulfates, it was treated with demineralized water at 45 °C for one day. The recrystallized material was ground in an agate mortar for 15 min and subsequently sieved into grain sizes of ≤ 50 µm for particle size-independent measurements. It was further separated into ≤ 20 µm, 20 µm - 25 µm, 25 µm - 32 µm, 32 µm - 36 µm, 32 µm - 50 µm, 50 µm - 53 µm, and 75 µm - 80 µm fractions for particle size-dependent experiments. Ethanol was used as the sieving agent. As gravitational separation of particles ≤ 20 µm is not expedient and, moreover, hardly possible, the respective fraction was not sieved into finer units.

Synthetic gypsum originating from one product batch was used to avoid diversification of sample-inherent influences on reaction kinetics, which is not an unusual phenomenon. As stated in Chapter 2, synthetic calcium sulfate dihydrate is structurally identical to gypsum, which made the usage of natural samples obsolete. This was an advantage as the latter often suffer from inhomogeneity which could affect experimental results negatively.

For dehydration experiments, further treatment of the sample powder prior to measurements was not necessary. Regarding rehydration experiments, only the $\beta$-modification of hemihydrate, and $\beta$-anhydrite were relevant as starting materials, as they are equivalent to the respective mineral phases. $\beta$-Hemihydrate (in the following simply called hemihydrate) was either produced *in situ* inside the respective sample chamber for non-ambient conditions or in a drying cabinet by heating it to 80 °C - 120 °C for several minutes to hours or days. The exact heat treatment is described for the respective experiments in Chapter 6. $\beta$-Anhydrite was produced by treating the gypsum powder at 300 °C for three months.

### 5-1-2 Standard materials

Powder XRD measurements to verify and control the sample height algorithm of the DIFFRAC.SUITE TOPAS software by Bruker (Bruker, AXS, 2009) were conducted using silicon powder, which was produced by powdering of a piece of a monocrystalline silicon wafer from Siltronic.

Raman spectroscopic measurements for temperature-control verification of the Linkam THMS600 sample stage were conducted using benzophenone crystals ($C_{13}H_{10}O$) with a melting point at 48.5 °C from Carl Roth (CAS 119-61-9). The humidity sensor of the Linkam RH95 controller, set up to regulate humidity values inside the THMS600 sample stage, was vetted with LiCl humidity standards by Rotronic.

### 5-1-3 Starting materials for salt solutions

For all *ex situ* long-term dehydration experiments, eight slightly supersaturated salt solutions based on four different salts, were prepared. When kept in enclosed chambers, these solutions generate characteristic, constant humidities. In particular, the metal halides $MgCl_2$, LiCl, $ZnBr_2$, and LiBr were selected. The first three salts were used to prepare solutions as follows. Circa 200 mL demineralized water was heated in a beaker using a heating plate. The temperatures were slightly higher than the respective target values of 60 °C and 80 °C. While monitoring the temperatures and stirring constantly, solutes were added until no more material dissolved and precipitation occurred. Based on salt solubilities at 25 °C as given by the GESTIS Substance Database (Institut für Arbeitsschutz der Deutschen Gesetzlichen Unfallversicherung, 2003), the needed quantities for saturated solutions of 200 mL at elevated temperatures were estimated. The fourth solution was obtained using $LiOH \cdot H_2O$ and HBr (aq) to produce LiBr according to the reaction below.

$$LiOH \cdot H_2O\,(l) + HBr\,(aq) \longrightarrow 2\,H_2O\,(l) + LiBr\,(aq)$$

Therefore, a reaction mixture of $LiOH \cdot H_2O$ and $H_2O$ was prepared by elutriating 100 g $LiOH \cdot H_2O$ with cold demineralized water. HBr (aq) was incrementally added until neutralization was reached and precipitation emerged. To neutralize 100 g (2.38 mol) $LiOH \cdot H_2O$, circa 130 mL (2.38 mol) of aqueous HBr (47%, $\rho = 1480\,g\,L^{-1}$) were needed. The yielded solution was split and concentrated at temperatures above 60 °C and 80 °C so that two supersaturated aqueous LiBr solutions at respective target temperatures were received. Information on utilized salts and starting materials is given in Table 5-1.

**Table 5-1:** Information on substances used for salt solutions.

| Substance | Manufacturer | CAS | Solubility |
|---|---|---|---|
| $MgCl_2$, purum: $\geq$ 98 % (KT) | Fluka Chemica (Sigma Aldrich since 1989) | 7786-30-3 | solubility at 20 °C: $727\,g\,L^{-1}$ resulting in $\gg$ 108.4 g salt for 200 mL solution at elevated temperatures |
| LiCl, purum: 98+% | Alfa Aesar | 7447-41-8 | solubility at 20 °C: $835\,g\,L^{-1}$ resulting in $\gg$ 166.4 g salt for 200 mL solution at elevated temperatures |
| $ZnBr_2$, purum: 99.9% metal basis | Alfa Aesar | 299465-28-4 | solubility at 20 °C: $4470\,g\,L^{-1}$ resulting in $\gg$ 894 g salt for 200 mL solution at elevated temperatures |
| $LiOH \cdot H_2O$, purum: 98% min (ACS) | VWR Chemicals | 1310-66-3 | solubility at 80 °C: $2680\,g\,L^{-1}$ (Lide, 2004) |
| HBr, 47%, AnalaR NORMAPUR analytical reagent | VWR Chemicals | 10035-10-6 | |

## 5-2 Methods and experimental set-ups

Followingly, the used methods and experimental set-ups are described. Information on data evaluation and analysis is stated.

### 5-2-1 (*In situ*) powder XRD

Temperature-, humidity- and time-dependent experiments were conducted with a CHCplus+ Cryo- and Humidity Chamber by Anton Paar. The CHCplus+ chamber was equipped with a resistance heater, compressed air cooling, a Pt 100 temperature sensor, a gas humidifier, and a calibrated relative humidity sensor. The chamber assembly and selected elements are shown in Figure 5-1.

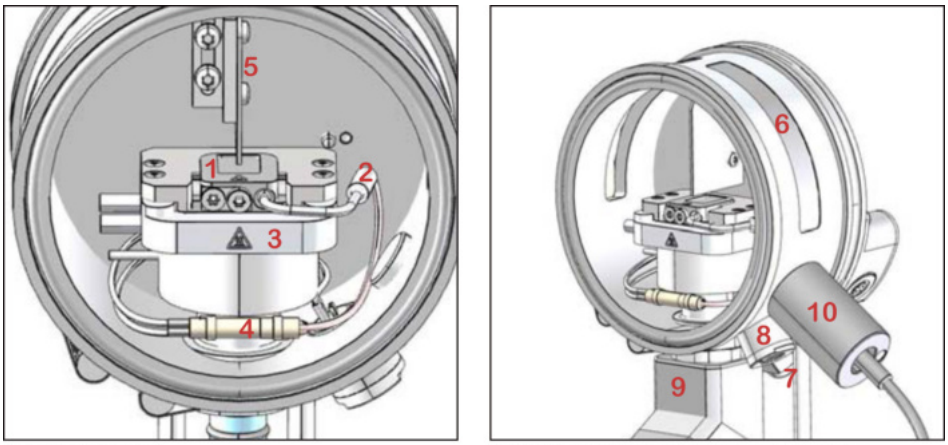


**Figure 5-1:** Internal parts and housing with connectors of the CHC plus+ Cryo & Humidity Chamber by Anton Paar, adapted from Anton Paar GmbH (2018).

The chamber itself was mounted on a X-ray powder diffractometer D8 Discover by Bruker. The device specifications are given in Table 5-2. Measurement operation was conducted with a CCU 100 combined control unit (−5 °C - 300 °C, 0.01 °C resolution, by Anton Paar) and a MHG-32 modular humidity generator using nitrogen carrier gas (5 % - 95 % at 5 °C - 80 °C, 0.01 % resolution, by proUmid). The temperature and humidity values were specified along with measurement parameters via the measuring software (Bruker DIFFRAC software package). For measurements below 80 °C, relative humidity values at the sample were set directly in the operating software. For measurements at higher temperatures, humidity control was not possible due to the chamber specifications. For experiments between 80 °C and 100 °C, the relative humidity values present at the sample could be derived by considering the humidity sensor temperature of 29 °C ± 0.01 °C (preset by the manufacturer), the sample temperature, and the relative humidity values (available for each measurement in the recorded experimental metadata) using Equation 5-1.

$$RH_{sample} = \frac{RH_{sensor} \cdot p^{sat}_{\mathrm{H_2O}}(T_{sensor})}{p^{sat}_{\mathrm{H_2O}}(T_{sample})} \tag{5-1}$$

with relative humidities $RH$ at the sample and the sensor, saturation vapor pressures of water $p^{sat}_{\mathrm{H_2O}}$, and temperature $T$. Relative humidities are defined as the ratio of the partial pressure of water-vapor to the saturation vapor pressure of water in air at a specific temperature: $RH = \frac{p_{\mathrm{H_2O}}}{p^{sat}_{\mathrm{H_2O}}(T)}$. The saturation water-vapor pressure values were calculated using the Magnus equation (Equation 5-2, Magnus, 1844) after Murray (1967). The equation is based on an empirical approximation for saturation vapor pressures over a surface of liquid water.

$$p^{sat}_{\mathrm{H_2O}}(T[^{\circ}\mathrm{C}]) = 6.1078\,\mathrm{hPa} \cdot \exp\left(\frac{17.269388 \cdot T[^{\circ}\mathrm{C}]}{237.30 + T[^{\circ}\mathrm{C}]}\right) \tag{5-2}$$

For experiments above 100 °C, $p_{\mathrm{H_2O}}$ values at the samples were calculated using the modified version of equation 5-2 as given in Expression 5-3 (Ritterbach and Becker, 2020).

$$p_{\mathrm{H_2O},sample} = \frac{RH_{sensor}[\%] \cdot 6.1078\,\mathrm{hPa} \cdot \exp\left(\frac{17.269388 \cdot T_{sensor}[^{\circ}\mathrm{C}]}{237.30 + T_{sensor}[^{\circ}\mathrm{C}]}\right)}{100} \tag{5-3}$$

Throughout dehydration and rehydration experiments, logging of temperature and humidity values was done to enable the exclusion of experiments exhibiting anomalies caused by regulation difficulties from analysis. These irregularities were only present during some rehydration experiments of hemihydrate at 95 % RH and likely caused by a damaged temperature sensor. Due to a local dew point underrun with water-vapor condensation at the knife edge, dripping of water droplets onto the sample and the sensor occurred. After fixing the sensor, regulation functioned normally and did not cause further problems.

Phase identification was done using the database PDF2 installed on the DIFFRAC.EVA software package by Bruker (Bruker, AXS, 2009). Quantitative determination of phase contents and lattice parameter refinements were conducted with the Rietveld method using JEdit (Evans, 2020) and the DIFFRAC.SUITE TOPAS software package by Bruker (Bruker, AXS, 2009). Calculation of diffraction patterns of calcium sulfate minerals and subhydrates was done using the RIETAN-FP software (Bragg-Brentano geometry, variable slits, $\mathrm{CuK}_{\alpha_1}$ radiation, pseudo-Voigt profile functions, Izumi and Momma, 2007) implemented in the VESTA 3 software (Momma and Izumi, 2008).

Powder XRD measurements with defined sample height-displacements were conducted in the CHCplus+ chamber at ambient temperature and humidity conditions from 27° - 58° 2Θ, with a step size of 0.02 and an exposure time of 1 s step$^{-1}$. Silicon powder was used as sample material and prepared with great care considering a plane sample surface. The vertical positioning of the sample stage for an accurate alignment of 0 mm height-displacement was determined with a $z$-scan.

Quantitative phase analysis results were used to derive the conversion fraction $\alpha$. As stated in Chapter 4, this is the integrity measure applied in kinetic analysis. Since the dehydration and rehydration experiments followed the conversion of a first into a second phase, the system was regarded as binary leading to Expression 5-4.

$$\alpha(product) = \frac{x_0^{product} - x_t^{product}}{x_0^{product} - x_{final}^{product}} \tag{5-4}$$

where $x_0$ is the initial molar fraction of the product phase, $x_t$ is the molar fraction after time $t$ and $x_{final}$ is the molar product fraction after completion of conversion. The experimental $\alpha - t$ curves were fitted using the Matlab software suite (Version R2019b, Math Works, Inc., 2019).

*In situ* measurements were conducted in the angular (2Θ) range of 10° - 50° with a step size of 0.02° and a counting time of 0.3 s step$^{-1}$. Samples were prepared by sieving a fine layer of sample powder onto a silicon zero-background sample holder. This technique was found to most likely reduce particle alignment and diffusion aspects to superimpose phase transformation kinetics.

Standard/*ex situ* powder XRD measurements were conducted either on a Bruker D8 Discover or a Stoe Stadi MP diffractometer (device specifications given in Table 5-2). Atacama soil samples and (synthetic equivalents of) calcium sulfate minerals (Chapters 6-1 and 6-2-1) were measured from 5° - 80° 2Θ on the Bruker D8 diffractometer with a step size of 0.015, irradiation of 1 s step$^{-1}$, and a sample rotation of 3 °min$^{-1}$. The analysis of powder samples used for long-term dehydration experiments were conducted from 10° - 50° (D8 Discover) or 10° - 80° (Stoe Stadi MP) 2Θ with a step size of 0.02 and 1 s step$^{-1}$ irradiation.

**Table 5-2:** X-ray powder diffractometer information.

| | **Bruker D8 Discover** | **Stoe Stadi MP** |
|---|---|---|
| **Geometry** | Reflexion (Bragg–Brentano) geometry | Transition (modified Guinier) geometry |
| **Detector** | One-dimensional energy dispersive strip detector (LynxEye XE) | Curved imaging plate detector (IP-PSD, 140° aperture) |
| **Soller slits** | 2.5° | - |
| **Filter** | Ni | - |
| **Monochromator** | - | Ge(111) |
| **Radiation** | Cu $K_{\alpha_1}$ | Cu $K_{\alpha_1}$ |
| **Divergence slits** | variable | non-variable |
| **Voltage/amperage** | 40kV/40mA | 40kV/30mA |

### 5-2-2 (*In situ*) Raman spectroscopy

Temperature-, humidity- and time-dependent Raman spectroscopy experiments were conducted using an apparatus consisting of a confocal $\mu$Raman microscope (inVia Qontor by Renishaw). The device was coupled with an optical microscope in 180° backscattering geometry (Eclipse LVDIA-N by Nikon), equipped with a motorized sample stage and a back-illuminated, highly sensitive photon sensor detector (Century 05TJ52 by Renishaw). The spectrometer was endowed with a THMS600 heating and freezing sample stage by Linkam, suitable for humidity control.

The THMS600 sample stage (ambient to 300 °C without external cooling) was operated with a T96 System Controller (using a PT100 sensor with 0.01 °C accuracy) and a RH95 Humidity Controller (using a combined temperature and humidity digital capacitance sensor, stability at control value ± 0.5%). The chamber humidity was set manually according to the humidity-sensor temperature and not the sample temperature. Through transformation of expression 5-1 and knowledge of the target humidity at the sample, the required sensor humidity was specified.

For experiments at elevated temperatures, it was necessary to know the correct humidity sensor temperatures to be able to set humidity values. Therefore, sensor temperatures were monitored during heating and are compiled, together with saturation vapor pressures, in Table 5-3.

**Table 5-3:** Sample and sensor temperatures $T_{sample}$, $T_{sensor}$ inside the THMS600 sample stage with corresponding saturation vapor pressures $p^{sat}_{\mathrm{H_2O}}$. The values base on the Magnus equation (Expression 5-2).

| $\boldsymbol{T_{sample}}$/°C | $\boldsymbol{T_{sensor}}$/°C | $\boldsymbol{p^{sat}_{\mathrm{H_2O},sample}}$/hPa | $\boldsymbol{p^{sat}_{\mathrm{H_2O},sensor}}$/hPa |
|---|---|---|---|
| 50.0 | 22.5 | 123.5 | 27.2 |
| 55.0 | 22.8 | 157.6 | 27.7 |
| 60.0 | 23.1 | 199.4 | 28.2 |
| 65.0 | 23.4 | 250.4 | 28.8 |
| 70.0 | 23.8 | 312.0 | 29.5 |
| 75.0 | 24.2 | 385.9 | 30.2 |
| 80.0 | 24.6 | 474.1 | 30.9 |
| 85.0 | 25.0 | 578.6 | 31.7 |
| 90.0 | 25.4 | 701.8 | 32.4 |
| 95.0 | 25.9 | 846.0 | 34.4 |
| 100.0 | 26.4 | 1013.0 | 34.4 |
| 105.0 | 27.0 | 1208.1 | 35.6 |
| 110.0 | 27.6 | 1433.2 | 36.9 |
| 115.0 | 28.1 | 1692.7 | 38.0 |
| 120.0 | 28.6 | 1988.6 | 39.1 |

Figure 5-2 shows the THMS600 sample stage interior and exterior without the covering lid. The lid itself had a 0.5 mm-thick and 22 mm-wide glass window suitable for confocal Raman measurements.

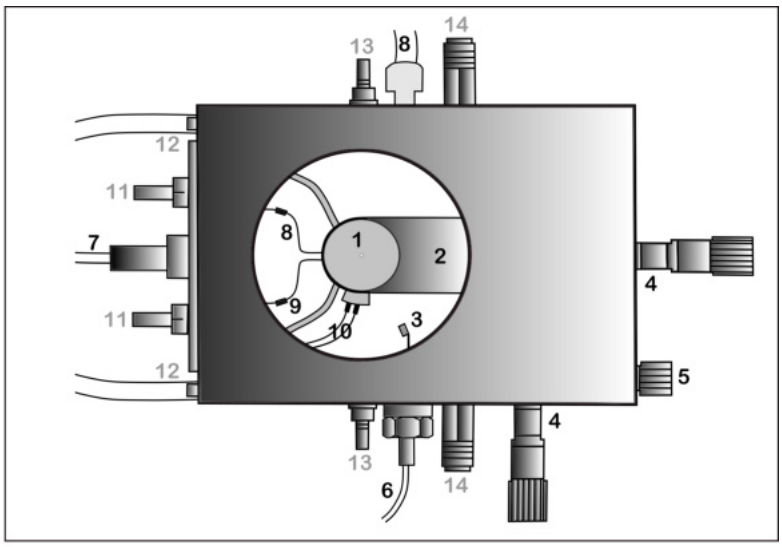


**1** Silver heating block (location of sample)
**2** Sample holder
**3** Humidity sensor
**4** Sample manipulator
**5** Door locking screw
**6** Humidity connector
**7** Lemo connector for stage lead
**8** Heating element wire
**9** Stainless steel cooling tube
**10** Pt temperature sensor
**11** Liquid nitrogen cooler connection
**12** Bypass stage body water cooling
**13** Stage body water connector
**14** Gas purge velve

**Figure 5-2:** THMS600 high-temperature stage assembly by Linkam including humidity sensor. Drawing without stage lid. The gray colored numbers mark elements that are irrelevant to the measurements carried out for this work.

All *in situ* measurements were conducted using a Nd-YAG laser source of 532 nm (output power of 100 mW) and a grating of 1800 l $mm^{-1}$. The spectral range was 100 $cm^{-1}$ - 4000 $cm^{-1}$. The SynchroScan method by Renishaw for artifact-free, wide-range spectra was used with an exposure time of 10 s. Usually, broad-range spectra are made by joining multiple spectra together. By applying the SynchroScan method, continuous scanning avoids mismatches at the joins (that can be caused by laser quenching or fluorescent backgrounds). A laser filter to reduce the laser power to 5% was applied and single acquisitions were performed. Solely, the temperature-dependently measurements (Chapter 6-2-3) were conducted from 373 $cm^{-1}$ - 1191 $cm^{-1}$ with a grating of 3000 l $mm^{-1}$, an exposure time of 2 s (100% laser power) and 30 accumulations per measurement. Temperature conditions were specified with the measuring parameters in the operating software WiRE 5.0 by Renishaw (Renishaw, 2019). Humidity values could not be defined in the software and were controlled manually. Hence, only logging of temperature values was possible but preliminary tests on humidity generation showed no regulation difficulties or oscillations.

As a result of external humidity control, rehydration experiments were exclusively conducted at 22 °C, which was the temperature prevailing in the laboratory for laser wavelength and spectrometer stabilization, and varying relative humidities. In doing so, a temperature fall of the sample stage housing below the dew point and condensation threshold was avoided. For example, a process temperature of 30 °C with a housing temperature of 22 °C has a relative humidity threshold of 62.35 %. The dew point ($T_d$) is usually approximated by an altered Magnus equation (Equation 5-5).

$$T_d = \frac{b_1\left(\ln RH + \frac{a_1 T[°C]}{b_1+T[°C]}\right)}{a_1 - \ln RH - \frac{a_1 T[°C]}{b_1+T[°C]}} \tag{5-5}$$

with relative humidity values $RH$, $a_1 = 7.625$ and $b_1 = 243.04\,°C$ (Alduchov and Eskridge, 1996; Lawrence, 2005).

Data acquisition of standard/*ex situ* measurements were conducted with the same device set-up, and laser source as *in situ* measurements. The spectra were obtained at 22 °C within $300\,cm^{-1}$ - $2000\,cm^{-1}$ and $2700\,cm^{-1}$ - $3700\,cm^{-1}$. The grating was 1800 l $mm^{-1}$. Data acquisition was performed by 3 s, 5 acquisitions, at full laser power.

To minimize differences of experimental sample conditions between powder XRD and Raman spectroscopic experiments, sample preparation for dehydration and rehydration measurements was done by applying fine powder layers of the 20 µm - 25 µm sample fraction onto thin glass platelets that were positioned directly on the silver heating block of the THMS600 sample stage. As a plane surface of the sample was necessary to reduce beam scattering, the powder was carefully pressed onto the sample holder. All spectral data was processed with the WiRE 5.0 software package by Renishaw and/or the open source curve analysis program Fityk (version 1.3.1, Wojdyr, 2010). Prior to measurements, the instrument was calibrated on a silicon sample using the $520.5\,cm^{-1}$ mode.

Quantitative analysis to derive $\alpha$ values for selected experiments was carried out according to the following procedure. Peak areas of gypsum's and hemihydrate's $\nu_1(H_2O)$ and $\nu_3(H_2O)$ modes from $3250\,cm^{-1}$ - $3750\,cm^{-1}$ were fitted employing the Levenberg-Marquardt algorithm for least squares optimization (Wojdyr, 2010). The modes are associated with the symmetric and asymmetric stretching of O – H bonds, respectively. The background of stated range was fitted with a linear equation to exclude it from factual peak area contributions, whereas the water modes were fitted using the built-in VoigtA profile function which is given by Equation 5-6.

$$y = \frac{a_0}{\sqrt{\pi} a_2} \int_{\infty}^{\infty} \frac{\exp(-t^2)}{a_3^2 + (\frac{x-a_1}{a_2} - t)^2} \mathrm{d}t \tag{5-6}$$

where $a_0$ denotes the height, $a_1$ is the center, $x$ is the shift from the line center, $a_2$ is proportional to the Gaussian width, and $a_3$ is proportional to the ratio of Lorentzian and Gaussian widths. Fitting the most prominent mode of all calcium sulfates, $\nu_1(SO_4)$, was not considered due to the controversy about an "additional" Raman band in hemihydrate close to the $\nu_1(SO_4)$ mode of gypsum (Chapter 6-2-3). Due to this circumstance, a clean separation of gypsum's and hemihydrate's $\nu_1(SO_4)$ modes could not be ensured.

For a gypsum → hemihydrate dehydration experiment, the linear relationship between the converted fraction $\alpha_{Hemihydrate} = 1$ - $\alpha_{Gypsum}$ and the peak area decrease of the $\nu_1(H_2O)$ and $\nu_3(H_2O)$ modes of gypsum can be used to calculate converted fractions. For this, it is further assumed that measurements with gypsum as single phase can be averaged and set to equal 1 ($\frac{1}{n}\sum_{i=1}^{n} Peak\ Area\,(100\%\ \text{Gypsum}) \stackrel{!}{=} 1 = \alpha_{Gypsum}$, with $n$ measurements exhibiting gypsum as single phase and $i = (1, ..., n)$). Subsequently, the converted fractions for each measurement can be calculated with this assumed reference ratio. For a hemihydrate → gypsum rehydration experiment, an analogous procedure was applied. This method is, however, not accurate. It was applied to receive an approximation of the conversion curves during *in situ* Raman experiments.

### 5-2-3 Temperature calibration of the THMS600 sample stage

As the sample stage was newly put into operation for the present work, the temperature control was vetted by conducting non-ambient measurements of benzophenone crystals of the $\alpha$-modification ($C_{13}H_{10}O$, space group $P2_12_12_1$ (Groom et al., 2016)). Benzophenone is known to be a common standard for accuracy revision of temperature readings (Groom et al., 2016). It has a melting point of 48.5 °C (Williams, 2006). Hence, SynchroScan spectra (measurement conditions equal to *in situ* measurement conditions: 100 $cm^{-1}$ - 4000 $cm^{-1}$, 5% laser power, 10 s laser exposure, 1 accumulation) of benzophenone were taken with a heating rate of 20 °C $min^{-1}$ at intervals of 0.1 °C within the temperature range of 45 °C - 50 °C. The suitable C=O stretching mode at circa 1650 $cm^{-1}$ (Zhang et al., 1995) was chosen to follow the melting process (Figure 5-3).

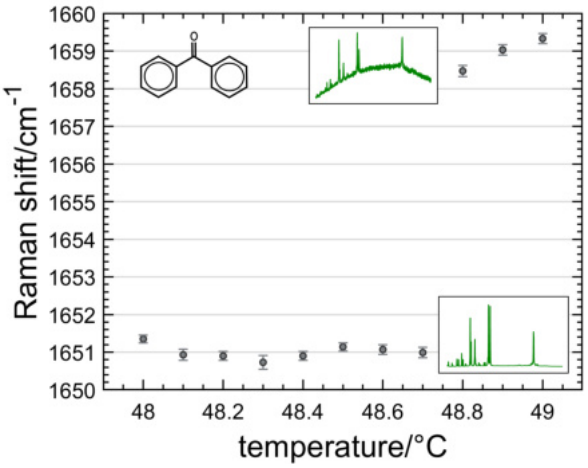


**Figure 5-3:** Temperature-induced melting of benzophenone during *in situ* Raman measurements. Each point represents the C=O stretching mode of benzophenone whose frequency has been followed with increasing temperature to detect melting. The insets show the respective Raman spectra at the adjacent data point. The molecular structure of benzophenone is given in the upper left corner.

According to the Raman line shift displayed in Figure 5-3, melting of benzophenone between 48.7 °C and 48.8 °C becomes apparent which is in acceptable accordance with the literature data of 48.5 °C, giving reason to surmise a stable and adequate temperature control during *in situ* experiments.

### 5-2-4 Long-term gypsum dehydration experiments

To monitor dehydration of calcium sulfate hydrates over extended time periods at 60 °C and 80 °C, eight supersaturated salt solutions were prepared as described above. Together with two powder samples each, the solutions were put into desiccators and kept in drying cabinets. As sample material, gypsum powder of the fraction 20 µm - 25 µm, and a phase mixture of gypsum and NaCl in a ratio of 1:1 was used. The latter also consisted of 20 µm - 25 µm grains and was chosen to determine acceleratory and/or inhibitory effects of the added salt crystallites on dehydration processes. The samples were dehydrated for six months and analyzed monthly by powder XRD.

At a given temperature, the concentration of the salt solution stays stable. By providing the solute in excess, the solution will remain saturated and create a fixed atmosphere with defined, constant $p_{H_2O}$ values despite gypsum and hemihydrate dehydration (Young, 1967). Based on the saturated salt solution data compiled by Greenspan et al. (1977), the salts were chosen according to their ability to induce specific humidities at 60 °C and 80 °C (Table 5-4), and their harmlessness. The humidity values result from the following expression.

$$\sum_{i=0}^{3} = A_i T^i \tag{5-7}$$

with temperature $T$ and coefficients $A_i$. Latter are given by *e.g.* Wilson (1921), Stokes and Robinson (1949), Gokcen (1951), Richardson and Malthus (1955), Hedlin and Trofimenkoff (1965), and Acheson (1965).

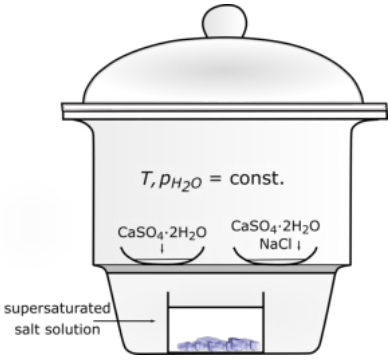


**Figure 5-4:** Desiccator with salt solution and samples.

With Equation 5-7, RH values generated by, *e.g.*, saturated $MgCl_2$ solutions at 60 °C are calculated according to $A_0 + A_1 \cdot 60 + A_3 \cdot 60^2$ with values $A_0$ = 33.6686, $A_1$ = -0.0079739, and $A_2$ = -0.00108988 yielding 29.26% RH. $A_i$ values for the remaining utilized salt solutions are given in Table B-2.

**Table 5-4:** Equilibrium relative humidites of selected saturated salt solutions according to Greenspan et al. (1977, and references therein).

| Temperature/°C | RH($MgCl_2$) | RH(LiCl) | RH($ZnBr_2$) | RH(LiBr) |
|---|---|---|---|---|
| 60 | 29.26% ± 0.18% | 10.95% ± 0.26% | 8.09% ± 0.19% | 5.33% ± 0.25% |
| 80 | 26.05% ± 0.34% | 10.51% ± 0.44% | 9.59% ± 0.19% | 5.20% ± 0.18% |

### 5-2-5 Scanning electron microscopy

Scanning electron microscopy (SEM) analysis was done to provide high-resolution direct imaging of calcium sulfate samples at different hydration stages as well as before, after, and during dehydration and rehydration processes, as the habit and morphology of crystallites was of interest. The images were taken with a GeminiSEM 300 microscope by Zeiss, equipped with a secondary electron (SE) detector and 30 µm slits. The applied voltage during imaging was 5 kV. Samples were used without conductive coating.

# Chapter 6

# Experimental results

In this Chapter, de- and rehydration processes in the $CaSO_4$ – $H_2O$ system at different time, temperature, and humidity conditions are discussed. Attention is given to possible result transferability to de- and rehydration reactions under environmental conditions present in the Atacama Desert. First, quantitative analysis of Atacama samples, as well as powder XRD and Raman spectroscopy measurements are presented with regard to correct phase discrimination and analysis during *in situ* experiments.

Followingly, the $CaSO_4 \cdot 2\,H_2O$ dehydration products are referred to as hemihydrate, $\gamma$-anhydrite and $\beta$-anhydrite. The dihydrate is, however, always referred to as gypsum. This is in agreement with most studies focusing on dehydration and rehydration processes. Here, when the natural phases of $CaSO_4 \cdot 0.5\,H_2O$ and $CaSO_4$ are meant, the mineral names bassanite and anhydrite are used.

## 6-1 Qualitative and quantitative analysis of Atacama samples by powder XRD

The use and analysis of samples from the Atacama Desert was not in focus of the present work as sample homogeneity was of great importance for the examination of dehydration and rehydration reactions in the $CaSO_4$ – $H_2O$ system. Sample heterogeneity is a hardly avoidable characteristic of natural samples so that field work was not incorporated in the project scope. However, as several soil and surface samples were collected during a kick-off excursion in March 2017 and during a study trip of principal investigators of all CRC 1211 projects in 2014, quantitative phase analysis of selected samples was done with regard to gypsum, bassanite, and anhydrite.

Table 6-1 gives phase contents of selected samples obtained by refinements after the Rietveld method. It becomes evident that bassanite is a rare constituent of the Atacama surface as it is only present as an accessory or minor component in five samples. As reviewed in Chapter 2-3, bassanite is a compulsory low-temperature dehydration product of gypsum. The lowest, experimentally determined dehydration temperatures of gypsum are around 45 °C (unspecified humidity conditions, Seufert et al., 2009). This is a frequently reached soil temperature-day maximum during summer months in some parts of the Atacama Desert (Chapter 3-2). Low summer air humidities that accompany elevated soil temperatures further support the presumption that gypsum dehydration conditions are reached and bassanite formation is possible. Small-scale Atacama landscape features like polygonal patterned surfaces or gypsum wedges are believed to result from gypsum → anhydrite volume changes induced by dehydration (Ritter, 2020). Furthermore, other hyper-arid and calcium sulfate (dihydrate)-dominated regions of the earth exhibit partial gypsum dehydration on soil surfaces (Hamdi-Aissa et al., 2004).

Accordingly, it can be hypothesized that gypsum dehydration is an abundant Atacama surface process and, therefore, bassanite should be an abundant dehydration product. However, phase contents contradict the assumption of bassanite prevalence. Possible explanation for this are: i) The hypothesis is imprecise as the factor time is not contemplated and the temperature and humidity conditions needed for dehydration are too short-lived. Only small amounts of gypsum dehydrate and geomorphologic features are not yielded solely by temperature- and humidity-promoted solid-state dehydration; ii) The analyzed phase content does not represent the on-site phase content correctly. Bassanite is a metastable phase and eventually rehydrates to gypsum at ambient conditions present in Cologne, Germany, where phase analysis was conducted (The time offset between sample collection and analysis amounted to several weeks - 3 years.); or iii) A combination of i) and ii) is the case.

To evaluate assumption i), *in situ* and *ex situ* long-term dehydration experiments were conducted which are discussed in Section 6-3. Supposition ii) could most suitably be examined through on-site phase evaluation with a field work-appropriate device like a handheld Raman spectrometer or a table X-ray diffractometer. Latter would require a logistically complex, cost-intensive excursion as power supply provided by a transportable generator would be necessary. Moreover, on-site phase analysis would result in lower measurement resolution and precision. Such difficulties could be overcome by collecting samples using hermetical sealing and subsequent laboratory analysis with caution to the exposure time at ambient humidity conditions. The question whether and/or how much the calcium sulfate phases in the present samples underwent alteration can retroactively not be solved. A simple hemihydrate rehydration experiment showed that exposure to laboratory temperature and humidity conditions results in minor gypsum formation. A finely ground hemihydrate sample (derived by heating gypsum at 90 °C for three days) was left in the laboratory and measured 2.5 years after production. Quantitative phase analysis showed that very small amounts of gypsum were detectable ($\approx$ 1%, Figure C-1). The exposure time of 2.5 years is approximately comparable to the maximum time span between sample collection and analysis. Yet, comparability of samples is not given, as the used hemihydrate sample did not contain further calcium sulfates or other phases affecting rehydration processes.

Also, the Atacama samples were only ground and prepared as powder samples shortly before the XRD measurements so that grain sizes are not comparable. Hence, drawing a profound conclusion whether and to what extent present samples were affected by alteration of bassanite must be omitted. Further contemplation of possible gypsum dehydration reactions follows in Section 6-3.

Besides gypsum, bassanite, and anhydrite, the samples predominantly contain halite, quartz, and a number of silicate minerals. Rare nitrate or other soluble salts that, *inter alia*, characterize the Atacama mineralogy were not detected. However, as the samples represent selective surface and subsurface compositions of the Atacama, the lack of rare minerals is not puzzling. For example, nitrates like darapskite, humberstonite and soda niter are likely deposited together in 1 m - 2 m depth below the surface (Ericksen, 1981).

Crystal structures of silicate minerals presumably differ from the applied ones. The structures are often highly complex regarding the exact composition due to element substitution. Aggravating for analysis, they are oftentimes poorly crystalline and layer silicates typically exhibit stacking faults. Concerning element or cation substitution, Li-enrichment of several silicate minerals seems plausible to assume. This supposition bases on the above-average Li occurrences of the Atacama: Aeolian erosion of Li-rich salars could lead to increased Li-incorporation in close by micas or clay minerals. However, only in one sample small amounts of lepidolite ($K(Li,Al)_3[(F,OH)_2(Si,Al)_4O_{10}]$), the most abundant Li-bearing mineral of the mica group, were found. The exact determination of each silicate mineral regarding stoichiometry and/or octahedral site occupation is beyond the scope of this work and the applied X-ray diffraction method.

**Table 6-1:** Quantitative phase analysis from powder XRD of selected Atacama surface and subsurface samples. The corresponding diffraction patterns, except for the first sample, are given in Figures C-2 - C-6.

| Sample description | Sample locality | Mineral phase content/wt.% [1] [2] [3] |
|---|---|---|
| Powdery chuca (poorly cemented 10 cm - 30 cm thick surface layer of silt, sand and calcium sulfates (Ericksen, 1981)) | 20°14′253″S, 69°59′337″W | Anhydrite/89, gypsum/3, bassanite[4]/2, bytownite/2, halite/4 |
| In a clay pan located 'gypsum' boulder | 21°32′332″S, 69°54′590″W | Gypsum/92, anhydrite/2, grunerite/5, hornblende accessory |
| Fragment of a gypsum vein | 21°09′240″S, 70°00′513″W | Gypsum/96, albite/3, hornblende accessory |

Continued on next page

continued.

| Sample description | Sample locality | Mineral phase content/wt.% |
|---|---|---|
| Rigid 'gypsum' surface crust | 21°05′260″S, 69°51′480″W | Gypsum/28, anhydrite/27, bassanite < 2, albite/25, muscovite/11, quartz/5, halite accessory, hornblende accessory |
| Crustal soil below the rigid surface crust | 21°05′260″S, 69°51′480″W | Gypsum/6, anhydrite/20, bassanite < 2, albite and anorthite/44, chlorite/13, quartz/9, halite < 2, hornblende < 2, kaolinite accessory, muscovite accessory |
| 'Gypsum' crust, marked by erosion | 21°05′260″S, 69°51′480″W | Gypsum/6, halite/6, anorthite/10, quartz/8, lepidolite/4, albite/33, anhydrite/9, kaolinite/2, muscovite/7, microcline/10, hornblende/3, augite/3 |
| Encrusted material of the subsurface (second encrusted layer, accessible where the upper crust was eroded) | 21°05′260″S, 69°51′480″W | Gypsum/45, anhydrite/5, albite/16, anorthite/30, chlorite/3, hornblende accessory |
| see above, sample taken at 10 cm depth below the soil surface | 21°05′260″S, 69°51′480″W | Anhydrite/63, gypsum accessory, albite/20, halite/6, quartz/7, hornblende < 2, chlorite accessory |
| see above, sample taken at 15 cm depth below the soil surface | 21°05′260″S, 69°51′480″W | Anhydrite 64, quartz < 2, albite/20, halite/8, illite < 2, calcite accessory, microcline/4 |
| Remnant of disintegrated gypsum crust below the soil surface | 5.6 km north-east of the above locality | Gypsum/4, anhydrite/41, bassanite accessory, albite/34, muscovite/18, hornblende < 2 |
| Brittle material without encrusted cover layer | Pisagua area (19°35′600″S, 70°13′00″W) | Gypsum/5, anhydrite/18, halite/5, quartz/4, muscovite/14, albite/48, eckermannite/3, orthoclase/3 |
| 'Gypsum' crust | 24°34′25.97″S, 70°20′08.30″W | Gypsum/30, anhydrite/5, quartz/6, muscovite/5, albite/54 |
| Clay pan material | 25°03′40.77″S, 70°07′12.35″W | Muscovite/25, quartz/9, albite/36, chlorite/11, eckermannite/14, montmorillonite/5 |

Continued on next page

continued.

| Sample description | Sample locality | Mineral phase content/wt.% |
|---|---|---|
| Thin 'gypsum' crust | Quebrada de Aroma area (19°59′04″S, 69°45′04″W, 1570 m above sea level) | Gypsum/8, illite/9, quartz/9, muscovite/32, clinochlore/6, orthoclase/8, eckermannite/9, albite/19 |
| Material below thin encrusted cover layer | Quebrada de Aroma area (19°59′04″S, 69°45′04″W, 1570 m above sea level) | Gypsum/11, quartz/7, chrysotile/15, eckermannite/17, illite/10, albite/40 |

[1]Silicon was added as an internal standard for powder XRD, percentages are normalized to 0 wt.-% silicon.

[2]Results of quantitative phase analysis should be considered with caution as the structure models for several silicate mineral phases base on type localities. Almost all silicate minerals exhibit moderate to strong variations regarding ion composition and disorder phenomena affecting quantitative phase evaluation based on the Rietveld method.

[3]ICSD codes (FIZ Karlsruhe, 2020) of crystal structures used for phase qualification and quantification: Anhydrite ICSD 40043; gypsum ICSD 160977; bassanite ICSD 92947; bytownite ICSD 30932; halite ICSD 53816; grunerite ICSD 24590; hornblende ICSD 64858; albite ICSD 100337; anorthite ICSD 86317; chlorite ICSD 63268; muscovite ICSD 92814; lepidolite ICSD 100634; kaolinite ICSD 63192; microcline ICSD 159347; augite ICSD 97030; calcite ICSD 5203; eckermannite ICSD 87639; orthoclase ICSD 31192; montmorillonite ICSD 159274; clinochlore ICSD 16912; illite (no ISCD entry) used crystal structure data from Drits et al. (2010).

[4]The content of bassanite in the analyzed samples can be in an altered state compared to on-site samples in the Atacama Desert due to transportation and storage under different air humidity conditions.

Figure 6-1 gives the powder XRD pattern corresponding to the first sample in Table 6-1, showing gypsum, anhydrite and bassanite presence.

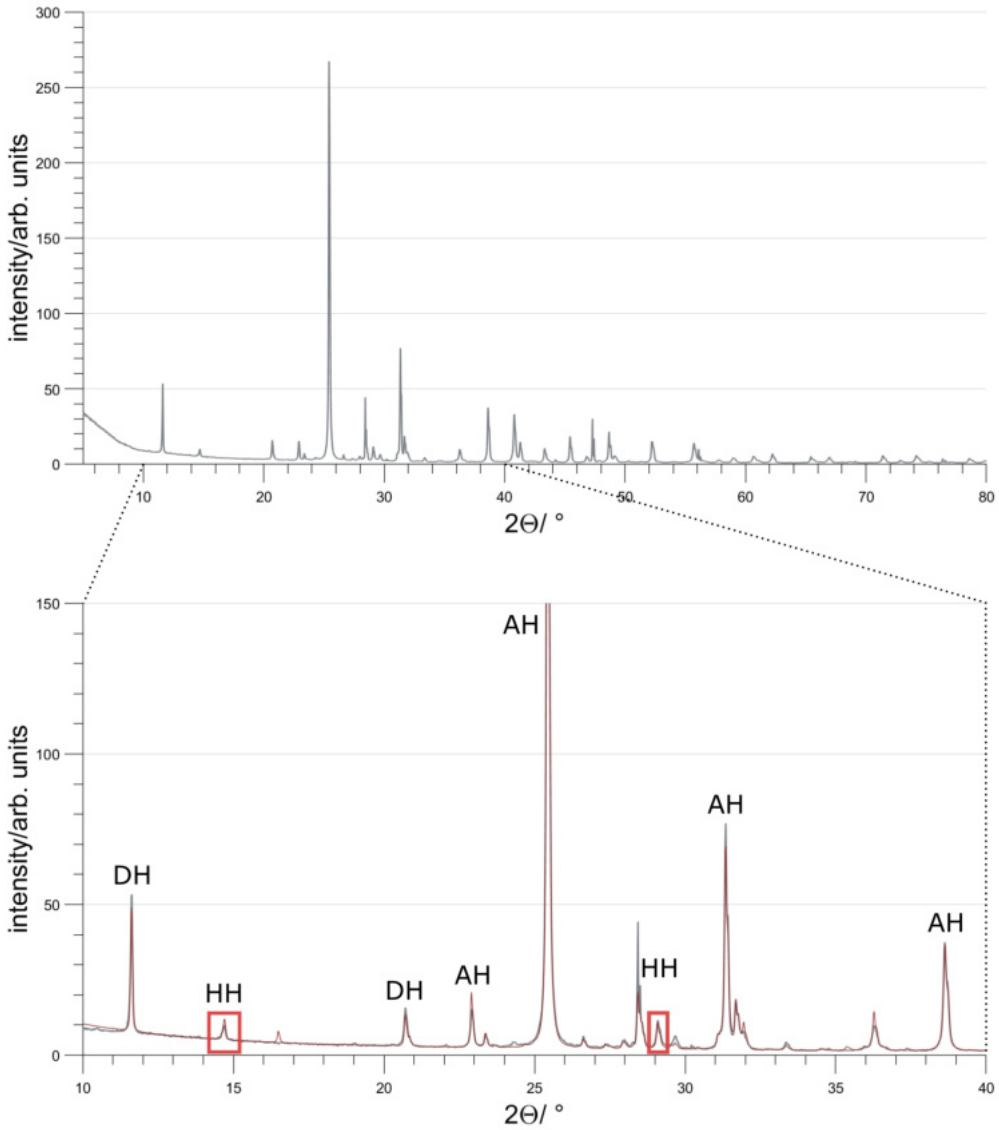


**Figure 6-1:** Powder X-ray diffractogram of a sample taken from an unconsolidated surface layer in the Atacama Desert (first entry in Table 6-1). The sample consists primarily of poorly cemented silt, sand, and calcium sulfates, known as powdery chuca. Prominent Bragg reflections are assigned and the red boxes mark the two strongest peaks of bassanite. The overall phase content of bassanite amounts to circa 2%. The observed intensities are given in grey and the calculated intensity curve according to the method by Rietveld is given in red for the magnified area.

## 6-2 Characterization of the crystalline phases in the $CaSO_4$ – $H_2O$ system

To ensure unambiguous analysis of calcium sulfate phases during *in situ* experiments, their X-ray powder patterns and Raman spectra are compared with respect to distinctive characteristics. Further, due to the transformation-induced volume change that accompanies de- and rehydration reactions of calcium sulfate phases, the influence of varying sample heights on analysis of powder XRD measurements are discussed.

### 6-2-1 Distinguishability of powder XRD patterns of calcium sulfate phases

Phase discrimination of the three calcium sulfate minerals via powder XRD is straight forward. Figure 6-2 shows powder XRD patterns of the synthetic equivalents of minerals as measured and calculated from crystal structure data. The large difference between the calculated and measured gypsum pattern (Figure 6-2, bottom and second from bottom patterns) results from the strong preferred orientation of powder crystallites caused by excellent cleavage parallel (010) resulting in frequent overemphasis of (0k0) peaks when measured in reflexion geometry (Grattan-Bellew, 1975). This impacts data analysis negatively (Kleeberg et al., 2008). In the best case, preferred orientation can be avoided due to a suitable sample preparation. Reducing texturing of the samples as far as possible for *in situ* measurements was done with the sample preparation technique explained in Chapter 5-2-1.

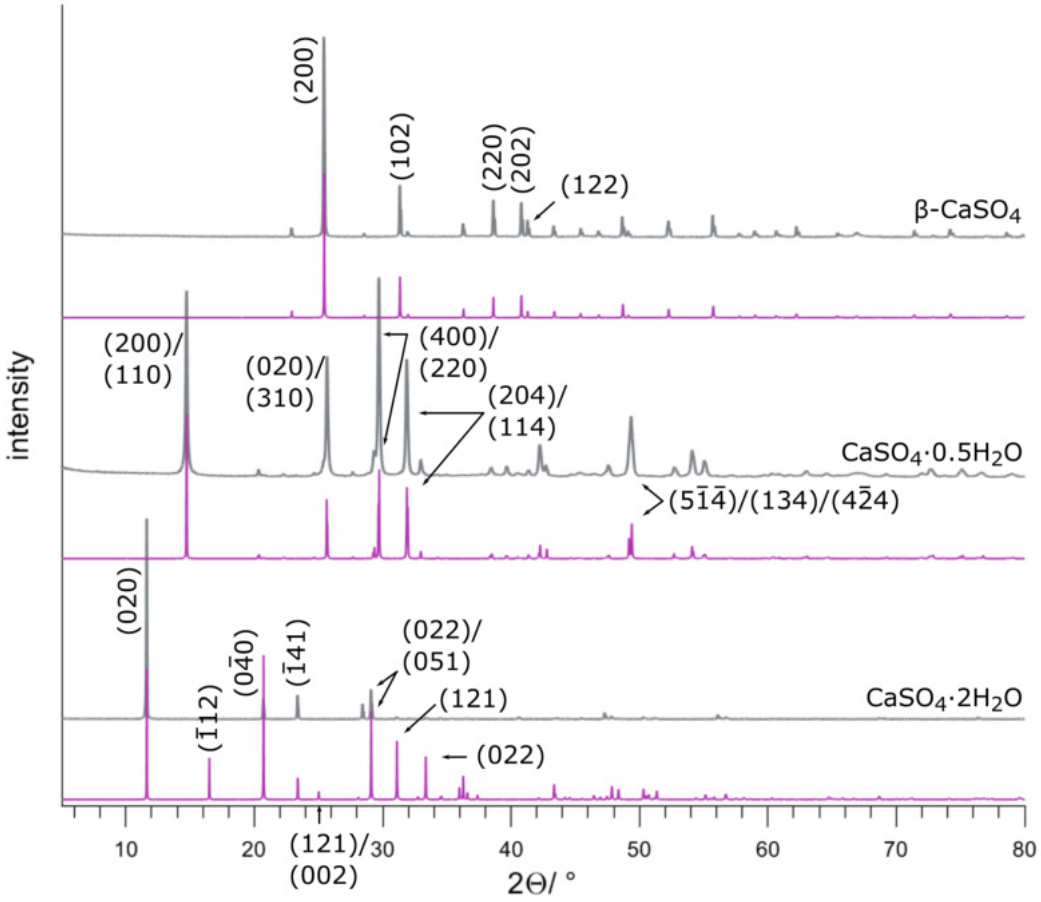


**Figure 6-2:** Measured (grey) and calculated (pink) powder XRD patterns of gypsum, hemihydrate, and $\beta$-anhydrite. Hemihydrate ($CaSO_4 \cdot 0.5\,H_2O$) and $\beta$-anhydrite ($\beta$-$CaSO_4$) were derived from gypsum ($CaSO_4 \cdot 2\,H_2O$) through heating small amounts of gypsum powder in bulk for three days at 90 °C and for three months at 300 °C, respectively. For calculation of powder patterns, crystal structure data by Schofield et al. (2000), Ballirano et al. (2001), and Hawthorne and Ferguson (1975), respectively, were used. Selected reflections are indexed.

Figure 6-3 shows the calculated powder patterns of $\gamma$-anhydrite and calcium sulfate subhydrates containing 0.6 (SH 0.6), 0.625 (SH 0.625), 0.67 (SH 0.67), and 0.8 (SH 0.8) $H_2O$ molecules per formula unit, respectively. In theory, patterns are similar but easily identifiable due to minor peak shifts of prominent reflections, intensity differences or incidences of characteristic, low-intensity reflections. The subhydrate phases were exclusively detected or synthesized at distinctive environmental conditions as described in Chapter 2-1-4. Thus, systematic powder XRD measurements of subhydrates were not possible and their emergence during dehydration and rehydration reactions remained uncertain prior to experiments.

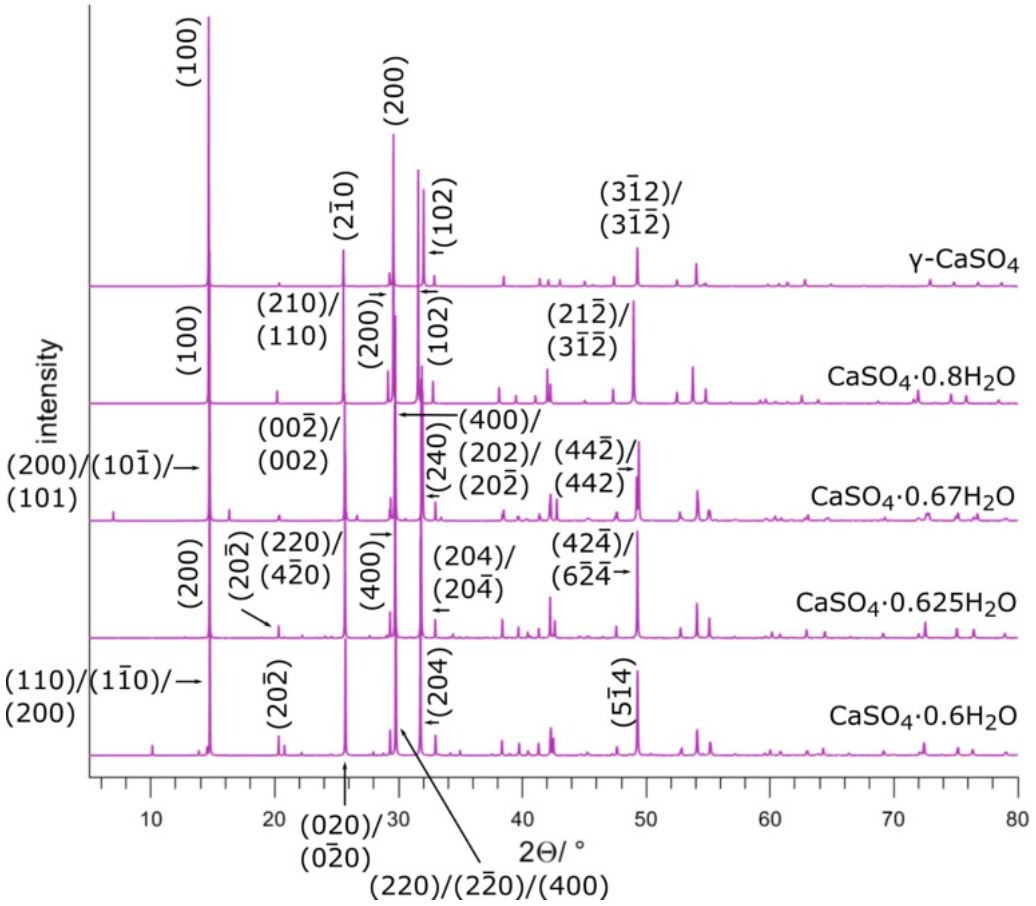


**Figure 6-3:** Calculated powder XRD patterns of $\gamma$-anhydrite ($\gamma$-$CaSO_4$), SH 0.6 ($CaSO_4 \cdot 0.6\,H_2O$), SH 0.625 ($CaSO_4 \cdot 0.625\,H_2O$), SH 0.67 ($CaSO_4 \cdot 0.67\,H_2O$), and SH 0.8 ($CaSO_4 \cdot 0.8\,H_2O$). The calculated powder patterns base on crystal structure data by Christensen et al. (2008), Bezou et al. (1995), Schmidt et al. (2011), Bushuev (1982), and Abriel (1983), respectively.

In the past, phase discrimination of hemihydrate and $\gamma$-anhydrite based on powder XRD led to confusion due to the structural similarities. In principal, patterns can be distinguished by monoclinic peak splitting of hemihydrate at 23.231°, 24.631°, 39.652° 2Θ (Ballirano et al., 2001). Disadvantageously, hemihydrate and $\gamma$-anhydrite obtained by heating gypsum, grow topotactically on the gypsum crystallites and the issue of preferred orientation during XRD in Bragg–Brentano geometry remains (Hildyard et al., 2011). This hampers visual differentiation based on extra monoclinic peaks. However, discrimination of hemihydrate and $\gamma$-anhydrite is feasible through a shift of the (200)/(110) peak of hemihydrate relative to the (100) peak of $\gamma$-anhydrite (Oetzel et al., 2000a; Robertson and Bish, 2013).

Figure 6-4 shows the gypsum, hemihydrate, and $\gamma$-anhydrite powder patterns depending on the temperature. As mentioned in Chapter 5-2-1, humidity control above 80 °C was not possible but log data reveal $p_{H_2O}$ values between 20 hPa and 126 hPa for the measurements between 100 °C and 150 °C.

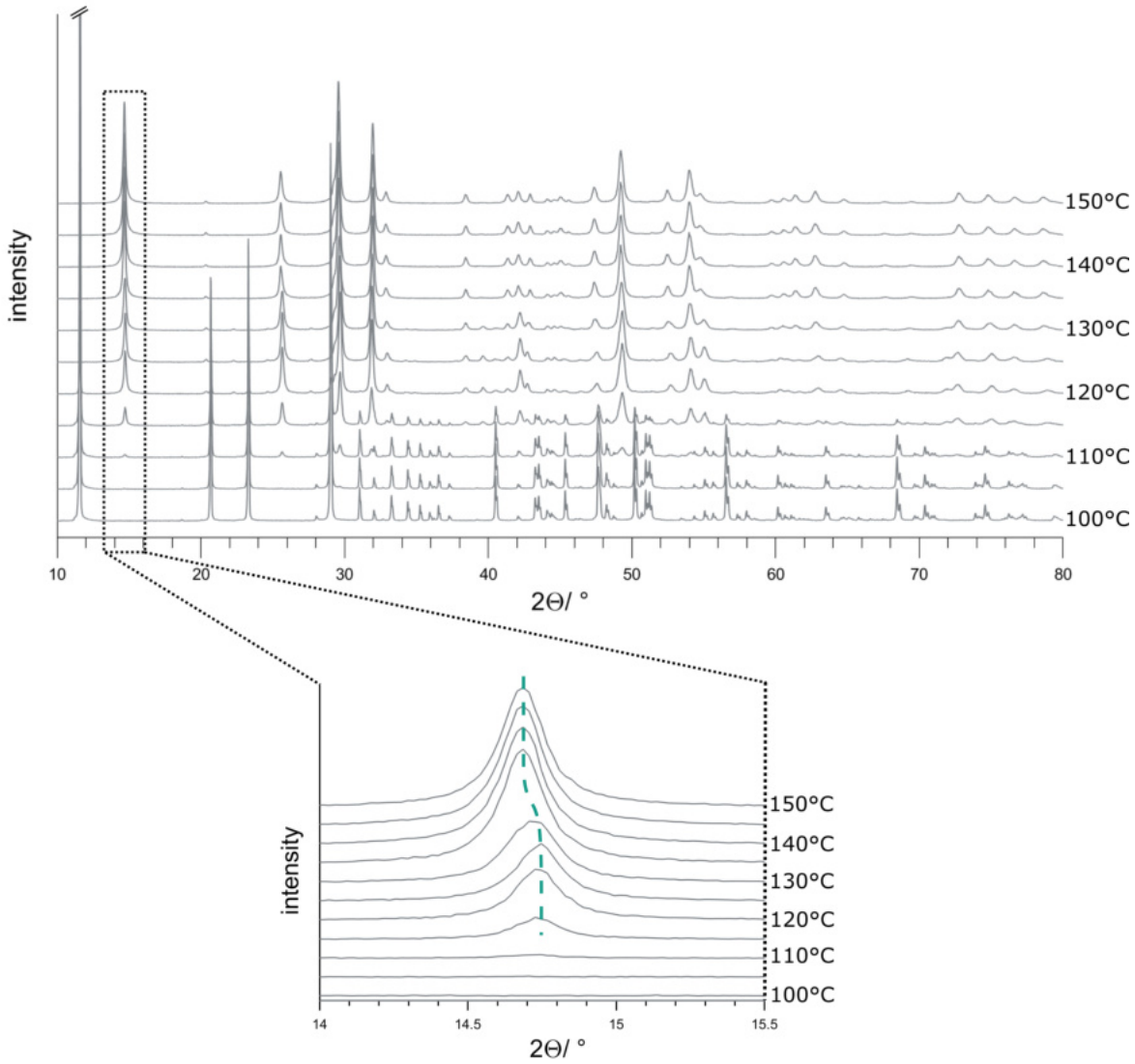


**Figure 6-4:** Temperature-dependently measured powder XRD patterns showing gypsum dehydration between 100 °C and 150 °C with $p_{H_2O} < 126$ hPa. Evolution of hemihydrate starts between measurements at 110 °C and 115 °C and further dehydrates to $\gamma$-anhydrite at $\approx$ 135 °C (time per temperature step: 5 min). The inset magnifies the region between 13.9° - 15.6° 2$\Theta$ and emphasizes the shift of peak positions of $\gamma$-anhydrite relative to those of hemihydrate on the example of the hemihydrate (200)/(110) (indexed with setting I2) - $\gamma$-anhydrite (100) peaks. The dashed line gives a guide to the eye.

Figure 6-5 shows the progression of the lattice parameter $b$ of hemihydrate (setting $I2$, crystal structure data from Ballirano et al. (2001)) with temperature as yielded by temperature-dependent powder XRD measurements displayed in Figure 6-4. The $b$-axes of both, the monoclinic hemihydrate (HH) and the hexagonal $\gamma$-anhydrite ($\gamma$-AH), can be compared considering axes correspondence of $\vec{b}_{\mathrm{HH}}$ to $\vec{b}_{\gamma-\mathrm{AH}}$ and $\frac{1}{2}(\vec{a}_{\mathrm{HH}} - \vec{b}_{\mathrm{HH}})$ to $\vec{a}_{\gamma-\mathrm{AH}}$, and $\frac{1}{2}\vec{c}_{\mathrm{HH}} \cdot \cos(\beta_{\mathrm{HH}} - 90))$ to $\vec{c}_{\gamma-\mathrm{AH}}$ with $\cos(\beta_{\mathrm{HH}} - 90)) \approx 1$.

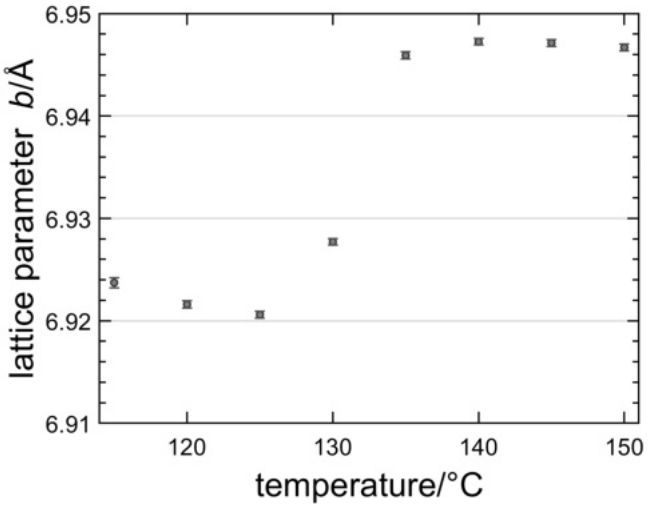


**Figure 6-5:** Evolution of lattice parameter $b$, refined on the basis of the hemihydrate crystal structure (setting *I2*), with temperature. The change between hemihydrate at lower temperatures and $\gamma$-anhydrite at higher temperatures can be monitored by tracking the shift of lattice parameters, *e.g.* $b$. The refinement was done according to the method by Rietveld from the XRD powder patterns measured between 110 °C and 150 °C (Figure 6-4), using crystal structure data by Ballirano et al. (2001).

### 6-2-2 Powder XRD measurements with respect to sample-height errors

A methodical problem concerning powder XRD in Bragg–Brentano geometry is posed by a possible sample-height displacement. Sample-displacement errors are caused by a height discrepancy between the sample surface of a powder XRD sample and the focusing circle of the diffractometer as shown in Figure 6-6. The effects of sample displacement are commonly manifested as systematic errors in peak positions which hampers subsequent data processing (Bish and Reynolds Jr, 1989).

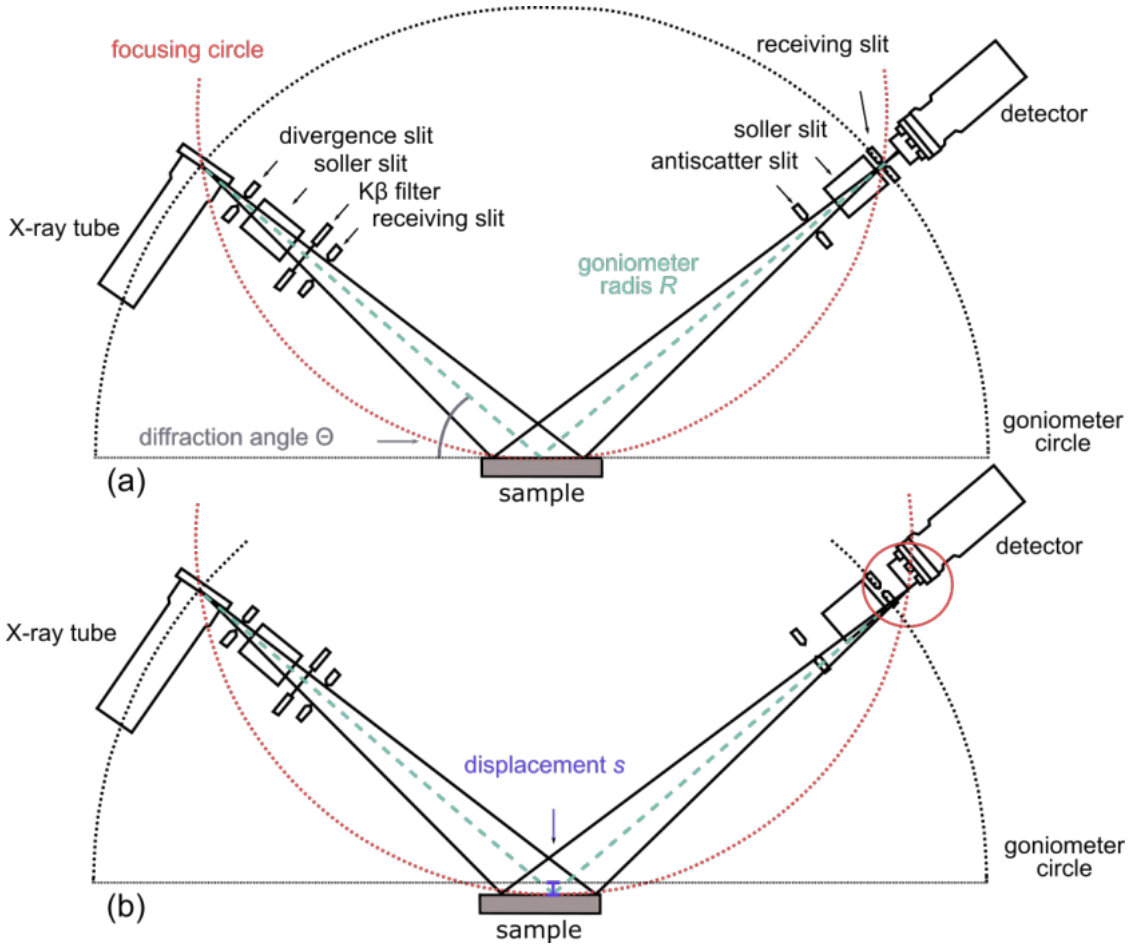


**Figure 6-6:** Schematic of Bragg–Brentano measuring geometry showing **(a)** accurate and **(b)** inaccurate alignment of the sample surface with the focusing circle of the diffractometer. The red circle in **(b)** emphasizes the displacement of the diffracted beam as a result of erroneous sample-height. With knowledge of the goniometer radius $R$, diffraction angle $\Theta$, and the sample-height displacement $s$, shifts in peak positions ($\Delta 2\Theta$) are yielded according to Equation 6-1. Illustration modified after Doebelin and Kleeberg (2015); Vermeulen (2005).

Equation 6-1 gives the differences in Bragg reflections $\Delta 2\Theta$ as a result of the sample-height displacement $s$. $R$ is the goniometer radius and $\Theta$ is the diffraction angle as shown in Figure 6-6.

$$\Delta 2\Theta[^\circ] = \frac{2s[\text{mm}]\ \cos\Theta}{R[\text{mm}]} \cdot \frac{180}{\pi} \tag{6-1}$$

Owing to the volume change that accompanies dehydration and rehydration processes of calcium sulfate phases, sample-height displacements during *in situ* experiments are presumable, requiring correction during further analysis. For example, the percentages of cell volumes per formula unit normalized to gypsum (100%) of $\beta$-anhydrite, $\gamma$-anhydrite, and hemihydrate are 62.5%, 72%, and 72%, respectively. With absolute cell volume differences based on one formula unit, volume increase and decrease values are yielded. Specifically, a volume growth of 60% for the $\beta$-anhydrite $\rightarrow$ gypsum rehydration and a volume shrinkage of 37.5% for the gypsum $\rightarrow$ $\beta$-anhydrite dehydration results. Likewise, a volume gain of 38.6% for the $\gamma$-anhydrite/hemihydrate $\rightarrow$ gypsum reaction and a volume decrease of 27.8% for the gypsum $\rightarrow$ $\gamma$-anhydrite/hemihydrate dehydration follows. This calculation is based on crystal structure data by Schofield et al. (2000), Ballirano et al. (2001), Hawthorne and Ferguson (1975), and Christensen et al. (2010), respectively. The numbers differ slightly from information by *e.g.* Zanbak and Arthur (1986). The authors give a gypsum to ($\beta$-)anhydrite shrinkage of 38.5% and a ($\beta$)-anhydrite to gypsum volume increase of 62.6%. The discrepancies may be caused by disparate cell volumes as starting values.

Powder XRD measurements with defined $s$ values were conducted to evaluate the accuracy of the sample-height algorithm implemented in the DIFFRAC.SUITE TOPAS software package by Bruker (Bruker, AXS, 2009). By driving the sample stage of the CHCplus chamber in $z$-direction, $s$ values of $\pm$ 0.05 mm, $\pm$0.1 mm and $\pm$0.15 mm were yielded.

According to the manufacturer, the CHC+ alignment stage offers an accuracy of $< 5\,\mu$m (Anton Paar GmbH, 2018). This is one to two orders of magnitude smaller than the applied displacements and should, therefore, not impact data significance. The data plotted in Figure 6-7 show that displacement values refined with the Rietveld method are slightly closer to the applied displacements than the manually calculated displacements with Equation 6-1 and $\Delta 2\Theta$ values obtained by peak fitting. Ideally, both data sets would yield a straight line with a slope of 1. The largest difference between the set and refined sample-height is 0.0075 mm at a specified ("real") displacement of -0.15 mm. Likewise, the manually calculated value differs the most at a set height-displacement of -0.15 mm with a discrepancy of 0.01 mm. Hence, it becomes evident that increased sample-height displacements cause poorer refined or manually calculated values. The slight differences between refined and manually calculated displacements might result from more precise $\Delta 2\Theta$ data obtained by refinements due to the influence of crystal structure information.

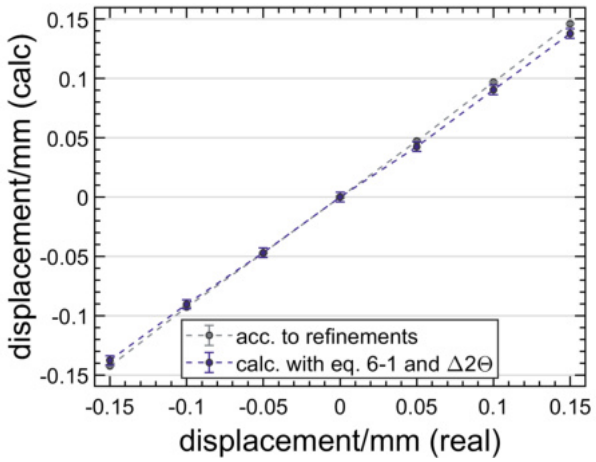


**Figure 6-7:** Displacement of the specimen surface. The $x$-axis gives the "real" displacement as set by the chamber's $z$ motor drive. The $y$-axis gives the calculated displacement according to the sample height displacement macro of the DIFFRAC.SUITE TOPAS software package (Bruker) applied in refinements according to the Rietveld method, and the displacement calculated with Ebassquation 6-1 and $\Delta 2\Theta$ values as yielded with peak fitting (also done using the DIFFRAC.SUITE TOPAS software package).

As the sample preparation technique used for all *in situ* measurements guarantees a fine powder layer of crystallites, a simple approach to assess the influence of sample-height displacements could be the following: A powder sample of cuboid gypsum crystallites of the size 25 µm · 15 µm · 15 µm consists of 10 layers of stacked crystallites. The particles are mostly piled along the 15 µm lengths. During gypsum dehydration to hemihydrate or $\gamma$-anyhdrite, a volume loss of circa 28% occurs. If the volume decrease is only caused by shrinkage along the 15 µm length, the cumulative sample-height of crystallite layers will go from 150 µm to 108 µm. The difference of 42 µm could be reasonably well refined with DIFFRAC.SUITE TOPAS sample height macro. This estimation does not represent the reality but shows that displacements due to volume changes of very small sample amounts can be adequately refined.

### 6-2-3 Distinguishability of Raman spectra of calcium sulfate phases

Raman modes of calcium sulfates are determined by vibrations of the $[SO_4]^{2-}$ groups, vibrations of $H_2O$, if present, and vibrations from interactions of $Ca^{2+}$ – O, with oxygen belonging either to $[SO_4]^{2-}$ ions or $H_2O$ molecules (Nakamoto, 2006). In aqueous solution, the $[SO_4]^{2-}$ group has four fundamental vibrational modes: $\nu_1$ symmetric stretching (non-degenerated, 981 $cm^{-1}$), $\nu_2$ symmetric bending (doubly degenerated, 451 $cm^{-1}$), $\nu_3$ asymmetric stretching (triply degenerated, 1104 $cm^{-1}$), and $\nu_4$ asymmetric bending (triply degenerated, 613 $cm^{-1}$, Lilley, 1973). Liquid water has the following vibrational modes associated with O – H bond stretching and bending: $\nu_1$ symmetric stretching (3657 $cm^{-1}$), $\nu_2$ bending (1595 $cm^{-1}$), and $\nu_3$ asymmetric stretching (3756 $cm^{-1}$) (Kohl et al., 1991).

In the solid state, splitting of above mentioned modes result from symmetry lowering of vibrational groups when going from the free ion or molecule to the rigid crystal structure (Ben Mabrouk et al., 2013).

Wave number variations of certain Raman modes that are present in all calcium sulfate phases derive from additional vibrational influences in their respective crystal lattices. Raman line positions and features are affected by the chemical environment of vibrating ionic groups. For example, in gypsum and hemihydrate, the oxygen coordination of $[SO_4]^{2-}$ groups is affected by the presence of hydrogen bonding which perceptibly changes the spectral patterns (Frost et al., 2003; Prieto-Taboada et al., 2014). The literature data of the most relevant, strongest Raman frequencies of gypsum, hemihydrate/bassanite and ($\beta$-)anhydrite with assignments are given in Table 6-8.

**Table 6-2:** Raman frequencies of calcium sulfate minerals. Data taken from Krishnamurthy and Soots (1971), Berenblut et al. (1971), Berenblut et al. (1973), Liu et al. (2009), and Schmid et al. (2020). The notation N/A indicates that information is not available.

| Assignment | Gypsum Frequency/cm$^{-1}$ | Bassanite Frequency/cm$^{-1}$ | Anhydrite Frequency/cm$^{-1}$ |
|---|---|---|---|
| Lattice vibrations | 90<br>110<br>123<br>134<br>145<br>164<br>170<br>183 | <br><br>128<br><br>149<br><br>173<br>196 | 65<br><br>124<br>132<br><br>163<br>170<br>188<br>225<br>232<br>268 |
| $\nu(OH \cdots O)$ | 210 | N/A | |
| $\nu_R(H_2O)$ [1] | 218<br>318 | N/A | |
| $\nu_2(SO_4)$ | 415<br>495 | 427<br>489 | 415<br>497 |
| $\nu_T(H_2O)$ [1] | 572 | N/A | |
| $\nu_4(SO_4)$ | <br>621<br>623<br>671 | 606<br><br>628<br>668 | 608<br><br>625<br>674 |
| $\nu_1(SO_4)$ | 1006 | 1016 | 1015 |
| $\nu_3(SO_4)$ | 1116<br>1132<br>1140 | 1116<br>1128<br>1151<br>1167<br>1181 | 1110<br>1129<br><br>1160 |
| $\nu_2(H_2O)$ | 1630<br>1679 | N/A | |
| $\nu_1(H_2O)$ | 3400<br>3405 | <br>3554 | |
| $\nu_3(H_2O)$ | 3490<br>3493 | <br>3616 | |

[1] $\nu_R$ and $\nu_T$ referring to rotational and translational modes, respectively.

The spectra of gypsum, hemihydrate, and $\beta$-anhydrite, given in Figure 6-8, show excellent distinguishability, especially concerning the signals caused by $H_2O$ in the crystal structure or the lack thereof (Figure 6-8 (b)).

The Raman spectra of all three phases consist of intense $\nu_1(SO_4)$ bands at $1006.9\,cm^{-1}$ (gypsum), $1014.1\,cm^{-1}$ (hemihydrate) and $1018.9\,cm^{-1}$ ($\beta$-anhydrite). The other characteristic bands were found at $413.5\,cm^{-1}$, $493.4\,cm^{-1}$, $616.8\,cm^{-1}$, $663.9\,cm^{-1}$, $1133.1\,cm^{-1}$, $3410.5\,cm^{-1}$, $3500.0\,cm^{-1}$ (gypsum); $428.4\,cm^{-1}$, $487.3\,cm^{-1}$, $627.5\,cm^{-1}$, $660.9\,cm^{-1}$, around $1150\,cm^{-1}$, $3555.7\,cm^{-1}$, $3617.7\,cm^{-1}$ (hemihydrate); and $417.4\,cm^{-1}$, $499.4\,cm^{-1}$, $609.2\,cm^{-1}$, $627.8\,cm^{-1}$, $675.7\,cm^{-1}$, $1110.7\,cm^{-1}$, $1128.5\,cm^{-1}$, $1159.3\,cm^{-1}$ ($\beta$-anhydrite). Assignments according to the literature data are given in Figure 6-8.

These values are similar to those reported in literature (Table 6-2). Discrepancies may be caused by temperature differences of the laboratory environment as slight discrepancies of vibration frequencies can be caused by thermal action of laser. Besides that, Raman shift is independent of excitation wavelength as it only influences the intensity.

The discrepancy between gypsum and hemihydrate regarding the frequency of $H_2O$ modes is explained by the increased $O(w)\cdots O$ distances of 2.95 Å and 3.02 Å in hemihydrate (Chio et al., 2004), compared to the $O(w)\cdots O$ distances in gypsum of 2.82 Å and 2.89 Å (Cole and Lancucki, 1974).

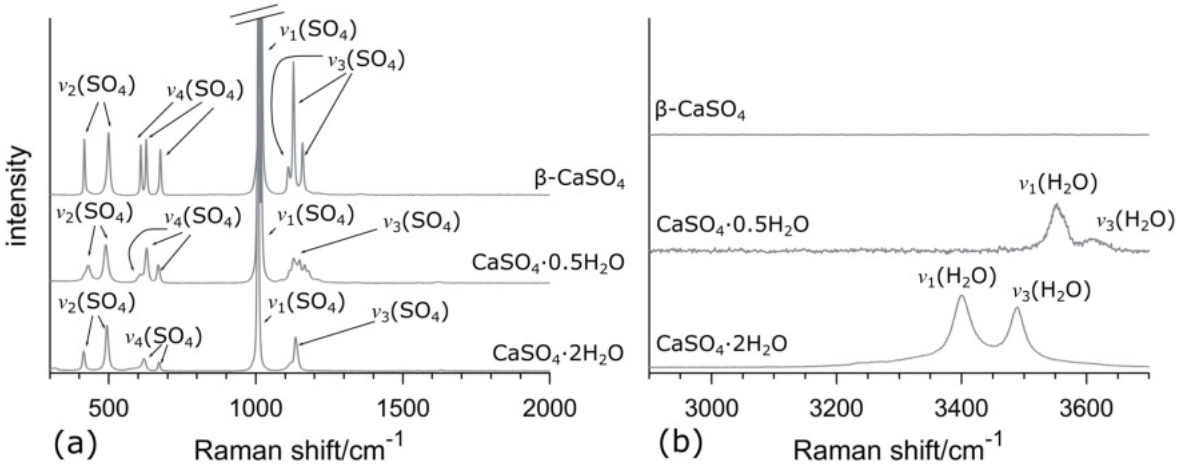


**Figure 6-8:** Raman spectra of gypsum, hemihydrate and $\beta$-anhydrite. **(a)** 'Internal' modes of sulfate ions in gypsum ($CaSO_4 \cdot 2\,H_2O$), hemihydrate ($CaSO_4 \cdot 0.5\,H_2O$), and $\beta$-anhydrite ($\beta$-$CaSO_4$). **(b)** Symmetric and antisymmetric stretching modes of water molecules in gypsum and hemihydrate. Hemihydrate and $\beta$-anhydrite formation conditions are given in the caption of Figure 6-2.

Concerning the main sulfate mode of hemihydrate, deconvolution (Figure 6-9) reveals band overlapping with an additional mode around 1006 $cm^{-1}$ that is evident in all hemihydrate spectra, independent of the temperature and humidity it was measured at. This Raman line has been detected during previous studies and is subject of speculation (Chio et al., 2004; Schmid et al., 2020; Prasad, 1999), as it is not clarified whether it stems from residual gypsum or if it is inherent to the hemihydrate phase.

Here, it is cautiously assumed that the line is characteristic for hemihydrate. The spectrum shows neither similar, potentially temperature-induced shifting of other gypsum modes, nor impurities of $H_2O$ belonging to gypsum (Figure 6-9). On the contrary, when gypsum was heated until $\gamma$-anhydrite evolved, it immediately rehydrated to hemihydrate after cooling to 22 °C (room temperature). The resulting hemihydrate spectrum also exhibited the same Raman line around 1006 $cm^{-1}$ (Figure C-7 (a)). It appears improbable that this Raman mode is caused by partial rehydration of $\gamma$-anhydrite to gypsum at ambient conditions of 22 °C and 30% RH within several seconds. During an *in situ* experiment at 110 °C and $p_{H_2O}$ = 35.8 hPa, no residuals of gypsum were visually apparent after 10 min measuring time (Figure 6-12, bottom panels). However, the presence of gypsum can not be categorically ruled out. The manufacturer does not specify a detection limit, since cross-sections for Raman scattering vary for individual phases. Overall, these findings are in accordance with Schmid et al. (2020), who assume band splitting due to coupling of vibrational motions. However, they recommended further investigations to explain this effect. Figure 6-9 shows the hemihydrate spectrum from 400 $cm^{-1}$ - 4000 $cm^{-1}$. The inset enlarges the main Raman mode of hemihydrate, $\nu_1(SO_4)$, and gives the curve fit.

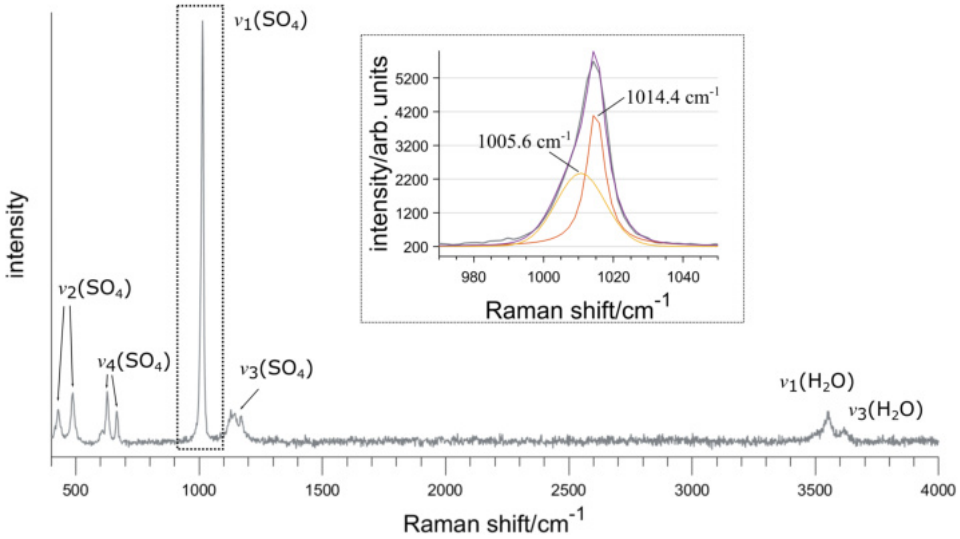


**Figure 6-9:** Raman spectrum of hemihydrate from 400 $cm^{-1}$ - 4000 $cm^{-1}$. The inset enlarges the main sulfate mode $\nu_1(SO_4)$. Curve analysis was done by fitting a linear combination of two Voigt profiles (orange and yellow lines) to the data. The sum of both profiles is given in purple. Here, hemihydrate was obtained by heating gypsum in the sample chamber at 90 °C for 20 h.

The Raman spectrum of $\gamma$-anhydrite (Figure 6-10) is dominated by an intense $\nu_1(SO_4)$ band at 1026.2 $cm^{-1}$. The other typical modes are found at 421.5 $cm^{-1}$, 490.3 $cm^{-1}$, 631.4 $cm^{-1}$, 674.2 $cm^{-1}$, 1169.2 $cm^{-1}$, and 1148.0 $cm^{-1}$, which is in overall accordance with published data by Prieto-Taboada et al. (2014) and Schmid et al. (2020). Due to the similar crystal structures of hemihydrate and $\gamma$-anhydrite, the shift of $\nu_1(SO_4)$ frequencies strikes. It is likely generated by the lack of hydrogen bond influence in $\gamma$-anhydrite. Hydrogen bonds weaken the internal sulfate bonds in hydrated phases and induce shift to higher wavelengths (*i.e.* lower wave numbers). Also, the differences between both spectra around 1150 $cm^{-1}$ might result from band splitting in hemihydrate caused by the presence of $H_2O$ molecules.

Similar to hemihydrate, $\gamma$-anhydrite also shows band overlapping concerning the main sulfate mode. Profile deconvolution reveals the presence of an additional mode around 1016 $cm^{-1}$ which is close to the $\nu_1(SO_4)$ line position of hemihydrate. Initially, this observation leads to the assumption of the presence of residual hemihydrate. Heating gypsum at 150 °C yielded an invariable $\gamma$-anhydrite spectrum after 72 h of measuring time (Figure C-7 (b)). This finding contradicts the assumption of hemihydrate remnants in the sample. As hydrogen bonds are thermosensitive and cannot persist above a compound-specific value, water of hydration is driven off once the respective temperature is reached (Dougherty, 1998). This temperature threshold differs for each mineral phase or compound depending on factors such as strength and number of hydrogen bonds. Literature data and results of the present work suggest immediate $\gamma$-anhydrite evolution above 110 °C - 130 °C, making residuals of hemihydrate throughout a treatment at 150 °C for three days unlikely. Hence, it is assumed that the additional line around 1015 $cm^{-1}$ is an intrinsic mode of $\gamma$-anhydrite. Yet, it is remarkable that both, hemihydrate and $\gamma$-anhydrite, exhibit additional bands that lie close to the $\nu_1(SO_4)$ modes of the respective preceding calcium sulfate phase. The resulting dissent about the residual or inherent origin might be solved by theoretical calculation of Raman spectra.

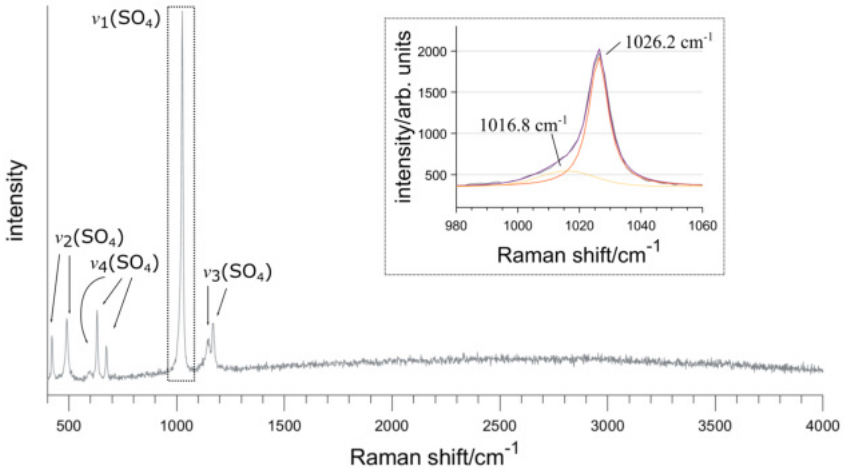


**Figure 6-10:** Characteristic vibrational Raman modes of $\gamma$-anhydrite (obtained from gypsum heating in the sample chamber at 110 °C for 20 h). The inset shows the most prominent sulfate mode $\nu_1(SO_4)$. Curve analysis was done by fitting a linear combination of two Voigt profiles (orange and yellow) to the data. The sum of both profiles is given in purple.

Pertaining to phase discrimination of $\gamma$-anhydrite from other calcium sulfates, the positions of the $\nu_1(SO_4)$ and other modes are unique and distinguishable. Measured or calculated Raman spectra of calcium sulfate subhydrates could not be found in the literature or databases. Figure 6-11 shows the main Raman bands of gypsum, hemihydrate, and $\gamma$- and $\beta$-anhydrite. Peak broadening of hemihydrate and $\gamma$-anhydrite is evident as both spectra were measured at elevated temperatures (20 h at 90 °C and 110 °C, respectively) and width of Raman lines increases with temperature (Narayanaswamy, 1948). Also, the modes about 1006 $cm^{-1}$ in the hemihydrate spectrum and about 1016 $cm^{-1}$ in the $\gamma$-anhydrite spectrum increase peak widths of the $\nu_1(SO_4)$ mode.

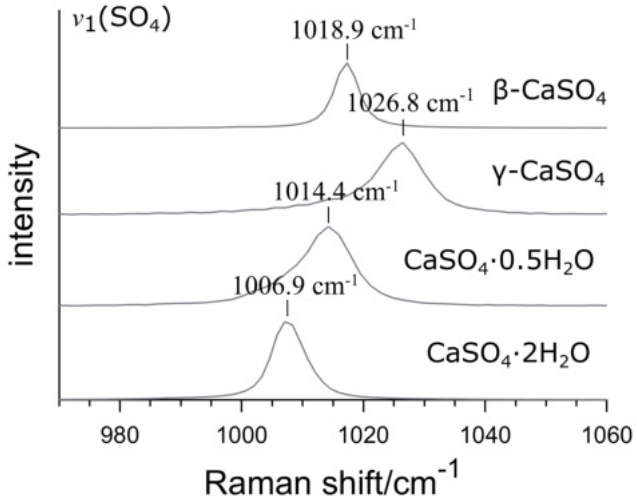


**Figure 6-11:** Raman shifts of the $\nu_1(SO_4)$ mode as measured for gypsum ($CaSO_4 \cdot 2\,H_2O$), hemihydrate ($CaSO_4 \cdot 0.5\,H_2O$), $\gamma$-anhydrite ($\gamma$-$CaSO_4$), and $\beta$-anhydrite ($\beta$-$CaSO_4$). The spectra of gypsum and $\beta$-anhydrite were measured at 22 °C. Hemihydrate and $\gamma$-anhydrite were measured at 90 °C and 110 °C, respectively.

Further, the evolution of calcium sulfate phases during incremental isothermal heating to 120 °C with 2.5 °C steps, held for 2 h each, at $p_{H_2O} < 120$ hPa, was studied. Figure 6-12 shows the resulting Raman spectra between 90 °C and 120 °C.

Compared to the corresponding XRD experiment (Figure 6-4), temperatures were held significantly longer and step sizes were reduced to avoid premature $\gamma$-anhydrite evolution as monitored in several preliminary spectroscopic experiments and in examinations described by Prasad et al. (2005) and Chio et al. (2004). They noticed $\gamma$-anhydrite without hemihydrate evolution and imputed it to the dynamic heating rate and temperature gradient in the sample. The water-vapor pressure prevailing at the sample also contributes to the pathway of gypsum dehydration. As Tang et al. (2019) state based on their thermodynamic calculations, gypsum undergoes the $CaSO_4 \cdot 2\,H_2O \rightarrow \gamma$-$CaSO_4$ or the $CaSO_4 \cdot 2\,H_2O \rightarrow CaSO_4 \cdot 0.5\,H_2O \rightarrow \gamma$-$CaSO_4$ pathway depending on $p_{H_2O}$ values. Here, the present measurement protocol does not provoke $\gamma$-anhydrite prior to hemihydrate formation.

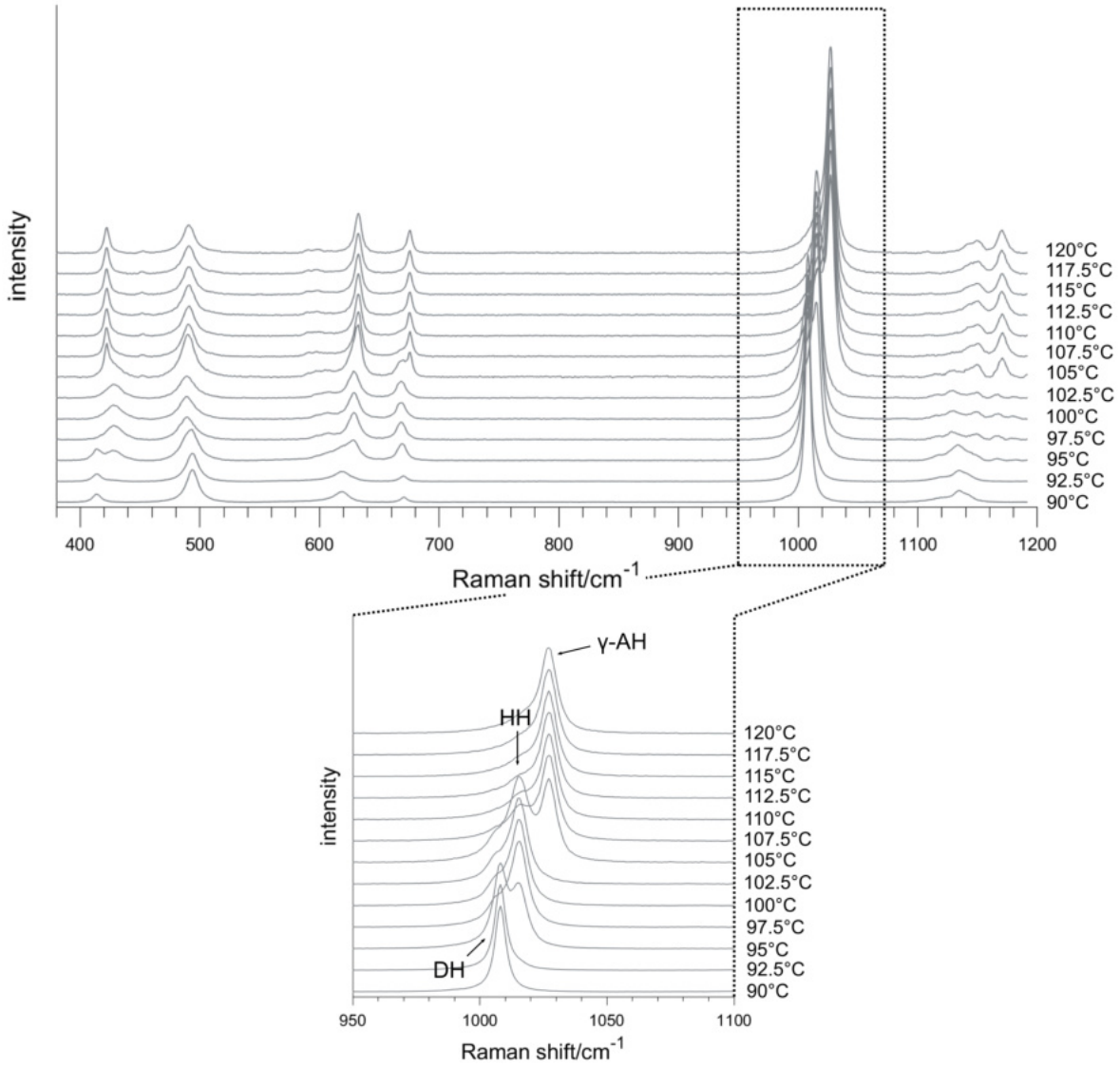


**Figure 6-12:** Temperature-dependently measured Raman spectra showing gypsum (DH) dehydration between 90 °C - 120 °C and $p_{H_2O} < 120$ hPa. Evolution of hemihydrate (HH) starts at 95 °C and further dehydrates to $\gamma$-anhydrite ($\gamma$-AH) upon 105 °C (time per temperature step: 2 h). The inset magnifies the area of 950 $cm^{-1}$ - 1100 $cm^{-1}$ to emphasize the consecutive gypsum $\rightarrow$ hemihydrate $\rightarrow$ $\gamma$-anhydrite evolution.

Differences between the two dehydration experiments are likely caused by the different measuring protocols and the differences between powder XRD and Raman spectroscopy. The applied Raman technique has a micrometer focus so that the dehydration process of a singular spot on a gypsum grain is tracked. Contrary, powder XRD allows for the analysis of the bulk sample material so that the dehydration of the sample entirety is measured. Discrepancies between dehydration processes base, *inter alia*, on measured sample volumes. Moreover, the different experimental conditions likely lead to result incongruities. Hemihydrate and $\gamma$-anyhdrite evolution during the Raman spectroscopy experiment starts at 15 °C - 20 °C and 25 °C - 30 °C lower temperatures than dehydration reactions investigated with powder XRD. As stated above, the measuring protocol was adapted to consecutively follow hemihydrate and $\gamma$-anhydrite evolution from gypsum.

## 6-3 Time-, temperature-, and humidity-dependent experiments

In the following, *in situ* powder XRD and Raman spectroscopy experiments are presented with focus on qualitative and quantitative aspects of $CaSO_4 \cdot n\,H_2O$ ($0 \leq n \leq 2$) dehydration and rehydration under defined temperature, humidity, and time conditions. If suitable, implications for such reactions in the Atacama Desert are considered.

### 6-3-1 Gypsum dehydration up to 110 °C

Part of the motivation for the present work is founded on the premise that temperature and humidity conditions prevailing in the Atacama Desert can promote dehydration and possibly rehydration processes of calcium sulfate phases within diurnal to seasonal time scales. Dehydration reactions of gypsum and hemihydrate have been extensively studied, often with focus on non-isothermal experiment set-ups without water-vapor control. As maximum soil temperatures in the Atacama do not exceed 60 °C, requirements for the experimental conditions of *in situ* dehydration measurements were framed as isothermal and isohumid with moderate to low temperatures and low water-vapor pressures. However, first measurements indicated that at temperatures below 60 °C, gypsum dehydration was not well monitorable despite prolonged measurement times. For example, gypsum treatment at 50 °C and 5% RH for 10 days yielded roughly 1% hemihydrate formation (Figure C-8). This result demonstrates the release of water of hydration within the desired temperature range but contradicts the kinetic description of processes. Hence, suitable working conditions concerning sample temperatures and measurement durations needed to be established.

Therefore, isothermal gypsum dehydration experiments at 80 °C, 90 °C, 100 °C, and 110 °C with a duration of 20 h, each, were performed. Sample particle-sizes were $\leq 50\,\mu m$. As stated earlier, humidity values above 80 °C could not be regulated. By evaluating humidity conditions at the sample according to the procedure described in Chapter 5-2-1, maximum and minimum humidities of 35.6 hPa (7.4% RH)/17.3 hPa (3.6% RH) at 80 °C, 20.4 hPa (2.9% RH)/12.4 hPa (1.8% RH) at 90 °C, 17.4 hPa/9.2 hPa at 100 °C and 27.7 hPa/16 hPa at 110 °C were recalculated. Generally, maximum values were dominant at the start, and minimum values towards the end of each measurement series.

Figure 6-13 shows the top view of powder XRD patterns obtained by heating gypsum at temperatures and humidities stated above. It becomes evident that gypsum does not dehydrate at 80 °C and $\leq$ 7.4% RH within the course of 20 h (Figure 6-13 (a), upper left panel). At 90 °C and $\leq$ 2.9% RH, the gypsum peak intensities first shrink and then disappear completely after $\approx$ 7 h. Accompanying, hemihydrate starts to form after about 0.5 h. The intensities increase parallel to the decrease of gypsum peak intensities so that both phases are present during a broad range of time (Figure 6-13 (b), left panel). No indications of structural modifications, such as shifting of individual peak positions, are present which indicates consistent lattice parameters and, therefore, unaltered crystal structures of both, gypsum and hemihydrate throughout the dehydration process. As stated in Ritterbach and Becker (2020), these characteristics imply that gypsum undergoes decomposition without prior structural changes. The deconstruction is then followed by the crystal growth of hemihydrate.

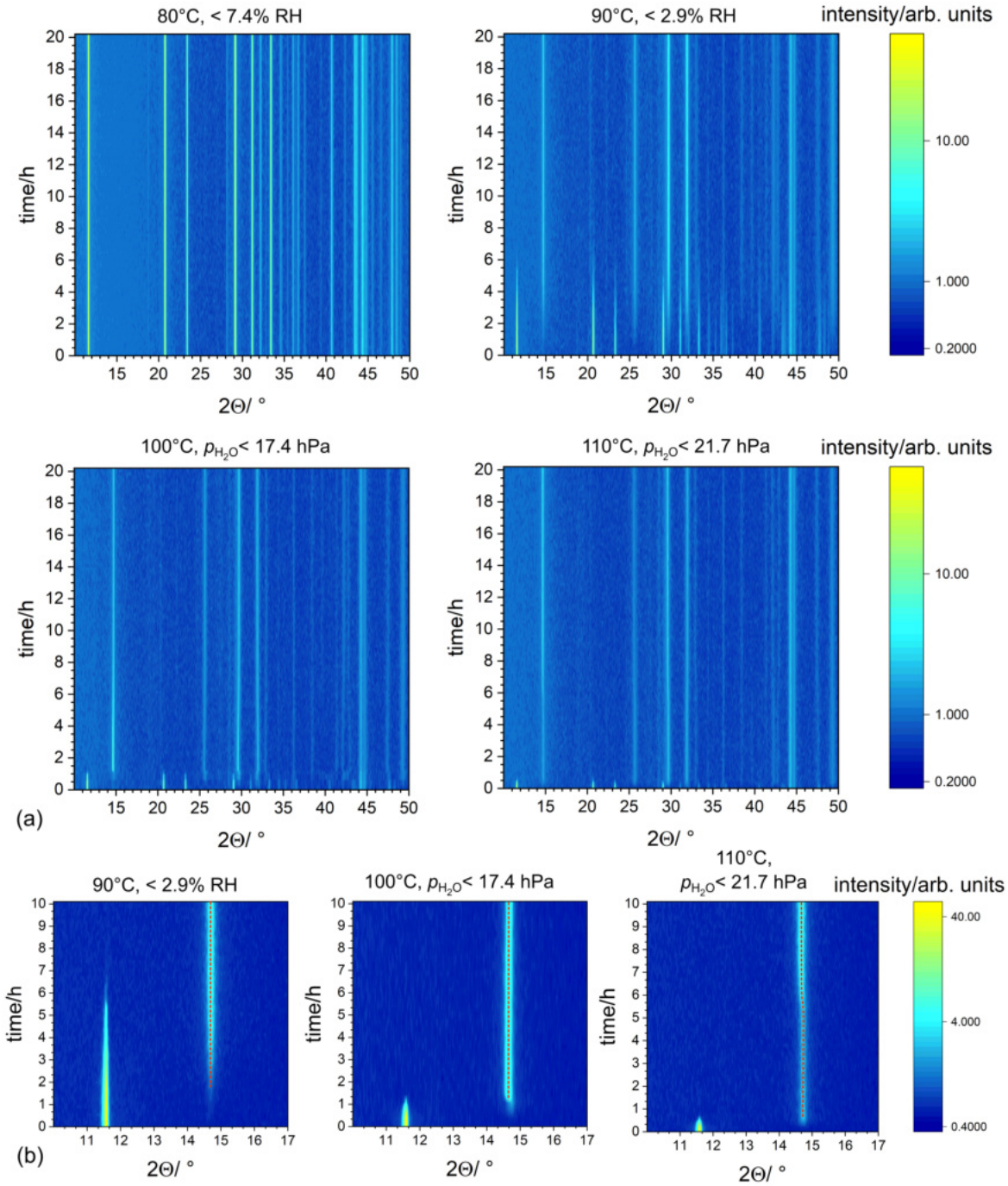


**Figure 6-13:** **(a)** Top views of isothermal powder XRD measurement series obtained by gypsum dehydration experiments between 80 °C and 110 °C. **(b)** The three bottom panels are close-ups of the 10° - 17° $2\Theta$ range of measurement series at 90 °C, 100 °C and 110 °C where dehydration occurred. At 110 °C, the shift of the (200)/(110) peak of hemihydrate towards smaller diffraction angles implies $\gamma$-anhydrite formation. The red dashed line gives a guide to the eye.

At 100 °C and $p_{H_2O} \leq 17.4$ hPa, gypsum dehydration to hemihydrate starts after ≈ 20 min and is finalized circa 1 h after reaching operating temperature (Figure 6-13 (b), middle panel). Hemihydrate remains the stable phase until the measurement ends in contrast to the dehydration experiment at 110 °C and $p_{H_2O} \leq 21.7$ hPa. Here, gypsum dehydrates shortly after reaching operating temperature (≈ 10 min) and hemihydrate forms. After 5 h, hemihydrate incrementally transforms into $\gamma$-anhydrite during circa 3 h which is recognizable by the peak shift from 14.7° 2Θ to smaller values (Figure 6-13 (b), right panel). The phase persists until the measurement is completed. The evolution of lattice parameter $b$ in Figure 6-14 also demonstrates the gradual $\gamma$-anhydrite formation.

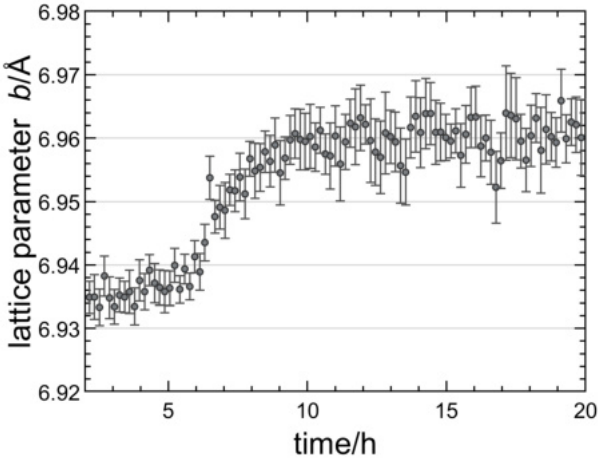


**Figure 6-14:** Lattice parameter evolution of $b$ over time at 110 °C and $p_{H_2O} < 21.7$ hPa based on measurements shown in Figure 6-13. The refinement was done using the structure model of hemihydrate given by Ballirano et al. (2001).

As opposed to the sluggish gypsum–hemihydrate transition, where gypsum decomposes prior to the growth of hemihydrate, $\gamma$-anhydrite evolves from hemihydrate through structural rearrangement induced by the loss of $H_2O$ molecules.

Figure 6-15 displays the results of gypsum dehydration at 90 °C (2.9% to 1.8% RH), corresponding to the lower left panel in Figure 6-13 (b), as a sequence of powder XRD patterns from a three-dimensional perspective. The parallel gypsum decrease and hemihydrate increase with time is evident. Likewise, the strong differences between gypsum and hemihydrate peak intensities are illustrated. The overemphasis of the (020) reflection of gypsum compared to the ($\bar{1}21$) reflection is explained with the grain sizes ranging up to 50 µm. Especially larger gypsum particles cause alignment due to pronounced (0k0) faces.

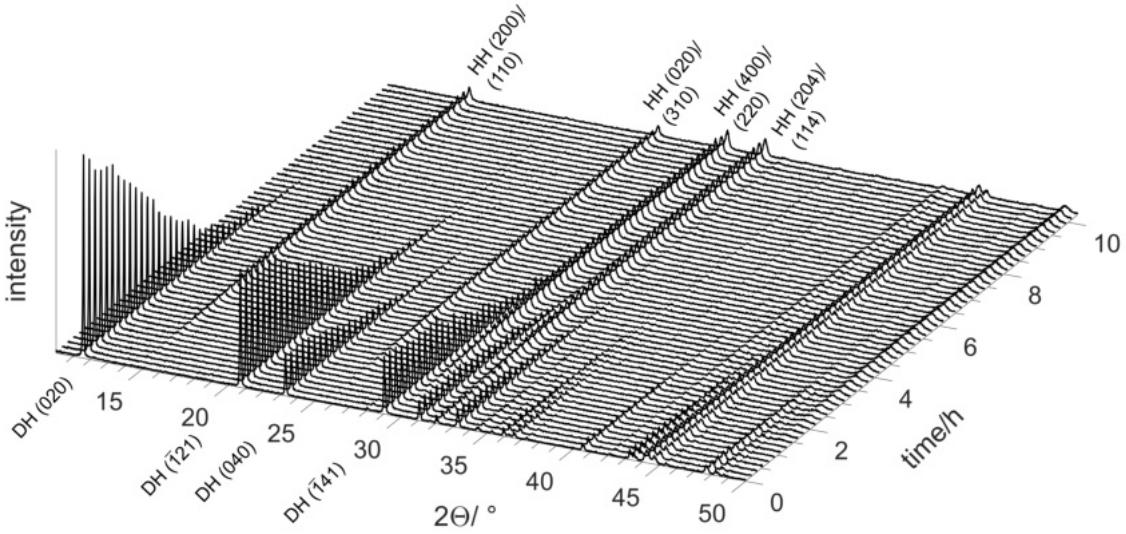


**Figure 6-15:** Dehydration of gypsum to hemihydrate illustrated by a sequence of powder XRD measurements taken at 90 °C and relative humidity values $\leq$ 2.9%. The strongest peaks of gypsum (DH) and hemihydrate (HH) are indicated.

To further investigate the gypsum dehydration process with focus on monitoring the loss of $H_2O$, corresponding isothermal and isohumid Raman spectroscopic experiments were conducted at 90 °C, 100 °C, and 110 °C. The humidity was set to 2.5% RH at 90 °C and equivalent $p_{H_2O}$ values of 25.3 hPa at 100 °C and 35.8 hPa at 110 °C. The results are shown as top views of Raman spectrum sequences in Figure 6-16.

At 90 °C, simultaneous decrease of gypsum and increase of hemihydrate is visible. The formation of hemihydrate starts around 3.5 h. The majority of gypsum dehydrates between 5 h and 6 h but low intensity $H_2O$ modes can be observed up to 7 h - 8 h (Figure 6-16, top panels). This indicates a sluggish transition. Hemihydrate pertains until the measurement finishes. At 100 °C, the dehydration of gypsum starts after $\approx$ 1 h. The process is rapidly completed (within circa 20 min) and hemihydrate remains the stable phase up to 20 h (Figure 6-16, middle panels). At 110 °C, gypsum is present during the first measurement taken 10 min after reaching operating temperature. Followingly, only $\gamma$-anhydrite is evident until the end of the experiment after 20 h. Hemihydrate formation is not detected (Figure 6-16, bottom panels).

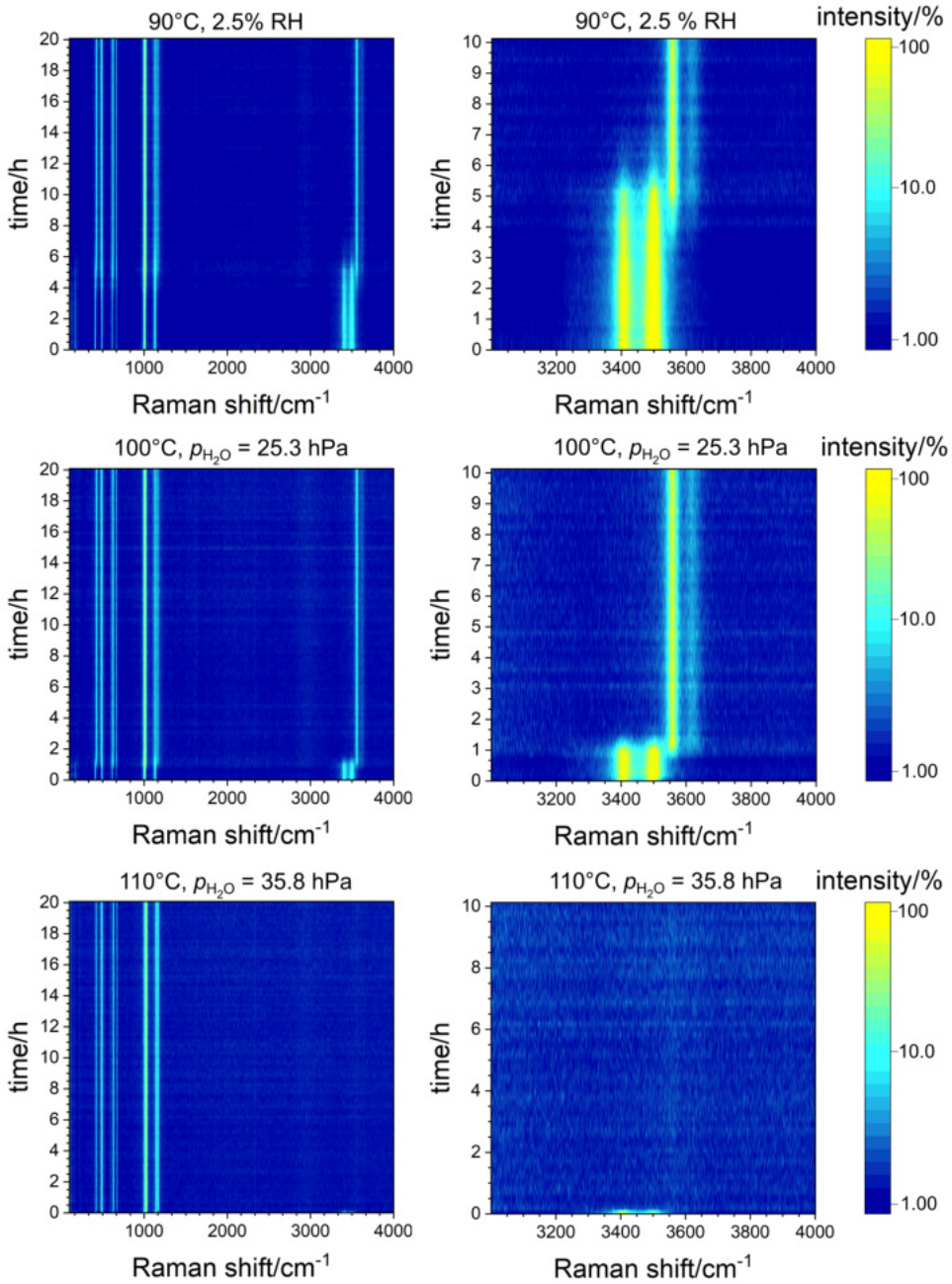


**Figure 6-16:** Top views of isothermal and isohumid Raman spectroscopic measurement series obtained by gypsum dehydration between 90 °C and 110 °C. The panels to the left show spectral ranges and measured time in total. The right panels provide close-ups of $H_2O$ presence or absence based on (lacking) characteristic hydroxyl-stretching modes between 3000 $cm^{-1}$ - 4000 $cm^{-1}$. The first ten hours of measurements are displayed.

In all three dehydration experiments, calcium sulfate phases can be clearly distinguished by the decline of preceding and the growth of succeeding phases. Concerning water modes of gypsum and hemihydrate, no shift in positions is evident.

This indicates invariable chemical environments of $H_2O$ molecules as bond lengths remain unaltered. Overall, Raman spectroscopic and powder XRD measurements show an identical trend pertaining to dehydration processes in dependence of low water-vapor pressures and temperatures of 90 °C, 100 °C, and 110 °C. Below 110 °C, hemihydrate remains the sole dehydration product and the gypsum–hemihydrate transition slows down with temperature. The formation path of $\gamma$-anhydrite at 110 °C seemingly differs from the powder XRD result as spectroscopic measurements reveal the lack of intermediate hemihydrate. A simple explanation could be that the temporal resolution of ten minutes between measurements is too imprecise. Differences between results of both experiment series possibly originate in the slight differences of water-vapor pressures and presumably arise from the differences between the two methods.

To narrow down the hemihydrate–$\gamma$-anhydrite threshold regime with the given experimental set-up conditions, further Raman spectroscopic experiments were conducted at 105 °C and $p_{H_2O} = 30.3$ hPa and at 107.5 °C and $p_{H_2O} = 32.9$ hPa. The respective $p_{H_2O}$ values correspond to 2.5% RH. In Figure 6-17 (a), the top view of measurement sequences of both experiments are shown. Here, only the spectral range of 980 $cm^{-1}$ - 1050 $cm^{-1}$ is displayed to follow the dehydration on the basis of the $\nu_1(SO_4)$ mode with frequencies of 1006.9 $cm^{-1}$ (gypsum), 1014.1 $cm^{-1}$ (hemihydrate), and 1026.2 $cm^{-1}$ ($\gamma$-anhydrite). At 105 °C, gypsum dehydration to hemihydrate is finalized after 30 min - 40 min (Figure 6-17 (b), lower panel). Within 20 h, no further dehydration to $\gamma$-anhydrite occurs. During the dehydration at 107.5 °C, gypsum is present within the first ten minutes. After 20 min, hemihydrate and $\gamma$-anhydrite formation begins, whereby the $\nu_1(SO_4)$ mode of $\gamma$-anhydrite is more intense than that of hemihydrate (Figure 6-17 (b), upper panel). Figure 6-17 (c) shows the respective deconvolved profile. After ten more minutes, gypsum is no longer detectable and hemihydrate and $\gamma$-anhydrite coexist until the measurement ends.

The early and advanced formation of $\gamma$-anhydrite at 107.5 °C could be caused by the presence of a reaction gradient in the sample promoted by the comparably high temperature of 107.5 °C: The surface of the measured grain could have firstly dehydrated to hemihydrate and secondly to $\gamma$-anhydrite, while the inside volume remained unaltered. This is possibly reinforced by heat transfer of the laser source. The influence of heat evolution on structural analysis depending on laser power and wavelengths was for example described by Novák et al. (2016). The laser-generated heat is consistent during all experiments. However, it could have supported surface dehydration from hemihydrate to $\gamma$-anhydrite by providing the heat amount that is required to surpass the $\gamma$-anhydrite formation threshold. A temperature gradient across the sample cannot be ruled out either. Additionally, the temporal resolution of the experiment appears to be contingently suitable for tracking the fast dehydration processes of gypsum at temperatures above $\approx$ 105 °C. To follow the gypsum–hemihydrate–$\gamma$-anhydrite succession of the grain surface at increased temperatures, it could be expedient to measure faster and more frequently within the first measurement hour.

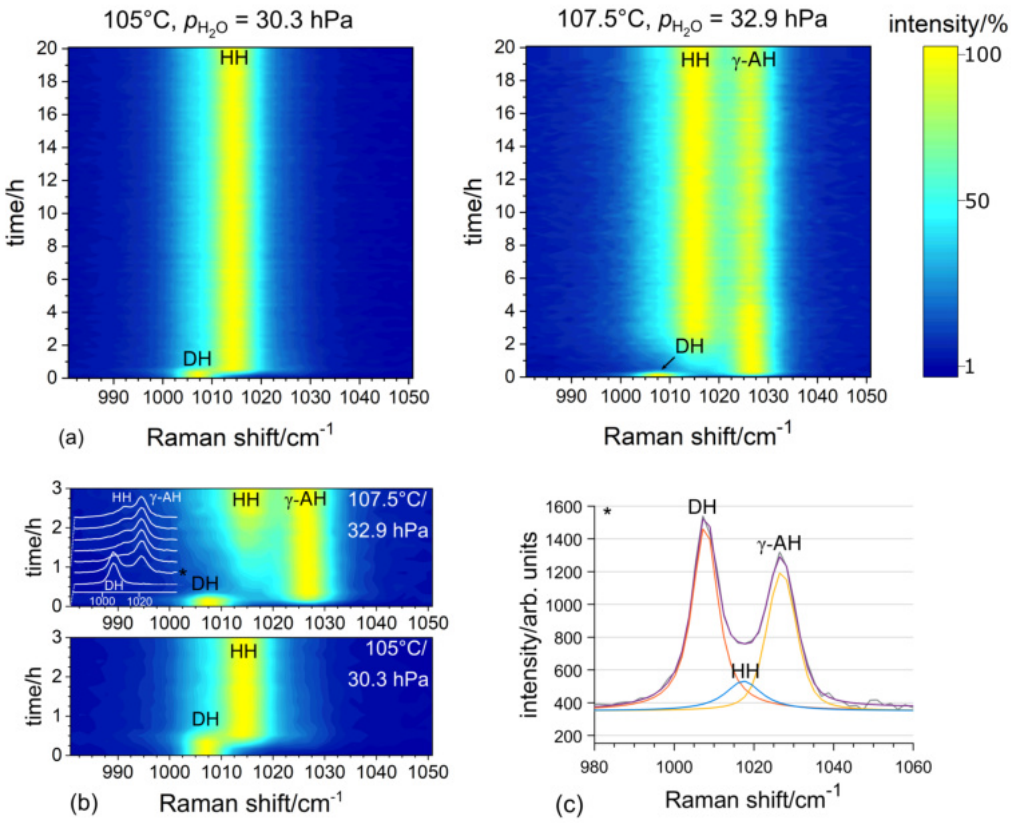


**Figure 6-17:** **(a)** Top views of isothermal and isohumid Raman spectroscopic measurement series obtained by gypsum dehydration experiments at 105 °C/30.3 hPa and 107.5 °C/32.9 hPa. The panels show the main sulfate mode $\nu_1(SO_4)$ of gypsum (DH), hemihydrate (HH) and $\gamma$-anhydrite ($\gamma$-AH). **(b)** Magnification of the first three hours of measurements. The inset in the upper panel gives the first seven measurements as stacked spectra. **(c)** Profile deconvolution of the $\nu_1(SO_4)$ modes measured after 20 min of the measurement start. The red, yellow, and blue lines show the contribution of gypsum, $\gamma$-anhydrite, and hemihydrate, respectively. The sum is given in purple.

Overall, the data suggest that low humidities ($p_{H_2O}$ values equivalent to 2.5% RH) and the present experimental conditions compel immediate to rapid $\gamma$-anhydrite formation at temperatures $\geq$ 107.5 °C. The temperature range where $\gamma$-anhydrite becomes the exclusive calcium sulfate phase shortly after reaching isothermal experiment conditions lies between 107.5 °C and 110 °C (Figures 6-16 and 6-17). According to XRD data, the formation of $\gamma$-anhydrite is characterized by the loss of water molecules from hemihydrate with non-destructive structural reorganization of the calcium sulfate channels. Based on the findings at hand, a direct formation of $\gamma$-anhydrite from gypsum $\leq$ 110 °C and given water vapor-pressures cannot be ruled out. Yet, it is surmised that the applied measurement protocols are unsuitable to follow the fast gypsum $\rightarrow$ hemihydrate $\rightarrow$ $\gamma$-anhydrite dehydration steps at the outer grain surface at $\geq$ 105 °C.

### 6-3-2 Particle size-dependent gypsum dehydration at 90 °C

As isothermal XRD and Raman spectroscopic dehydration experiments showed, 90 °C proved to be a suitable temperature to follow gradual gypsum dehydration. Since particle sizes and shapes largely influence dehydration or rehydration reactions (*e.g.* Taylor and York, 1998; Zhu and Grant, 2001; Koga and Tanaka, 1997; Criado et al., 2014), particle size-dependence of hemihydrate formation from gypsum was studied. Two measurement series were conducted with fractions of $< 20$ µm, 20 µm - 25 µm, 25 µm - 32 µm, 32 µm - 50 µm (Series I); and 20 µm - 25 µm, 32 µm - 36 µm, 50 µm - 53 µm, 75 µm - 80 µm (Series II).

Concerning the first series, the mean relative humidities at the sample were recalculated to 1.9%, 2.7%, 1.8%, and 3.1%, respectively (Figure 6-18, left panel). Due to the constant sample temperature of 90 °C, the moderate variability of stated values is attributed to differing humidities at the sample prior to the start of measurements. To enhance constancy of sample humidities throughout the second series, humidities inside the CHCplus+ chamber were lowered to 5% RH previous to the start of isothermal heating. With this remedy, humidity conditions at the sample were kept virtually constant as the mean relative humidities of 2.2%, 2.1%, 2.5%, and 2.1%, respectively, suggest (Figure 6-18, right panel).

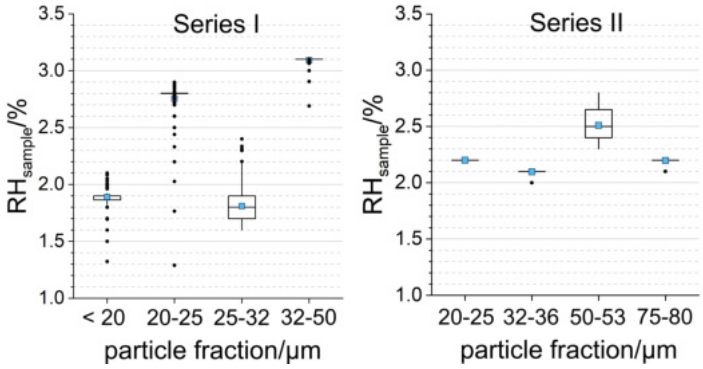


**Figure 6-18:** Relative humidities (RH) at the sample during particle size-dependent gypsum dehydration at 90 °C. The distribution of $RH_{sample}$ is displayed as following: The boxes represent the 25th to 75th percentile (interquartile range, IQR), the whiskers symbolize the range within 1.5 · IQR, the line gives the median, the sphere denotes the outliers, and the mean is depicted as square (light blue).

To quantify the influence of particle sizes on gypsum dehydration, $\alpha$ values were time-dependently obtained. In Figure 6-19, $\alpha - t$ or (fraction of) conversion curves, are given. The upper panels show the results of measurement series I and the lower panels give the results of measurement series II. The data are fitted with the kinetic models according to Johnson, Mehl, Avrami, Erofe'ev, and Kolmogorow (JMAEK, left panels) and Prout-Tompkins (right panels). The strong dependence of dehydration kinetics on grain sizes becomes obvious in both cases.

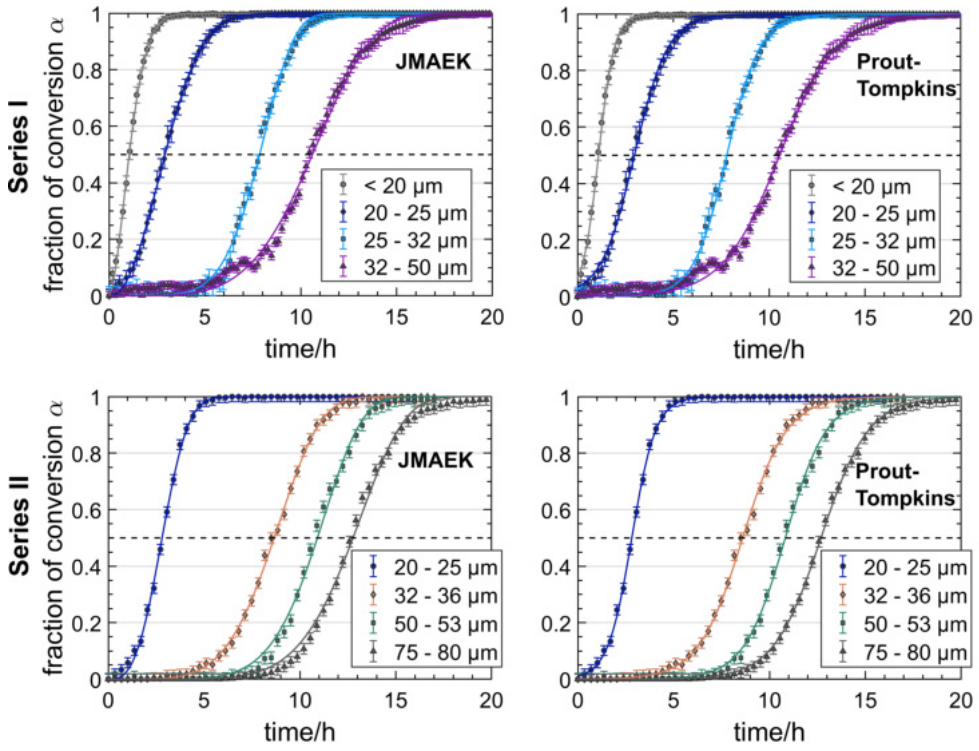


**Figure 6-19: (a)** Converted hemihydrate fraction ($\alpha$) vs. $t$ curves for particle size-dependent dehydration of gypsum at 90 °C. $\alpha$ values were calculated from quantitative phase analysis data of isothermal powder XRD measurements. Data were fitted with the JMAEK and Prout-Tompkins kinetic models (lines between markers).

Series I includes particles $\leq$ 20 µm. This fraction reaches 50% completion of dehydration after approximately 75 min (1.25 h). The fractions 20 µm - 25 µm, 25 µm - 32 µm, and 32 µm - 50 µm exhibit 50% conversion times of 3.0 h, 7.9 h, and 10.6 h, respectively (Figure 6-19, upper panels). For series II, the measurement of the 20 µm - 25 µm fraction was repeated for comparability. Here, this fraction reaches 50% conversion by 2.8 h. The fractions 32 µm - 36 µm and 50 µm - 53 µm show conversion times of 8.5 h, respectively 10.67 h for 50% bassanite formation. The largest fraction of 75 µm - 80 µm reaches an $\alpha$ value of 0.5 after 12.6 h (Figure 6-19, lower panels).

The 50% dehydration of the 20 µm - 25 µm particles during series II compared to series I was 12 min faster. This might be caused by the slightly lower mean relative humidity of approximately 0.5% (Figure 6-18). The further measurements of series I can not be compared directly to those of series II as the particle size-ranges of series II were reduced to enhance uniformity. However, some considerations can be made: The 32 µm - 36 µm fraction of series II reaches 50% conversion circa 35 min after the 25 µm - 32 µm fraction of series I reaches the benchmark. The modest temporal difference seems to be comprehensible considering that both fractions are rate-limited by the dehydration velocity of the largest grains, which only differ by 4 µm. The mean relative humidities at the sample diverged 0.3%. Considering the same principle, the small gap of nearly 5 min between conversion times of 32 µm - 50 µm (series I) and 50 µm - 53 µm particles (series II) appears coherent. The differences in sample humidities were 0.7%. In total, the dehydration of the 75 µm - 80 µm fraction is slowest which corresponds to the large particle sizes.

In general, the $\alpha - t$ curves of series II exhibit a more uniform appearance and reduced data scattering compared to the curves of series I. Possibly, the constricted particle size-ranges and decreased variable humidity values of series II led to more homogeneous hemihydrate nucleation and growth conditions. The symmetric sigmoidal shape of all conversion curves is evident. Therefore, the curves were fitted using the JMAEK and Prout-Tompkins kinetic models (Chapter 4-1). The JMAEK reaction model was introduced by Avrami in 1940 for quantification of the liquid–solid phase transition kinetics in metals. Briefly stated, it assumes the following: i) Tiny germ nuclei of the new phase exist in the old phase. Their effective number can be altered by temperature. ii) The number of germ nuclei changes as some become growth nuclei and some are swallowed by the growth nuclei. iii) Impingement of grains and subsequent growth termination also influences the converted volume of the new phase. iv) The converted fraction $\alpha$ is approximately independent of temperature (and concentration) in a given "isokinetic range" (Avrami, 1939, 1940). Besides the rate-constant $k$, the model specifies the exponential factor $n$, which ranges from 1 to 4 and contains, among others, the growth dimensionality $1-n$.

Due to its simplicity, the model is frequently applied to various kinetic data sets which puts over-interpretation of experimental results at risk according to Fanfoni and Tomellini (1998). Modifications of the JMAEK model that consider, *e.g.*, finite size effects of the macroscopic system and non-uniform nucleation, anisotropic particle formation, and transient nucleation effects were proposed (Weinberg et al., 1997).

Compared to the JMAEK model, the reaction model attributed to Prout and Tompkins 1944 assumes different aspects and constraints concerning the nuclei growth rate. The presumption of constant nucleation rates is, however, common to both. The Prout-Tompkins reaction model, originally composed to kinetically describe the observations of thermal decomposition of potassium permanganate, is based on the concept of nucleus branching. By this, multiplication of nuclei is meant due to structural changes, such as crack propagation (Brown and Glass, 1999). The authors made the following premises: i) The probability of branching termination depends linearly on $\alpha$. ii) The ratio of branching termination and branching is independent of $\alpha$. iii) An equal nucleation and branching rate (yielding symmetrical conversion curves) is the case. Alongside $k$, an integration constant $C$ is declared. The value of $C$ is not restricted as a general criterion for a suitable choice of $C$ is not claimed by the authors. The reaction model is often criticized for the assumptions necessary for its derivation. Especially, the simplification of equal branching and termination rates is ill-suited for many solid state reaction (Brown and Glass, 1999; Brown, 1997; Bohn, 2014). A modification of the model for those cases was, *inter alia*, given by Jacobs (1997).

The fitted parameters $k$, $n$, and $C$ are given in Table 6-3. The summed squares of residuals (SSE) that measure the discrepancy between data and estimation model are noted as well.

**Table 6-3:** Rate constants $k$, growth dimensionality $n$ and integration constant $C$ as yielded by fits of the JMAEK ($g(\alpha) = (-\ln(1-\alpha))^{1/n} = kt$) and Prout-Tompkins ($g(\alpha) = \ln(\alpha/(1-\alpha)) + C = kt$) reaction models to $\alpha - t$ curves of particle size-dependent gypsum to hemihydrate dehydration at 90 °C and low RH values (Figure 6-19). SSE is the summed square of residuals.

| | JMAEK | | | |
|---|---|---|---|---|
| | **Particle size/µm** | $k$ | $n$ | **SSE** |
| **Series I** | $< 20$ | 0.639(9) | 1.70(2) | 0.00383 |
| | 20 - 25 | 0.06(2) | 2.20(2) | 0.00495 |
| | 25 - 36 | $2(1) \cdot 10^{-6}$ | 6.0(1) | 0.03373 |
| | 36 - 50 | $8(3) \cdot 10^{-6}$ | 4.8(1) | 0.06409 |
| **Series II** | 20 - 25 | 0.03(3) | 3.010(3) | 0.003702 |
| | 32 - 36 | $1.2(3) \cdot 10^{-5}$ | 5.0(2) | 0.006179 |
| | 50 - 53 | $1.0(4) \cdot 10^{-7}$ | 6.5(1) | 0.02043 |
| | 75 - 80 | $2.8(5) \cdot 10^{-8}$ | 6.6(6) | 0.02192 |
| | **Prout - Tompkins** | | | |
| | **Particle size/µm** | $k$ | $C$ | **SSE** |
| **Series I** | $< 20$ | 2.42(6) | -2.66(8) | 0.009832 |
| | 20 - 25 | 1.14(2) | 3.39(7) | 0.01283 |
| | 25 - 36 | 1.15(3) | 9.0(2) | 0.01994 |
| | 36 - 50 | 0.67(1) | 7.1(2) | 0.04097 |
| **Series II** | 20 - 25 | 1.60(6) | -4.51(8) | 0.001636 |
| | 32 - 36 | 0.86(2) | 7.4(2) | 0.006422 |
| | 50 - 53 | 0.92(3) | 10.0(3) | 0.009099 |
| | 75 - 80 | 0.80(3) | -10.2(1) | 0.004613 |

The $\alpha - t$ curves can be fitted well with both kinetic models in the case of particle size-fractions $\leq$ 20 µm, 20 µm - 25 µm (series I), and 20 µm - 25 µm, 32 µm - 36 µm (series II). This is corroborated by SSE values. The other fits are significantly poorer according to SSE values. Especially, the differences between data and fits regarding the accelerating and decelerating parts of the curves is evident. Concerning both series, the visual fits according to the Prout-Tompkins model are slightly closer to the data than the fits based on the JMAEK model (Figure 6-19).

Concerning the JMAEK reaction model fits, solely fractions $\leq$ 20 µm and 20 µm - 25 µm of series I and 20 µm - 25 µm of series II have $n$ values that are $\leq 4$ and fall in the validity range described by Avrami (1940). The other $\alpha - t$ curves could only be fitted with $n$ values $\geq 4.8$. Larger $n$ values coincide with prolonged induction periods. Here, the term 'induction period' refers to the initial slow stage of a reaction. Based on the results of grain sizes $\geq$ 25 µm, the dependence of induction period duration on increasing particle sizes becomes clear. As mentioned above, larger particles have less surface area per volume unit than smaller particles. Hence, the probability of successive nucleus formation events is lowered as the volume-related reaction surface, that promotes these events, decreases with size. The induction period is eventually overcome when nucleation approaches the steady-state nucleation rate and the reaction proceeds.

The phenomenon of a variable nucleation rate is reflected in the Avrami exponent $n$. It entails information about the growth dimension $n - 1$, if the prerequisites of constant nucleation rate and crystal growth velocity are met (Pries et al., 2019, supporting information). An Avrami exponent $\geq 4$ is only possible for crystallization processes where nucleation rates show a time dependent transient, non-linear behavior until the steady-state nucleation rate is reached (Christian, 2002, pp. 529-552; Kelton and Greer, 2010, p. 82). These relations might explain the increased values of $n$ obtained by the JMAEK model fits for particle sizes $\geq 25\,\mu m$. The discrepancy of $\approx 1$ concerning $n$ values of the two 20 µm - 25 µm fractions can not be clarified further.

Parameter $n$ is a compound term. It can be expressed as the sum of $\lambda + \beta$, where $\lambda$ gives the growth dimension with $\beta$ successive events that are necessary to form the growth nucleus (Khawam and Flanagan, 2006). A unique determination of $\lambda$ and $\beta$ is not obtainable (Brown et al., 1980) and the evaluation of a reaction mechanism based on fitted $n$ values not expedient (Ballirano and Melis, 2009b).

The assessment of $C$ values obtained by fits according to the Prout-Tompkins reaction model is omitted since the values do not contain further physical information. In general, rating the physical soundness of both reaction models beyond SSE value assessment and the visual control is difficult. Both reaction models seem to satisfactorily describe the conversion curves of particle sizes $\leq 20\,\mu m$ and 20 µm - 25 µm. In many cases, it is challenging to prefer one over the other due to the equally good fits provided by both models according to *e.g.* Brown et al. (1994). The Prout-Tompkins model fits of $\alpha - t$ curves of the 32 µm - 36 µm, 50 µm - 53 µm, and 75 µm - 80 µm fractions agree slightly better with the experimental data than the JMAEK model fits. The conversion curves of 25 µm - 36 µm and 36 µm - 50 µm particles exhibit the largest discrepancies between data and model fits.

As stated in Chapter 2-3, several authors investigated the kinetics of gypsum dehydration reactions under various conditions. Among them, Gardet et al. (1976) and Strydom et al. (1995) could fit parts of their data with the Prout-Tompkins reaction model, whereas Ball and Norwood (1969), Heide (1969), Vakhlu et al. (1985), Hudson-Lamb et al. (1996), and Ballirano and Melis (2009b) found the JMAEK reaction model to fit large parts of their data best. Ball and Norwood (1969) and Ballirano and Melis (2009b) conducted comprehensive isothermal gypsum dehydration studies. Ball and Norwood (1969) found formal kinetics to vary with temperature and water-vapor pressure. Between 80 °C - 110 °C and $p_{H_2O} = 6.1$ hPa - 22.7 hPa, they found nucleation and nuclei growth with $n = 2$ to be the rate-controlling step. Ballirano and Melis (2009b) yielded $n$ values from 4.50(5) to 7.4(3) for experiments at 75 °C - 130 °C in a first run. In a second run, they fixed $n$ at 6 and obtained satisfying fits for the greater part of $0.05 \leq \alpha \leq 0.9$. Restrictions of $\alpha$ prior to model fitting are used in many studies dealing with solid phase transformations. However, the confined $\alpha$ ranges vary, which questions the physical meaning of such procedures.

Concerning the present data, a clear assertion concerning a reasonable reaction model is omitted as falsification of one or the other is not reasonable. However, the slightly better fits of the autocatalytic Prout-Tompkins model to conversion curves of larger particle sizes are noticeable. In combination with Avrami exponents > 4, which suggests changing nucleation rates, this may point to either autocatalytic control throughout or a particle size-dependent change of reaction mechanisms.

Overall, particle sizes 20 µm - 25 µm appeared to be the most suitable fraction to chose for further dehydration and rehydration experiments. In general, large particle sizes are not desirable to use for powder XRD experiments. Likewise, the issue of preferred particle orientation increases with grain sizes. In contrast, the 20 µm - 25 µm fraction exhibits negligible preferred particle orientation.

### 6-3-3 Gypsum dehydration between 76 °C and 92 °C

The dehydration of gypsum was further studied by isothermal XRD experiments with particle sizes 20 µm - 25 µm at 76 °C, 80 °C, 84 °C, 88 °C, and 92 °C. Efforts were made to keep the sample humidities virtually constant by regulating the chamber humidity to a minimum before the start of experiments. The mean relative humidities prevailing at the sample were recalculated to 3.3%, 2.9%, 2.4%, 2.1%, and 1.7%, respectively.

In Figure 6-20, the converted hemihydrate fractions are plotted against time (upper left panel). Experiments at 76 °C and 80 °C were performed for 60 h. Experiments at 84 °C, 88 °C, 92 °C were conducted for 20 h or until conversion was completed. The shapes of conversion curves obtained by dehydration at 84 °C, 88 °C, and 92 °C are sigmoidal, similar to those yielded by the particle size-dependent experiments at 90 °C. Regarding the $\alpha - t$ time curve attained at 80 °C, a clear categorization of the curve shape appears to be invalid. $\alpha$ values seemingly exhibit two different processes of dehydration. Over the first 20 h, a linear time-dependent dehydration yielding 13% conversion is apparent. This is followed by a second process that manifests in an S-shaped conversion curve with $\approx$ 96% hemihydrate formation after 60 h. At 76 °C, gypsum dehydrates to 11% hemihydrate after 60 h. The comparably slow dehydration shows a linear time dependence, similar to the first dehydration process described for the experiment at 80 °C. Therefore, a change of process appears likely, if the measurement time was prolonged.

The symmetric sigmoidal conversion curves obtained at 84 °C, 88 °C, and 92 °C were fitted using the JMAEK and Prout-Tompkins reaction models. The experimental data and fits are given in the two bottom panels in Figure 6-20. Corresponding parameters $k$, $n$ and $C$ are given in Table 6-4.

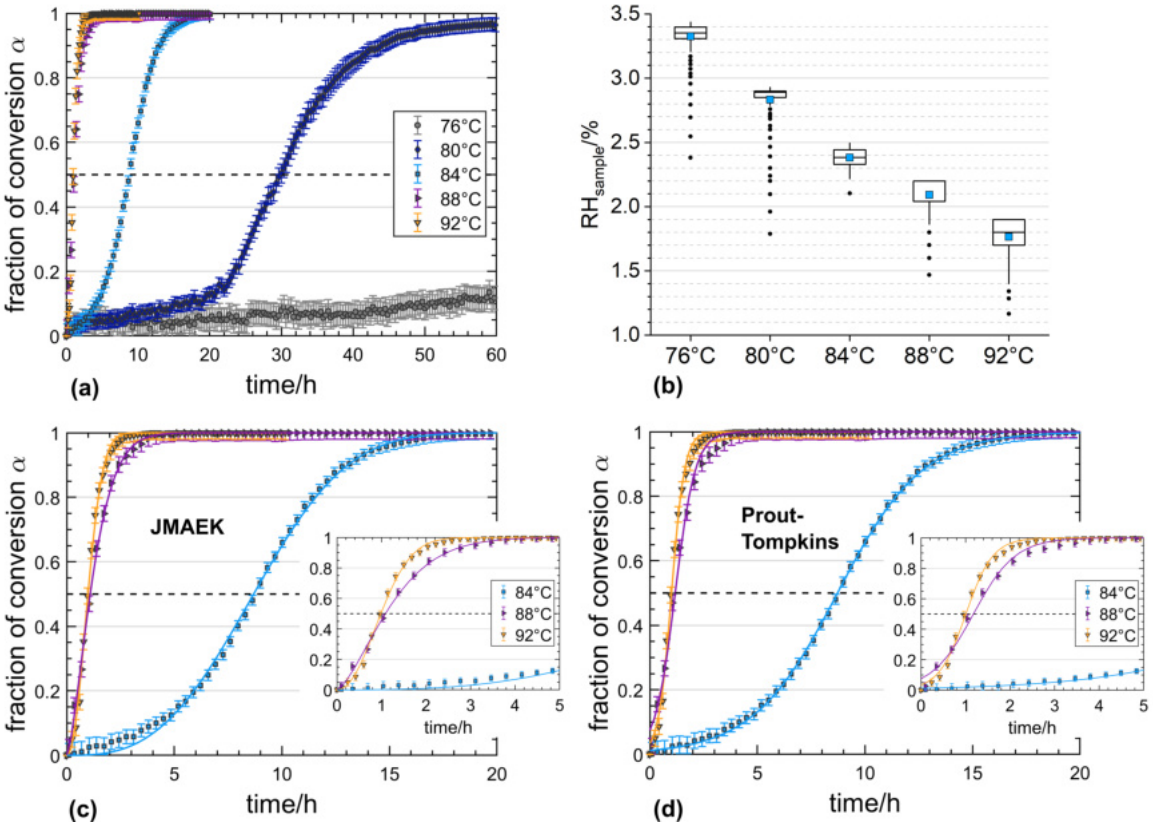


**Figure 6-20:** **(a)** Isothermal gypsum to hemihydrate conversion of the 20 µm - 25 µm fraction at 76 °C - 92 °C. $\alpha$ values were calculated from quantitative phase analysis data of isothermal powder XRD measurements. **(b)** The distribution of relative humidities at the sample, $RH_{sample}$, are displayed as following: The boxes represent the 25th to the 75th percentile (Interquartile Range, IQR), the whiskers symbolize the range within 1.5 · IQR, the line gives the median, the sphere denotes the outliers and the mean values are given by the blue squares. **(c)** JMAEK and **(d)** Prout-Tompkins fits (lines) to the data obtained at 84 °C, 88 °C and 92 °C. The insets magnify the first five measurement hours.

**Table 6-4:** Rate constant $k$, growth dimensionality $n$ and integration constant $C$ obtained by fits of the JMAEK ($g(\alpha) = (-\ln(1-\alpha))^{1/n} = kt$) and Prout-Tompkins ($g(\alpha) = \ln(\alpha/(1-\alpha)) + C = kt$) reaction models to $\alpha - t$ curves of gypsum (20 µm - 25 µm particles) to hemihydrate dehydration at 84 °C, 88 °C, 92 °C and low relative humidities (Figure 6-20 (b)). SSE is the summed squares of residuals.

| | JMAEK | | | Prout - Tompkins | | |
|---|---|---|---|---|---|---|
| **T/°C** | $k$ | $n$ | **SSE** | $k$ | $C$ | **SSE** |
| 84 | 0.0011(2) | 2.94(7) | 0.01294 | 0.206(5) | 4.41(4) | 0.00205 |
| 88 | 0.61(1) | 1.47(3) | 0.00302 | 2.1(1) | 2.5(1) | 0.00188 |
| 92 | 0.71(2) | 2.11(8) | 0.00745 | 3.3(1) | 3.3(1) | 0.01342 |

The JMAEK model appears to describe the conversion curves yielded by gypsum dehydration at 88 °C and 92 °C rather adequately. In contrast, the data obtained at 84 °C can not be satisfyingly fitted with the JMAEK equation. Significant deviations regarding the accelerating part of the $\alpha - t$ curve, *i.e.* the first 5 h - 6 h, are evident. This is also corroborated by SSE values (Table 6-4).

In regard to the Prout-Tompkins model fits, the situation is reversed. Whereas the model describes the converted hemihydrate fractions as calculated from gypsum dehydration at 84 °C reasonably well, the data collected at 88 °C and 92 °C are ill-fitted. This is especially apparent for the decelerating parts of conversion curves at the end of the transformation. Despite the good agreement with data obtained at 84 °C, the significance of the Prout-Tompkins model fit is regarded with caution. As stated above, it is not obvious if the measurement is dominated by a single- or multiple-step dehydration.

Discrepancies between findings of gypsum dehydration at 80 °C displayed here and those shown in Figure 6-13 most likely result from differences in particle sizes and relative sample humidities. The humidity values during the preliminary dehydration experiment at 80 °C ranged from 7.4% RH to 3.6% RH. According to the distribution of relative humidities (Figure 6-20 (b)), mean relative humidities were considerably lower during the measurements presented here. In general, the temperature dependency is overt. Gypsum dehydration is severely slowed down at temperatures $\leq$ 80 °C. The time required for 50% hemihydrate formation suggests an exponential dependency on sample temperature at humidities $\leq \approx$ 3.3% RH. This would prompt an Arrhenius-distributed temperature dependency which would be in accordance with the usually observed behavior of thermally activated processes.

As Figure 6-20 (b) shows, the mean relative humidities at the sample depend on the applied temperature as they decrease with increased temperature values. The dehydration process at temperatures $\geq$ 88 °C is rapid. To exclusively study the influence of temperature, strictly isohumid conditions were necessary which was not achieved here.

The exponential temperature dependency is also recognizable from isothermal and isohumid Raman spectroscopic experiments performed at 76 °C, 80 °C, 84 °C, 88 °C, and 92 °C with sample humidities of 2.5% RH. Figure 6-21 shows the top view of serial measurements obtained by gypsum dehydration at respective temperatures (and constant humidity) conducted for 20 h, 40 h or 60 h. Here, the spectral range is restricted to 3300 $cm^{-1}$ - 3700 $cm^{-1}$ to follow the consecutive loss of 1.5 water molecules per formula unit. Gypsum dehydration is approximately finalized by 28.5 h (80 °C), 15.6 h (84 °C), 10.1 h ( 88 °C), and 5.8 h (92 °C). At 76 °C, very low intensity $\nu_1(H_2O)$ and $\nu_3(H_2O)$ modes of gypsum are still evident. Hence, at temperatures $\geq$ 76 °C, hemihydrate is the stable product at the end of experiments (Figure 6-21 (a)).

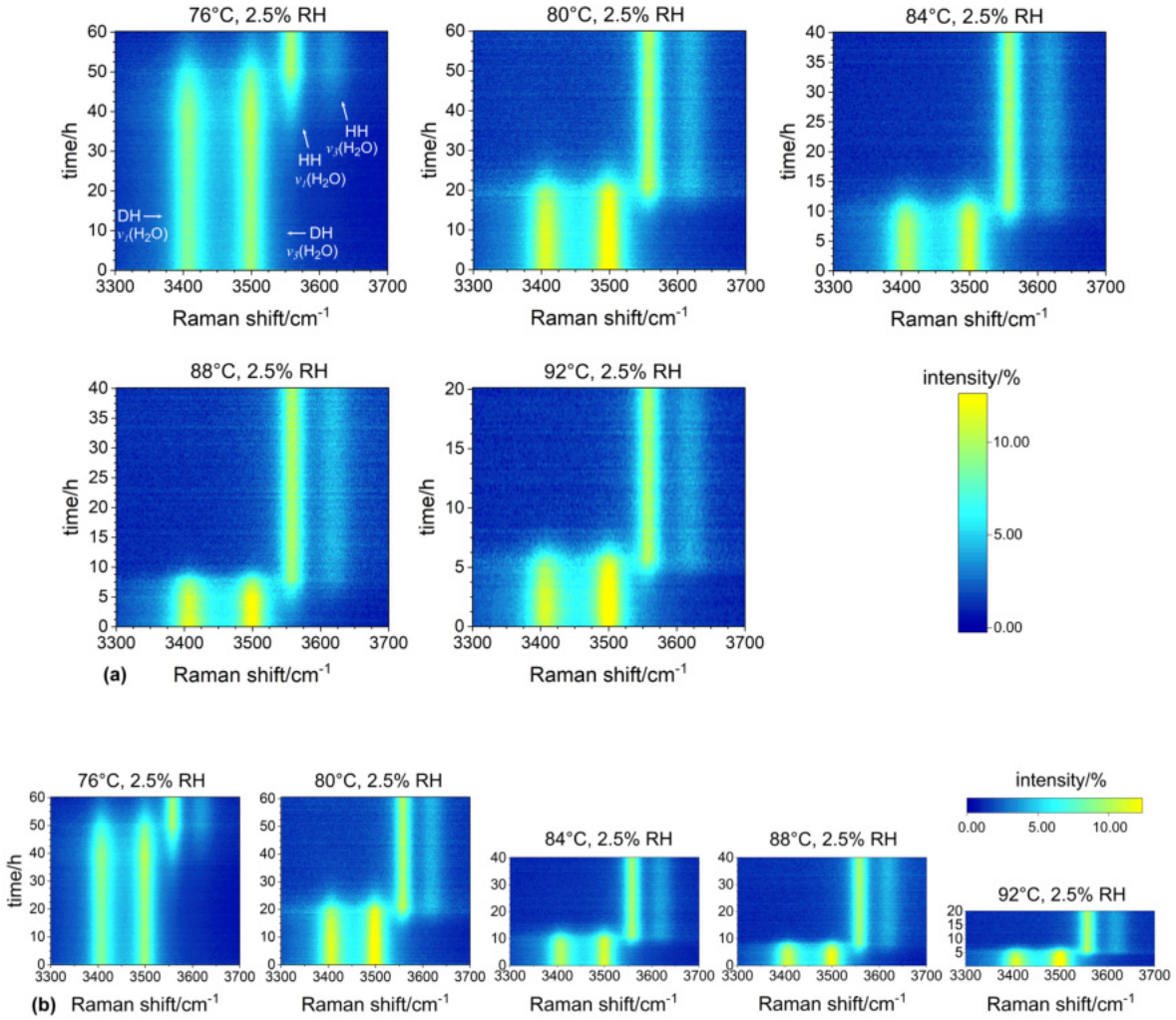


**Figure 6-21:** **(a)** Top views of isothermal and isohumid Raman spectroscopic measurement sequences obtained by gypsum dehydration at 76 °C, 80 °C, 84 °C, 88 °C, 92 °C, and 2.5% relative humidty (RH). The five panels show the spectral ranges between 3300 $cm^{-1}$ - 3700 $cm^{-1}$ to focus on symmetric and asymmetric hydroxyl stretching modes in gypsum (DH) and hemihydrate (HH). **(b)** Representation of measurement sequences with regard to temporal comparability.

Within the examination of the $CaSO_4 - H_2O$ system, Raman spectroscopy is usually applied to follow the evolution of $H_2O$ during dehydration experiments (*e.g.* Chang et al., 1999; Comodi et al., 2012). In kinetic analysis, it is not common to quantify converted fractions using Raman spectroscopy. In general, the technique is more frequently affiliated with molecular structure determination and qualitative aspects of phase analysis than quantitative ones (Pelletier, 2003). However, it has been applied for the quantitative analysis of mixed compounds, most often by authors working in pharmaceutics (*e.g.* Skoulika and Georgiou, 2001; Fini, 2004; Strachan et al., 2007).

To explore the possibility of obtaining kinetic information from sequences of Raman spectra, $\alpha - t$ curves based on measurements shown in Figure 6-21 were calculated according to the method described in Chapter 5-2-2. Essentially, approximate $\alpha$ values were derived by peak integration of the $\nu_1(H_2O)$ and $\nu_3(H_2O)$ modes of gypsum. Peak areas were calculated for all measurements where the modes were recognizably present. The obtained conversion curves are shown in Figure 6-22.

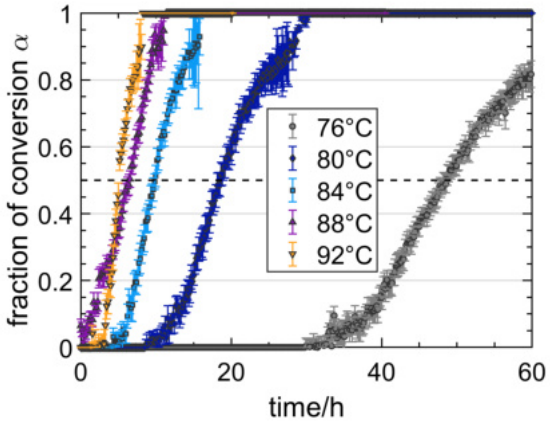


**Figure 6-22:** Isothermal and isohumid gypsum to hemihydrate conversion of the 20 µm - 25 µm fraction at 76 °C - 92 °C and 2.5% relative humidity. $\alpha$ values were calculated from Raman spectra shown in Figure 6-21 as described in Chapter 5-2-2.

The determination of $\alpha$ values at measurement starts and ends with the applied method is problematic. Conversion curves measured at 80 °C, 84 °C, 88 °C and 92 °C exhibit significantly increasing error margins towards the reaction end. A moderate sigmoidal curve shape of measurement series collected at 80 °C and 76 °C is notable. Based on the yielded $\alpha$ values, the dehydration process $\geq$ 88 °C is rapid. 50% hemihydrate formation is achieved after 48.7 h (76 °C), 18.8 h (80 °C), 10.0 h (84 °C), 6.5 h (88 °C), 5.1 h (92 °C), respectively. These values differ from the results obtained by powder XRD measurements, where 50% gypsum dehydration is reached after 8.7 h (84 °C), 1.1 h (88 °C), 1.0 h (92 °C), respectively.

This might indicate that, among all experiment- and technique-related differences, the sample humidity is the most crucial parameter to influence the present gypsum dehydration processes. The Raman spectroscopic measurements were performed at 2.5% RH. The powder XRD measurements at 92 °C and 88 °C had respective mean values of 1.7% RH and 2.1% RH, promoting comparatively swifter dehydration reactions. At 84 °C, the mean relative sample humidity during powder XRD measurements is 2.4% which might explain the comparable 50% conversion times. In contrast, powder XRD results of experiments conducted at 80 °C and 76 °C have mean values $>$ 2.5% RH. They exhibit considerably slower gypsum dehydration than findings yielded by corresponding Raman spectroscopic measurements.

The plausibility and significance of present $\alpha - t$ curves is, however, difficult to classify. Here, it is only regarded as tendency-giving due to the imprecise calculation method of $\alpha$ and the overall appearance of conversion curves. Hence, model-fitting kinetic analysis was not performed. Moreover, the comparative considerations above are stated with caution.

To obtain $E_a$ values, isokinetic analysis based on rate constants $k$ (Table 6-4), as well as differential and integral isoconversional kinetic analysis were performed. The advanced isoconversional method according to Vyazovkin (1997) was excluded, as it was developed to cache temperature deviations while heating dynamically. Model-fitting analysis was conducted using results from powder XRD experiments at 84 °C, 88 °C, 90 °C, and 92 °C. Isoconversional analysis also includes the experiment at 80 °C. It is important to note that such few isothermal experiments render the calculation of activation energies rather uncertain and doubtful.

Figure 6-23 (a) shows the results of isokinetic and Figure 6-23 (b) displays the results of isconversional analysis. From the $\ln k$ vs. $\frac{1}{T}$ plot (Arrhenius plot), yielded $E_a$ values of 777 kJ mol$^{-1}$ and 360 kJ mol$^{-1}$, respectively, are not trustworthy. The linear regression for $k$ values obtained by JMAEK model fits is moreover inapplicable: The coefficients of determination, $R^2$, were calculated to 0.6555 (JMAEK) and 0.8568 (Prout-Tompkins). Here, $R^2$ values give the quality of data prediction from independent variables used for the linear regression. The values can range from 0 (improper) to 1 (perfect). In both cases, it might be possible that $k$ values yielded at 88 °C or 2.769 $\cdot 10^{-3}$ K$^{-1}$ are outliers. If the differences between slopes were accurate, they would indicate model-dependent $E_a$ values. This conclusion, however, is not drawn here since the validity of data is questionable.

The $E_a$ values obtained by isoconversional analysis were calculated for nine different values of $\alpha$. An increment of $\Delta\alpha = 0.1$ was chosen. The two isoconversional methods are eligible to apply if they prove to be independent from $\alpha$. If both methods result in the same $\alpha$-independent $E_a$ values, results are usually regarded as meaningful. In contrast, the variation of $E_a$ values with $\alpha$ points to a change of reaction mechanism.

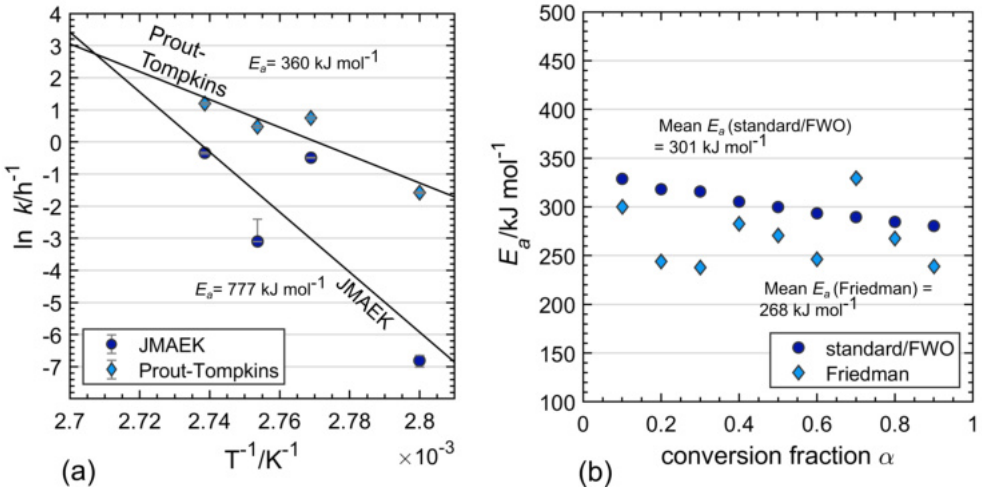


**Figure 6-23: (a)** Arrhenius $\ln k$ versus $\frac{1}{T}$ plot for the gypsum to hemihydrate dehydration. $k$ values are given in Table 6-4. The linear regressions are given by lines and have $R^2$ values of 0.8568 (Prout-Tompkins) and 0.6555 (JMAEK). The $E_a$ values, yielded by the slope of linear fits, are given in the plot. **(b)** $E_a$ values obtained by the standard/Flynn-Wall-Ozawa (FWO) and the Friedman method for respective $\alpha$ values. Error margins could not be determined since interpolation of $t$ and $\frac{d\alpha}{dt}$ at corresponding $\alpha$ values was necessary, resulting in indefinite error progression concerning $E_a$ values.

The $E_a$ values obtained by the standard/Flynn-Wall-Ozawa or integral method reveal a slightly negative trend with increasing $\alpha$ values. The mean value is 301 kJ mol$^{-1}$. Activation energies yielded from the differential or Friedman method scatter relatively broadly around the mean value of 268 kJ mol$^{-1}$. Based on the present values, a change of reaction mechanism could be supposed.

The literature reports a multitude of $E_a$ values for the gypsum → hemihydrate process as mentioned in Table 2-4. In particular, values of 90.3 kJ mol$^{-1}$ (Putnis et al., 1990), 92.25 kJ mol$^{-1}$, (Sarma et al., 1998), 95 kJ mol$^{-1}$ - 392 kJ mol$^{-1}$ (Strydom et al., 1995), 88 kJ mol$^{-1}$ - 137 kJ mol$^{-1}$ (Hudson-Lamb et al., 1996), and 130 kJ mol$^{-1}$ (Heide, 1969) have been reported using various experimental set-ups and analytical methods. Moreover, Ball and Norwood (1969) calculated an $E_a$ value of 246 kJ mol$^{-1}$ at $p_{H_2O} \approx 6$ hPa for the temperature range 80 °C - 88.5 °C. Recalculation of 6 hPa to relative humidities yields 1.3% at 80 °C and 0.9% at 88.5 °C. The $E_a$ value corresponds to a nucleation controlled reaction. Overall, they specified several $E_a$ values dependent on the kinetic model. McAdie (1964) yielded values of 109 kJ mol$^{-1}$ at $p_{H_2O} = 0$ hPa and 201 kJ mol$^{-1}$ at $p_{H_2O} = 133$ hPa (at jacket temperatures of 100 °C - 139 °C). Ballirano and Melis (2009b) determined a value of 109 kJ mol$^{-1}$ at constant cabinet surroundings of 50% RH at 23 °C, which unfortunately leaves the sample humidity unknown.

The present mean $E_a$ values determined by isoconversional methods rank in the upper range of published activation energies. They are somewhat close to the value given by Ball and Norwood (1969) who conducted isothermal and isohumid dehydration experiments. Yet, due to the (moderate) variability with $\alpha$ values, the presence of a single process is questioned and the literature data should not be supplemented by the values at hand.

Overall, several conclusions can be drawn from these and preceding results. Reliable and reproducible kinetic analysis of gypsum dehydration must include accurate humidity control at the sample. To follow the reaction mechanism(s) of gypsum dehydration at moderate temperatures and low $p_{h_2O}$ values, it appears useful to conduct isothermal and isohumid experiments with increments of 1% or 2% RH. For example, experiments with 1% - 5% RH at 85 °C, 90 °C and 95 °C, respectively, could further clarify the influence of very low to low water vapor-pressures on hemihydrate formation. Also, isohumid experiments at different temperatures would solely show the temperature dependence of dehydration reaction. It is regrettable that this was not possible during the present work as sample humidities during powder XRD measurements could not be regulated manually. The regulation of the CHCplus+ chamber humidity was restricted to temperatures ≤ 80 °C and humidities ≥ 5% RH. Hence, the temperature and humidity ranges of interest are by default excluded from regulation. According to the manufacturer, this circumstance cannot be bypassed.

In general, experiments conducted at constant temperatures and humidities are not observable, respectively controllable, during the first few moments of establishing working conditions. This factor averts thorough parameter control at all times. Therefore, it renders systematic studies with constant conditions more complex, even if the technical circumstances were flawless. Concerning $E_a$ values, the use of non-isothermal data obtained at different heating rates is usually preferential as several isoconversional methods are available enabling result crosschecking.

This is, however, not recommendable for the examination of de- and rehydration processes as the $p_{H_2O}$ atmosphere should be controlled. This can not be provided if the sample is dynamically heated. The control of particle sizes is mandatory. Thereby, particle-fractions as uniform as possible are desirable. Particle size-dependent measurements showed that the range should be $\leq 5\,\mu m$. Using grains $\leq 50\,\mu m$ appears to be advisable for kinetic analysis.

These findings can be interpreted with regard to possible gypsum dehydration reactions in the Atacama Desert. Temperatures $\leq 107.5\,°C$ and low $p_{H_2O}$ values do not promote dehydration to $\gamma$-anhydrite, and even less to $\beta$-anhydrite within the course of 20 h and given experimental conditions. Taking the exponential dependency into account, temperature-induced ($\beta$)-anhydrite formation in the Atacama Desert on diurnal time-scales must be rejected. Yet, anhydrite is a main constituent of surface crusts in the Atacama Desert, which motivated long-term dehydration experiments (Section 6-3-8) with focus on $\beta$-anhydrite evolution at moderate temperatures.

Moreover, extrapolation based on $\alpha$ values given in Figure 6-20 to lower temperatures, resembling Atacama Desert soil temperatures, was done. For this, particle sizes $\leq 25\,\mu m$ and persistence of bassanite as stable dehydration product were assumed. Using the time needed for 50% bassanite formation, the projection yields over 5000 h (circa 30 weeks) of constant exposure at 60 °C with $\leq$ 3% RH to dehydrate 50% of gypsum. As described in Chapter 3-2, 60 °C is a rarely reached temperature maximum of Atacama Desert surfaces. The mean soil temperatures are around 20 °C (Table 3-1 and Wierzchos et al. (2011)). However, at this low temperature, gypsum is the thermodynamically stable phase and the occurrence of dehydration reactions should be strongly doubted.

For comparison, times of 50% gypsum dehydration to hemihydrate of dehydration experiments conducted by Ballirano and Melis (2009b) were also extrapolated to 60 °C. The authors did not give information on water vapor-pressures but stated that particle sizes of 2 µm - 10 µm were used. Extrapolating their data to 60 °C yields 533 h of constant heat exposure to gain 50% hemihydrate from gypsum dehydration. Figure 6-24 shows the respective 50% conversion times as measured by this study, Ballirano and Melis (2009b), and Ball and Norwood (1969).

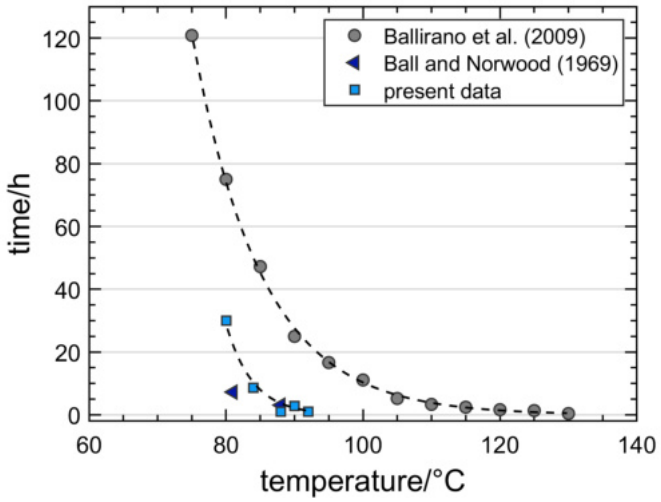


**Figure 6-24:** Plot of sample temperature against the time required for the dehydration of 50% gypsum to hemihydrate. Data are taken from $\alpha - t$ curves given in Figure 6-20, and from Ballirano and Melis (2009b) and Ball and Norwood (1969). The dashed lines indicate an exponential fit to the data.

Compared to the present data, values by Ballirano and Melis (2009b) yield a weaker exponential increase. This is caused by the higher number of experimental runs with 50% conversion times being comparatively closer together. In consequence, this renders shorter dehydration times at lower temperatures. In general, the 50 % conversion times obtained from data by Ballirano and Melis (2009b) range above those obtained in the present study (Figure 6-24). It appears likely that the differences result from values of $p_{H_2O}$ at the sample and the specimen preparation. In contrast to the fine powder layer used here, the authors used compressed powder samples. Sample preparation plays a non-negligible role for dehydration process rates.

Also, the few isothermal measurements conducted during the present work hamper the significance of data extrapolation. It would have been desirable to condense the temperature range of *e.g.* 80 °C - 100 °C but the lack of humidity control stood against that. Testifying claims for gypsum dehydration reactions on Atacama surfaces based on extrapolation of the present *in situ* experimental results appears not to be expedient. Experimental results depend on a variety of influencing parameters which complicates transferability to natural environments. In addition, the assumption of bassanite persisting as stable gypsum dehydration product over time is unlikely.

Yet, some key information can be summarized: Dehydration at temperatures lower than 80 °C is severely slowed down. Abundant gypsum dehydration on seasonal time scales promoted by temperature appears implausible, considering typical soil temperatures of 35 °C - 40 °C that are reached during few hours per day. This is also sustained by the low abundance of bassanite in the Atacama as noted in Section 6-1. If (solely) temperature- and $p_{H_2O}$-dependent gypsum dehydration was a prominent Atacama phenomenon, surfaces should contain larger quantities of bassanite. This discussion is again picked up in Section 6-3-8 and Chapter 7.

### 6-3-4 Hemihydrate rehydration conditions and particle size-dependency

Rehydration processes fostered by high relative humidities, if present, would be expected during humid nights and fog events. In the Atacama, such events are spatially and temporally variable. However, data by Cereceda et al. (2008) suggest maximum fog evolution around 07:10 UTC during summer and winter. Measurements of Atacama temperature conditions (Chapter 3-2) revealed night-time and early morning soil temperatures ranging between 10 °C and 20 °C. Hence, this temperature range is of interest concerning possible bassanite and anhydrite rehydration.

As reviewed in Chapter 2-3-2, ($\beta$)-anhydrite rehydration in slurry solutions is a kinetically hindered process. Therefore, hydration induced by high relative humidities is assumed to play a minor role in natural environments. Hydration of synthetic and natural anhydrite ($\beta$-$CaSO_4$) was attempted in two orientation-giving experiments that are described in Section 6-3-7. Bassanite has been found to be a limited constituent of the Atacama surfaces and soil crust. This points to a subordinate geological significance of the bassanite rehydration process. However, based on the lack of literature concerning solid-state hemihydrate hydration under controlled humidity, temperature and time conditions, the process was investigated and is discussed here and in Section 6-3-5. The study of $\gamma$-anhydrite rehydration is obsolete as the phase becomes unstable below ≈105 °C.

To determine whether hemihydrate hydration could proceed within short time ranges, at low relative humidities, or low temperatures, a first isothermal experiment series was conducted. The sample material was treated at 10 °C, 20 °C, 30 °C, 40 °C, and 50 °C with incrementally increased humidities from 5% to 95%. Each humidity step was kept for 5 minutes with step sizes of 5%. The used hemihydrate samples were obtained by heating gypsum at 90 °C for 1d. The material was subsequently blended with 1% gypsum to facilitate crystal growth. Powder XRD measurements were carried out. As no signs of hemihydrate rehydration could be detected within this short time periods (Figure C-9), isohumid treatment of hemihydrate at maximum relative humidity of 95% and temperatures between 10 °C and 30 °C were perfomed. Hemihydrate hydration showed to be well monitorable at 30 °C.

Figure 6-25 (a) gives the top view and Figure 6-25 (b) a three-dimensional view of the XRD powder pattern sequences obtained at 30 °C and 95% RH. The formation of gypsum can be tracked on the basis of the growing (020) Bragg reflection of gypsum and the vanishing (200)/(110) Bragg reflections of hemihydrate. The hydration is not completed within 45 h as evident by the hemihydrate peaks.

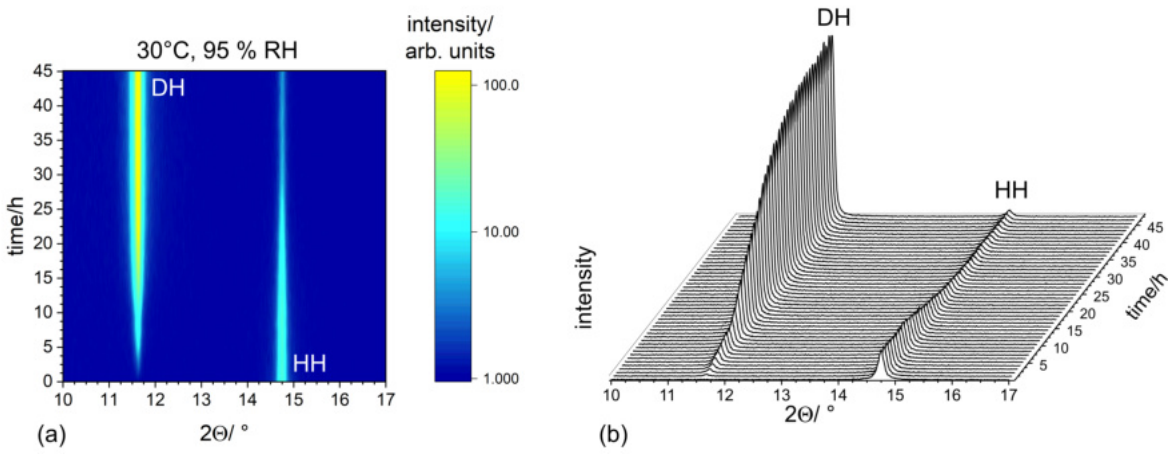


**Figure 6-25: (a)** Top view of an isothermal and isohumid powder XRD measurement series obtained by hemihydrate rehydration at 30 °C and 95% relative humidity. **(b)** Three-dimensional view of the respective powder patterns illustrating gradual gypsum formation from hemihydrate. The 2Θ range from 10° - 17° is displayed to follow the evolution of the (020) peak of dihydrate (DH) and the (200)/(110) peak of hemihydrate (HH) over time.

Similar to the first gypsum dehydration experiments described in Section 6-3-2, particle sizes were restricted to ≤ 50 µm in a first step. With such prepared samples, hydration measurements of hemihydrate were performed for 20 h at 10 °C, 20 °C and 30 °C and 95% RH. In a second step, particle fractions of ≤ 20 µm, 20 µm - 25 µm, 25 µm - 32 µm and 32 µm - 50 µm were sieved and measured at 30 °C with 95% RH.

During experiments conducted at 10 °C, 20 °C, and 30 °C with 95% relative humidity, nearly complete hemihydrate to gypsum conversion was observed after almost 13 h at 10 °C, 4.5 h at 20 °C, and circa 55 min at 30 °C (Figure C-10) as stated in Ritterbach and Becker (2020). In hindsight, this statement must be regarded with great caution as these measurements were affected by moderately to strongly increased background that evolved at a seemingly random point during measurements. After the publishing, it was found out that the enhanced underground was not a sign of amorphous phase formation but caused by liquid water droplets. The high relative humidity of 95% caused condensation on the permanently installed knife edge due to a dew point underrun. This led to the formation of water droplets that fell onto the sample material. To avoid underruns, the chamber housing was heated several degrees above the respective dew points. Apparently, heating the knife edge sufficiently was not achievable. This enabled the formation of liquid water. It is likely that water formation due to constant high humidity in the CHCplus+ chamber caused consecutive sensor damage, leading to incorrect humidity controlling during some measurements (Chapter 6-3-6). Subsequently, the sensor was replaced and the humidity values for further hydration experiments were kept within a maximum limit of 93.5 %.

In the following, hemihydrate rehydration measurements at 30 °C and 95% RH without increased background were selected for particle size-dependent analysis. The hemihydrate samples were heated at 90 °C for 20 h inside the CHCplus+ chamber. The dependencies of converted gypsum fractions on time as results of grain sizes are displayed in Figure 6-26.

The conversion curves of fractions 25 µm - 32 µm and 32 µm - 50 µm fractions exhibit an altered deceleratory curve shape between $\alpha$ values of 0.8 to 1. These results might be superimposed by the existance of small quantities of liquid water. Yet, it becomes obvious how the conversion fractions depend on grain sizes in a reverse manner compared to particle size-dependent gypsum dehydration results. Here, large particles rehydrate considerably faster than smaller particles.

For particles between 32 µm - 50 µm, 50% conversion is reached after approximately 20 min. The conversion of particle sizes 25 µm - 32 µm and 20 µm - 25 µm takes roughly 60 min and 70 min, respectively (inset in Figure 6-26). Grain size fractions of 25 µm - 32 µm and 32 µm - 50 µm completely rehydrate to gypsum, whereas particles $\leq$ 25 µm do not exhibit finalized rehydration. Particles $\leq$ 20 µm rehydrate only to the extent of 37% within 20 h and particles from 20 µm - 25 µm reach around 65% reaction completeness.

Refraining from interpreting conversion curves of the two larger grain size fractions, due to possible measurement impairments, rehydration of hemihydrate appears to be rate-controlled by other processes at given temperature and humidity conditions than gypsum to hemihydrate dehydration above 84 °C. This is discussed later.

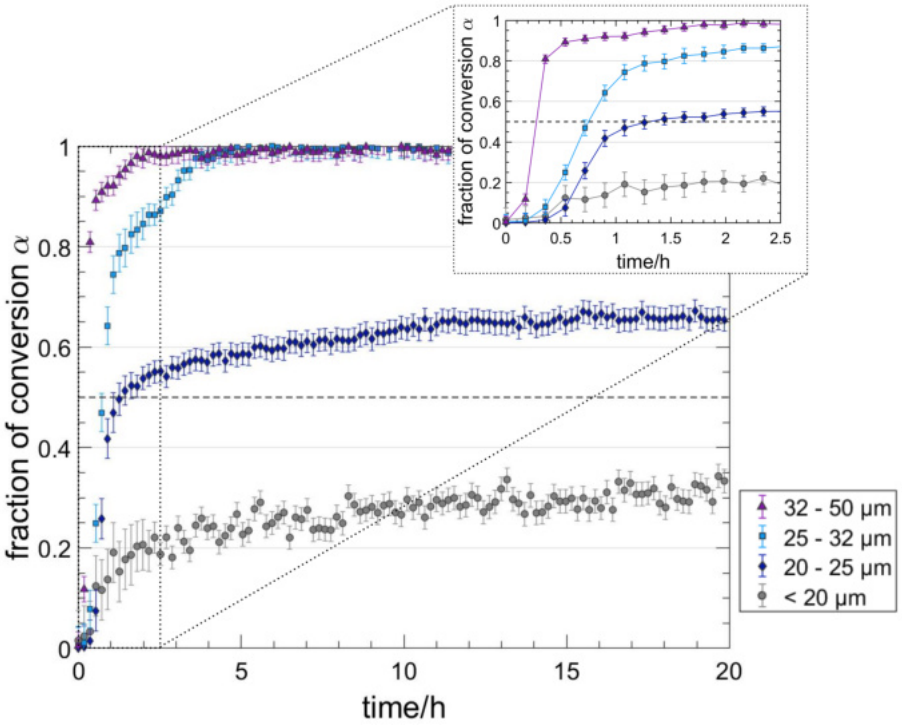


**Figure 6-26:** Particle size-dependent hemihydrate to gypsum conversion in the form of $\alpha - t$ curves measured at 30 °C and 95% RH, calculated from quantitative phase analysis of powder XRD measurements. The hemihydrate samples were obtained by dehydrating gypsum in the sample chamber at 90 °C for 20 h. The inset gives a magnification of the initial time interval up to 2.5 h. Lines between the markers are a guide to eye and do not represent data fits.

The fast rehydration of larger particles and the slow dehydration of smaller particles is a somewhat surprising result. Smaller particles offer a larger surface area per volume and, therefore, an augmented reaction front for gypsum crystallization to take place and proceed. It is conceivable that larger particles could still contain remnants of gypsum (of quantities below the detection limit of powder XRD), that act as seeds for gypsum crystallization. Hence, particle size-dependence might be superposed by effects of nuclei growth processes of remaining dihydrate quantities. Particle size-dependent measurements of hemihydrate rehydration were not repeated. To keep consistency with the dehydration measurements, following rehydration measurements were conducted with the particle fraction of 20 µm - 25 µm.

### 6-3-5 Hemihydrate rehydration at 15 °C - 40 °C and 86 % - 93.5 % RH

Before each powder XRD experiment, gypsum particles were heated for 1 h at 120 °C inside the CHCplus+ chamber to $\gamma$-anhydrite. Due to the instability of $\gamma$-anhydrite $\leq$ 105 °C, the samples readily rehydrated to hemihydrate at room temperature. By this, the probability of remaining gypsum quantities in the hemihydrate sample was lowered before starting the rehydration experiments.

Isohumid and isothermal powder XRD experiments were conducted at temperatures from 15 °C - 40 °C and constant relative humidity of 91%, and at relative humidities from 86% - 93.5% and a constant temperature of 30 °C. The conversion fractions are given in Figure 6-27. Experiments were conducted for 120 h each. For hemihydrate rehydration at 35 °C and 91% RH, measuring time was extended to 180 h. The corresponding $\alpha - t$ plot is shown in Figure 6-29.

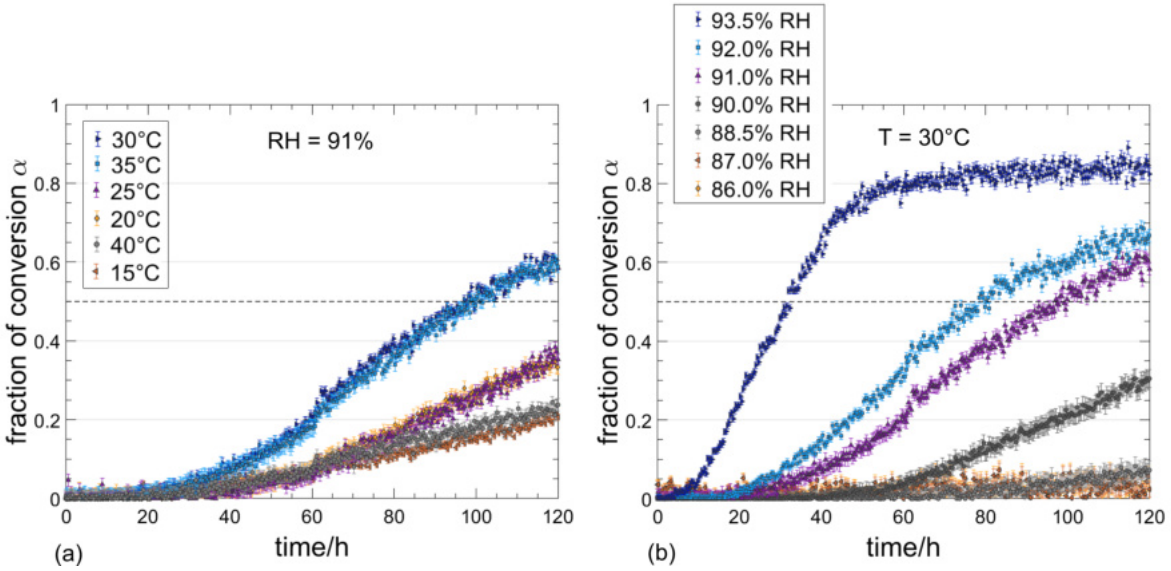


**Figure 6-27:** $\alpha - t$ curves of **(a)** temperature- and **(b)** humidity-dependent rehydration of hemihydrate to gypsum with particle sizes 20 µm - 25 µm. $\alpha$ values are calculated from quantitative phase analysis of isothermal powder XRD measurements. The hemihydrate samples were obtained by dehydrating gypsum in the sample chamber at 120 °C for 1 h.

Regarding experiments at a constant relative humidity of 91%, a temperature dependence becomes evident with increasing reaction pace up to ≈ 30 °C. At 35 °C and 40 °C, rehydration slows down whereby a drastic decrease of the reaction speed at 40 °C is apparent. The final converted gypsum fractions are given in Figure 6-28 for better overview.

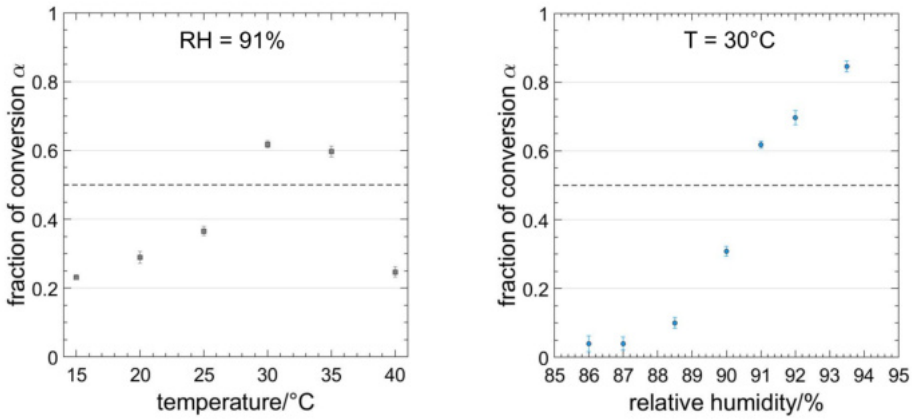


**Figure 6-28:** Converted gypsum fractions ($\alpha$ values) yielded after 120 h of constant treatment at 15 °C - 40 °C and 91% RH, and 86% - 93.5% RH and 30 °C, respectively. The $\alpha$ values correspond to the data shown in Figure 6-27.

It appears that hemihydrate hydration approximately shows an exponential temperature dependence for temperatures up to 30 °C. For higher temperatures up to 40 °C, hydration still proceeds but is strongly slowed down compared to 30 °C or 35 °C. In several studies, temperatures around 40 °C are associated with the gypsum–anhydrite equilibrium. Hence, the temperature regime where anhydrite is the stable phase, is reached. However, the high relative humidity works against temperature and induces gypsum formation. Similar observations were made by Sievert et al. (2005), who studied the rehydration process of $\beta$-anhydrite in aqueous and salt solutions.

The experiments at a constant temperature of 30 °C reveal a strong dependence of gypsum formation on the applied humidities. Hydration at relative humidities $< 90\%$ is very slow, so that $\leq 10\%$ gypsum is formed after 120 h. At humidities $\geq 90\%$, the reaction accelerates considerably. At the highest value of 93.5%, around 85% hemihydrate to gypsum conversion is yielded (Figure 6-28, right panel). Compared to the applied temperature range of 15 °C - 40 °C for experiments at constant humidity, the humidity range of 86% - 93.5% RH at constant temperature is rather narrow but appears to have a more pronounced influence on hemihydrate hydration behavior.

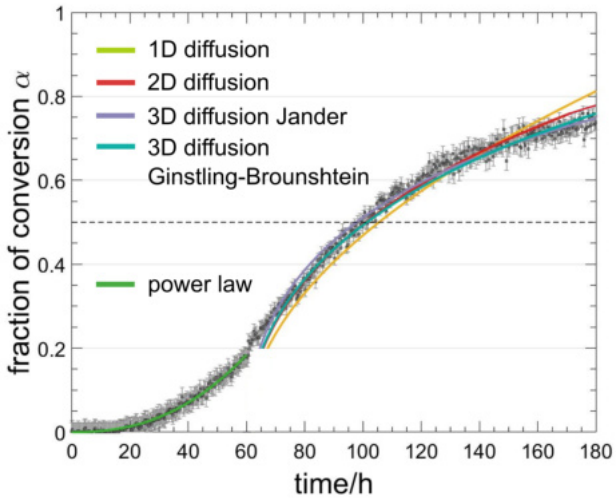


**Figure 6-29:** $\alpha - t$ curve of hemihydrate to gypsum hydration obtained by powder XRD measurements at 35 °C and 91% RH. The lines represent fits to the data according to the kinetic reaction models given in Table 6-5.

The shapes of $\alpha - t$ curves given in Figures 6-27 and 6-29 appear disparate and depend on the applied temperature and humidity regimes. Lower temperatures ($< 30$ °C/91% RH, Figure 6-27 (a)) and lower humidity values ($< 91\%$ RH/30 °C, Figure 6-27 (b)) cause closely linear conversion vs. time dependencies. The hydration reactions are comparably slow. The $\alpha - t$ curves of experiments conducted at 30 °C/91% RH, 35 °C/91% RH (Figures 6-27 (a) and 6-29), and 30 °C/92% RH (Figure 6-27 (b)) are similar to each other. They exhibit a flattened S-shape. The decelerating part of the curves might be characterized by different reaction rates than the accelerating parts.

The fraction of conversion curve obtained by hemihydrate rehydration at 30 °C/93.5% RH (Figure 6-27 (b)) differs notably from the latter described curves. It seemingly lacks an accelerating part as the conversion starts rapidly after 2.3 h. The reaction proceeds nearly linear up to 55 h when approximately 80% gypsum has formed. This is followed by a hydration rate drop. Subsequently, the reaction proceeds very slowly. Omitting the temporal differences, this distinct reaction rate decrease coincides with the data yielded by particle size-dependent experiments at 30 °C/95% RH of fractions $< 20\,\mu m$ and $20\,\mu m$ - $25\,\mu m$.

Based on these observations, choosing an appropriate reaction models is difficult. None of the standard reaction models reviewed in Chapter 4-1 appear to be a suitable choice for the conversion curves of interest ($\geq$ 50% conversion). It is uncertain whether one or multiple rate-controlling steps are involved. The conversion curve obtained by hemihydrate hydration at 35 °C/91% RH (Figure 6-29) was selected for exemplary model-fitting approaches. None of the kinetic models could be fitted over the whole temporal range. Consecutively, the accelerating part of the $\alpha - t$ curve was fitted with the power law. This usually suffices the description of many experimental $\alpha - t$ curves at the reaction start. The decelerating part of the curve was fitted to all eligible reaction models, *i.e.* geometric, reaction order, and diffusion models. Solely the diffusion models yielded roughly acceptable fits. The respective fits are given in Figure 6-29. The values of rate constants $k$ and power law exponent $n$ are given in Table 6-5.

**Table 6-5:** Rate constants $k$ and parameter $n$ yielded by fits of power ($g(\alpha) = \alpha^{1/n} = kt$) and diffusion laws ($g(\alpha) = \alpha^2 = kt$ (1D), $g(\alpha) = (1-\alpha)\ln(1-\alpha) + \alpha = kt$ (2D), $g(\alpha) = (1-(1-\alpha)^{1/3})^2 = kt$ (3D Jander), $g(\alpha) = 1 - \frac{2}{3}\alpha - (1-\alpha)^{2/3} = kt$ (3D Ginstling-Brounshtein) to selective parts of the $\alpha - t$ curves of hemihydrate rehydration at 35 °C and 91% RH given in Figure 6-29. SSE is the summed square of residuals.

| | $k$ | $n$ | **SSE** |
|---|---|---|---|
| power law | 0.0081(2) | 2.36(6) | 0.005946 |
| 1D diffusion | 0.0054(2) | | 0.6187 |
| 2D diffusion | 0.00375[1] | | |
| 3D diffusion Jander | 0.001(1) | | 0.1706 |
| 3D diffusion Ginstling-Brounshtein | 0.00089[1] | | |

[1] not uniquely solvable for $\alpha$. $k$ was tested iteratively.

The three-dimensional diffusion models according to Jander (1927) and Ginstling and Brounshtein (1950) appear to yield the most suitable fit. The kinetic model after Ginstling and Brounshtein (1950) is not uniquely solvable for $\alpha$. Here, $k$ was assessed by iterative fitting.

Both models are, *inter alia*, applied to describe the hydration kinetics of portland cement particles (Shi et al., 2003). In this context, Provis (2016) discussed the frequent preference of the Jander model over the Ginstling-Brounshtein model. They argue that, due to the erroneous of the Jander model, it was preferable to instead use the Ginstling-Brounshtein equation for experimental data fitting. Since the Jander model uses an approximation which neglects the curvature of particle surfaces, it is only correct for very small $\alpha$ values (Provis, 2016). Hence, it is concluded here, that the choice of the Ginstling-Brounshtein model is preferable over the Jander equation as makes is physically sound assumptions.

Ridge (1964) and Schiller (1962) have given thought to the topic of kinetic model fitting specifically for the hydration of hemihydrate. Both conducted experiments that either isothermally or adiabatically followed the setting behavior of hemihydrate in concentrated aqueous suspensions (Chapter 2-3-2). During earlier isothermal experiments at 0 °C - 50 °C, Ridge (1959) found the temperature to exert a comparatively small effect on the hemihydrate hydration rate with a feeble maximum at 25 °C. The observation of a comparatively weak influence of temperature (in relation to relative humidity) was also described here. However, the present data suggest a maximum is around 30 °C. Comel et al. (1979) found the maximum rate to occur at 35 °C during hemihydrate hydration in slurries. These temperature values render the range of 25 °C - 35 °C as most likely to exhibit maximum gypsum formation rates independent from the hydration medium (aqueous solution vs. air humidity).

In following experiments, Ridge and Surkevicius (1962) described the kinetics of hemihydrate rehydration as strongly self-accelerating and calculated activation energies of 17 kJ mol$^{-1}$. Schiller (1962) proposed a kinetic model that describes the reaction in terms of one parameter. It depends on the slurry density, effective nuclei and growth rate of gypsum, solubility differences of gypsum and hemihydrate, and the shape of newly formed gypsum crystals. Ridge (1964) also suggested a kinetic reaction model which most dominantly considers the rate of gypsum growth depending on the dissolution rate of calcium sulfate. The hydration rate is therefore linked to the surface/mass ratio of hemihydrate particles of two thirds. The reaction models are visualized for $k = 0.001$ in Figure 6-30. Equations 6-2 (Ridge) and 6-3 (Schiller) give the respective model expressions.

$$g(\alpha) = \frac{1}{2}\ln(1-(1-\alpha)^{\frac{1}{3}})^2 - \frac{1}{2}\ln(1+(1+\alpha)^{\frac{1}{3}}+(1-\alpha)^{\frac{2}{3}} - \sqrt{3}\arctan\frac{((1-\alpha)^{\frac{1}{3}}+1)}{\sqrt{3}} - C = kt \tag{6-2}$$

$$g(\alpha) = \alpha^{\frac{1}{3}} + 1 - (1-\alpha)^{\frac{1}{3}} = kt \tag{6-3}$$

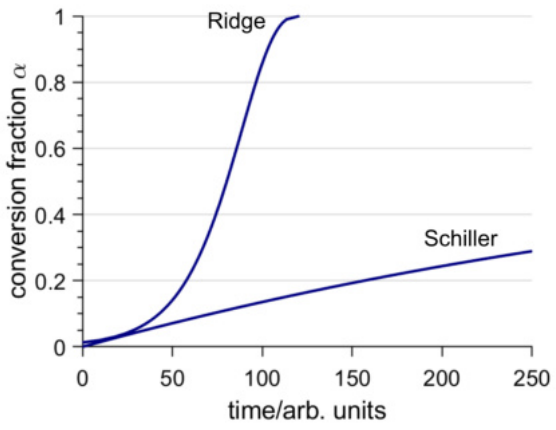


**Figure 6-30:** Visualization of the kinetic models according to Schiller (1962) and Ridge (1964) for $k$ = 0.001 arb. time units$^{-1}$ and $C$ = –15.

The models could not be fitted to the present data. This is comprehensible since both authors developed the models for hydration in slurries and not for hydration promoted by water vapor-pressure. It is conceivable that the hydration reactions differ depending on the surrounding medium.

Overall, it is difficult to deduce valuable information about the underlying mechanisms of hemihydrate hydration at 35 °C and 91% RH with the approach of (standard) kinetic model fitting. The curve can be sufficiently well described with a combination of power law and three-dimensional diffusion. Concerning the presented hydration experiments, it has become clear that the influence of relative sample humidity is more decisive concerning completeness of conversion within a certain time frame than the temperature regime. More experiments at relative humidities above 91% and temperatures between 0 °C and 40 °C would help to corroborate this finding.

To further study the influence of temperature, it would be helpful to condense data especially regarding a hydration maximum at temperatures between 30 °C and 35 °C. Also, the application of temperatures > 40 °C would be of interest. As this is close to the minimum value of the experimentally determined gypsum–anhydrite equilibrium in $H_2O$, it is plausible that gypsum formation at higher temperatures does not proceed and hemihydrate stays the (meta-)stable phase. Experiments of this type would require longer time periods since $p_{H_2O}$-induced gypsum formation has shown to be time-consuming. However, the absence of gypsum formation from hemihydrate within a certain time could not prove the inability of hemihydrate rehydration at higher temperatures. Yet, enlarged time scales without gypsum formation could strengthen the assumption.

The low conversion fractions of temperature-dependent rehydration experiments at 91% RH do not allow for a calculation of activation energies according to the Arrhenius equation based on isoconversional analysis for a broader range of $\alpha$ values. Based on the measurement times corresponding to 20% gypsum formation, the activation energy is 31 kJ mol$^{-1}$ (15 °C - 30 °C, standard method). This is considerably lower than reported values for gypsum–hemihydrate dehydration and ranks in the same magnitude as the value given by Ridge and Surkevicius (1962). Tekkouk et al. (2012) yielded a similar activation energy of 30 kJ mol$^{-1}$ for hemihydrate setting based on isothermal calorimetry experiments under microwave irradiation. However, the shapes of $\alpha - t$ curves indicate temperature and water vapor-pressure regime-dependent reaction mechanisms.

To further study the effect of $p_{H_2O}$ on hemihydrate rehydration, expansion of relative humidities to values close to water-vapor saturation would preferably be of interest. Data condensation between 86% - 93.5% RH at a constant temperature of 30 °C is negligible as the here applied humidity steps are very narrow.

If one would understand the hemihydrate–gypsum rehydration as a system of coordinates with the axes temperature, time and humidity, each point had a specific $\alpha$ value representing the transformed gypsum. The present data depict two specific profiles that are shown in Figure 6-31. By conducting multiple isohumid and isothermal experiments, sequences of profiles would be obtained which together span the "vector space" of temperature, humidity, and time.

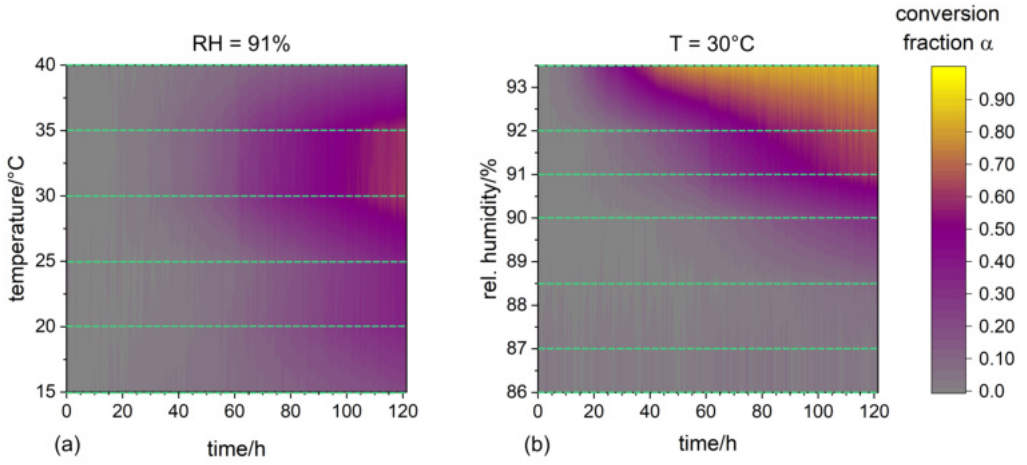


**Figure 6-31:** Interpolated $\alpha$ values over **(a)** time and temperature at a constant relative humidity of 91%, and over **(b)** time and humidity at a constant temperature of 30 °C obtained by isothermal and isohumid hemihydrate rehydration. The green lines indicate the measured powder XRD data on which the interpolation is based on.

To complement the powder XRD experiments, corresponding Raman spectroscopy experiments have been conducted with focus on the evolution of $H_2O$ modes during the hydration process. The gypsum samples were heated to 120 °C for 1 h prior to the hemihydrate rehydration experiments in the THMS 600 sample stage, equivalent to the sample treatment for powder XRD. Here, only humidity dependent experiments from 86% - 93.5% RH at a constant temperature of 22 °C were conducted. Higher temperatures, for example $\geq$ 30 °C, posed a problem due to the possibility of dew point underruns. With the used experimental set-up, the relative humidity is regulated externally and heating of sample stage housing is not possible. The housing temperature was therefore expected to be 22 °C according to the surrounding room temperature. According to Equation 5-5, the threshold dew point of 22 °C for a relative humidity of, *e.g.*, 91% requires sample temperatures $\leq$ 23.5 °C.

Figures 6-32, 6-33, and 6-34 show the top views of Raman spectra measurement series obtained at respective relative humidities and 22 °C. It seems to be inherent in all experiments that a very weak $\nu_1(H_2O)$ mode of gypsum is present during the first measurement of every run (right panels). Perhaps, this points to the abundance of gypsum traces at the outer grain surface caused by the high relative humidities that experiments were conducted at. Depending on the working humidity, the traces either remain unaltered or foster consecutive growth of gypsum.

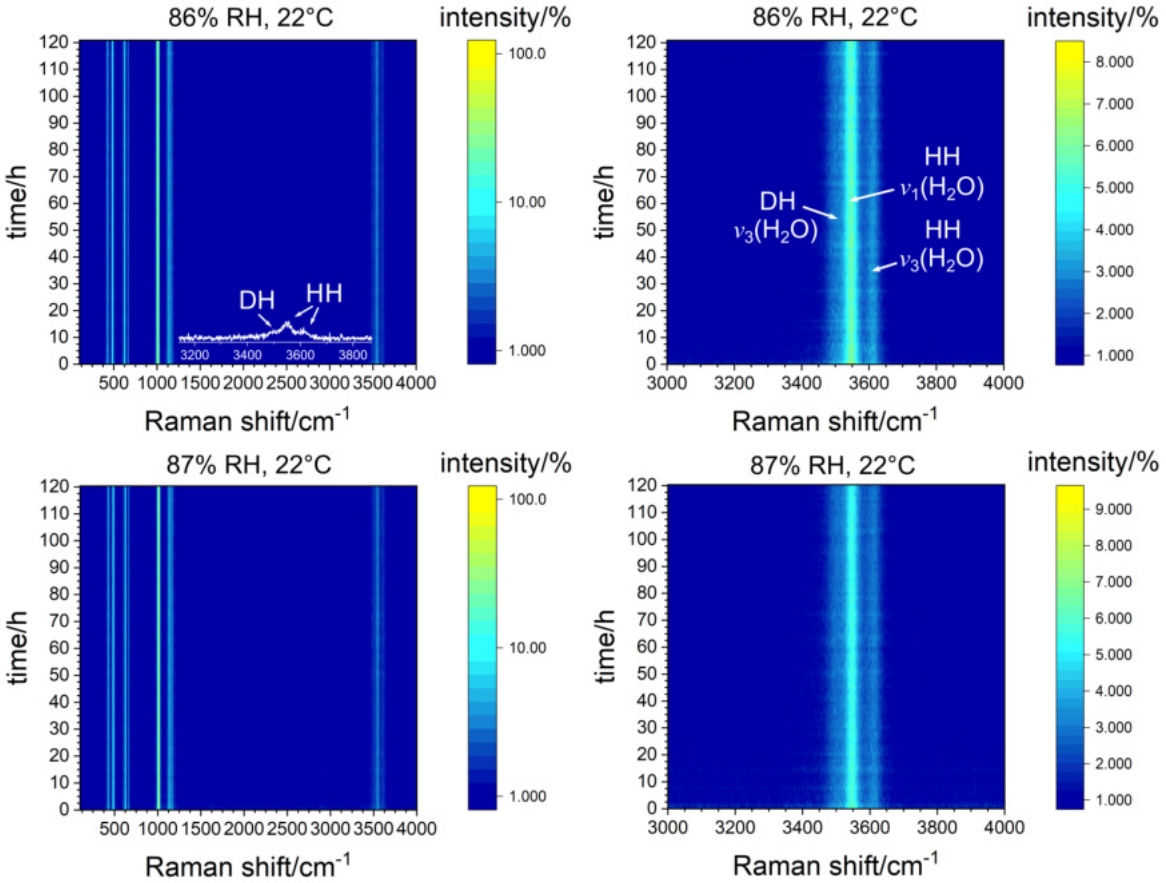


**Figure 6-32:** Top view of isothermal and isohumid sequences of Raman spectra obtained during hemihydrate hydration experiments. The sample temperature was constantly held at 22 °C. The relative humidities were 86% and 87%. The left panels give the whole spectral range of 400 $cm^{-1}$ - 4000 $cm^{-1}$ and the right panels show a magnification of the $H_2O$ modes. Additionally, the inset (upper left panel)) illustrates the $H_2O$ modes of the first spectrum taken after establishment of isohumid and isothermal conditions. In the upper right panel, water modes of gypsum (DH) and hemihydrate (HH) are labeled for better overview.

At 86% RH and 87% RH, water modes of hemihydrate are unchanged after 120 h (Figure 6-32, right panels). At 88.5% RH, two distinct water modes of gypsum are evident after 90 h of experiment time (Figure 6-33, upper right panel). The conversion is, however, not finalized as water modes of hemihydrate prevail until the end of the measurement. A similar behavior is observed for the experiment at 90% RH (Figure 6-33, middle right panel). At 91% RH, strong intensities of gypsum water modes have evolved after $\approx$ 60 h. Only weak hemihydrate modes are identifiable by the end of the experiment (Figure 6-33, lower right panel).

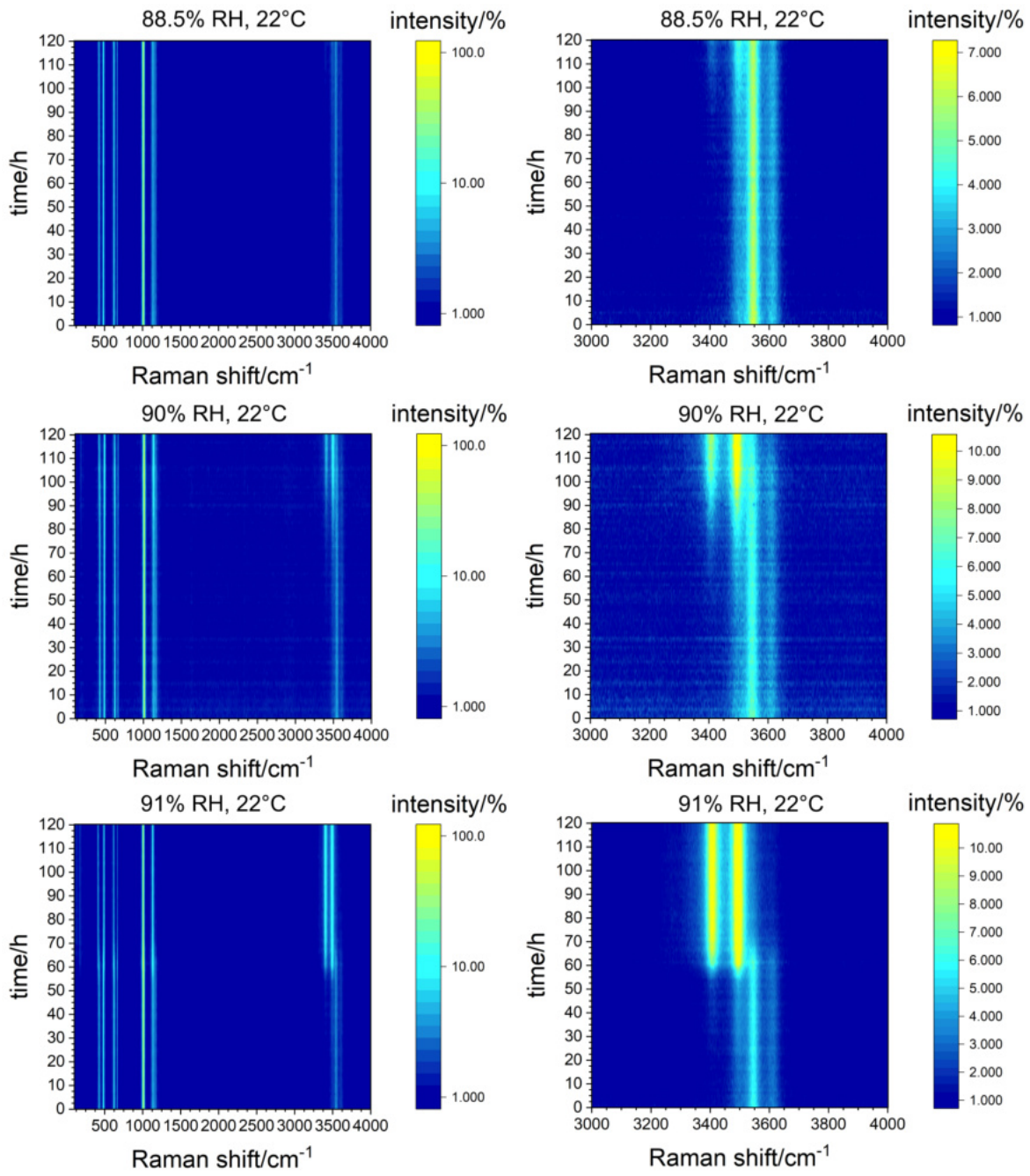


**Figure 6-33:** Top view of isothermal and isohumid sequences of Raman spectra obtained during hemihydrate hydration experiments. The sample temperature was constantly held at 22 °C. The relative humidities were 88.5%, 90%, and 91%. The left panels give the whole spectral range of 400 $cm^{-1}$ - 4000 $cm^{-1}$ and the right panels show a magnification of the $H_2O$ modes.

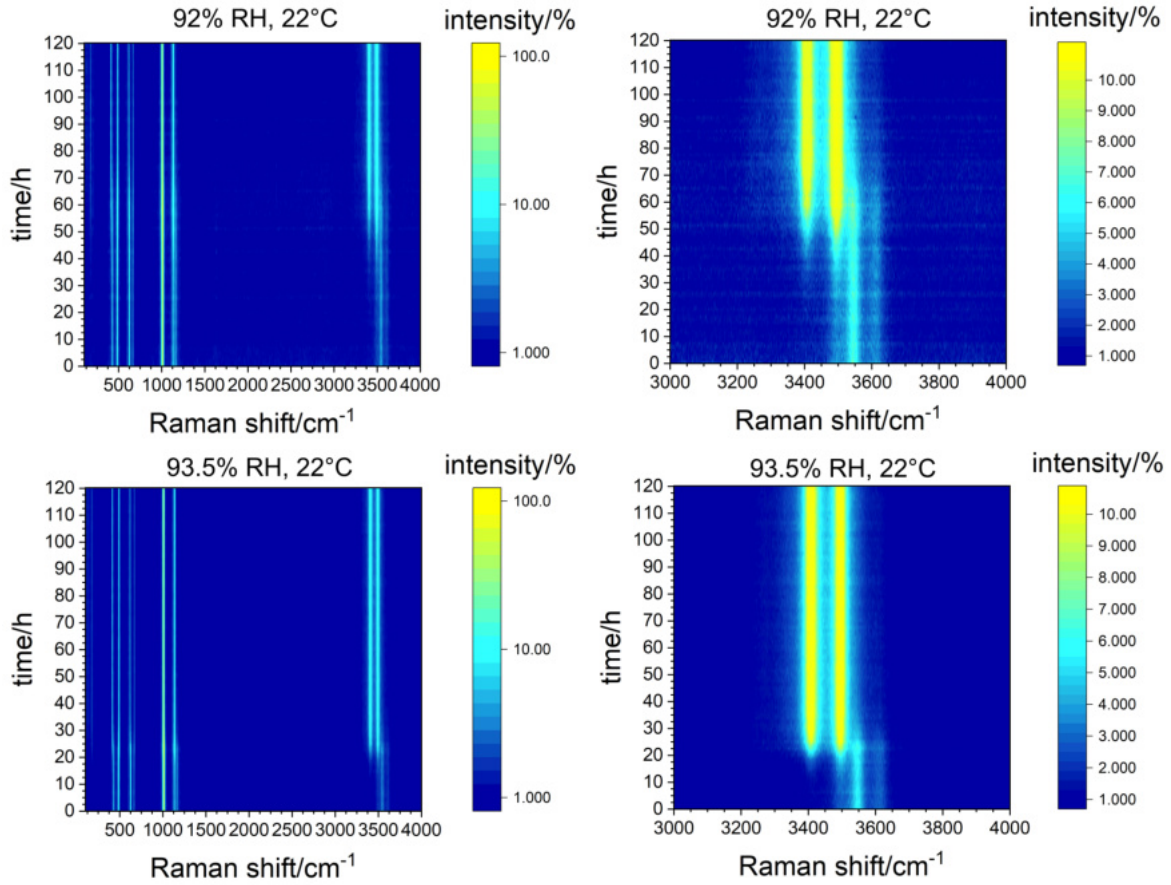


**Figure 6-34:** Top view of isothermal and isohumid sequences of Raman spectra obtained during hemihydrate hydration experiments. The sample temperature was constantly held at 22 °C. The relative humidities were 92% and 93.5%. The left panels give the whole spectral range of 400 $cm^{-1}$ - 4000 $cm^{-1}$ and the right panels show a magnification of the $H_2O$ modes.

For experiments performed at 92% RH and 93.5% RH, high intensity gypsum modes emerge after ≈ 50 h and ≈ 25 h, respectively (Figure 6-34, right panels). In both cases, very feeble remnants of the $\nu_1(H_2O)$ mode of hemihydrate are observable after 120 h.

The present data corroborates the overall trend of RH values constituting a strong influence on hemihydrate hydration that was found by powder XRD experiments. The gradual gypsum growth and hemihydrate decomposition can be very well followed on the basis of increasing, respectively decreasing characteristic $H_2O$ modes of the two compounds.

Despite the observed minor occurrences of bassanite in Atacama surfaces and subsurfaces, the question arises whether temperature and humidity conditions would geologically allow for gypsum formation from available bassanite surface contents. It has been shown that the temperature regime of 15 °C - 20 °C produces roughly 20% gypsum after a treatment of 91% RH for 120 h (particle sizes 20 µm - 25 µm). Likely, the gypsum percentage would be higher at higher relative humidity values, as the present *in situ* Raman spectroscopic and powder XRD experiments suggest.

Exposure time plays a crucial role for the hydration process but this concerns only the hydration of pure hemihydrate. The presence of a gypsum and bassanite phase mixture exposed on Atacama surfaces during a night with relative humidities close to 100% would possibly facilitate the formation of gypsum from bassanite within fewer hours. To understand the morphological differences between rehydrated calcium sulfate in aqueous solutions and by exposure to relative humidities, SEM analysis has been carried out.

Figure 6-35 shows the untreated gypsum powder (a and b) and the same powder after treatment at 120 °C for 1 h (c and d). Figure 6-36 a and b displays the material after rehydration with liquid water for 12 h at 35 °C. In contrast, Figure 6-36 c and d shows the morphology of powder grains after hemihydrate rehydration at 30 °C and 93.5% relative humidity for 120 h. The sample was rehydrated inside the CHCplus+ chamber as described above. The total gypsum content of this sample was 85% (Figure 6-28). The starting material for both rehydration paths was the hemihydrate powder shown in Figure 6-35 c and d. This powder exhibits flakiness which is a typical characteristic of the $\beta$-modification according to Singh and Middendorf (2007).

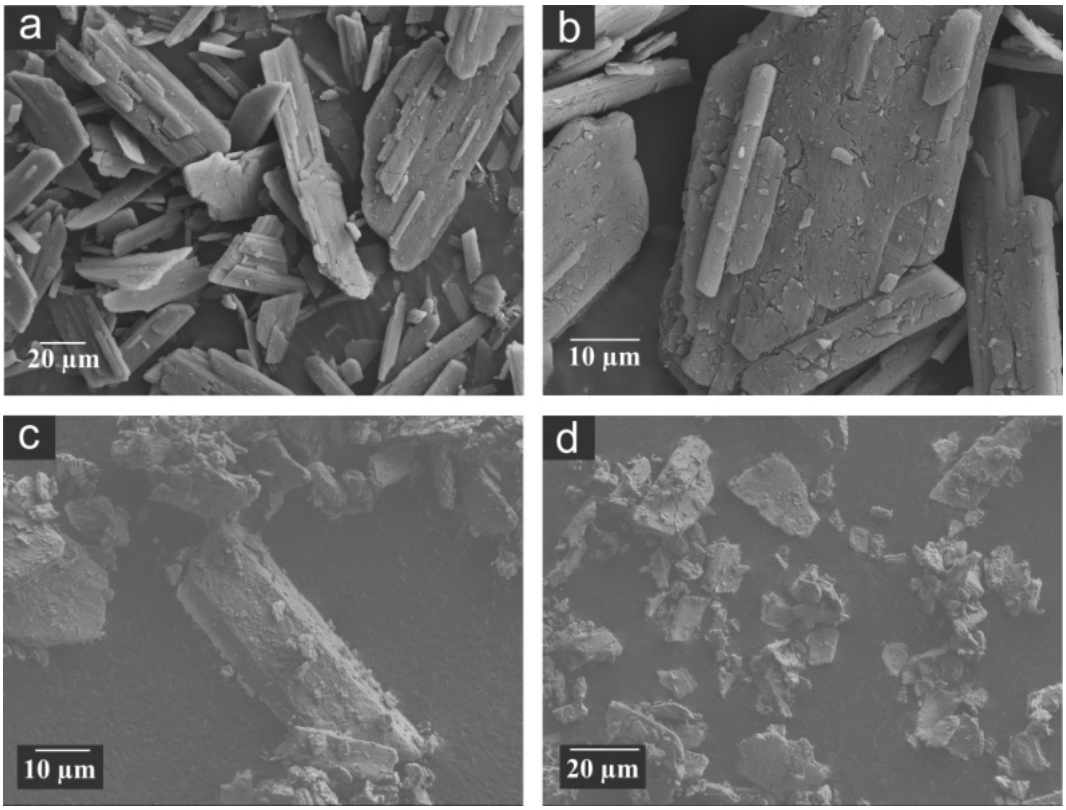


**Figure 6-35:** SEM images of untreated gypsum powder (a and b) and hemihydrate powder obtained by heating gypsum to 120 °C for 1 h (c and d).

The gypsum crystals obtained by hydration in suspension (Figure 6-36 a and b) are needle-shaped or platy and have a high degree of interlocking. This is usually the case for gypsum obtained by treating hemihydrate with liquid water (setting process, Lanzón and García-Ruiz, 2012). Contradicting, the grains in Figure 6-36 c and d appear brittle or even porous.

The surfaces exhibit smaller and larger cracks and the crystal edges lack sharpness. Crystallite interlocking is not evident. The grains were loosely distributed on the sample holder, similar to the prepared hemihydrate sample powder used as starting material. Moreover, it appears that the initial grain form of hemihydrate is still recognizable. The gypsum crystallites shown in Figure 6-36 a and b were were yielded by hemihydrate dissolution and reprecipitation of gypsum, whereas Figure 6-36 c and d shows gradual gypsum formation from hemihydrate hydration induced by relative humidities. Hence, the different crystal morphologies yielded by treatment in aqueous suspension and at high $p_{H_2O}$ values become clear.

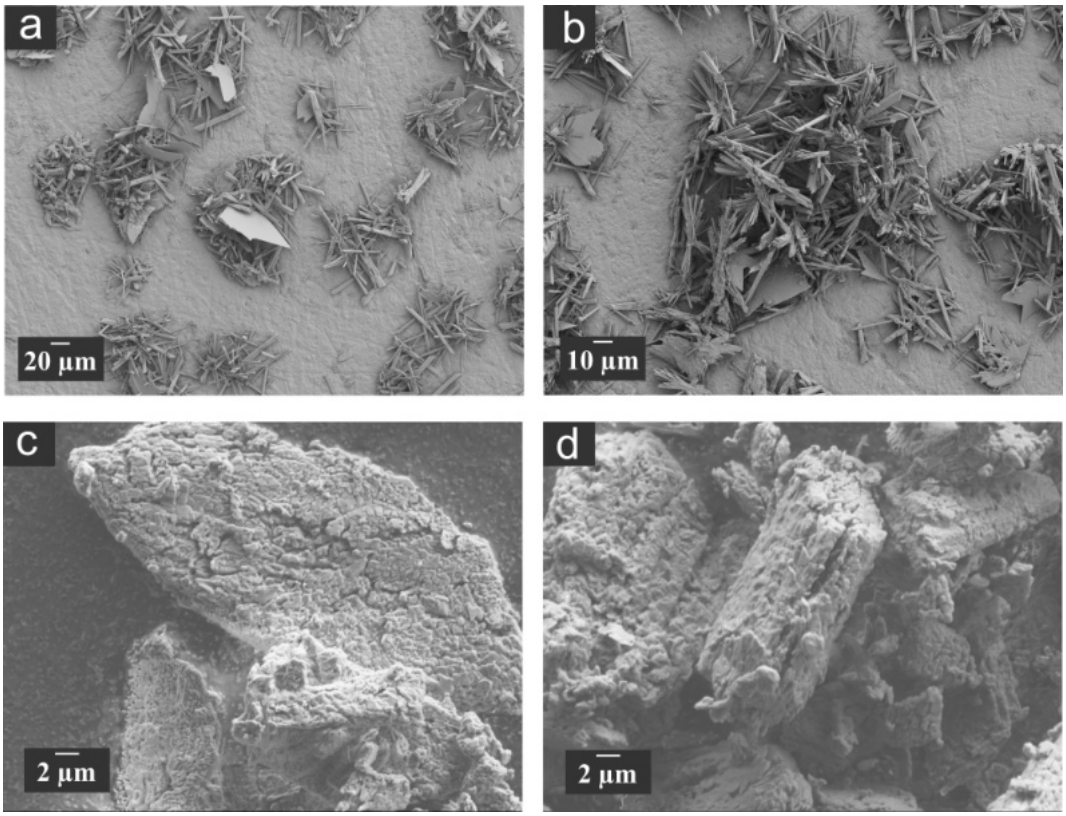


**Figure 6-36:** SEM images of de- and subsequently rehydrated sample material in aqueous suspension (**a** and **b**) and at 30 °C/93.5% RH for 120 h (**c** and **d**). The gypsum crystals shown in panels **a** and **b** were precipitated on a silicon platelet. The starting material for both rehydration processes was hemihydrate powder obtained by heating gypsum at 120 °C for 1 h.

Referring to the Atacama and the term 'gypsum *crust*', these findings indicate that bassanite hydration promoted by air humidity and fog, if present, is unlikely to contribute to the formation of case-hardened crust formation. It is conceivable that this also applies to potential, humidity-related anhydrite rehydration. According to the present SEM images, liquid water plays an important role for the process of encrustation. Gypsum precipitation from a calcium sulfate solution yields crystallization and growth of near macroscopic gypsum crystals that build up an interlocking structure and thus create the necessary strength, firmness, and rigidity that characterize gypcretes as present in the Atacama. This is not the case during de- and rehydration cycles with applied air humidity, only, as it is seen in Figure 6-36 c and d. Here, the formation of new-grown interlocking gypsum crystals is not observed.

This assumption is in agreement with the general conception that duricrust formation is provoked by the presence of liquid water reacting with surrounding soils, rocks, and atmosphere (Finkl, 1984). However, the rehydration of bassanite grains to gypsum under air humidity and temperature conditions as present in the Atacama Desert appears principally probable. It is, however, regarded to be a minor process due to the low abundance of the phase.

### 6-3-6 Discussion on calcium sulfate subhydrate emergence

During a few hemihydrate rehydration experiments at 91% - 95% RH affected by humidity regulation anomalies, one observation was made whenever RH values showed irregularities towards the dew point. Several peak positions of hemihydrate shifted slightly for a short time period (< 30 min) and finally moved back to their original positions. Concurrently, the peak positions of gypsum did not alter. In particular, the reflections at 14.7° (200)/(110), 29.7° (400)/(220), 31.9° ($11\bar{4}$), 42.7° (006), and 49.4° (134)/(424) $2\Theta$ (setting $I2$ of hemihydrate) exhibited position shifting.

One possible scenario that could explain the selective variation of reflections is the spontaneous emergence of a subhydrate phase. The sudden excess supply of water molecules could have been partly compensated by incorporation of extra water molecules in the hemihydrate channel structure. Thus, hemihydrate might have hosted $\geq 0.5$ $H_2O$ per structural unit. The formation of liquid free water seems to not have appeared, as no increased background was present. The subhydrates are known to be less stable than hemihydrate. Provided that a subhydrate had formed, the phase did not persist and eventually released the surplus of water.

According to Ballirano et al. (2001), the surrounding $p_{H_2O}$ is particularly decisive for the emergence of subhydrates. This observation could second the speculation that some type of calcium sulfate subhydrate could have formed. However, these measurements were accidental and did not happen under controlled circumstances. Repetitive experiments showed that only humidity sensor failures, independent of the applied temperature, could cause these specific peak shifts. Hence, it can not be ruled out that this observation is an experimental artifact as environmental conditions in the CHCplus+ chamber were effectively unknown and not reconstructable.

Exemplary for all occurrences, Figure 6-37 (a) shows the top views of a series of 30 powder XRD measurements that were obtained during hemihydrate rehydration experiments at 30 °C and a nominal value of 91% RH. The total time between the start of each two measurements was 30 min. Several peak shifts of hemihydrate are evident, possibly due to the corrupt humidity control (Figure 6-37 (a)). For emphasis, Figure 6-37 (b) gives magnifications of 30° - 35°, 40° - 44°, and 48° - 50° $2\Theta$.

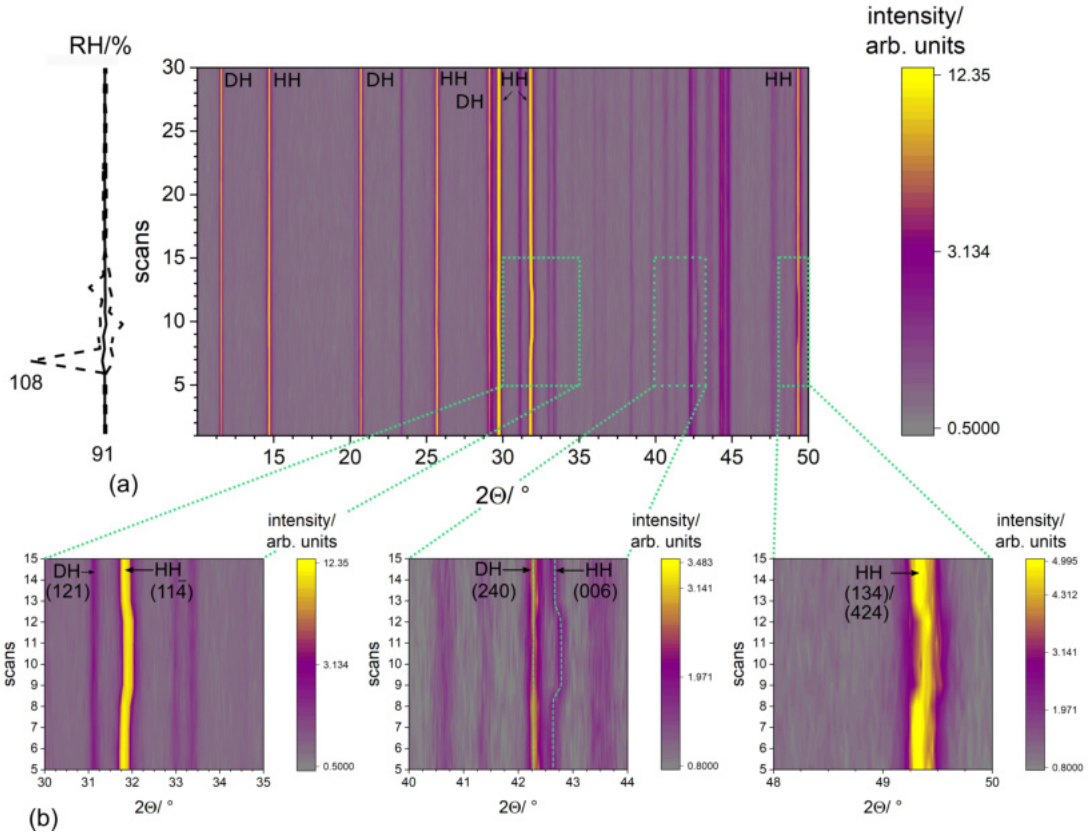


**Figure 6-37:** **(a)** Top view of a series of 30 powder XRD measurements obtained during hemihydrate hydration experiments at 30 °C and a nominal value of 91% RH showing shifting of several hemihydrate peaks. The logged relative humidities are given on the left. The mean values are indicated by the straight line whereas the minimum and maximum values are given by dashed lines. **(b)** The top views magnify selected $2\Theta$ ranges. In the middle panel, the green dashed lines give a guide to the eye.

Figure 6-38 gives the evolution of lattice parameters associated with the peak shifts displayed in Figure 6-37. The parameters were calculated by the Rietveld method using the hemihydrate structure (setting $I2$, Ballirano et al. 2001) as structural model. RH values as logged in the meta data of the *in situ* XRD measurements are plotted as well. The maximum value of circa 108 % does not represent the measured value. It is yielded by recalculation using Equation 5-1. The value corresponds to a sensor humidity of $\approx$ 81.5% at a sensor temperature of 35 °C. Hence, values above 100% RH merely illustrate the limit value overrun.

According to the data given in Figure 6-38, all lattice parameters exhibit changes except for $b$. Parameters $a$ and $\beta$ increase and $c$ decreases. Set up in space group $I2$, the channels present in the hemihydrate crystal structure that host $H_2O$ molecules run parallel to the $c$-axis. Likewise, water channels of subhydrates SH 0.6 (setting $I2$), SH 0.625 (setting $P3_221$), SH 0.67 (setting $C2$) and SH 0.8 (setting $P3_121$) also form along respective $c$-axes.

The axes correspondences of subhydrates to hemihydrate are given in Table 6-6. The following applies: $\sin(\beta_{\mathrm{HH}} - 90) \approx 0$.

**Table 6-6:** Axes correspondences of subhydrates (SH) to hemihydrate (HH).

| SH 0.6 | SH 0.625 | SH 0.67 | SH 0.8 |
|---|---|---|---|
| $\vec{a}_{\mathrm{SH\ 0.6}}$ to $\vec{a}_{\mathrm{HH}} \cdot (1 + \sin(\beta_{\mathrm{HH}} - 90))$ | $\vec{a}_{\mathrm{SH\ 0.625}}$ to $\vec{a}_{\mathrm{HH}} \cdot (1 + \sin(\beta_{\mathrm{HH}} - 90))$ | $\vec{a}_{\mathrm{SH\ 0.6}}$ to $\vec{a}_{\mathrm{HH}}$ | $\vec{a}_{\mathrm{SH\ 0.8}}$ to $\frac{1}{2}\vec{a}_{\mathrm{HH}} \cdot (1 + \sin(\beta_{\mathrm{HH}} - 90))$ |
| $\vec{b}_{\mathrm{SH\ 0.6}}$ to $\vec{b}_{\mathrm{HH}}$ | $\vec{b}_{\mathrm{SH\ 0.625}}$ to $2\vec{b}_{\mathrm{HH}} - \frac{1}{2}\vec{a}_{\mathrm{HH}}$ | $\vec{b}_{\mathrm{SH\ 0.67}}$ to $\vec{b}_{\mathrm{HH}}$ | $\vec{b}_{\mathrm{SH\ 0.8}}$ to $\vec{b}_{\mathrm{HH}} - \frac{1}{2}\vec{a}_{\mathrm{HH}}$ |
| $\vec{c}_{\mathrm{SH\ 0.6}}$ to $\vec{c}_{\mathrm{HH}}$ | $\vec{c}_{\mathrm{SH\ 0.625}}$ to $\vec{c}_{\mathrm{HH}}$ | $\vec{c}_{\mathrm{SH\ 0.67}}$ to $\vec{c}_{\mathrm{HH}}$ | $\vec{c}_{\mathrm{SH\ 0.8}}$ to $\frac{1}{2}\vec{c}_{\mathrm{HH}}$ |

The marked decrease of $c$ and the increase of $a$ and $\beta$ could point to the intake of $H_2O$. The additional hydrogen bonds could tighten of the structure along one direction while the incorporated $H_2O$ molecules could simultaneously take up more space in other directions. Averagely, the cell volume increases around 11% during the incident of humidity regulation fail.

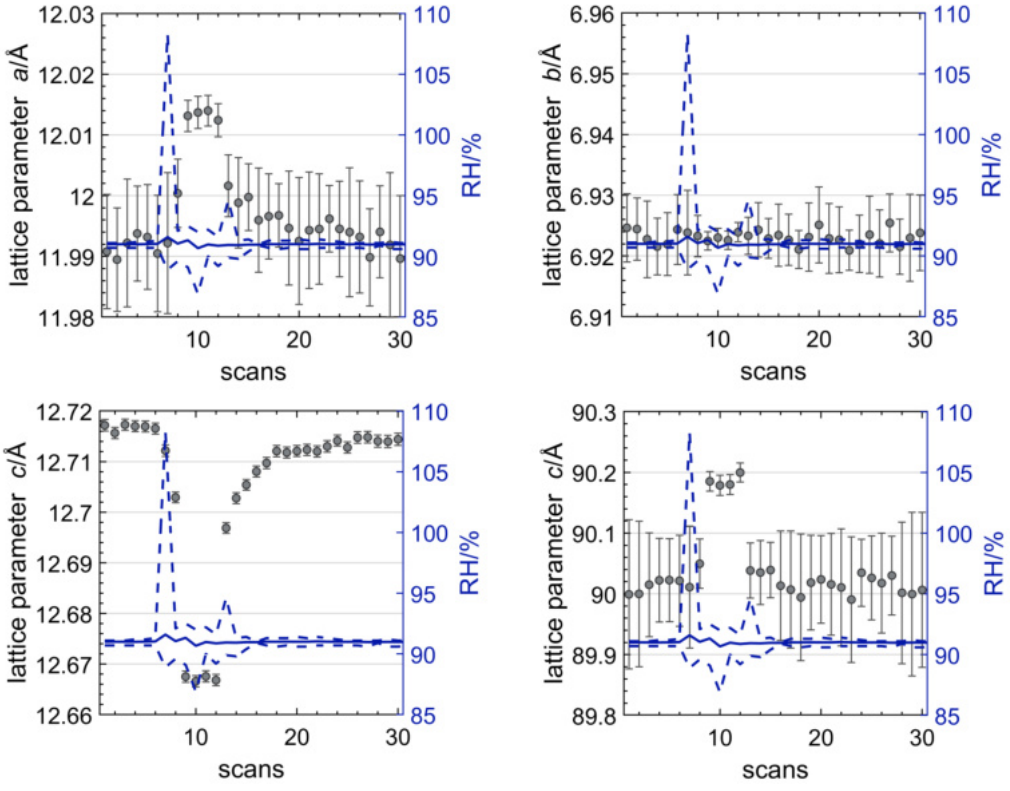


**Figure 6-38:** Lattice parameter evolution of $a$, $b$, $c$, and $\beta$ obtained by the Rietveld method using the hemihydrate structure model (setting $I2$). Corresponding RH values of *in situ* powder XRD measurements are given in blue. Structure data of hemihydrate was taken from Ballirano et al. (2001).

A comparison of theoretical diffraction patterns of published subhydrate structures (Chapter 2-1-4) with the patterns in question is exemplary shown in Figure 6-39 (a). The pink lines give the calculated patterns of the subhydrates, the dashed grey line corresponds to the powder pattern of the gypsum/hemihydrate mixture and the blue line corresponds to the measurement affected by humidity irregularities. The phase mixture is denoted as $CaSO_4 \cdot 2\,H_2O + CaSO_4 \cdot n\,H_2O$ to emphasize the unknown $H_2O$ content $n$. Figure 6-39 (b) gives again the top view of selected scans that show the shift of the $(11\bar{4})$ peak of hemihydrate to higher $2\Theta$ values. It is included for better overview. Figure 6-39 (c) magnifies the range of 30° - 35° $2\Theta$ of Figure 6-39 (a).

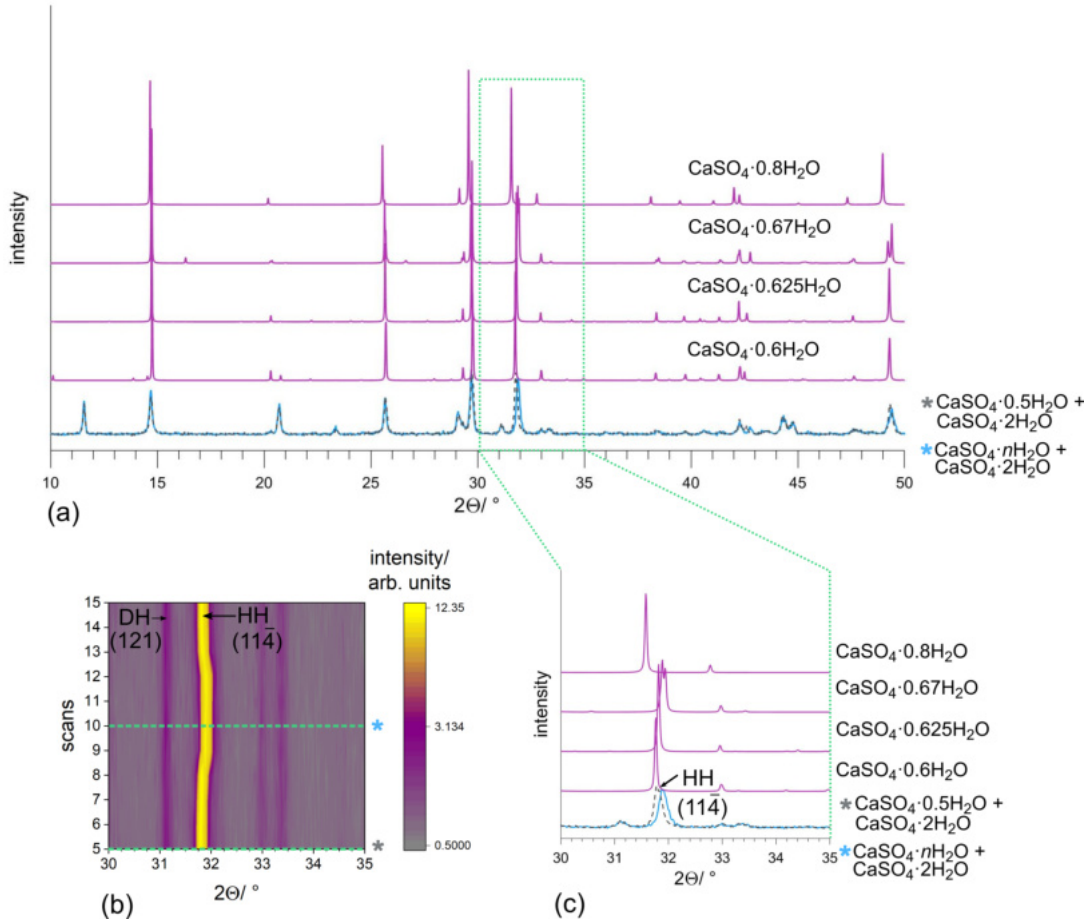


**Figure 6-39:** **(a)** Theoretical diffraction patterns of subhydrates (pink lines), and measured powder patterns of hemihydrate + gypsum (dashed grey line) and a potential subhydrate ($CaSO_4 \cdot n\,H_2O$) + gypsum (blue line). The powder patterns of subhydrates were calculated with crystal structure data by Bezou et al. (1995); Schmidt et al. (2011); Bushuev (1982); Abriel (1983). **(b)** Top view of selected powder XRD patterns that emphasize the shift of the $(11\bar{4})$ peak of hemihydrate to higher $2\Theta$ values due to humidity regulation problems. The dashed green lines denote the scans of hemihydrate + gypsum and $CaSO_4 \cdot n\,H_2O$ + gypsum. **(c)** Magnification of the stacked powder patterns given in **(a)**, corresponding to the angular range displayed in **(b)**.

The comparison of peak positions points to an approximate accordance of $CaSO_4 \cdot n\,H_2O$ with SH 0.67. However, due to the lack of further indications, it is unclear whether a subhydrate has formed. Among the published subhydrate structures, three were hydrothermally synthesized or grown from aqueous solution, whereas two were found to emerge at specific relative humidities. In particular, these were subhydrates SH 0.625 and SH 0.6. Schmidt et al. (2011) described the emergence of SH 0.625 at 75% RH at ambient temperature conditions from hemihydrate. Bezou et al. (1995) prepared SH 0.6 from hemihydrate at room temperature and 95% RH. During the present work, controlled air humidity and temperature conditions that favor the evolution of subhydrates could not be established. All *in situ* hemihydrate hydration experiments yielded the direct formation of gypsum which is the thermodynamically stable phase at applied temperature conditions. It is conceivable that the kinetically controlled formation of subhydrates depends on several other parameters such as crystallite size and sample preparation.

### 6-3-7 A brief outlook on anhydrite rehydration

As stated above, the hydration of $\beta$-anhydrite under controlled air humidity and temperature conditions was not of primary concern. Due to the kinetic checks of gypsum formation from anhydrite in aqueous solutions, it was conceivable that $p_{H_2O}$-induced rehydration of anhydrite would be kinetically hindered as well. To estimate whether the mineral would further rehydrate, a natural sample with traces of gypsum was prepared for powder XRD and measured at 30 °C and 95% RH at the sample for 2 h. Prior to rehydration, the gypsum content was about 1%. After two hours, ≈ 5% gypsum was present. The corresponding powder XRD patterns are given in Figure 6-40.

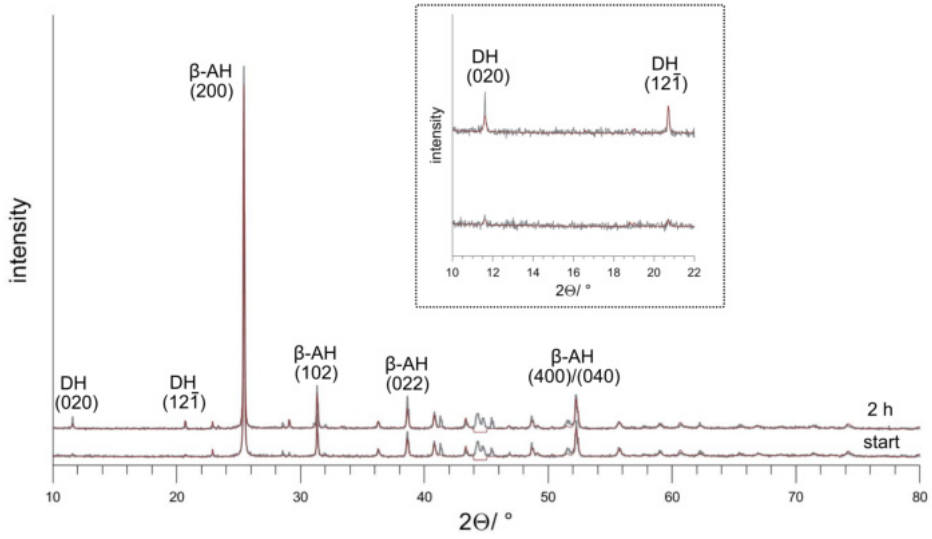


**Figure 6-40:** Powder XRD patterns of a natural anhydrite sample obtained before and after treatment at 30 °C and 95% RH for 2 h. The observed intensities are given in grey and the calculated intensity curve according to the method by Rietveld is given in red. The area from 44° - 45° 2Θ was excluded from data fitting as the peaks are caused by the silicon sample holder. The inset magnifies the 2Θ region of 10° - 22°.

$\beta$-Anhydrite, obtained by heating gypsum at 300 °C for three months, was also exposed to relative humidities of 93.5% at 30 °C for 120 h. Here, no gypsum formation was observed (Figure C-11). As it became clear that hydration experiments of pure $\beta$-anhydrite would likely require extensive measuring times and different approaches than *in situ* measurements, the rehydration of $\beta$-anhydrite was not further pursued by *in situ* methods.

Based on the gypsum formation from the natural sample, however, long term experiments of $\beta$-anhydrite doped with *e.g.* 1%, 5%, and 10% gypsum could be feasible. Storing the sample material in a chamber at room temperature with high RH values (*e.g.* 95%) would pose a workable laboratory option to study the hydration behavior of $\beta$-anhydrite induced by water vapor-pressure, if regular quantification of the sample contents was possible. Such a chamber equipped with a temperature and humidity sensor, and humidity generator could be build inhouse. Depending on the chamber size, further hemihydrate samples and samples containing inhibiting or accelerating salts (present in the Atacama Desert) could also be scrutinized.

### 6-3-8 Long-term gypsum dehydration measurements

*In situ* gypsum dehydration experiments showed that reaction kinetics significantly slow down $< 80$ °C under the given experimental conditions. This, together with the lack of $\beta$-anhydrite production at low temperatures within applied measurement times, motivated the study of gypsum dehydration over the course of six months. Gypsum powder and a mixture of 50% gypsum and 50% NaCl were treated at 60 °C and 80 °C at different relative humidities, that were established by supersaturated aqueous salt solutions (Table 5-4). From the samples that were kept under the thus defined, constant temperature and humidity conditions, small amounts were taken and monthly analyzed by powder XRD.

The time-dependent quantitative results are complied in Figure 6-41. Unfortunately, the results of gypsum dehydration at 80 °C with humidity regulation by the $ZnBr_2$ solution could not be included. The respective desiccator was found opened in the second month (slightly displaced lid) so that the solution evaporated, perhaps caused by the vapor pressure of bromine. Prior to that observation, the smell of bromine was noticed when opening the desiccator.

$\beta$-Anhydrite formation from gypsum proceeds at 60 °C and humidity values $< 11\%$ within six months (Figure 6-41, left panels). At 80 °C, $\beta$-anhydrite formation results at all applied humidities (Figure 6-41, second to right panels).

Dehydration of gypsum powder at 60 °C shows that gypsum stays stable at $\approx 29\%$ RH. In contrast, hemihydrate formation is detected in the third month at $\approx 11\%$ RH and in the first month at $\approx 8\%$ and $\approx 5\%$ RH. At latter humidity, $\beta$-anhydrite formation is also observed in the first month. Traces of gypsum remain up to the sixth month at $\approx 11\%$ RH, and the third and second month at $\approx 8\%$ RH and $\approx 5\%$ RH, respectively. For the applied measurement conditions and used powder samples, the limit of detection of quantitative phase analysis was experimentally found to be $\approx 0.5$ wt.%.

These results mirror the experimental conditions as lower RH values cause swifter dehydration reactions. The respective percentages show consistency for each sample. However, it appears incoherent that after six months, 14.3% $\beta$-anhydrite would form at $\approx$ 11% RH and only 7.2% and 13.1% would form at $\approx$ 8% and $\approx$ 5% RH, respectively. Nevertheless, the values are in the same order of magnitude. Moreover, making such fine-drawn distinctions would require a higher sample batch. Here, only one sample per desiccator was used.

At 80 °C, the presence of gypsum is evident up to the second month at $\approx$ 26% RH. At higher RH values, only hemihydrate and $\beta$-anhydrite are present. Overall, the $\beta$-anhydrite contents of powder samples are notably higher compared to findings at 60 °C. Several result contradictions are noticable. RH values of $\approx$ 26% promote 43% of $\beta$-anhydrite, whereas $\approx$ 11% and $\approx$ 5% RH yield 40.4% and 22.0% of $\beta$-anhydrite, respectively. These findings could be explained with the experimental set-up and accompanying uncertainties. To analyze the phase contents, the powder samples were sequentially taken out of the desiccators. During this procedure, hermetically sealed isohumid and isothermal conditions were interrupted. Potentially, sample contamination or random nucleation of $\beta$-anhydrite could have promoted premature formation and growth of $\beta$-anhydrite during the experiments in question.

Regarding powder samples containing 50% gypsum and 50% NaCl, observations at 60 °C and 80 °C point to an accelerating effect on hemihydrate formation and a decelerating influence on $\beta$-anhydrite formation (Figure 6-41, second to left and right panels). Only the sample treated at 80 °C and $\approx$ 26% RH shows $\beta$-anhydrite formation. Once more, this finding is unexpected but consistent when compared to the results of the corresponding experiment using gypsum powder.

The hygroscopic behavior of NaCl is well-known. The present results indicate that the first gypsum dehydration step to hemihydrate is facilitated by the the addition of NaCl. It is conceivable that NaCl readily adsorbs available $H_2O$ molecules which could cause locally lower $p_{H_2O}$ values for surrounding gypsum crystallites. Hence, hemihydrate evolution would be fostered. In contrast, the second dehydration step of gypsum is not favored by the affinity of NaCl for atmospheric moisture. It appears as if the salt had a buffering effect. It might be possible that, after a while, NaCl causes a locally balanced moisture content that inhibits further dehydration of hemihydrate.

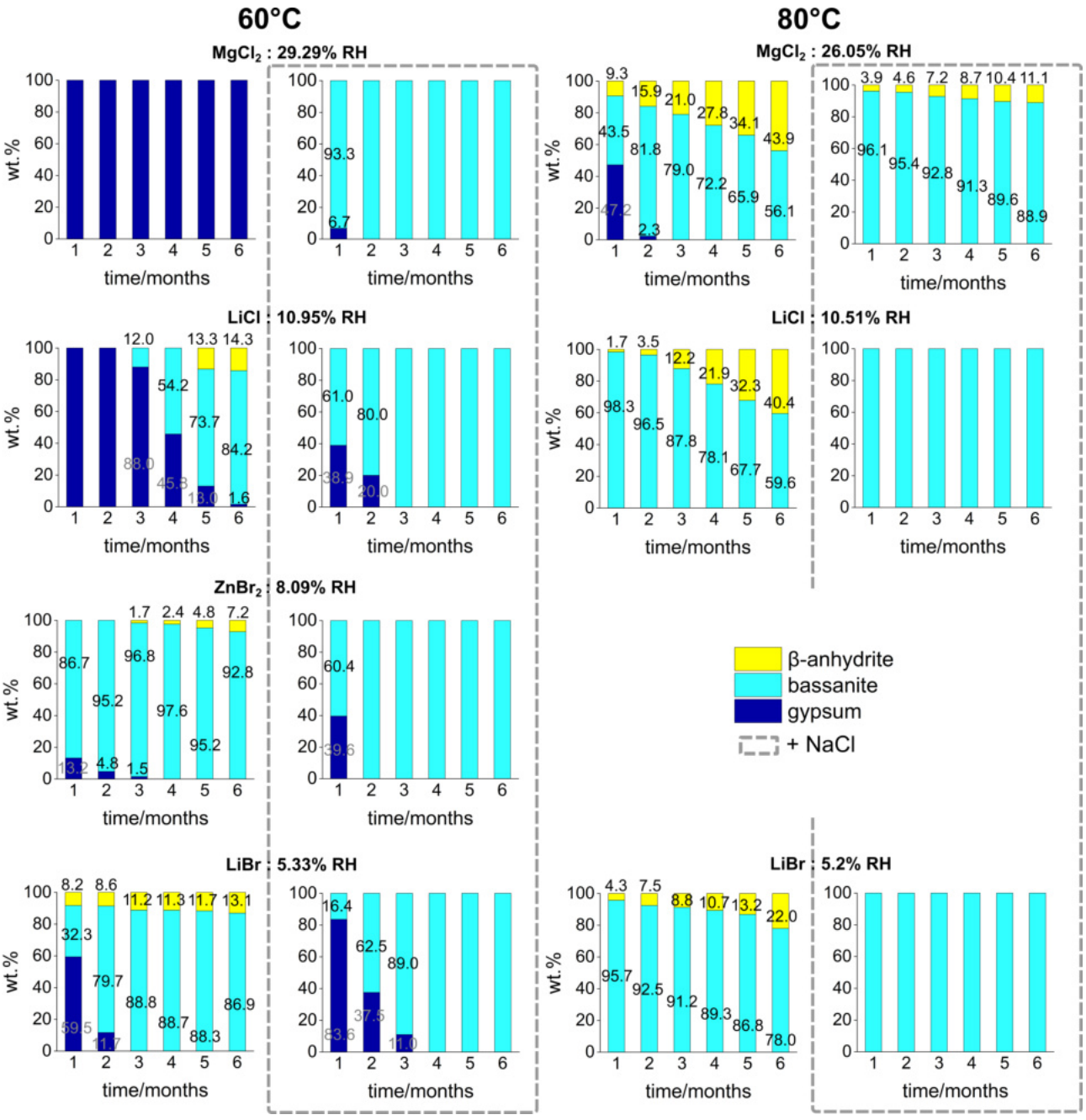


**Figure 6-41:** Percentages of gypsum, hemihydrate and $\beta$-anhydrite after one to six months of dehydration at 60 °C and 80 °C and different relative humidities (RH) generated by the supersaturated salt solutions. The notation '+ NaCl' indicates that the starting material consisted of gypsum and NaCl (1:1). The percentages of respective samples were normalized to 100% $CaSO_4 \cdot n\,H_2O$ with $0<n<2$. Errors of quantitative analysis are within $\pm$ 1%.

Due to the partially unexpected results, especially concerning the findings at 80 °C and ≈ 26% RH (Figure 6-41, upper right panels), RH values were revised using a FreeTec temperature and humidity data logger. Since the operating temperature range was restricted to −40 °C - 60 °C, the desiccators were taken out of the drying cabinets and left at ambient temperature. The data logger was then placed inside the desiccator for 30 min. This short time period was chosen due the following reasons: The salt solutions needed to be kept at respective temperatures to avoid precipitation at room temperature. Also, when desiccators were kept outside the drying cabinets for > 30 min, it was found that desiccator lids could not be readily removed because of the prevailing pressure conditions. The obtained RH values, with corresponding temperatures in brackets, are given in Table 6-7. The nominal RH values according to Greenspan et al. (1977, and references therein) and differences between measured and nominal values are also stated.

**Table 6-7:** Relative humidity (RH) values in desiccators measured by a FreeTec data logger and (nominal values) according to Greenspan et al. (1977, and references therein). The measured values represent the recorded humidities and corresponding temperatures inside the desiccators after 30 min. The differences between nominal and measured values is given by $\Delta_{n,m}$.

| | **$MgCl_2$** | | **LiCl** | |
|---|---|---|---|---|
| solut. treated at: | **60 °C** | **80 °C** | **60 °C** | **80 °C** |
| nominal | 31.60% RH (40 °C) | 29.93% RH (55 °C) | 11.21% RH (40 °C) | 11.10% RH (50 °C) |
| measured | 51% RH (40 °C) | 45% RH (55 °C) | 25% RH (50 °C) | 23% RH (50 °C) |
| $\Delta_{n,m}$ | 19.4% | 15.07% | 13.79% | 11.90% |
| | **$ZnBr_2$** | | **LiBr** | |
| solut. treated at: | **60 °C** | **80 °C** | **60 °C** | **80 °C** |
| nominal | 7.62% RH (30 °C) | | 5.65% RH (45 °C) | 5.42% RH (55 °C) |
| measured | 20% RH (30 °C) | | 13% RH (45 °C) | 16% RH (55 °C) |
| $\Delta_{n,m}$ | 12.38% | | 7.35% | 10.58% |

The large differences between calculated literature and measured values strikes. The relative humidities generated by the binary salt solutions are 13% higher on average than nominal values. It appears that these findings are impaired by the short measurement time. It can be assumed that the equilibrium humidities were not established. Hence, the measurement values are likely unsuited to provide a reliable vetting of RH values. Generally, the measure of permanently controlling humidity values with adequate devices for this experimental set-up appears useful. In hindsight, the application of a temperature sensor that could be kept at elevated temperatures would have been useful to constantly monitor the prevailing sample conditions.

The strong time dependence of $\beta$-anhydrite formation in samples exposed to temperatures above the gypsum–anhydrite equilibrium temperature is well-known. Overall, the present results show the possibility of $\beta$-anhydrite formation from gypsum at temperatures ≥ 60 °C within one to six months at RH values lower than ≈ 11%. The selected powder XRD measuring interval is adequate to follow the gradual gypsum–hemihydrate–$\beta$-anhydrite evolution.

With regard to experiments using a phase mixture of gypsum and NaCl, a prolonged measuring time of more than six months would have been desirable. Also, this long-term experiment would have benefited from continuous monitoring of temperature and RH conditions. Due to the experimental set-up, the existence of $\gamma$-anhydrite could not be validated. However, it is likely that the phase would also be present in several samples under the given humidity and temperature values. In such samples, the $\gamma$-anhydrite phase content would be retrievable in the hemihydrate percentages.

Concerning the geoscientific significance of gypsum and bassanite dehydration, it was shown that long-term approaches are better suited to study moderate to low temperature dehydration behavior than *in situ* experiments over several hours to days or even weeks. The experiment using LiBr is the only experiment conducted at 60 °C that exhibits $\beta$-anyhdrite evolution in all six months. Using these quantitative results, a linear regression can be determined that is $y\,[\%\beta\text{-AH}] = 0.9686 \cdot x\,[\text{months}] + 7.2933$ with $R^2 = 0.9106$. According to that, 95.7 months of constant exposure at 60 °C would yield 100% $\beta$-anhydrite. If a soil temperature of 60 °C accompanied by $\approx$ 5% RH was evident for 1 h each day during six months of the year, approximately 377 years would be necessary to promote complete gypsum dehydration. This estimation can not be regarded as significant due to the lack of further corroborating dehydration results. However, it might help to understand the duration of anhydrite formation from gypsum at Atacama temperature and humidity conditions.

# Chapter 7

# Conclusions

The present work describes an *in situ* powder XRD and Raman spectroscopy study of the nature of de- and rehydration processes in the $CaSO_4$ – $H_2O$ system under controlled temperature, water vapor-pressure, and time conditions. The underlying project goal of this thesis was to assess whether temperature and air humidity conditions prevailing in the Atacama Desert, could foster de- and rehydrational transformations of calcium sulfate phases on a diurnal to seasonal time scale. Gypsum and anhydrite are two abundant minerals that characterize Atacama soils and surfaces. Small-scale geomorphological features (polygonal patterned surfaces, gypsum wedges) are assumed to result from phase transformations caused by the uptake or loss of $H_2O$ molecules via air humidity. This, together with the need for water vapor-pressure control of gypsum dehydration and the data lack of hemihydrate hydration induced by $p_{H_2O}$, motivated the here presented experimental study.

Prior to *in situ* powder XRD experiments, sample height-displacement measurements were performed. These measurements were based on the volume change of calcium sulfate phases when water of hydration is released or taken up. The volume increase or shrinkage of any sample material causes a misalignment of the sample surface with the focusing circle of the diffractometer. This results in erroneous $2\Theta$ positions of Bragg reflections. Hence, correction of such an error during data processing was required. It was found that, due to the small sample volumes, the dehydration- and rehydration-induced height variations of sample surfaces can be well taken into account during refinement calculations using the DIFFRAC.SUITE TOPAS software suite.

Phase discrimination is unambiguous with both, powder XRD and Raman spectroscopy. Characteristic Bragg reflections or wave numbers of prominent vibrational modes enable the monitoring of phase evolution during *in situ* experiments. Using powder XRD, the structural similarity of hemihydrate and $\gamma$-anhydrite is apparent. The discrimination based on extra monoclinic, weak reflections is in many cases not expedient: A small proportion of one phase, diffraction pattern impairments due to preferred particle orientation, or poor peak-to-background ratios render it beneficial to base phase differentiation on stronger reflections (Robertson and Bish, 2013).

The *in situ* powder XRD measurements showed that the (200)/(110) peak shift of hemihydrate relative to the (100) peak of $\gamma$-anhydrite is suitable to apply as distinguishing criterion. This is corroborated by lattice parameter evolution results based on refinements using the Rietveld method. The practicability to discriminate between hemihydrate and $\gamma$-anhydrite via powder XRD has also been reported by Oetzel et al. (2000a), Seufert et al. (2009), and Robertson and Bish (2013).

During Raman spectroscopic measurements, it became evident that hemihydrate as well as $\gamma$-anhydrite exhibit Raman modes that each have wave numbers close to the main sulfate mode, $\nu_1(SO_4)$, of the respective precursory calcium sulfate phase. In the case of hemihydrate, the 'additional' line at $\approx 1008\,cm^{-1}$ is close to the $\nu_1(SO_4)$ mode of gypsum. For $\gamma$-anhydrite, the mode at $\approx 1015\,cm^{-1}$ has a similar position to the $\nu_1(SO_4)$ mode of hemihydrate. In both cases, the assumption of residual traces of the preceding calcium sulfate phase initially stands to reason. Regarding hemihydrate, this observation has also been described by Sarma et al. (1998), Prasad (1999), and Schmid et al. (2020). The authors declare that the mode at $1008\,cm^{-1}$ might be explainable with the presence of possibly disordered gypsum remnants. In the course of their study, Schmid et al. (2020) rejected this assumption and identified the mode as intrinsic for hemihydrate. They attributed the mode to band splitting caused by coupling of vibrational motions. In the present work, both 'additional' modes are regarded as inherent parts of the respective spectra for the following reasons. Whenever gypsum samples were fully dehydrated to $\gamma$-anhydrite, the phase persisted at temperatures $\geq 105\,°C$ under the given experimental conditions. Upon cooling, $\gamma$-anhydrite readily rehydrated to hemihydrate due to the re-entering of $H_2O$ molecules. Uniformly, these hemihydrate spectra included the mode at $1008\,cm^{-1}$. This leaves the assumption of remaining gypsum traces rather unlikely. By heating a gypsum sample to $\gamma$-anhydrite at $150\,°C$ for three days and analyzing the final Raman spectrum, it was found that the $1015\,cm^{-1}$ mode remained. Again, this extensive heat treatment implies that the mode in question is intrinsic and not caused by hemihydrate remnants in the $\gamma$-anhydrite sample. Moreover, corresponding powder XRD experiments indicate that hemihydrate formed from $\gamma$-anhydrite rehydration at ambient conditions is free of gypsum. Likewise, the treatment of gypsum samples at temperatures above $120\,°C$ corroborates the hemihydrate-free presence of $\gamma$-anhydrite within minutes after reaching operating temperature.

It is well known that dehydration and rehydration reactions depend on several influencing factors including sample characteristics (*e.g.* Bish and Duffy, 1990; Khoo et al., 2010). Therefore, efforts were made to ensure consistent sample preparation and sample volumes during *in situ* measurements. It was found that preparing the sample by sieving a fine powder layer on a sample holder was most expedient. Consecutively, the quantitative influence of particle sizes on gypsum–hemihydrate conversion at $90\,°C$ and relative humidities between 1.8% - 3.1% was studied. It was established that particle fractions must have a range of $\leq 5\,\mu m$ to allow for reproducible and uniform $\alpha - t$ curves. The increase of grain sizes is accompanied by prolonged induction periods. Together with a kinetic model fitting approach using the JMAEK reaction model and evaluating the fitted Avrami-exponents, this could point to the change of nucleation rates throughout the dehydration process. The fraction of conversion curves were also fitted with the Prout-Tompkins autocatalytic reaction model. Brown and Galwey (1979), Brown et al. (2000), Brown and Glass (2003), and Moser et al. (2018) emphasize the difficulty of establishing which of these kinetic expressions describes sets of experimental data best.

This also applies to the present work. The fraction of conversion curves can be satisfactorily fitted with both equations. However, it could be supposed that the $\alpha$ vs. time curves of larger particle size-fractions agree slightly better with the autocatalytic reaction model according to Prout and Tompkins. The applicability of fitting other kinetic reaction models to the present data is excluded due to the characteristic symmetrical sigmoidal shapes of conversion curves.

The hemihydrate formation from gypsum was further studied at 76 °C - 92 °C with relative humidity values of 3.3% - 1.7% by *in situ* powder XRD. The temperature range was not expanded on the grounds that values > 92 °C yielded very rapid and temperatures <76 °C yielded very slow hemihydrate evolution. In both cases, it is difficult to adequately track the conversion by the *in situ* methods applied here. At temperatures $\geq$ 84 °C, sigmoidal $\alpha - t$ curves are yielded that were fitted with the JMAEK and Prout-Tompkins kinetic reaction models. Again, the choice of one reaction model over the other is inconclusive. With great caution, it could be stated that the JMAEK expression fits the data obtained at 92 °C and 88 °C better, whereas the Prout-Tompkins model provides a more adequate description for the data measured at 84 °C. This would imply a temperature-dependent change of reaction mechanism. This supposition could also be made considering the findings at 80 °C and 76 °C. The considerably slower hemihydrate evolution appears to be determined by different, possibly more than one, rate-controlling steps than reactions at higher temperatures. However, it cannot be ruled out that the lack of accurate sample humidity control impacts the here obtained data. Due to the technical provisions set by the manufacturer, the humidity regulation of the CHCplus+ chamber was not possible $\geq$ 80 °C and < 5% RH. Despite the made efforts to keep sample humidities virtually constant, the differences in constant temperatures caused slightly different relative humidities at the sample. This hampered the evaluation of temperature as the sole influencing factor on gypsum decomposition under 'isohumid' conditions. Based on preliminary measurements of gypsum at 80 °C, it became evident, that relative humidities of averagely 5.5% RH prevented dehydration within 20 h. In comparison, $\approx$ 12.5% hemihydrate was formed after 20 h at sample humidities of 2.8% RH and 80 °C. This, and the overall findings of gypsum dehydration experiments, point to a strong influence of minor differences of $p_{H_2O}$ values prevailing at the sample on dehydration kinetics. The experiment-inherent inability to control the system within the first seconds or until working conditions are established, might also have an influence on the here investigated dehydration processes.

The Arrhenius-type temperature-dependence of the gypsum–hemihydrate conversion is evident. This is corroborated by corresponding *in situ* Raman spectroscopy measurements of gypsum dehydration to hemihydrate. It has also been described by *e.g.* Ballirano and Melis (2009b). Quantitative analysis of Raman spectra to obtain fraction of conversion curves was done. The curves were compared to those yielded by powder XRD experiments. Apart from the method-related differences and the possibly imprecise $\alpha$ values calculated from Raman measurements, it is carefully surmised that discrepancies in water vapor-pressures prevailing at the sample majorly cause results discrepancies in respect of time dependency of the dehydration process. Due to the manually controllable humidities in the THMS600 sample chamber of the Raman set-up, the humidities were set to 2.5% RH during isothermal heating from 76 °C to 92 °C.

Isokinetic determination of $E_a$ values was not expedient. The non-linear dependence of rate constants on $\frac{1}{T}$ values might indicate more than one mechanism of dehydration. This would be in accordance with the findings by, *inter alia*, Ball and Norwood (1969), Abriel et al. (1990), and Badens et al. (1998). However, due to the few isothermal and virtually isohumid experiments performed here, this statement must be regarded with care. For the same reason, the activation energy values yielded by isoconversional methods are difficult to judge. Compared to published data, the values of $301\,\mathrm{kJ\,mol^{-1}}$ and $368\,\mathrm{kJ\,mol^{-1}}$ are in the upper range of available $E_a$ data. Due to the moderate variability of $E_a$ values with $\alpha$, the assumption of multiple dehydration mechanisms is strengthened.

The hydration of hemihydrate was studied at humidities up to 95% RH and temperatures $\leq 40\,^{\circ}\mathrm{C}$. In particular, the isothermal and isohumid powder XRD experiments at relative humidities between 86% and 93.5% and a constant temperature of 30 °C, and at temperatures between 15 °C and 40 °C and a constant relative humidity of 91% gave new insights in the hemihydrate hydration process promoted by $p_{\mathrm{H_2O}}$. At constant humidities of 91% RH, it became clear that the maximum rate of hydration is close to 30 °C. Similar observations have been made by hemihydrate rehydration in aqueous suspensions. At 40 °C, the reaction is noticeably tardy which is attributed to the proximity of the gypsum–anhydrite equilibrium temperature. At ambient pressure, this threshold temperature has been determined to range between 42 °C and 58 °C (Freyer and Voigt, 2003). Judging from the applied relative humidities at a constant temperature of 30 °C, the water vapor-pressure is much more decisive for the completeness of conversion than the temperature. The applied range of 86% - 93.5% RH yields roughly 4% to 85% of gypsum, respectively. In contrast, the range of 15 °C - 30 °C at 91% RH causes 23% to 62% gypsum formation. The results of both measurement series indicate an exponential temperature and $p_{\mathrm{H_2O}}$ influence on $\alpha$ values. Concerning sample humidities, Raman spectroscopic measurements at a constant temperature of 22 °C corroborated this finding. Since the THMS600 sample stage housing could not be heated externally, temperatures were not varied. This is reasoned by the respective dew points. A temperature fall of the stage housing below this threshold would cause condensation and the formation of liquid water.

Based on the shapes of $\alpha - t$ curves, it is assumed that the underlying time-controlling hydration mechanism is dependent on the the temperature and humidity regime. However, the continually slow hemihydrate hydration reactions are difficult to assign unambiguously. Exemplary, the conversion of hemihydrate to gypsum at 35 °C and 91% RH was used for kinetic model-fitting. The $\alpha - t$ curve could not be fitted with a single expression. By fitting the accelerating part of the curve with the power law equation and the decelerating part to the 3D diffusion equation according to Ginstling-Brounshtein, the curve can be reasonably well described. The incompleteness of the rehydration processes inhibits the calculation of activation energies based on isoconversional methods over the total range of $\alpha$ values. Based on the present data, a value of $31\,\mathrm{kJ\,mol^{-1}}$ was obtained. This is comparable to the $E_a$ values given for hemihydrate setting in slurries of *e.g.* $30\,\mathrm{kJ\,mol^{-1}}$ according to Tekkouk et al. (2012).

In the present work, isohumid and isothermal treatment of hemihydrate yielded direct gypsum formation. Provided that temperature and humidity control was accurate, treating hemihydrate at high $p_{H_2O}$ values did not promote intermediate subhydrate evolution. In accordance with the distinct crystal structures, decomposition of hemihydrate and the nucleation and growth of gypsum is found to be the sole pathway to form gypsum. It is, however, surmised that several impaired hydration experiments show subhydrate evolution originating from hemihydrate. During these experiments, failure of the humidity sensor led to short-lived regulation anomalies which caused peak shifts of hemihydrate. In contrast, gypsum was not affected. This could be explained by a gradual uptake of $H_2O$ in the hemihydrate structure.

The interest in $\beta$-anhydrite formation at moderate to low temperatures, motivated long-term gypsum dehydration experiments. As operating temperatures, 60 °C and 80 °C were chosen. The constant humidity values generated by supersaturated salt solutions were between 5.4% and 31.6% RH. It was found that the experiment duration of six months was sufficiently long to promote $\beta$-anhydrite evolution in the full range of applied relative humidities at 80 °C and at relative humidities $\leq$ 11% in the samples treated at 60 °C. In samples with added NaCl, the salt's acceleratory effect on hemihydrate formation and its inhibitory effect on $\beta$-anhydrite evolution was evident.

Overall, the findings point out the crucial influence of sample humidities. The temperature dependence of gypsum dehydration is well-known. Here, it was found that small differences in $p_{H_2O}$ become decisive when moderate to low temperatures are applied. For hemihydrate hydration, the surrounding water vapor-pressures have a greater influence on the reaction than temperature values. The rate-controlling processes are found to vary with the respective temperature and $p_{H_2O}$ conditions.

The present findings can be used to make several considerations pertaining potential reactions of calcium sulfate phases in the Atacama Desert. Based on *in situ* measurements using powder samples, the diurnal conversion of gypsum $\rightarrow$ bassanite and gypsum$\rightarrow$ anhydrite appears unlikely. Vítek et al. (2016) make similar assumptions concerning gypsum dehydration based on an experiment from Yechieli and Wood (2002). They yielded complete gypsum dehydration to $\beta$-anhydrite at 80 °C after 800 h at undefined $p_{H_2O}$ values.

Dehydration processes of gypsum within extended time scales are more probable considering the findings yielded from long-term dehydration experiments. At a constant temperature of 60 °C and $\approx$ 5% RH, circa 8% of $\beta$-anhydrite and 30% hemihydrate were formed within the first month. Taking the exponential temperature-dependency and a maximum day temperature in the Atacama Desert of averagely 40 °C for one hour into account, it is conceivable that time periods of months to years could promote dehydration of small gypsum grains in the top layer of the soil surfaces. The present experimental findings point to a strong dependence of conversion rates on small changes of the surrounding air humidity. Hence, whenever relative humidities close to 0% are prevalent, they supposedly act beneficial to dehydration processes at low temperatures such as prevailing in the Atacama.

At low temperatures (< 110 °C), hemihydrate is the compulsory, intermediate dehydration product of gypsum prior to $\gamma$-/$\beta$-anhydrite. The minor presence of bassanite in natural samples could indicate that very small fractions of gypsum undergo the dehydration process that eventually could promote anhydrite formation. *Vice versa*, this implies that abundant, large-scale gypsum dehydration induced by soil temperature and air humidities would cause the prevalence of bassanite in large amounts. On marsian surfaces, which are often considered comparable to Atacama Desert pavements, such predominances of bassanite have been confirmed by *e.g.* Wray et al. (2010), Rapin et al. (2016), and Vaniman et al. (2018). Usually, these occurrences are attributed to the environmental temperature and humidity conditions promoting gypsum dehydration (Wilson and Bish, 2011). However, by studying nucleation pathways of hemihydrate from solution, Stawski et al. (2020) have aimed at providing an alternate explanation for the abundant occurrence of bassanite on the surface of Mars.

On earth, significant quantities of bassanite were described by *e.g.* Gunatilaka et al. (1985) in the evaporite pans of the continental sabkha in Kuwait. The authors report that the onset of dry (gypsum dehydration promoted by low $p_{H_2O}$ and higher $T$ conditions) and wet season (bassanite rehydration by availability of rain water) cause the sabkha surface layer to alterate seasonally. This study could second the supposition that the prevailing bassanite quantities might be regarded as a proxy for the scope of ongoing dehydration processes. Yet, the present sample batch of natural samples is not sufficiently large to make secured claims on large-scale bassanite abundance in the Atacama. Moreover, the alteration extent of samples is retrospectively not ascertainable. Regarding the calcium sulfate phase content of Atacama soils, Wei et al. (2015) made an interesting observation. In one sample, they detected 20% $\gamma$-anhydrite by performing *in situ* characterization of mineral assemblages using a Mars Micro-beam Raman Spectrometer (MMRS) on-board a rover. The phase was found in 20 cm - 30 cm depth. The authors acknowledged the discrepancy of this finding with the literature data on the stability regime of $\gamma$-anhydrite and attribute the prevalence to a natural mechanism that prevents the rehydration of $\gamma$-anhydrite to bassanite. Such findings demonstrate the need for further in-depth and *in situ* characterization of local environments in the Atacama.

The here performed hemihydrate hydration measurements showed that hydration rates are approximately exponentially dependent on relative humidities. The applied temperatures also impact the conversion but to a lesser extent. Given enough bassanite as starting material, it is conceivable that night-time temperatures of 10 °C - 20 °C and humidities close to 100% or fog events would foster significant hemihydrate rehydration, possibly within several hours. The SEM analysis of consecutively de- and rehydrated grains, however, demonstrated that $p_{H_2O}$-related gypsum formation does not yield interlocked, felt-like crystallites that in bulk could constitute a rigid surface such as the gypcrete ('gypsum crust') in the Atacama Desert. The encrustation process requires the presence of liquid water. Thereby, gypsum crystals can grow from solution and develop the necessary rigidity that generally characterizes duricrusts. Claims on anhydrite hydration must be omitted as only two orientation-giving experiments were conducted.

In summary, based on the here performed sample analysis, *in situ* measurements and long-term dehydration experiments, the diurnal occurrence of gypsum dehydration is found to be unlikely, in contrast to the possibility of dehydration of small amounts within months to years. Principally, the hydration of bassanite is considered feasible within shorter time frames. These statements do not include the aspect of mutual process interference and consider only the pure $CaSO_4 - H_2O$ system without the presence of additives and liquid water. Additives can influence the dehydration and rehydration behaviour of calcium sulfate phases significantly. It is supposable that accompanying salts present on Atacama soils and surfaces alter the respective de- and rehydration reactions. Likewise, the presence of biota likely affects the hydration state of calcium sulfate minerals. Under water-limited conditions, gypsum can be a source for bio-available $H_2O$ for microorganisms (Wilson and Bish, 2011). This was corroborated by Palacio et al. (2014), who used the distinct isotopic composition of structurally bonded water in gypsum to show that it is used by plants. Further, Huang et al. (2020) proposed a microbial water extraction mechanism, that causes a gypsum–anhydrite conversion. They claim that a "dry biofilm" and the gypsum crystal form a contact zone in which (0kk) faces are dehydrated to provide $H_2O$ for bacteria. Taking such findings into account, the diverse interaction of influences on de- and rehydration processes in natural environments such as the Atacama Desert, becomes evident.

# Acknowledgements

I would like to express my gratitude and appreciation to my supervisors, coworkers and fellow PhD students. First of all, thank you to my supervisor Prof. Dr. Petra Becker-Bohatý for providing guidance, advice and feedback throughout this project. The regular discussions of our working group were extremely helpful, as well as the supportive correspondence and review of my thesis during "Corona-times". I would also like to thank Prof. Dr. Sandro Jahn for his support and teachings. Thank you to Dr. Christoph Lenting, Dr. Maria Wierzbicka-Wieczorek, Gunter Pillunat, Steffi Seidel, Andreas Vogt, Hanna Cieszynski, Imke Wank and Jochen Scheld for their technical support or help in the laboratory. Further, I want to thank Anja Becker-Haumann for advice on literature research and Sarah Raeder and Miriam Scheld for answering all the small and big organizational questions. Thank you to Dr. Benedikt Ritter for knowing the answers to my Atacama-related questions.

Thanks to Linda Kerkhoff and Johannes Stefanski for their friendship and the great office atmosphere. I would also like to thank all of my colleagues for the pleasant time at the University of Cologne. Thanks to my partner Dario Fußmann, my parents and family, as well as old and new friends for the support and making the PhD experience more than worthwhile!

Cologne, University of Cologne Laura Maria Ritterbach

# Erklärung der Eigenständigkeit

Ich versichere, dass ich die von mir vorgelegte Dissertation selbständig angefertigt, die benutzten Quellen und Hilfsmittel vollständig angegeben und die Stellen der Arbeit – einschließlich Tabellen, Karten und Abbildungen –, die anderen Werken im Wortlaut oder dem Sinn nach entnommen sind, in jedem Einzelfall als Entlehnung kenntlich gemacht habe; dass diese Dissertation noch keiner anderen Fakultät oder Universität zur Prüfung vorgelegen hat; dass sie – abgesehen von unten angegebenen Teilpublikationen – noch nicht veröffentlicht worden ist, sowie, dass ich eine solche Veröffentlichung vor Abschluss des Promotionsverfahrens nicht vornehmen werde. Die Bestimmungen der Promotionsordnung sind mir bekannt. Die von mir vorgelegte Dissertation ist von Prof. Dr. Petra Becker-Bohatý betreut worden.

Köln, 23.02.2021

Folgende Teilpublikationen liegen vor:
Ritterbach, L., & Becker, P. (2020). Temperature and humidity dependent formation of $CaSO_4 \cdot xH_2O$ (x= 0...2) phases. Global and Planetary Change, 187, 103132.

# Bibliography


Abriel, W. (1983). Calcium sulfat subhydrat, $CaSO_4 \cdot 0.8\,H_2O$. *Acta Crystallographica Section C: Crystal Structure Communications*, 39(8):956–958.

Abriel, W., Reisdorf, K., and Pannetier, J. (1990). Dehydration reactions of gypsum: A neutron and X-ray diffraction study. *Journal of Solid State Chemistry*, 85(1):23–30.

Acheson, D. T. (1965). Vapor pressure of saturated aqueous salt solutions. *Humidity and Moisture*, 3:521.

Akahira, T. and Sunose, T. (1971). "Joint Convention of Four Electrical Institutes" Report of Research. *SciTechnol*, 16:22.

Akpokodje, E. G. (1984). The occurrence of bassanite in some Australian arid-zone soils. *Chemical Geology*, 47(3-4):361–364.

Alduchov, O. A. and Eskridge, R. E. (1996). Improved Magnus form approximation of saturation vapor pressure. *Journal of Applied Meteorology*, 35(4):601–609.

Alimi, F., Elfil, H., and Gadri, A. (2003). Kinetics of the precipitation of calcium sulfate dihydrate in a desalination unit. *Desalination*, 158(1-3):9–16.

Allen, R. D. and Kramer, H. (1953). Occurrence of bassanite in two desert basins in southeastern California.

Allmann, R. (1994). Das Verhalten von Bassanit bei Variation des äußeren Wasserdampfpartialdruckes. *European Journal of Mineralogy*, 6:3. Beiheft.

Alpers, C. N. and Brimhall, G. H. (1988). Middle Miocene climatic change in the Atacama Desert, northern Chile: Evidence from supergene mineralization at La Escondida. *Geological Society of America Bulletin*, 100(10):1640–1656.

Antao, S. (2011). Crystal-structure analysis of four mineral samples of anhydrite, $CaSO_4$, using synchrotron high-resolution powder X-ray diffraction data. *Powder Diffraction*, 26(4):326–330.

Anton Paar GmbH (2018). *Reference Guide CHC plus+*.

Arrhenius, S. (1889). Über die Reaktionsgeschwindigkeit bei der Inversion von Rohrzucker durch Säuren. *Zeitschrift für Physikalische Chemie*, 4(1):226–248.

Atkins, P. and de Paula, J. (2016). *Physical Chemistry, Volume 1: Thermodynamics and Kinetics*. Macmillan Higher Education.

Atoji, M. and Rundle, R. (1958). Neutron diffraction study of gypsum, $CaSO_4 \cdot 2\,H_2O$. *The Journal of Chemical Physics*, 29(6):1306–1311.

Augis, J. A. and Bennett, J. E. (1978). Calculation of the Avrami parameters for heterogeneous solid state reactions using a modification of the Kissinger method. *Journal of Thermal Analysis*, 13(2):283–292.

Avrami, M. (1939). Kinetics of phase change. I. General theory. *The Journal of Chemical Physics*, 7(12):1103–1112.

Avrami, M. (1940). Kinetics of phase change. II. Transformation-time relations for random distribution of nuclei. *The Journal of Chemical Physics*, 8(2):212–224.

Azimi, G., Papangelakis, V., and Dutrizac, J. (2007). Modelling of calcium sulphate solubility in concentrated multi-component sulphate solutions. *Fluid Phase Equilibria*, 260(2):300–315.

Badens, E., Llewellyn, P., Fulconis, J., Jourdan, C., Veesler, S., Boistelle, R., and Rouquerol, F. (1998). Study of gypsum dehydration by controlled transformation rate thermal analysis (CRTA). *Journal of Solid State Chemistry*, 139(1):37–44.

Ball, M. and Norwood, L. (1969). Studies in the system calcium sulphate–water. Part I. Kinetics of dehydration of calcium sulphate dihydrate. *Journal of the Chemical Society A: Inorganic, Physical, Theoretical*, pages 1633–1637.

Ball, M. and Urie, R. (1970). Studies in the system calcium sulphate–water. Part II. The kinetics of dehydration of $\beta$-$CaSO_4 \cdot \frac{1}{2}\,H_2O$. *Journal of the Chemical Society A: Inorganic, Physical, Theoretical*, pages 528–530.

Ballirano, P., Maras, A., Meloni, S., and Caminiti, R. (2001). The monoclinic *I2* structure of bassanite, calcium sulphate hemihydrate $CaSO_4 \cdot 0.5\,H_2O$. *European Journal of Mineralogy*, 13(5):985–993.

Ballirano, P. and Melis, E. (2009a). Thermal behaviour and kinetics of dehydration in air of bassanite, calcium sulphate hemihydrate ($CaSO_4 \cdot 0.5\,H_2O$), from X – ray powder diffraction. *European Journal of Mineralogy*, 21(5):985–993.

Ballirano, P. and Melis, E. (2009b). Thermal behaviour and kinetics of dehydration of gypsum in air from *in situ* real-time laboratory parallel-beam X-ray powder diffraction. *Physics and Chemistry of Minerals*, 36(7):391–402.

Ballirano, P. and Melis, E. (2009c). The thermal behaviour of $\gamma$-$CaSO_4$. *Physics and Chemistry of Minerals*, 36(6):319–327.

Bamford, C. H. and Tipper, C. F. H. (1972). *Comprehensive Chemical Kinetics: The Theory of Kinetics*, volume 13. Elsevier.

Bärnighausen, H. (1980). Group-subgroup relations between space groups: A useful tool in crystal chemistry. *MATCH, Communications in Mathematical Chemistry*, 9:139–175.

Barret, P. et al. (1973). *Cinétique hétérogène*. Gauthier-Villars.

Baumgartner, J., Dey, A., Bomans, P., Le Coadou, C., and Fratzl, P. (2013). Nucleation and growth of magnetite from solution. *Nature Materials*, 12:310–314.

Becker, R. and Döring, W. (1935). Kinetische Behandlung der Keimbildung in übersättigten Dämpfen. *Annalen der Physik*, 416(8):719–752.

Ben Mabrouk, K., Kauffmann, T. H., Aroui, H., and Fontana, M. D. (2013). Raman study of cation effect on sulfate vibration modes in solid state and in aqueous solutions. *Journal of Raman Spectroscopy*, 44(11):1603–1608.

Berenblut, B., Dawson, P., and Wilkinson, G. (1971). The Raman spectrum of gypsum. *Spectrochimica Acta Part A: Molecular Spectroscopy*, 27(9):1849–1863.

Berenblut, B., Dawson, P., and Wilkinson, G. (1973). A comparison of the Raman spectra of anhydrite $CaSO_4$ and gypsum $CaSO_4 \cdot 2\,H_2O$. *Spectrochimica Acta Part A: Molecular Spectroscopy*, 29(1):29–36.

Berthold, C., Presser, V., Huber, N., and Nickel, K. G. (2011). 1+1= 3: Coupling $\mu$-XRD$^2$ and DTA. New insights in temperature-dependent phase transitions: The gypsum–bassanite–anhydrite system as an example. *Journal of Thermal Analysis and Calorimetry*, 103(3):917–923.

Bezou, C., Nonat, A., Mutin, J.-C., Christensen, A. N., and Lehmann, M. (1995). Investigation of the crystal structure of $\gamma$-$CaSO_4$, $CaSO_4 \cdot 0.5\,H_2O$, and $CaSO_4 \cdot 0.6\,H_2O$ by powder diffraction methods. *Journal of Solid State Chemistry*, 117(1):165–176.

Bish, D. and Duffy, C. (1990). Thermogravimetric analysis of minerals. *Thermal Analysis in Clay Science*, 3:96–157.

Bish, D. L. and Reynolds Jr, R. (1989). Sample preparation for X-ray diffraction. *Modern Powder Diffraction*, 20:73–99.

Bishop, J., Lane, M., Dyar, M., King, S., Brown, A., and Swayze, G. (2014). Spectral properties of Ca-sulfates: Gypsum, bassanite, and anhydrite. *American Mineralogist*, 99(10):2105–2115.

Block, J. and Waters, O. (1968). $CaSO_4$–$Na_2SO_4$–NaCl–$H_2O$ system at 25° to 100°C. *Journal of Chemical and Engineering Data*, 13(3):336.

Bobrov, B., Romashkov, A., and Andreeva, E. (1987). The mechanism of formation and growth of crystals of a-semi water gypsum. *Bulletin of the Academy of Sciences of the USSR, Series Inorganic Substances*, 23:497–500.

Bock, E. (1961). On the solubility of anhydrous calcium sulphate and of gypsum in concentrated solutions of sodium chloride at 25°C, 30°C, 40°C, and 50°C. *Canadian Journal of Chemistry*, 39(9):1746–1751.

Boeyens, J. and Ichharam, V. (2002). Redetermination of the crystal structure of calcium sulphate dihydrate, $CaSO_4 \cdot 2\,H_2O$. *Zeitschrift für Kristallographie - New Crystal Structures*, 217(1):9–10.

Böhm, C., Reyers, M., Schween, J. H., and Crewell, S. (2020). Water vapor variability in the Atacama Desert during the 20th century. *Global and Planetary Change*, 190:103192.

Bohn, M. A. (2014). Problems and faulty uses with the Prout–Tompkins description of autocatalytic reactions and the solutions. *Journal of Thermal Analysis and Calorimetry*, 116(2):1061–1072.

Borgel, O. (1973). The coastal desert of Chile. In Amiran, D. and Wilson, A., editors, *Coastal deserts, their natural and human environments*, pages 111–114.

Borisenko, E. M. (1965). The kinetics of the dehydration of calcium sulphate dihydrate and the hydration of its dehydration products. *Russian Journal of Inorganic Chemistry*, pages 171–182.

Boswell, P. G. (1980). On the calculation of activation energies using a modified Kissinger method. *Journal of Thermal Analysis and Calorimetry*, 18(2):353–358.

Bradley, R. (1931). XXIII. Reaction rate in the system solid-solid-gas. *The London, Edinburgh, and Dublin Philosophical Magazine and Journal of Science*, 12(76):290–296.

Bradley, R. (1956). The energetics and statistical mechanics of the kinetics of solid–solid reactions. *The Journal of Physical Chemistry*, 60(10):1347–1354.

Brown, M. E. (1997). The Prout-Tompkins rate equation in solid-state kinetics. *Thermochimica Acta*, 300(1-2):93–106.

Brown, M. E., Dollimore, D., and Galwey, A. K. (1980). Reactions in the Solid State. In Bamford, C. H. and Tipper, F. H., editors, *Comprehensive Chemical Kinetics*, chapter 3. Elsevier.

Brown, M. E. and Galwey, A. K. (1979). The distinguishability of selected kinetic models for isothermal solid-state reactions. *Thermochimica Acta*, 29(1):129–146.

Brown, M. E., Galwey, A. K., Mohamed, M. A., and Tanaka, H. (1994). A mechanism for the thermal decomposition of potassium permanganate crystals based on nucleation and growth. *Thermochimica Acta*, 235(2):255–270.

Brown, M. E. and Glass, B. D. (1999). Pharmaceutical applications of the Prout–Tompkins rate equation. *International Journal of Pharmaceutics*, 190(2):129–137.

Brown, M. E. and Glass, B. D. (2003). Decomposition of solids accompanied by melting - Bawn kinetics. *International Journal of Pharmaceutics*, 254(2):255–261.

Brown, M. E., Maciejewski, M., Vyazovkin, S., Nomen, R., Sempere, J., Burnham, A., Opfermann, J., Strey, R., Anderson, H. L., Kemmler, A., et al. (2000). Computational aspects of kinetic analysis: Part A: The ICTAC kinetics project-data, methods and results. *Thermochimica Acta*, 355(1-2):125–143.

Bruker, AXS (2009). Topas V4. 2: General profile and structure analysis software for powder diffraction data. *Bruker AXS, Karlsruhe, Germany*.

Budnikoff, P. P. (1928). Die Beschleuniger und Verzögerer der Abbindegeschwindigkeit des Stuckgipses. *Kolloid-Zeitschrift*, 44(3):242–249.

Bundesverband der Gipsindustrie e.V. (2013). *GIPS-Datenbuch*.

Bushuev, N. (1982). Water of crystallization in the $CaSO_4 \cdot 0.67\,H_2O$ and $CaSO_4 \cdot 0.5\,H_2O$ structures. *Russian Journal of Inorganic Chemistry*, 27(3):344–347.

Bushuev, N., Maslennikov, B., and Borisov, V. (1983). Phase transformations in the dehydration of $CaSO_4 \cdot 2\,H_2O$. *Russian Journal of Inorganic Chemistry*, 28(10):1404–1407.

Cáceres, L., Gómez-Silva, B., Garró, X., Rodríguez, V., Monardes, V., and McKay, C. P. (2007). Relative humidity patterns and fog water precipitation in the Atacama Desert and biological implications. *Journal of Geophysical Research: Biogeosciences*, 112(G4).

Carbone, M., Ballirano, P., and Caminiti, R. (2008). Kinetics of gypsum dehydration at reduced pressure: An energy-dispersive X-ray diffraction study. *European Journal of Mineralogy*, 20(4):621–627.

Caspari, W. (1936). Calcium sulphate hemihydrate and the anhydrites. I. Crystallography. *Proceedings of the Royal Society of London. Series A - Mathematical and Physical Sciences*, 155(884):41–48.

Cavazzi, A. (1913). Das gelatinöse Kalziumsulfat und das Abbinden des Gipses. *Zeitschrift für Chemie und Industrie der Kolloide*, 12(4):196–201.

Centnerazwer, M. and Bružs, B. (1926). Zerfallsgeschwindigkeit fester Stoffe. III.: Geschwindigkeit der Dissoziation des Silberkarbonats. *Zeitschrift für Physikalische Chemie*, 123(1):111–126.

Cereceda, P., Larrain, H., Osses, P., Farías, M., and Egaña, I. (2008). The spatial and temporal variability of fog and its relation to fog oases in the Atacama Desert, Chile. *Atmospheric Research*, 87(3-4):312–323.

Chang, H., Huang, P., and Hou, S. (1999). Application of thermo-Raman spectroscopy to study dehydration of $CaSO_4 \cdot 2\,H_2O$ and $CaSO_4 \cdot 0.5\,H_2O$. *Materials Chemistry and Physics*, 58(1):12–19.

Chang, L., Howe, R., and Zussman, J. (1996). *Rock-forming minerals. Non-silicates: Sulphates, Carbonates, Phosphates, Halides*. Longman, Harlow, Essex.

Charola, A., Pühringer, J., and Steiger, M. (2006). Gypsum: A review of its role in the deterioration of building materials. *Environmental Geology*, 52(2):339–352.

Cheng, G. and Zussman, J. (1963). The crystal structure of anhydrite ($CaSO_4$). *Acta Crystallographica*, 16(8):767–769.

Chio, C. H., Sharma, S. K., and Muenow, D. W. (2004). Micro-raman studies of gypsum in the temperature range between 9K and 373K. *American Mineralogist*, 89(2-3):390–395.

Christensen, A., Jensen, T., and Nonat, A. (2010). A new calcium sulfate hemi-hydrate. *Dalton Transactions*, 39(8):2044–2048.

Christensen, A., Olesen, M., Cerenius, Y., and Jensen, T. (2008). Formation and transformation of five different phases in the $CaSO_4$–$H_2O$ system: Crystal structure of the subhydrate $\beta$-$CaSO_4 \cdot 0.5\,H_2O$ and soluble anhydrite $CaSO_4$. *Chemistry of Materials*, 20(6):2124–2132.

Christian, J. W. (2002). *The Theory of Transformations in Metals and Alloys*. Newnes.

Clarke, J. D. (2006). Antiquity of aridity in the Chilean Atacama Desert. *Geomorphology*, 73(1-2):101–114.

Clegg, S. L., Rard, J. A., and Pitzer, K. S. (1994). Thermodynamic properties of 0 – 6 mol $kg^{-1}$ aqueous sulfuric acid from 273.15 to 328.15K. *Journal of the Chemical Society, Faraday Transactions*, 90(13):1875–1894.

Clifton, J. R. (1971). Thermal Analysis of Calcium Sulfate Dihydrate and Supposed ct and P Forms of Calcium Sulfate Hemihydrate from 25 to 500°C. *Journal of Research of the National Bureau of Standards: Physics and Chemistry. Section A.*, 76:41.

Cole, W. and Lancucki, C. (1974). A refinement of the crystal structure of gypsum $CaSO_4 \cdot 2\,H_2O$. *Acta Crystallographica Section B: Structural Crystallography and Crystal Chemistry*, 30(4):921–929.

Cölfen, H. and Antonietti, M. (2005). Mesocrystals: Inorganic superstructures made by highly parallel crystallization and controlled alignment. *Angewandte Chemie International Edition*, 44(35):5576–5591.

Comel, C., Karmazsin, E., and Murat, M. (1979). Theoretical interpretation of the existence at 35°C of an absolute maximum of the hydration rate of calcium sulfate hemihydrate. *Thermochimica Acta*, 31(1):71–77.

Comodi, P., Kurnosov, A., Nazzareni, S., and Dubrovinsky, L. (2012). The dehydration process of gypsum under high pressure. *Physics and Chemistry of Minerals*, 39(1):65–71.

Comodi, P., Nazzareni, S., Zanazzi, P., and Speziale, S. (2008). High-pressure behavior of gypsum: A single-crystal X-ray study. *American Mineralogist*, 93(10):1530–1537.

Conley, R. and Bundy, W. (1958). Mechanism of gypsification. *Geochimica et Cosmochimica Acta*, 15(1-2):57–72.

Cordes, H. F. (1968). Preexponential factors for solid-state thermal decomposition. *The Journal of Physical Chemistry*, 72(6):2185–2189.

Criado, Y. A., Alonso, M., and Abanades, J. C. (2014). Kinetics of the $CaO/Ca(OH)_2$ Hydration/Dehydration Reaction for Thermochemical Energy Storage Applications. *Industrial & Engineering Chemistry Research*, 53(32):12594–12601.

Cunningham, W., Dunham, R., and Antes, L. (1952). Hydration of gypsum plaster. *Industrial & Engineering Chemistry*, 44(10):2402–2408.

D'Ans, J. (1933). *Die Lösungsgleichgewichte der Systeme der Salze ozeanischer Salzablagerungen*. Verlagsgesellschaft für Ackerbau.

D'Ans, J. (1968). Der Übergangspunkt Gips-Anhydrit. *Kali und Steinsalz*, 11:17–38.

D'Ans, J., Bredtschneider, D., Eick, H., and Freund, H. (1955). Untersuchungen über die Kalziumsulfate. *Kali und Steinsalz*, 1:17–38.

De la Torre, A., López-Olmo, M.-G., Alvarez-Rua, C., García-Granda, S., and Aranda, M. (2004). Structure and microstructure of gypsum and its relevance to Rietveld quantitative phase analyses. *Powder Diffraction*, 19(3):240–246.

De Marignac, J.-C. G. (1873). Sur la solubilité du sulfate de chaux et sur l'etat de sur saturation de ses dissolution. Annales de Chimie et de Physique.

De Waele, J., Carbone, C., Sanna, L., Vattano, M., Galli, E., and Forti, P. (2017). Secondary minerals from halite caves in the Atacama Desert (Chile). In *17th International Congress of Speleology*, number I, pages 242–246. Australian Speleological Federation.

De Waele, J., Forti, P., Picotti, V., Galli, E., Rossi, A., Brook, G., Zini, L., Cucchi, F., et al. (2009). Cave deposits in Cordillera de la Sal (Atacama, Chile). In *Geological Constrains on the Onset and Evolution of an Extreme Environment: The Atacama area. Geoacta, Special Publication*, volume 2, pages 113–117.

De Yoreo, J. (2013). Crystal nucleation: More than one pathway. *Nature Materials*, 12(4):284–285.

Deutsch, Y., Nathan, Y., and Sarig, S. (1994). Thermogravimetric evaluation of the kinetics of the gypsum–hemihydrate–soluble anhydrite transitions. *Journal of Thermal Analysis and Calorimetry*, 42(1):159–174.

Dixon, E. M., Elwood Madden, A. S., Hausrath, E. M., and Elwood Madden, M. E. (2015). Assessing hydrodynamic effects on jarosite dissolution rates, reaction products, and preservation on Mars. *Journal of Geophysical Research: Planets*, 120(4):625–642.

Dixon, J. C. and McLaren, S. J. (2009). Duricrusts. In *Geomorphology of Desert Environments*, pages 123–151. Springer.

Doebelin, N. and Kleeberg, R. (2015). Profex: A graphical user interface for the Rietveld refinement program BGMN. *Journal of Applied Crystallography*, 48(5):1573–1580.

Dong, H., Rech, J. A., Jiang, H., Sun, H., and Buck, B. J. (2007). Endolithic cyanobacteria in soil gypsum: Occurrences in Atacama (Chile), Mojave (United States), and Al-Jafr Basin (Jordan) Deserts. *Journal of Geophysical Research: Biogeosciences*, 112(G2).

Dougherty, R. C. (1998). Temperature and pressure dependence of hydrogen bond strength: A perturbation molecular orbital approach. *The Journal of Chemical Physics*, 109(17):7372–7378.

Dowdy, D. R. (1987). Meaningful activation energies for complex systems. *Journal of Thermal Analysis*, 32(1):137–147.

Drits, V. A., Zviagina, B. B., McCarty, D. K., and Salyn, A. L. (2010). Factors responsible for crystal-chemical variations in the solid solutions from illite to aluminoceladonite and from glauconite to celadonite. *American Mineralogist*, 95(2-3):348–361.

Dunai, T. J., López, G. A. G., and Juez-Larré, J. (2005). Oligocene–Miocene age of aridity in the Atacama Desert revealed by exposure dating of erosion-sensitive landforms. *Geology*, 33(4):321–324.

Dunai, T. J., Melles, M., Quandt, D., Knief, C., and Amelung, W. (2020). Whitepaper: Earth–Evolution at the dry limit. *Global and Planetary Change*, 193:103275.

Ericksen, G. E. (1981). Geology and origin of the Chilean nitrate deposits.

Ericksen, G. E. (1983). The Chilean Nitrate Deposits: The origin of the Chilean nitrate deposits, which contain a unique group of saline minerals, has provoked lively discussion for more than 100 years. *American Scientist*, 71(4):366–374.

Erofe'ev, B. (1946). Generalized equation of chemical kinetics and its application in reactions involving solids. *Proceedings of the USSR Academy of Sciences*, 52:511–514.

Evans, J. (2020). Using jEdit with Topas. `http://community.dur.ac.uk/john.evans/topas_academic/topas_main.htm`.

Fan, C., Kan, A., Fu, G., Tomson, M., Shen, D., et al. (2010). Quantitative evaluation of calcium sulfate precipitation kinetics in the presence and absence of scale inhibitors. *Spe Journal*, 15(04):977–988.

Fanfoni, M. and Tomellini, M. (1998). The Johnson-Mehl-Avrami-Kolmogorov model: A brief review. *Il Nuovo Cimento D*, 20(7-8):1171–1182.

Farnsworth, M. (1925). The Hydration of Anhydrite. *Industrial & Engineering Chemistry*, 17(9):967–970.

Fatu, D. (2001). Kinetics of gypsum dehydration. *Journal of Thermal Analysis and Calorimetry*, 65(1):213–220.

Feitknecht, W. (1931). Zur Kinetik der Umwandlung der verschiedenen Formen und Hydratstufen des Calciumsulfats (vorläufige Mitteilung). *Helvetica Chimica Acta*, 14(1):85–90.

Fernández López, S. R., Chong, G., Quinzio, L. A., and Wilke, H.-G. (1994). The upper Bajocian and Bathonian in the Cordillera de Domeyko, North-Chilean Precordillera: Sedimentological and biostratigraphical results. *Geobios*, 17:187–201.

Fernandez-Martinez, A., Román-Ross, G., Cuello, G., Turrillas, X., Charlet, L., Johnson, M., and Bardelli, F. (2006). Arsenic uptake by gypsum and calcite: Modelling and probing by neutron and X-ray scattering. *Physica B: Condensed Matter*, 385:935–937.

Fini, G. (2004). Applications of Raman spectroscopy to pharmacy. *Journal of Raman Spectroscopy*, 35(5):335–337.

Finkl, C. W. (1984). *The Encyclopedia of Applied Geology*. Van Nostrand Reinhold, New York.

FIZ Karlsruhe (2020). International Crystal Structure Database. `https://icsd.products.fiz-karlsruhe.de`.

Flahaut, J., Martinot, M., Potts, N., and Davies, G. (2015). VNIR spectroscopy of the Atacama salars: An analogue study for Mars evaporate deposits. *Europlanet Science Congress*, 84.

Flanders, D., Jacobs, E., and Pinizzotto, R. (1997). Activation energies of intermetallic growth of Sn-Ag eutectic solder on copper substrates. *Journal of Electronic Materials*, 26(7):883–887.

Flörke, O. (1952a). Die Hochtemperaturmodifikationen von Kalzium-, Strontium-und Variumsulfat. *Naturwissenschaften*, 39(20):478–479.

Flörke, O. (1952b). Kristallographische und Röntgenometrische Untersuchungen im System $CaSO_4$ – $CaSO_4 \cdot 2\,H_2O$. *Neues Jahrbuch für Mineralogie-Abhandlungen*, 4:189–240.

Flynn, J. H. and Wall, L. A. (1966). General treatment of the thermogravimetry of polymers. *Journal of Research of the National Bureau of Standards. Section A, Physics and Chemistry*, 70(6):487.

Follner, S., Wolter, A., Preusser, A., Indris, S., Silber, C., and Follner, H. (2002). The setting behaviour of $\alpha$-and $\beta$-$CaSO_4 \cdot 0.5\,H_2O$ as a function of crystal structure and morphology. *Crystal Research and Technology: Journal of Experimental and Industrial Crystallography*, 37(10):1075–1087.

Frenkel, J. (1939). A general theory of heterophase fluctuations and pretransition phenomena. *The Journal of Chemical Physics*, 7(7):538–547.

Freundlich, H. (1922). *Kapillarchemie, eine Darstellung der Chemie der Kolloide und verwandter Gebiete*. Akademische Verlagsgesellschaft.

Freyer, D. and Voigt, W. (2003). Crystallization and phase stability of $CaSO_4$ and $CaSO_4$–based salts. *Monatshefte für Chemie/Chemical Monthly*, 134(5):693–719.

Friedman, H. L. (1964). Kinetics of thermal degradation of char-forming plastics from thermogravimetry. Application to a phenolic plastic. In *Journal of Polymer Science Part C: Polymer Symposia*, volume 6, pages 183–195. Wiley Online Library.

Frost, R. L., Kloprogge, J. T., and Williams, P. A. (2003). Raman spectroscopy of lead sulphate-carbonate minerals – implications for hydrogen bonding. *Neues Jahrbuch für Mineralogie-Monatshefte*, 2003(12):529–542.

Fuentealba, E., Ferrada, P., Araya, F., Marzo, A., Parrado, C., and Portillo, C. (2015). Photovoltaic performance and LCoE comparison at the coastal zone of the Atacama Desert, Chile. *Energy Conversion and Management*, 95:181–186.

Fujii, K. and Kondo, W. (1986). Kinetics of hydration of calcium sulphate hemihydrate. *Journal of the Chemical Society*, (4):729–731.

Gallitelli, P. (1933). Calcium sulfate hemihydrate and soluble anhydrite. *Periodico di Mineralogica*, 4:1–42.

Galwey, A. K. (2003). What is meant by the term 'variable activation energy' when applied in the kinetic analyses of solid state decompositions (crystolysis reactions)? *Thermochimica Acta*, 397(1-2):249–268.

Galwey, A. K. and Brown, M. E. (1999). Kinetic models for solid-state reactions. *Studies in Physical and Theoretical Chemistry*, page 75.

Gao, Y. Q. and Wang, W. (1986). On the activation energy of crystallization in metallic glasses. *Journal of Non-Crystalline Solids*, 81(1-2):129–134.

Gardet, J.-J., Guilhot, B., and Soustelle, M. (1976). The dehydration kinetics of calcium sulphate dihydrate influence of the gaseous atmosphere and the temperature. *Cement and Concrete Research*, 6(5):697–706.

Garner, W. E. and Hailes, H. R. (1933). Thermal decomposition and detonation of mercury fulminate. *Proceedings of the Royal Society of London. Series A*, 139(839):576–595.

Garreaud, R. D., Molina, A., and Farias, M. (2010). Andean uplift, ocean cooling and Atacama hyperaridity: A climate modeling perspective. *Earth and Planetary Science Letters*, 292(1-2):39–50.

Gartner, E. M. and Gaidis, J. M. (1989). Hydration Mechanisms I. *Materials Science of Concrete*.

Gibbs, J. W. (1878). On the equilibrium of heterogeneous substances. *American Journal of Science*, (96):441–458.

Gill, A. C. (1918). Notes on the hydration of anhydrite and dead-burned gypsum. *Journal of the American Ceramic Society*, 1(1):65–71.

Ginstling, A. and Brounshtein, B. (1950). Concerning the diffusion kinetics of reactions in spherical particles. *Journal of Applied Chemistry of the USSR*, 23(12):1327–1338.

Gmelin, L. (1957). Ca: System 28, Part A. In *Gmelins Handbuch der anorganischen Chemie*, pages 244–272. Verlag Chemie GmbH.

Godfrey, L. and Álvarez-Amado, F. (2020). Volcanic and saline lithium inputs to the Salar de Atacama. *Minerals*, 10(2):201.

Gokcen, N. A. (1951). Vapor pressure of water above saturated lithium chloride solution. *Journal of the American Chemical Society*, 73(8):3789–3790.

Golikeri, S. V. and Luss, D. (1972). Analysis of activation energy of grouped parallel reactions. *American Institute of Chemical Engineers Journal*, 18(2):277–282.

Grahmann, W. (1920). Über Barytocölestin und das Verhältnis von Anhydrit zu Cölestin und Baryt. *Neues Jahrbuch für Mineralogie*, 1:1–23.

Grattan-Bellew, P. (1975). Effects of preferred orientation on X-ray diffraction patterns of gypsum. *American Mineralogist: Journal of Earth and Planetary Materials*, 60(11-12):1127–1129.

Greenspan, L. et al. (1977). Humidity fixed points of binary saturated aqueous solutions. *Journal of Research of the National Bureau of Standards*, 81(1):89–96.

Grilli Caiola, M., Ocampo-Friedmann, R., and Friedmann, E. (1993). Cytology of long-term desiccation in the desert cyanobacterium chroococcidiopsis (chroococcales). *Phycologia*, 32(5):315–322.

Groom, C. R., Bruno, I. J., Lightfoot, M. P., and Ward, S. C. (2016). The Cambridge Structural Database. *Acta Crystallographica Section B: Structural Science, Crystal Engineering and Materials*, 72(2):171–179.

Groves, A. W. (1958). *Gypsum and Anhydrite*. Overseas Geological Surveys, London.

Gualtieri, A. (2001). Synthesis of sodium zeolites from a natural halloysite. *Physics and Chemistry of Minerals*, 28(10):719–728.

Guldberg, C. M. and Waage, P. (1879). Über die chemische Affinität. *Journal für praktische Chemie*, 127:69–114.

Gunatilaka, A., Al-Temeemi, A., Saleh, A., and Nassar, N. (1985). A new occurrence of bassanite in recent evaporitic environments, Kuwait, Arabian Gulf. *Journal of the University of Kuwait (Science)*, 12:157–166.

Gurgul, S., Seng, G., and Williams, G. (2019). A kinetic and mechanistic study into the transformation of calcium sulfate hemihydrate to dihydrate. *Journal of Synchrotron Radiation*, 26(3).

Gutt, W. and Smith, M. (1967). Studies of sub-system $CaO - CaO \cdot SiO_2 - CaSO_4$. *Transactions of the British Ceramic Society*, 66(11):557.

Hamada, A. and Takeda, E. (1994). Hot-electron trapping activation energy in PMOSFET's under mechanical stress. *IEEE Electron Device Letters*, 15(1):31–32.

Hamdi-Aissa, B., Vallès, V., Aventurier, A., and Ribolzi, O. (2004). Soils and brine geochemistry and mineralogy of hyperarid desert playa, Ouargla Basin, Algerian Sahara. *Arid Land Research and Management*, 18(2):103–126.

Hand, R. (1994). The kinetics of hydration of calcium sulphate hemihydrate: A critical comparison of the models in the literature. *Cement and Concrete Research*, 24(5):885–895.

Hand, R. (1997). Calcium sulphate hydrates: A review. *British Ceramic Transactions*, 96(3):116–120.

Hanic, F., Galikova, L., Havlica, J., Kapralik, I., and Ambruz, V. (1985). Kinetics of the thermal decomposition of $CaSO_4$ in air. *Transactions and Journal of the British Ceramic Society*, 84(1):22–25.

Hansen, W. (1930). Hydration of gypsum. *Industrial & Engineering Chemistry*, 22(6):611–613.

Hardie, L. A. (1967). The gypsum–anhydrite equilibrium at one atmosphere pressure. *American Mineralogist: Journal of Earth and Planetary Materials*, 52(1-2):171–200.

Harris, J., Cousins, C., and Claire, M. (2016). Spectral identification and quantification of salts in the Atacama Desert. In *Earth Resources and Environmental Remote Sensing/GIS Applications VII*, volume 10005, page 100050I. International Society for Optics and Photonics.

Harrison, T. (2012). Experimental VNIR reflectance spectroscopy of gypsum dehydration: Investigating the gypsum to bassanite transition. *American Mineralogist*, 97(4):598–609.

Hartley, A. J., Chong, G., Houston, J., and Mather, A. E. (2005). 150 million years of climatic stability: Evidence from the Atacama Desert, northern Chile. *Journal of the Geological Society*, 162(3):421–424.

Hartman, P. (1989). On the unit cell dimensions and bond lengths of anhydrite. *European Journal of Mineralogy*, pages 721–722.

Hawthorne, F. and Ferguson, R. (1975). Anhydrous sulphates: II. Refinement of the crystal structure of anhydrite. *The Canadian Mineralogist*, 13(3):289–292.

He, S., Oddo, J. E., and Tomson, M. B. (1994). The nucleation kinetics of calcium sulfate dihydrate in NaCl solutions up to 6$m$ and 90°C. *Journal of Colloid and Interface Science*, 162(2):297–303.

Hedlin, C. and Trofimenkoff, F. (1965). Relative humidities over saturated solutions of nine salts in the temperature range from 0 to 90°F.

Heide, K. (1969). Zur thermischen Zersetzung des Gipses $CaSO_4 \cdot 2\,H_2O$. *Silikattechnik*, 20:232–243.

Hildyard, R. C., Llana-Fúnez, S., Wheeler, J., Faulkner, D. R., and Prior, D. J. (2011). Electron backscatter diffraction (EBSD) analysis of bassanite transformation textures and crystal structure produced from experimentally deformed and dehydrated gypsum. *Journal of Petrology*, 52(5):839–856.

Hill, A. E. (1937). The transition temperature of gypsum to anhydrite. *Journal of the American Chemical Society*, 59(11):2242–2244.

Hoehne, E. (1962). A more accurate determination of the crystal structure of anhydrite, $CaSO_4$. *Kristallografiya*, 7:690–700.

Hoffmeister, D. (2017). Meteorological and soil measurements of the permanent master weather station 13 - Cerros de Calate, Chile. [Accessed 2. June 2020].

Hoffmeister, D. (2018a). Meteorological and soil measurements of the permanent master weather station 23 - Cerro Constancia, Chile. [Accessed 2. June 2020].

Hoffmeister, D. (2018b). Meteorological and soil measurements of the permanent master weather station 33 - Quebrada Grande, Chile. [Accessed 2. June 2020].

Huang, W., Ertekin, E., Wang, T., Cruz, L., Dailey, M., DiRuggiero, J., and Kisailus, D. (2020). Mechanism of water extraction from gypsum rock by desert colonizing microorganisms. *Proceedings of the National Academy of Sciences*, 117(20):10681–10687.

Hudson-Lamb, D., Strydom, C., and Potgieter, J. (1996). The thermal dehydration of natural gypsum and pure calcium sulphate dihydrate (gypsum). *Thermochimica Acta*, 282:483–492.

Hulett, G. A. and Allen, L. E. (1902). The solubility of gypsum. *Journal of the American Chemical Society*, 24(7):667–679.

Institut für Arbeitsschutz der Deutschen Gesetzlichen Unfallversicherung (2003). GESTIS-Stoffdatenbank, Gefahrstoffinformationssystem der Deutschen Gesetzlichen Unfallversicherung.

Isern, E. R. and Messing, G. L. (2016). Direct foaming and seeding of highly porous, lightweight gypsum. *Journal of Materials Research*, 31(15):2244–2251.

Izumi, F. and Momma, K. (2007). Three-dimensional visualization in powder diffraction. In *Solid State Phenomena*, volume 130, pages 15–20. Trans Tech Publications.

Jacobs, P. (1997). Formation and growth of nuclei and the growth of interfaces in the chemical decomposition of solids: New insights. *The Journal of Physical Chemistry B*, 101(48):10086–10093.

Jacobs, P. and Tompkins, F. (1955). Classification and Theory of Solid Reactions. In *Chemistry of the Solid State*, chapter 7. Butterworths, London.

Jander, W. (1927). Reaktionen im festen Zustande bei höheren Temperaturen. Reaktionsgeschwindigkeiten endotherm verlaufender Umsetzungen. *Zeitschrift für anorganische und allgemeine Chemie*, 163(1):1–30.

Johnson, W. A. (1939). Reaction kinetics in processes of nucleation and growth. *Transactions of the American Institute of Mining, Metallurgical, and Petroleum Engineers Incorporated*, 135:416–458.

Jones, F. (2012). Infrared investigation of barite and gypsum crystallization: Evidence for an amorphous to crystalline transition. *CrystEngComm*, 14(24):8374–8381.

Jungers, M. C., Heimsath, A. M., Amundson, R., Balco, G., Shuster, D., and Chong, G. (2013). Active erosion–deposition cycles in the hyperarid Atacama Desert of Northern Chile. *Earth and Planetary Science Letters*, 371:125–133.

Kalikmanov, V. I. (2013). Classical nucleation theory. In *Nucleation theory*, pages 17–41. Springer.

Kalyanaraman, R., Yeatts, L. B., and Marshall, W. L. (1973). Solubility of calcium sulfate and association equilibria in $CaSO_4 + Na_2SO_4 + NaClO_4 + H_2O$ at 273 to 623 K. *The Journal of Chemical Thermodynamics*, 5(6):899–909.

Karni, J. et al. (1995). Gypsum in construction: Origin and properties. *Materials and Structures*, 28(2):92–100.

Karthika, S., Radhakrishnan, T., and Kalaichelvi, P. (2016). A review of classical and nonclassical nucleation theories. *Crystal Growth & Design*, 16(11):6663–6681.

Keattch, C. (1967). The analysis of gypsum plasters and minerals by thermogravimetry. *Journal of Applied Chemistry*, 17(1):27–28.

Kelley, K., Southard, J., and Anderson, C. (1941). *Thermodynamic properties of gypsum and its dehydration products*, volume 625. US Government Printing Office.

Kelton, K. and Greer, A. L. (2010). *Nucleation in Condensed Matter: Applications in Materials and Biology*. Elsevier.

Kelton, K. F. and Frenkel, D. (2016). Special Topic on Nucleation: New Concepts and Discoveries (Preface). *The Journal of Chemical Physics*, 145(21):1.

Khalil, A. A. (1982). Kinetics of gypsum dehydration. *Thermochimica Acta*, 55(2):201–208.

Khalil, A. A. and Gad, G. M. (1972). Gypsum plasters. I. Preparation of $\beta$-hemihydrates. *Journal of Applied Chemistry and Biotechnology*, 22(6):697–701.

Khasanov, R., Khasanova, N., Nizamutdinov, N., and Izotov, V. (2015). Insoluble anhydrite as product gypsum dehydration according to electron paramagnetic resonance spectra. In *International Multidisciplinary Scientific GeoConference: Surveying Geology & Mining Ecology Management*, pages 253–260.

Khasanov, R., Nizamutdinov, N., Khasanova, N., Gubauidullin, A., and Vinokurov, V. (2008). Low-temperature dehydration of gypsum single crystals. *Crystallography Reports*, 53(5):806–811.

Khawam, A. and Flanagan, D. R. (2005). Role of isoconversional methods in varying activation energies of solid-state kinetics: I. Isothermal kinetic studies. *Thermochimica Acta*, 429(1):93–102.

Khawam, A. and Flanagan, D. R. (2006). Solid-state kinetic models: Basics and mathematical fundamentals. *The Journal of Physical Chemistry B*, 110(35):17315–17328.

Khoo, J. Y., Williams, D. R., and Heng, J. Y. Y. (2010). Dehydration kinetics of pharmaceutical hydrate: Effects of environmental conditions and crystal forms. *Drying Technology*, 28(10):1164–1169.

Kirfel, A. and Will, G. (1980). Charge density in anhydrite, $CaSO_4$, from X-ray and neutron diffraction measurements. *Acta Crystallographica Section B: Structural Crystallography and Crystal Chemistry*, 36(12):2881–2890.

Kissinger, H. E. (1957). Reaction kinetics in differential thermal analysis. *Analytical Chemistry*, 29(11):1702–1706.

Kleeberg, R., Monecke, T., and Hillier, S. (2008). Preferred orientation of mineral grains in sample mounts for quantitative XRD measurements: How random are powder samples? *Clays and Clay Minerals*, 56(4):404–415.

Klepetsanis, P. G. and Koutsoukos, P. G. (1989). Precipitation of calcium sulfate dihydrate at constant calcium activity. *Journal of Crystal Growth*, 98(3):480–486.

Knacke, O. and Gans, W. (1977). The thermodynamics of the system $CaSO_4$–$H_2O$. *Zeitschrift für Physikalische Chemie*, 104(1-3):41–48.

Koga, N. (1994). A review of the mutual dependence of Arrhenius parameters evaluated by the thermoanalytical study of solid-state reactions: The kinetic compensation effect. *Thermochimica Acta*, 244:1–20.

Koga, N. and Criado, J. M. (1998). Kinetic analyses of solid-state reactions with a particle-size distribution. *Journal of the American Ceramic Society*, 81(11):2901–2909.

Koga, N. and Tanaka, H. (1997). Kinetics and mechanism of the isothermal dehydration of zinc acetate dihydrate. *Thermochimica Acta*, 303(1):69–76.

Kogel, J. E., Trivedi, N. C., Barker, J. M., and Krukowski, S. T. (2006). *Industrial Minerals & Rocks: Commodities, Markets, and Uses*. Society for Mining, Metallurgy, and Exploration.

Kohl, W., Lindner, H., and Franck, E. (1991). Raman spectra of water to 400°C and 3000 bar. *Berichte der Bunsengesellschaft für physikalische Chemie*, 95(12):1586–1593.

Kolmogorov, A. N. (1937). On the statistical theory of the crystallization of metals. *Bulletin of the Academy of Sciences of the USSR, Mathematical Series*, 1(3):355–359.

Kontrec, J., Kralj, D., and Brečević, L. (2002). Transformation of anhydrous calcium sulphate into calcium sulphate dihydrate in aqueous solutions. *Journal of Crystal Growth*, 240(1-2):203–211.

Korovyakov, V., Ferronskaya, A., and Chumakov, L. (2004). Gypsum materials and products (production and use). Publishing House ASV, Moscow.

Krishnamurthy, N. and Soots, V. (1971). Raman spectrum of gypsum. *Canadian Journal of Physics*, 49(7):885–896.

Kruchenko, V. (1985). Gypsum solubility in aqueous solutions of magnesium salts at 25°C, 40°C and 50°C. *Zhurnal Neorganicheskoi Khimii*, 30(6):1566–1571.

Kuntze, R. (1965). Effect of water vapor on the formation of modifications. *Canadian Journal of Chemistry*, 43(9):2522–2529.

Kuzel, H.-J. and Hauner, M. (1987). Chemical and crystallographical properties of calcium sulfate hemihydrate and anhydrite III. *Zement Kalk Gips, Edition A*, 40(12):628–32.

Lager, G., Armbruster, T., Rotella, F., Jorgensen, J., and Hinks, D. (1984). A crystallographic study of the low-temperature dehydration products of gypsum, $CaSO_4 \cdot 2\,H_2O$, hemihydrate, $CaSO_4 \cdot 0.5\,H_2O$, and $\gamma$-$CaSO_4$. *American Mineralogist*, 69(9-10):910–919.

Lanzón, M. and García-Ruiz, P. (2012). Effect of citric acid on setting inhibition and mechanical properties of gypsum building plasters. *Construction and Building Materials*, 28(1):506–511.

Lavoisier, A. (1765). Oeuvres Complètes.

Lawrence, M. G. (2005). The relationship between relative humidity and the dewpoint temperature in moist air: A simple conversion and applications. *Bulletin of the American Meteorological Society*, 86(2):225–234.

Le Châtelier, H. (1887). Recherches experimentales sur la constitution des mortiers hydrauliques (Experimental Researches on the Constitution of Hydraulic Mortars). In *Annales des Mines*, pages 345–465.

Lee, Y. F. and Dollimore, D. (1998). The identification of the reaction mechanism in rising temperature kinetic studies based on the shape of the DTG curve. *Thermochimica Acta*, 323(1-2):75–81.

Lewis, G. N. (1905). Zersetzung von Silberoxyd durch Autokatalyse. *Zeitschrift für Physikalische Chemie*, 52(1):310–326.

Lewry, A. and Williamson, J. (1994). The setting of gypsum plaster. *Journal of Materials Science*, 29(23):6085–6090.

Lide, D. R. (2004). *CRC Handbook of Chemistry and Physics*, volume 85. CRC Press.

Lilley, T. H. (1973). *Raman Spectroscopy of Aqueous Electrolyte Solutions*, pages 265–299. Springer US, Boston, MA.

Linck, G. and Jung, H. (1924). Concerning the dehydration and rehydration of gypsum. *Zeitschrift für Anorganische Allgemeine Chemie*, 142:407–417.

Liu, Y., Wang, A., and Freemen, J. (2009). Raman, MIR, and NIR spectroscopic study of calcium sulfates: Gypsum, bassanite, and anhydrite. *Lunar and Planetary Information Bulletin*, page 2128.

Lou, W., Guan, B., and Wu, Z. (2011). Dehydration behavior of FGD gypsum by simultaneous TG and DSC analysis. *Journal of Thermal Analysis and Calorimetry*, 104(2):661–669.

Lu, Z., Streets, D. G., Zhang, Q., Wang, S., Carmichael, G. R., Cheng, Y. F., Wei, C., Chin, M., Diehl, T., and Tan, Q. (2010). Sulfur dioxide emissions in China and sulfur trends in East Asia since 2000. *Atmospheric Chemistry & Physics*, 10(13).

MacDonald, G. J. (1953). Anhydrite–gypsum equilibrium relations. *American Journal of Science*, 251(12):884–898.

Macdonald, J. Y. and Hinshelwood, C. N. (1925). The formation and growth of silver nuclei in the decomposition of silver oxalate. *Journal of the Chemical Society*, 127:2764–2771.

Madgin, W. and Swales, D. (1956). Solubilities in the system $CaSO_4$–NaCl–$H_2O$ at T = 25°C and T = 35°C. *Journal of Applied Chemistry*, 6(11):482–487.

Magnus, G. (1844). Versuche über die Spannkräfte des Wasserdampfs. *Annalen der Physik*, 137(2):225–247.

Marcela, S. R., Valentina, F. L., and Pagés-Camagna, S. (2013). Copper pigment-making in the Atacama Desert (northern Chile). *Latin American Antiquity*, 24(4):467–482.

Marshall, W. L. and Slusher, R. (1966). Thermodynamics of Calcium Sulfate Dihydrate in Aqueous Sodium Chloride Solutions, 0 – 110°C. *The Journal of Physical Chemistry*, 70(12):4015–4027.

Math Works, Inc. (2019). Computer software.

May, M. and Hoffmeister, D. (2018). Hourly time-lapse images at weather station 13 - Cerros de Calate, Chile from April 2017 to September 2017. [Accessed 2. June 2020].

McAdie, H. (1964). The effect of water vapor upon the dehydration of $CaSO_4 \cdot 2\,H_2O$. *Canadian Journal of Chemistry*, 42(4):792–801.

McKay, C. P., Friedmann, E. I., Gómez-Silva, B., Cáceres-Villanueva, L., Andersen, D. T., and Landheim, R. (2003). Temperature and moisture conditions for life in the extreme arid region of the Atacama Desert: Four years of observations including the El Niño of 1997 – 1998. *Astrobiology*, 3(2):393–406.

Menzinger, M. and Wolfgang, R. (1969). The meaning and use of the Arrhenius activation energy. *Angewandte Chemie International Edition*, 8(6):438–444.

Mirwald, P. (2008). Experimental study of the dehydration reactions gypsum–bassanite and bassanite–anhydrite at high pressure: Indication of anomalous behavior of $H_2O$ at high pressure in the temperature range of 50 – 300°C. *The Journal of Chemical Physics*, 128(7):074502.

Molony, B. and Ridge, M. (1968). Kinetics of the dehydration of calcium sulphate dihydrate *in vacuo*. *Australian Journal of Chemistry*, 21(4):1063–1065.

Momma, K. and Izumi, F. (2008). VESTA: A three-dimensional visualization system for electronic and structural analysis. *Journal of Applied Crystallography*, 41(3):653–658.

Morikawa, H., Minato, I., Tomita, T., and Iwai, S. (1975). Anhydrite: A refinement. *Acta Crystallographica Section B: Structural Crystallography and Crystal Chemistry*, 31(8):2164–2165.

Moser, G., Tschamber, V., Schönnenbeck, C., Brillard, A., and Brilhac, J.-F. (2018). Kinetic Analysis and Modelling of Mg Powder Slow Combustion. Proceedings of the 3rdWorld Congress on Momentum, Heat and Mass Transfer (MHMT'18).

Murat, M. and Comel, C. (1971). Die Kinetik der Gipsdehydratation untersucht mittels der Differential-Thermo-Analyse. *Tonindustrie-Zeitung*, 95:29–35.

Murat, M., El Hajjouji, A., and Comel, C. (1987). Investigation on some factors affecting the reactivity of synthetic orthorhombic anhydrite with water. I. Role of foreign cations in solution. *Cement and Concrete Research*, 17(4):633–639.

Murray, F. (1967). On the computation of saturation vapor pressure. *Journal of Applied Meteorology*, 6:203–204.

Murray, R. (1964). Origin and diagenesis of gypsum and anhydrite. *Journal of Sedimentary Research*, 34(3):512–523.

Nakamoto, K. (2006). Infrared and Raman Spectra of Inorganic and Coordination Compounds Part A: Theory and Applications in Inorganic Chemistry. *Handbook of Vibrational Spectroscopy*.

Narayanaswamy, P. K. (1948). Influence of temperature on the Raman spectra of crystals. In *Proceedings of the Indian Academy of Sciences-Section A*, volume 28, page 40. Springer.

Navarro-González, R., Rainey, F. A., Molina, P., Bagaley, D. R., Hollen, B. J., de la Rosa, J., Small, A. M., Quinn, R. C., Grunthaner, F. J., Cáceres, L., et al. (2003). Mars-like soils in the Atacama Desert, Chile, and the dry limit of microbial life. *Science*, 302(5647):1018–1021.

Negro, A. and Stafferi, L. (1972). Sur la anetique de deshydration de quelques varietes de sulfate de calcium dihydrate. In *Eurogypsum Congress Stockholm*.

Neville, H. A. and Jones, H. C. (1929). *Volume Changes During Hydration of Gelatin, Cement and Plaster of Paris*. Number 22. Lehigh University.

Ng, W.-L. (1975). Thermal decomposition in the solid state. *Australian Journal of Chemistry*, 28(6):1169–1178.

Nic, M., Hovorka, L., Jirat, J., Kosata, B., and Znamenacek, J. (2005). *IUPAC Compendium of Chemical Terminology - The Gold Book*. International Union of Pure and Applied Chemistry.

Nicholson, S. E. (2011). *Dryland climatology*. Cambridge University Press.

Novák, P., Očenášek, J., Prušáková, L., Vavruňková, V., Savková, J., and Rezek, J. (2016). Influence of heat generated by a Raman excitation laser on the structural analysis of thin amorphous silicon film. *Applied Surface Science*, 364:302–307.

Oetzel, M., Heger, G., and Koslowski, T. (2000a). Einfluss von Umgebungsfeuchte und Temperatur auf die Phasenumwandlungen im System $CaSO_4 – H_2O$: Ein Beitrag zur Herstellung von phasenreinen Bindemitteln aus REA-Gips. *Zement Kalk Gips International*, 53(6):354–361.

Oetzel, M., Scherberich, F.-D., and Heger, G. (2000b). Heating device for high temperature X-ray powder diffraction studies under controlled water-vapour pressure (0 – 1000 mbar) and gas temperature (20 – 200°C). *Powder Diffraction*, 15(1):30–37.

Onorato, E. (1932). Semidrato del sulfato di calcio e anidrite solubile. *Periodico di Mineralogia*, 3:137.

Ossorio, M., Van Driessche, A., Pérez, P., and García-Ruiz, J. (2014). The gypsum–anhydrite paradox revisited. *Chemical Geology*, 386:16–21.

Ostwald, W. (1894). *Manual of physico-chemical measurements*. Macmillan and Company.

Ostwald, W. (1897). Studien über die Bildung und Umwandlung fester Körper. *Zeitschrift für Physikalische Chemie*, 22:289–330.

Ozawa, T. (1965). A new method of analyzing thermogravimetric data. *Bulletin of the Chemical Society of Japan*, 38(11):1881–1886.

Packter, A. (1974). The precipitation of calcium sulphate dihydrate from aqueous solution: Induction periods, crystal numbers and final size. *Journal of Crystal Growth*, 21(2):191–194.

Palacio, S., Azorín, J., Montserrat-Martí, G., and Ferrio, J. (2014). The crystallization water of gypsum rocks is a relevant water source for plants. *Nature Communications*, 5:4660.

Partridge, E. P. and White, A. H. (1929). The solubility of calcium sulfate from 0 to 200°C. *Journal of the American Chemical Society*, 51(2):360–370.

Pattrick, R. (2001). Sulfate Minerals: Crystallography, Geochemistry and Environmental Significance. *Reviews in Mineralogy and Geochemistry*, 40(6):817–818.

Paulik, F., Paulik, J., and Arnold, M. (1992). Thermal decomposition of gypsum. *Thermochimica Acta*, 200:195–204.

Pedersen, B. and Semmingsen, D. (1982). Neutron diffraction refinement of the structure of gypsum, $CaSO_4 \cdot 2\,H_2O$. *Acta Crystallographica Section B: Structural Crystallography and Crystal Chemistry*, 38(4):1074–1077.

Pelletier, M. (2003). Quantitative analysis using Raman spectrometry. *Applied Spectroscopy*, 57(1):20A–42A.

Perez-Maqueda, L., Criado, J., and Sanchez-Jimenez, P. (2006). Combined kinetic analysis of solid-state reactions: A powerful tool for the simultaneous determination of kinetic parameters and the kinetic model without previous assumptions on the reaction mechanism. *The Journal of Physical Chemistry A*, 110(45):12456–12462.

Polak, A. F. (1960). Kinetics of hydration and of intergrowth structure crystallization development of monomineral binding substances of the gypsum type. *Kolloidnyi Zhurna*, 22(6):689–701.

Polanyi, M. and Wigner, E. (1928). The interference of characteristic vibrations as the cause of energy fluctuations and chemical change. *Zeitschrift für Physikalische Chemie*, 139:439.

Posnjak, E. (1938). The system $CaSO_4$–$H_2O$. *American Journal of Science*.

Powell, D. (1958). Transformation of the $\alpha$-and $\beta$-forms of calcium sulphate hemihydrate to insoluble anhydrite. *Nature*, 182(4638):792–792.

Power, W., Fabuss, B., and Satterfield, C. (1966). Transient Solubilities and Phase Changes of Calcium Sulfate in Aqueous Sodium Chloride. *Journal of Chemical and Engineering Data*, 11(2):149–154.

Prasad, P. (1999). Raman intensities near gypsum–bassanite transition in natural gypsum. *Journal of Raman spectroscopy*, 30(8):693–696.

Prasad, P., Chaitanya, V., Prasad, K., and Rao, D. (2005). Direct formation of the $\gamma$-$CaSO_4$ phase in dehydration process of gypsum: *In situ* FTIR study. *American Mineralogist*, 90(4):672–678.

Prasad, P., Pradhan, A., and Gowd, T. (2001). *In situ* micro-Raman investigation of dehydration mechanism in natural gypsum. *Current Science*, pages 1203–1207.

Pratap, A., Rao, T. S., Lad, K. N., and Dhurandhar, H. D. (2007). Isoconversional vs. Model fitting methods. *Journal of Thermal Analysis and Calorimetry*, 89(2):399–405.

Preturlan, J. G., Vieille, L., Quiligotti, S., and Favergeon, L. (2019). Comprehensive thermodynamic study of the calcium sulfate–water vapor system. Part 1: Experimental measurements and phase equilibria. *Industrial & Engineering Chemistry Research*, 58(22):9596–9606.

Pries, J., Wei, S., Wuttig, M., and Lucas, P. (2019). Switching between crystallization from the glassy and the undercooled liquid phase in phase change material $Ge_2Sb_2Te_5$. *Advanced Materials*, 31(39):1900784.

Prieto-Taboada, N., Gomez-Laserna, O., Martinez-Arkarazo, I., Olazabal, M. A., and Madariaga, J. M. (2014). Raman spectra of the different phases in the $CaSO_4$–$H_2O$ system. *Analytical Chemistry*, 86(20):10131–10137.

Prout, E. and Tompkins, F. C. (1944). The thermal decomposition of potassium permanganate. *Transactions of the Faraday Society*, 40:488–498.

Provis, J. L. (2016). On the use of the Jander equation in cement hydration modelling. *RILEM Technical Letters*, 1:62–66.

Putnis, A., Winkler, B., and Fernandez-Diaz, L. (1990). *In situ* IR spectroscopic and thermogravimetric study of the dehydration of gypsum. *Mineralogical Magazine*, 54(374):123–128.

Raju, K. U. and Atkinson, G. (1990). The thermodynamics of "scale" mineral solubilities. 3. Calcium sulfate in aqueous sodium chloride. *Journal of Chemical and Engineering Data*, 35(3):361–367.

Ramsdell, L. and Partridge, E. (1929). The crystal forms of calcium sulphate. *American Mineralogist: Journal of Earth and Planetary Materials*, 14(2):59–74.

Rapin, W., Meslin, P.-Y., Maurice, S., Vaniman, D., Nachon, M., Mangold, N., Schröder, S., Gasnault, O., Forni, O., Wiens, R., et al. (2016). Hydration state of calcium sulfates in Gale crater, Mars: Identification of bassanite veins. *Earth and Planetary Science Letters*, 452:197–205.

Rashad, M., Mahmoud, M., Ibrahim, I., and Abdel-Aal, E. (2004). Crystallization of calcium sulfate dihydrate under simulated conditions of phosphoric acid production in the presence of aluminum and magnesium ions. *Journal of Crystal Growth*, 267(1-2):372–379.

Rech, J. A., Quade, J., and Hart, W. S. (2003). Isotopic evidence for the source of Ca and S in soil gypsum, anhydrite and calcite in the Atacama Desert, Chile. *Geochimica et Cosmochimica Acta*, 67(4):575–586.

Reich, M., Palacios, C., Vargas, G., Luo, S., Cameron, E. M., Leybourne, M. I., Parada, M. A., Zúñiga, A., and You, C.-F. (2009). Supergene enrichment of copper deposits since the onset of modern hyperaridity in the Atacama Desert, Chile. *Mineralium Deposita*, 44(5):497.

Renishaw (2019). *WiRE 5 Manual*.

Richardson, G. and Malthus, R. (1955). Salts for static control of humidity at relatively low levels. *Journal of Applied Chemistry*, 5(10):557–567.

Ridge, M. (1959). Effect of temperature on the rate of setting of gypsum plaster. *Nature*, 184(4679):47–48.

Ridge, M. (1964). Hydration of calcium sulphate hemihydrate. *Nature*, 204(4953):70–71.

Ridge, M. (1965). Hydration of calcium sulphate hemihydrate. *Nature*, 205(4977):1209–1209.

Ridge, M. and Surkevicius, H. (1962). Hydration of calcium sulphate hemihydrate. I. Kinetics of the reaction. *Journal of Applied Chemistry*, 12(6):246–252.

Ritter, B. (2020). Private communication.

Ritterbach, L. and Becker, P. (2020). Temperature and humidity dependent formation of $CaSO_4 \cdot xH_2O$ (x= 0... 2) phases. *Global and Planetary Change*, 187:103132.

Robertson, K. and Bish, D. (2007). The dehydration kinetics of gypsum: The effect of relative humidity on its stability and implications in the Martian environment. In *Lunar and Planetary Science Conference*, volume 38, page 1432.

Robertson, K. and Bish, D. (2013). Constraints on the distribution of CaSO4 · nH2O phases on Mars and implications for their contribution to the hydrological cycle. *Icarus*, 223(1):407–417.

Rutllant, J. A., Masotti, I., Calderón, J., and Vega, S. A. (2004). A comparison of spring coastal upwelling off central Chile at the extremes of the 1996 – 1997 ENSO cycle. *Continental Shelf Research*, 24(7-8):773–787.

Saha, A., Lee, J., Pancera, S. M., Braeu, M. F., Kempter, A., Tripathi, A., and Bose, A. (2012). New insights into the transformation of calcium sulfate hemihydrate to gypsum using time-resolved cryogenic transmission electron microscopy. *Langmuir*, 28(30):11182–11187.

Samoilov, Dudnikova, K. (1963). Solubility of gypsum in aqueous solutions of salting-out agents. *Soviet Radiochemistry*, (5):644–646.

Sarma, L., Prasad, P., and Ravikumar, N. (1998). Raman spectroscopic study of phase transitions in natural gypsum. *Journal of Raman Spectroscopy*, 29(9):851–856.

Sborgi, U. and Bianchi, C. (1940). The solubilities, conductivities and X-ray analyses of anhydrous and semihydrated calcium sulphate. *Gazzetta Chimica Italiana*, 70:823–835.

Schiller, K. (1962). Mechanism of re-crystallisation in calcium sulphate hemihydrate plasters. *Journal of Applied Chemistry*, 12(3):135–144.

Schlüter, J. and Malcherek, T. (2007). Haydeeite, $Cu_3Mg(OH)_6Cl_2$, a new mineral from the Haydee mine, Salar Grande, Atacama desert, Chile. *Neues Jahrbuch für Mineralogie-Abhandlungen: Journal of Mineralogy and Geochemistry*, 184(1):39–43.

Schmalzried, H. and Pelton, A. (1981). *Solid state reactions*. Verlag Chemie Weinheim.

Schmid, T., Jungnickel, R., and Dariz, P. (2020). Insights into the $CaSO_4$–$H_2O$ System: A Raman-Spectroscopic Study. *Minerals*, 10(2):115.

Schmidt, H., Paschke, I., Freyer, D., and Voigt, W. (2011). Water channel structure of bassanite at high air humidity: Crystal structure of $CaSO_4 \cdot 0.625\,H_2O$. *Acta Crystallographica Section B: Structural Science*, 67(6):467–475.

Schofield, P., Wilson, C., Knight, K., and Stretton, I. (2000). Temperature related structural variation of the hydrous components in gypsum. *Zeitschrift für Kristallographie - Crystalline Materials*, 215(12):707–710.

Schween, J. H., Hoffmeister, D., and Löhnert, U. (2020). Filling the observational gap in the Atacama Desert with a new network of climate stations. *Global and Planetary Change*, 184:103034.

Seidell, A. and Smith, J. G. (1904). The solubility of calcium sulphate in solutions of nitrates. *The Journal of Physical Chemistry*, 8(7):493–499.

Serafeimidis, K. and Anagnostou, G. (2015). The solubilities and thermodynamic equilibrium of anhydrite and gypsum. *Rock Mechanics and Rock Engineering*, 48(1):15–31.

Šesták, J. (1984). *Thermophysical properties of solids: Their measurements and theoretical thermal analysis*, volume 12. Elsevier.

Šesták, J. and Berggren, G. (1971). Study of the kinetics of the mechanism of solid-state reactions at increasing temperatures. *Thermochimica Acta*, 3(1):1–12.

Seufert, S., Hesse, C., Goetz-Neunhoeffer, F., and Neubauer, J. (2009). Discrimination of bassanite and anhydrite III dehydrated from gypsum at different temperatures. *Zeitschrift für Kristallographie*, 30:447–452.

Shannon, R. D. (1964). Activated complex theory applied to the thermal decomposition of solids. *Transactions of the Faraday Society*, 60:1902–1913.

Shi, C., Roy, D., and Krivenko, P. (2003). *Alkali-activated Cements and Concretes*. CRC press.

Shternina, E. (1949). Solubility of gypsum in salt solutions. *Proceedings of the USSR Academy of Sciences*, 17:351–369.

Shternina, E. (1957). Maximums on the solubility isotherms for calcium sulfate and calcium carbonate. *Zhurnal Neorganicheskoi Khimii*, 2:933–937.

Sievert, T., Wolter, A., and Singh, N. (2005). Hydration of anhydrite of gypsum ($CaSO_4$.II) in a ball mill. *Cement and Concrete Research*, 35(4):623–630.

Sillitoe, R. H. and McKee, E. H. (1996). Age of supergene oxidation and enrichment in the Chilean porphyry copper province. *Economic Geology*, 91(1):164–179.

Šimon, P. (2009). Material stability predictions applying a new non-Arrhenian temperature function. *Journal of Thermal analysis and Calorimetry*, 97(2):391–396.

Singh, N. and Middendorf, B. (2007). Calcium sulphate hemihydrate hydration leading to gypsum crystallization. *Progress in Crystal Growth and Characterization of Materials*, 53(1):57–77.

Skoulika, S. G. and Georgiou, C. A. (2001). Rapid quantitative determination of ciprofloxacin in pharmaceuticals by use of solid-state FT-Raman spectroscopy. *Applied Spectroscopy*, 55(9):1259–1265.

Skrdla, P. J. (2004). Use of coupled rate equations to describe nucleation-and-branching rate-limited solid-state processes. *The Journal of Physical Chemistry A*, 108(32):6709–6712.

Skrdla, P. J. and Robertson, R. T. (2007). Dispersive kinetic models for isothermal solid-state conversions and their application to the thermal decomposition of oxacillin. *Thermochimica Acta*, 453(1):14–20.

Smeets, P. J., Finney, A. R., Habraken, W. J., Nudelman, F., Friedrich, H., Laven, J., De Yoreo, J. J., Rodger, P. M., and Sommerdijk, N. A. (2017). A classical view on nonclassical nucleation. *Proceedings of the National Academy of Sciences*, 114(38):E7882–E7890.

Sosso, G. C., Chen, J., Cox, S. J., Fitzner, M., Pedevilla, P., Zen, A., and Michaelides, A. (2016). Crystal nucleation in liquids: Open questions and future challenges in molecular dynamics simulations. *Chemical Reviews*, 116(12):7078–7116.

Southard, J. (1940). Heat of hydration of calcium sulfates. *Industrial & Engineering Chemistry*, 32(3):442–445.

Stanley, K. K. and Luzio, J. P. (1978). The Arrhenius plot behaviour of rat liver 5-nucleotidase in different lipid environments. *Biochimica et Biophysica Acta (BBA)-Biomembranes*, 514(2):198–205.

Starink, M. J. (1997). On the applicability of isoconversion methods for obtaining the activation energy of reactions within a temperature-dependent equilibrium state. *Journal of Materials Science*, 32(24):6505–6512.

Stawski, T. M., Besselink, R., Chatzipanagis, K., Hövelmann, J., Benning, L. G., and Van Driessche, A. (2020). Nucleation pathway of calcium sulfate hemihydrate (bassanite) from solution: Implications for calcium sulfates on Mars. *The Journal of Physical Chemistry C*, 124(15):8411–8422.

Stawski, T. M., van Driessche, A. E., Ossorio, M., Rodriguez-Blanco, J. D., and Benning, L. G. (2016). Formation of calcium sulfate through the aggregation of sub-3 nm anhydrous primary species. *Nature Communications*.

Stokes, R. and Robinson, R. (1949). Standard solutions for humidity control at 25°C. *Industrial & Engineering Chemistry*, 41(9):2013–2013.

Strachan, C. J., Rades, T., Gordon, K. C., and Rantanen, J. (2007). Raman spectroscopy for quantitative analysis of pharmaceutical solids. *Journal of Pharmacy and Pharmacology*, 59(2):179–192.

Strydom, C., Hudson-Lamb, D., Potgieter, J., and Dagg, E. (1995). The thermal dehydration of synthetic gypsum. *Thermochimica Acta*, 269:631–638.

Tang, Y., Gao, J., Liu, C., Chen, X., and Zhao, Y. (2019). Dehydration pathways of gypsum and the rehydration mechanism of soluble anhydrite $\gamma$-$CaSO_4$. *ACS Omega*, 4(4):7636–7642.

Taplin, J. (1965). Hydration kinetics of calcium sulphate hemihydrate. *Nature*, 205(4974):864–866.

Taylor, J. and Baines, J. (1970). Kinetics of the calcination of calcium sulphate dihydrate. *Journal of Applied Chemistry*, 20(4):121–122.

Taylor, L. S. and York, P. (1998). Effect of particle size and temperature on the dehydration kinetics of trehalose dihydrate. *International Journal of Pharmaceutics*, 167(1-2):215–221.

Tekkouk, A., Karmazsin, E., and Samai, M. L. (2012). Theoretical interpretation of the existence at 40°C of an absolute maximum of the hydration rate of calcium sulphate hemi hydrate under microwave irradiation. *Open Journal of Civil Engineering*, 2(2):49–52.

Thanh, N. T., Maclean, N., and Mahiddine, S. (2014). Mechanisms of nucleation and growth of nanoparticles in solution. *Chemical Reviews*, 114(15):7610–7630.

Thompson, C. V. and Spaepen, F. (1979). On the approximation of the free energy change on crystallization. *Acta Metallurgica*, 27(12):1855–1859.

Topley, B. (1932). The mechanism and molecula statistics of the reaction $CuSO_4 \cdot 5\,H_2O = CuSO_4 \cdot H_2O + 4\,H_2O$. *Proceedings of the Royal Society of London. Series A*, 136(829):413–428.

Traube, J. (1919). Kolloide Vorgänge beim Binden des Gipses, Strukturen in Gips. *Kolloid-Zeitschrift*, 25(2):62–66.

Tritschler, U., Kellermeier, M., Debus, C., Kempter, A., and Cölfen, H. (2015a). A simple strategy for the synthesis of well-defined bassanite nanorods. *CrystEngComm*, 17(20):3772–3776.

Tritschler, U., Van Driessche, A. E., Kempter, A., Kellermeier, M., and Cölfen, H. (2015b). Controlling the selective formation of calcium sulfate polymorphs at room temperature. *Angewandte Chemie International Edition*, 54(13):4083–4086.

Truhlar, D. G. and Kohen, A. (2001). Convex Arrhenius plots and their interpretation. *Proceedings of the National Academy of Sciences*, 98(3):848–851.

Turnbull, D. and Fisher, J. C. (1949). Rate of nucleation in condensed systems. *The Journal of Chemical Physics*, 17(1):71–73.

Vakhlu, V., Bassi, P., and Mehta, S. (1985). Thermoanalytical studies on gypsum dehydration. *Transactions of the Indian Ceramic Society*, 44(2):29–32.

Valero-Garcés, B. L., Grosjean, M., Kelts, K., Schreier, H., and Messerli, B. (1999). Holocene lacustrine deposition in the Atacama Altiplano: Facies models, climate and tectonic forcing. *Palaeogeography, Palaeoclimatology, Palaeoecology*, 151(1-3):101–125.

Van Driessche, A., Benning, L., Rodriguez-Blanco, J., Ossorio, M., Bots, P., and García-Ruiz, J. (2012). The role and implications of bassanite as a stable precursor phase to gypsum precipitation. *Science*, 336(6077):69–72.

Van Driessche, A., Stawski, T., Benning, L., and Kellermeier, M. (2017). Calcium sulfate precipitation throughout its phase diagram. In *New Perspectives on Mineral Nucleation and Growth*, pages 227–256. Springer.

Vaniman, D., Bish, D., and Chipera, S. (2009). Bassanite on Mars. In *Lunar and Planetary Science*, volume 40.

Vaniman, D. T., Martínez, G. M., Rampe, E. B., Bristow, T. F., Blake, D. F., Yen, A. S., Ming, D. W., Rapin, W., Meslin, P.-Y., Morookian, J. M., et al. (2018). Gypsum, bassanite, and anhydrite at Gale crater, Mars. *American Mineralogist: Journal of Earth and Planetary Materials*, 103(7):1011–1020.

Van't Hoff, J., Armstrong, E., Hinrichsen, W., Weigert, F., and Just, G. (1903). Gips und Anhydrit. *Zeitschrift für Physikalische Chemie*, 45:257–306.

Van't Hoff, J. H. (1896). *Études de dynamique chimique*. F. Mueller.

Vargas, G., Ortlieb, L., and Rutllant, J. (2000). Aluviones históricos en Antofagasta y su relación con eventos El Niño/oscilación del Sur. *Revista geológica de Chile*, 27(2):157–176.

Venkatesh, M., Ravi, P., and Tewari, S. P. (2013). Isoconversional kinetic analysis of decomposition of nitroimidazoles: Friedman method vs Flynn–Wall–Ozawa method. *The Journal of Physical Chemistry A*, 117(40):10162–10169.

Vermeulen, A. C. (2005). The Sensitivity of Focusing, Parallel Beam and Mixed Optics to Alignment Errors in XRD Residual Stress Measurements. In *Materials Science Forum*, volume 490, pages 131–136. Trans Tech Publications.

Vítek, P., Ascaso, C., Artieda, O., and Wierzchos, J. (2016). Raman imaging in geomicrobiology: endolithic phototrophic microorganisms in gypsum from the extreme sun irradiation area in the Atacama Desert. *Analytical and bioanalytical chemistry*, 408(15):4083–4092.

Vítek, P., Cámara-Gallego, B., Edwards, H. G., Jehlička, J., Ascaso, C., and Wierzchos, J. (2013). Phototrophic community in gypsum crust from the Atacama Desert studied by Raman spectroscopy and microscopic imaging. *Geomicrobiology Journal*, 30(5):399–410.

Voigt, C., Klipsch, S., Herwartz, D., Chong, G., and Staubwasser, M. (2020). The spatial distribution of soluble salts in the surface soil of the Atacama Desert and their relationship to hyperaridity. *Global and Planetary Change*, 184:103077.

Voigtländer, H., Winkler, B., Depmeier, W., Knorr, K., and Ehm, L. (2003). Host–Guest Interactions in Bassanite, $CaSO_4 \cdot 0.5\,H_2O$. In *Host-Guest-Systems Based on Nanoporous Crystals*, pages 280–305. Wiley Online Library.

Volmer, M. and Weber, A. (1926). Keimbildung in übersättigten Gebilden. *Zeitschrift für Physikalische Chemie*, 119(1):277–301.

Vyazovkin, S. (1997). Advanced isoconversional method. *Journal of Thermal Analysis and Calorimetry*, 49(3):1493–1499.

Vyazovkin, S. (2000). Kinetic concepts of thermally stimulated reactions in solids: A view from a historical perspective. *International Reviews in Physical Chemistry*, 19(1):45–60.

Vyazovkin, S., Burnham, A. K., Criado, J. M., Pérez-Maqueda, L. A., Popescu, C., and Sbirrazzuoli, N. (2011). ICTAC Kinetics Committee recommendations for performing kinetic computations on thermal analysis data. *Thermochimica Acta*, 520(1-2):1–19.

Vyazovkin, S. and Sbirrazzuoli, N. (2006). Isoconversional kinetic analysis of thermally stimulated processes in polymers. *Macromolecular Rapid Communications*, 27(18):1515–1532.

Vyazovkin, S. and Wight, C. (1997). Kinetics in solids. *Annual Review of Physical Chemistry*, 48(1):125–149.

Vyazovkin, S. and Wight, C. A. (1998). Isothermal and non-isothermal kinetics of thermally stimulated reactions of solids. *International Reviews in Physical Chemistry*, 17(3):407–433.

Walk, J., Stauch, G., Reyers, M., Vásquez, P., Sepúlveda, F. A., Bartz, M., Hoffmeister, D., Brückner, H., and Lehmkuhl, F. (2020). Gradients in climate, geology, and topography affecting coastal alluvial fan morphodynamics in hyperarid regions – the Atacama perspective. *Global and Planetary Change*, 185:102994.

Wang, Y.-W., Kim, Y.-Y., Christenson, H. K., and Meldrum, F. C. (2012). A new precipitation pathway for calcium sulfate dihydrate (gypsum) via amorphous and hemihydrate intermediates. *Chemical Communications*, 48(4):504–506.

Warren-Rhodes, K., Weinstein, S., Dohm, J., Piatek, J., Minkley, E., Hock, A., Cockell, C., Pane, D., Ernst, L., Fisher, G., et al. (2007). Searching for microbial life remotely: Satellite-to-rover habitat mapping in the Atacama Desert, Chile. *Journal of Geophysical Research: Biogeosciences*, 112(G4).

Watson, A. (1979). Gypsum crusts in deserts. *Journal of Arid Environments*, 2(1):3–20.

Wei, J., Wang, A., Lambert, J. L., Wettergreen, D., Cabrol, N., Warren-Rhodes, K., and Zacny, K. (2015). Autonomous soil analysis by the Mars Micro-beam Raman Spectrometer (MMRS) on-board a rover in the Atacama Desert: A terrestrial test for planetary exploration. *Journal of Raman Spectroscopy*, 46(10):810–821.

Weinberg, M. C., Birnie III, D. P., and Shneidman, V. A. (1997). Crystallization kinetics and the JMAK equation. *Journal of Non-Crystalline Solids*, 219:89–99.

Weiser, H., Milligan, W., and Ekholm, W. (1936). The mechanism of the dehydration of calcium sulfate hemihydrate. *Journal of the American Chemical Society*, 58(7):1261–1265.

Weiser, H. and Moreland, F. (1932). The setting of plaster of Paris. *The Journal of Physical Chemistry*, 36(1):1–30.

Weiss, H. and Braeu, M. (2009). How much water does calcined gypsum contain? *Angewandte Chemie International Edition*, 48(19):3520–3524.

Wierzchos, J., Cámara, B., de Los Rios, A., Davila, A., Sánchez Almazo, I., Artieda, O., Wierzchos, K., Gomez-Silva, B., McKay, C., and Ascaso, C. (2011). Microbial colonization of Ca-sulfate crusts in the hyperarid core of the Atacama Desert: Implications for the search for life on Mars. *Geobiology*, 9(1):44–60.

Williams, M. (2006). The Merck Index: An Encyclopedia of Chemicals, Drugs, and Biologicals.

Wilson, R. E. (1921). Some new methods for the determination of the vapor pressure of salt-hydrates. *Journal of the American Chemical Society*, 43(4):704–725.

Wilson, S. A. and Bish, D. L. (2011). Formation of gypsum and bassanite by cation exchange reactions in the absence of free-liquid H2O: Implications for Mars. *Journal of Geophysical Research: Planets*, 116(E9).

Wirsching, F. (2000). Calcium sulfate. In *Ullmann's Encyclopedia of Industrial Chemistry*, pages 519–550. Wiley Online Library.

Wojdyr, M. (2010). Fityk: A general-purpose peak fitting program. *Journal of Applied Crystallography*, 43(5-1):1126–1128.

Wondratschek, H., Müller, U., and International Union of Crystallography (2004). *International Tables for Crystallography*. Kluwer Academic.

Wooster, W. (1936). On the Crystal Structure of Gypsum, $CaSO_4 \cdot 2\,H_2O$. *Zeitschrift für Kristallographie – Crystalline Materials*, 94(1-6):375–396.

Wray, J. J., Squyres, S. W., Roach, L. H., Bishop, J. L., Mustard, J. F., and Dobrea, E. Z. N. (2010). Identification of the Ca-sulfate bassanite in Mawrth Vallis, Mars. *Icarus*, 209(2):416–421.

Yeatts, L. B. and Marshall, W. L. (1969). Aqueous systems at high temperature. XXI. Apparent invariance of activity coefficients of calcium sulfate at constant ionic strength and temperature in the system calcium sulfate–sodium sulfate–sodium nitrate–water to the critical temperature of water. Association equilibriums. *The Journal of Physical Chemistry*, 73(1):81–90.

Yechieli, Y. and Wood, W. W. (2002). Hydrogeologic processes in saline systems: Playas, sabkhas, and saline lakes. *Earth-Science Reviews*, 58(3-4):343–365.

Young, D. (1966). *Decomposition of Solids*. Pergamon Press Oxford.

Young, J. F. (1967). Humidity control in the laboratory using salt solutions – A review. *Journal of Applied Chemistry*, 17(9):241–245.

Zambonini, F. (1910). XXX. Krystallographische Untersuchung anorganischer Verbindungen. *Zeitschrift für Kristallographie – Crystalline Materials*, 47(1-6):620–629.

Zanbak, C. and Arthur, R. (1986). Geochemical and engineering aspects of anhydrite/gypsum phase transitions. *Bulletin of the Association of Engineering Geologists*, 23(4):419–433.

Zdanovskii, A. and Vlasov, G. (1968). Determination of the boundaries of the reciprocal transformation of $CaSO_4 \cdot 2\,H_2O$ and $\gamma$-$CaSO_4$ in $H_2SO_4$ solutions. *Russian Journal of Inorganic Chemistry*, 13:1318–1319.

Zen, E. (1965). Solubility Measurements in the System $CaSO_4 - NaCl - H_2O$ at 35, 50, and 70°C and one atmosphere Pressure. *Journal of Petrology*, 6(1):124–164.

Zhang, D., Lan, G., Hu, S., Wang, H., and Zheng, J. (1995). Raman scattering study of benzophenone under high pressure. *Journal of Physics and Chemistry of Solids*, 56(1):27–33.

Zhang, Y. and Muhammed, M. (1989). Solubility of calcium sulfate dihydrate in nitric acid solutions containing calcium nitrate and phosphoric acid. *Journal of Chemical and Engineering Data*, 34(1):121–124.

Zhu, H. and Grant, D. J. W. (2001). Dehydration behavior of nedocromil magnesium pentahydrate. *International Journal of Pharmaceutics*, 215(1-2):251–262.

# Appendix A

## Classical Nucleation Theory (CNT)

Underpinned by Gibbs' thermodynamic calculations of droplet formation in a supersaturated vapor in the late 1800s, Volmer and Weber derived kinetic aspects of the classical nucleation theory for vapor condensation in the early 1900s (Gibbs, 1878; Volmer and Weber, 1926). Further fundamental contributions were made by Becker and Döring (1935) and Frenkel (1939). Some years later, Turnbull and Fisher (1949) extended the theory to nucleation phenomena in condensed matters. Modern research including computer simulations and experimental studies have shown that the CNT is improper and, depending on the system, incorrect (Kelton and Frenkel, 2016). Regardless, most nucleation data are analyzed within the CNT framework (Karthika et al., 2016; Kelton and Frenkel, 2016).

Under the use of (outdated) simplifying assumptions and approximations - like the merest nucleus having the same properties as the crystalline phase - the theory constitutes that nuclei must surpass a critical nucleus size $n^*$ and, therefore, a critical Gibbs free energy barrier $\Delta G^*$ to grow and form a mature thermodynamic bulk phase.

Figure A-1 illustrates the dependence of the nucleation barrier $\Delta G^*$ on the nucleus radius $r^*$. With the Arrhenius equation (Arrhenius, 1889) and knowledge of $\Delta G^*$, the nucleation rate is reasonably well predicted (Karthika et al., 2016). The corresponding equation of homogeneous, liquid phase nucleation in is given by

$$\Delta G = \Delta G_V + \Delta G_O \tag{A-1}$$

$$\Delta G_O = 4\pi r^2 \sigma \tag{A-2}$$

$$\Delta G_V = \frac{-4\pi r^3 \rho}{4} \cdot \Delta g_V \tag{A-3}$$

with bulk free energy $\Delta G$, volume energy $\Delta G_V$, interfacial energy $\Delta G_O$, radius $r$, specific surface energy $\sigma$, phase density $\rho$ and specific Gibbs free energy difference $\Delta g_V$ (Sosso et al., 2016).

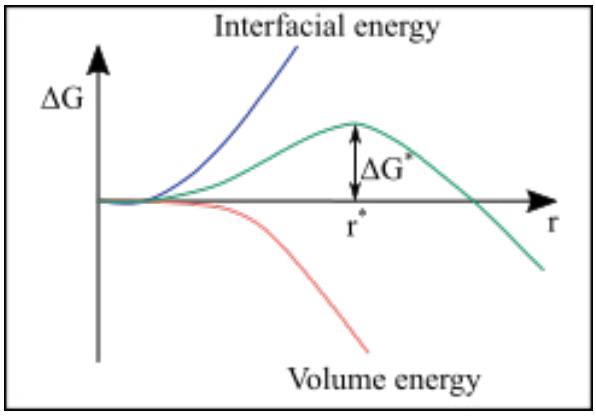


**Figure A-1:** Nucleation barrier $\Delta G$ vs. nucleus radius $r$ according to classical nucleation theory.

The latter is proportional to the supercooling $\Delta T = T - T_m$ where $T_m$ is the melting temperature. Several approximations for the temperature dependence of $\Delta g_V$ are available that depend on the supercooled liquid (Thompson and Spaepen, 1979). After differentiating $\Delta G$ with respect to $r$, $\Delta G^*$ is yielded with

$$\Delta G^* = \frac{16\pi\sigma^3}{3\Delta g^2}. \tag{A-4}$$

The nucleation rate $J$ is given by the Arrhenius equation (reaction velocity) where $k_B$ is the Boltzmann constant and $A$ is the so called pre-exponential factor and obtained by kinetic experiments, respectively considerations (Kalikmanov, 2013; Sosso et al., 2016)

$$J = A \exp\left(\frac{\Delta G^*}{k_B T}\right). \tag{A-5}$$

The following sections focus on several studies about gypsum, hemihydrate and $\beta$-anhydrite in aqueous suspensions that pay attention to the nucleation and growth processes.

# Appendix B

**Table B-1:** Used substances with corresponding links.

| **Substance** | **url** |
|---|---|
| Calcium sulfate dihydrate | `https://www.merckmillipore.com/DE/de/product/Calcium-sulfate-dihydrate,MDA_CHEM-102161` |
| Benzophenone | `https://www.carlroth.com/de/de/von-a-bis-z/benzophenon/p/0963.1` |
| LiCl (humidity standard) | `https://www.rotronic.com/en-us/eaxx-scs.html` |
| $MgCl_2$ | `https://www.sigmaaldrich.com/catalog/product/sigma/m8266?lang=de&region=DE` |
| LiCl | `https://www.alfa.com/de/catalog/A10531/` |
| $ZnBr_2$ | `https://www.fishersci.de/shop/products/zinc-bromide/-hydrate-99-9/-metals-basis-2/p-7059232/keyword=299465-28-4` |
| LiOH | `https://us.vwr.com/store/product/7488321/lithium-hydroxide-/monohydrate-98-acs` |
| HBr | `https://in.vwr.com/store/product/2344533/hydrobromic/-acid-47/-analar-normapur/-analytical-reagent` |

**Table B-2:** Least squares fits to $RH = \sum_{i=0}^{3} = A_i T^i$ for the used salt solutions according to Greenspan et al. (1977, and references therein).

| **Salt** | $A_0$ | $A_1$ | $A_2$ |
|---|---|---|---|
| $MgCl_2$ | 33.6686 | -0.00797397 | -0.108988 $\cdot 10^{-2}$ |
| LiCl | 11.2323 | -0.00824245 | -0.214890 $\cdot 10^{-3}$ |
| $ZnBr_2$ | 9.28455 | -0.0906508 | 0.118143 $\cdot 10^{-2}$ |
| LiBr | 7.75437 | -0.0654994 | 0.420737 $\cdot 10^{-3}$ |

# Appendix C

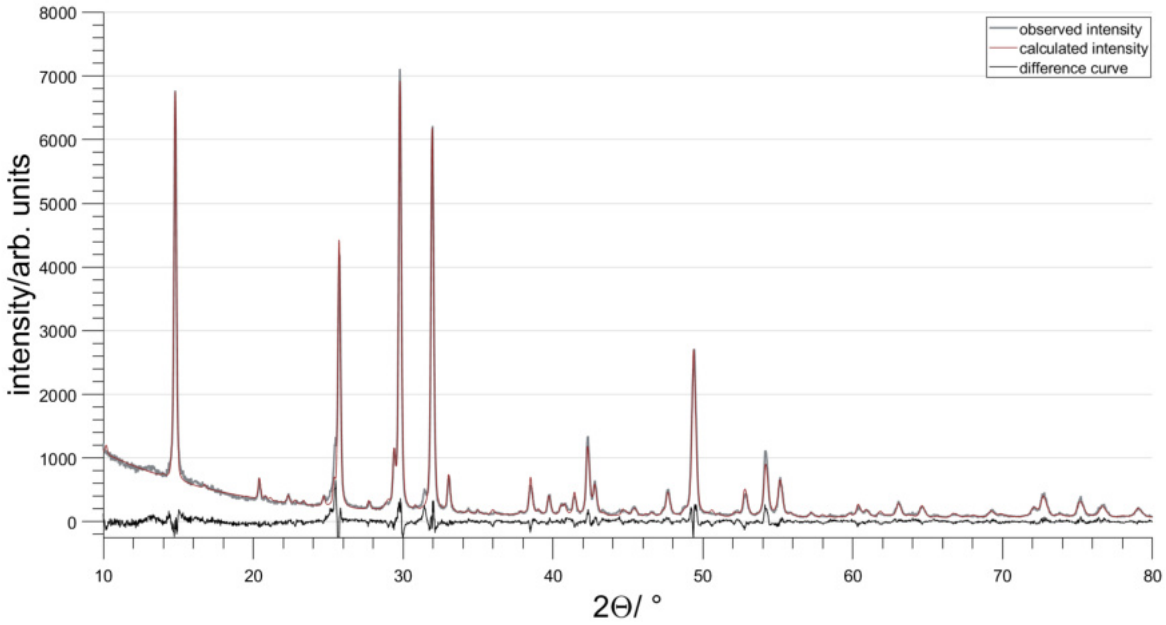


**Figure C-1:** Powder pattern of a hemihydrate sample after 2.5 years of exposure to ambient temperature and humidity conditions. The amount of gypsum is $\approx$ 1 wt.%

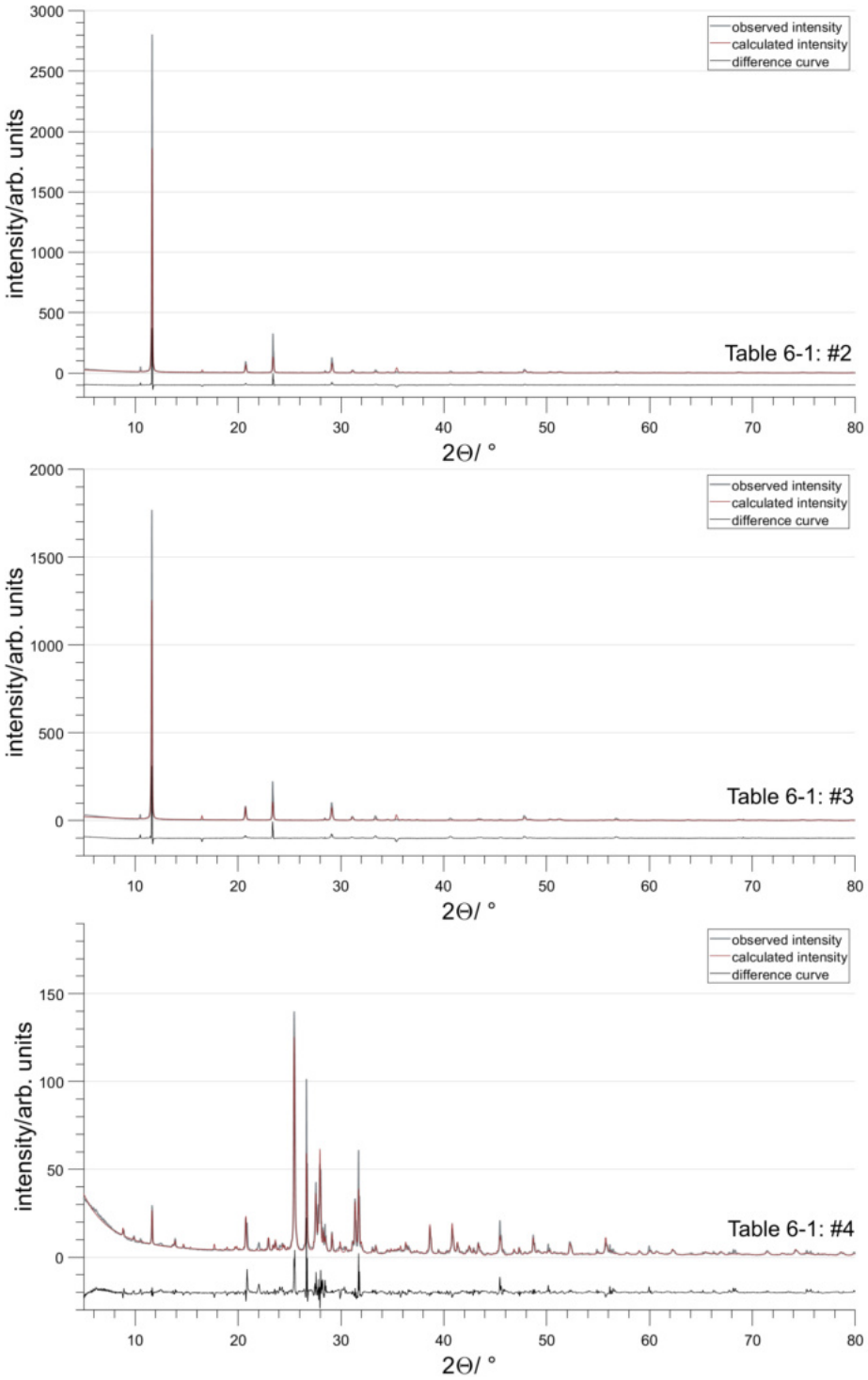


**Figure C-2:** Powder patterns of Atacama samples corresponding to Table 6-1 (I).

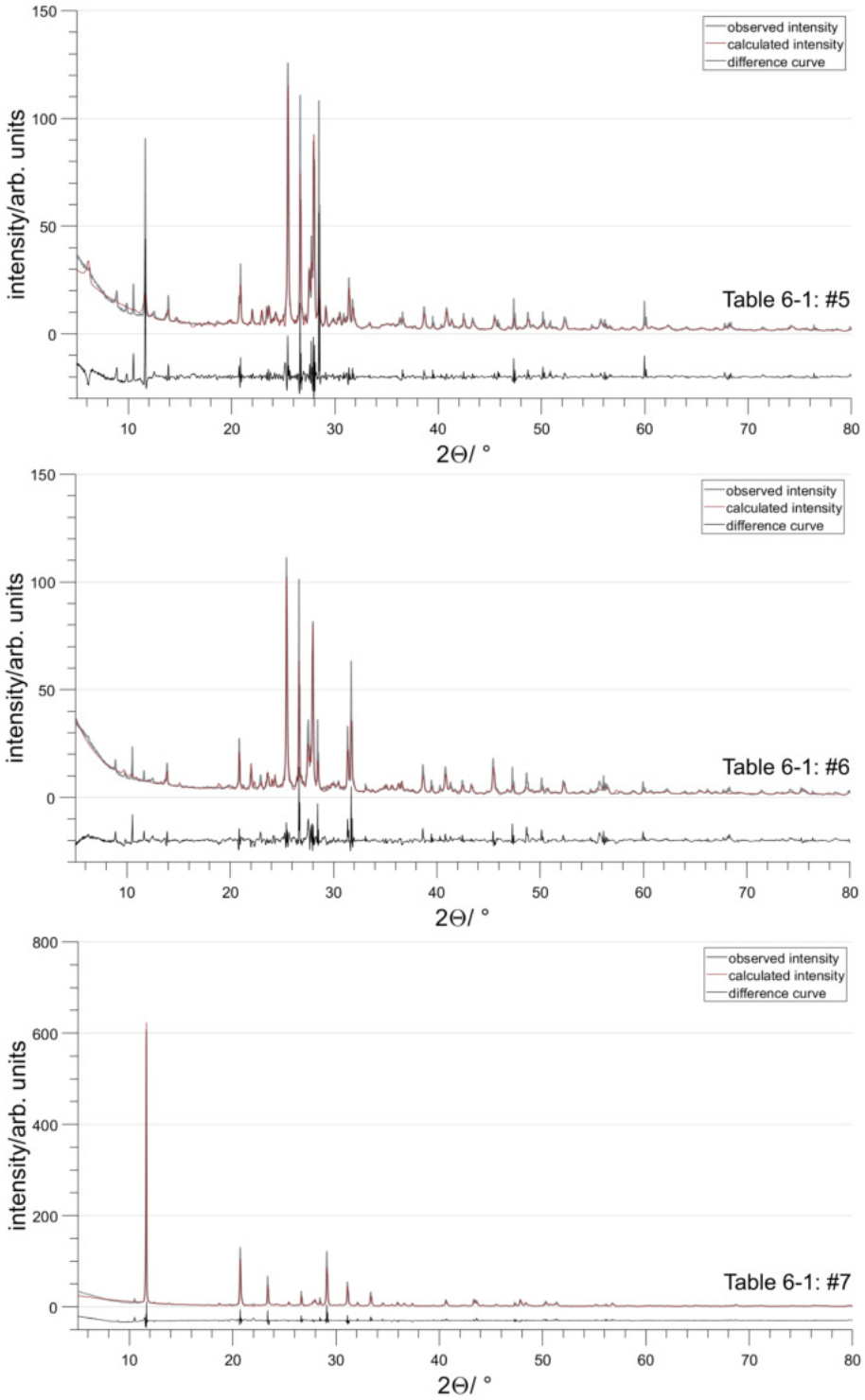


**Figure C-3:** Powder patterns of Atacama samples corresponding to Table 6-1 (II).

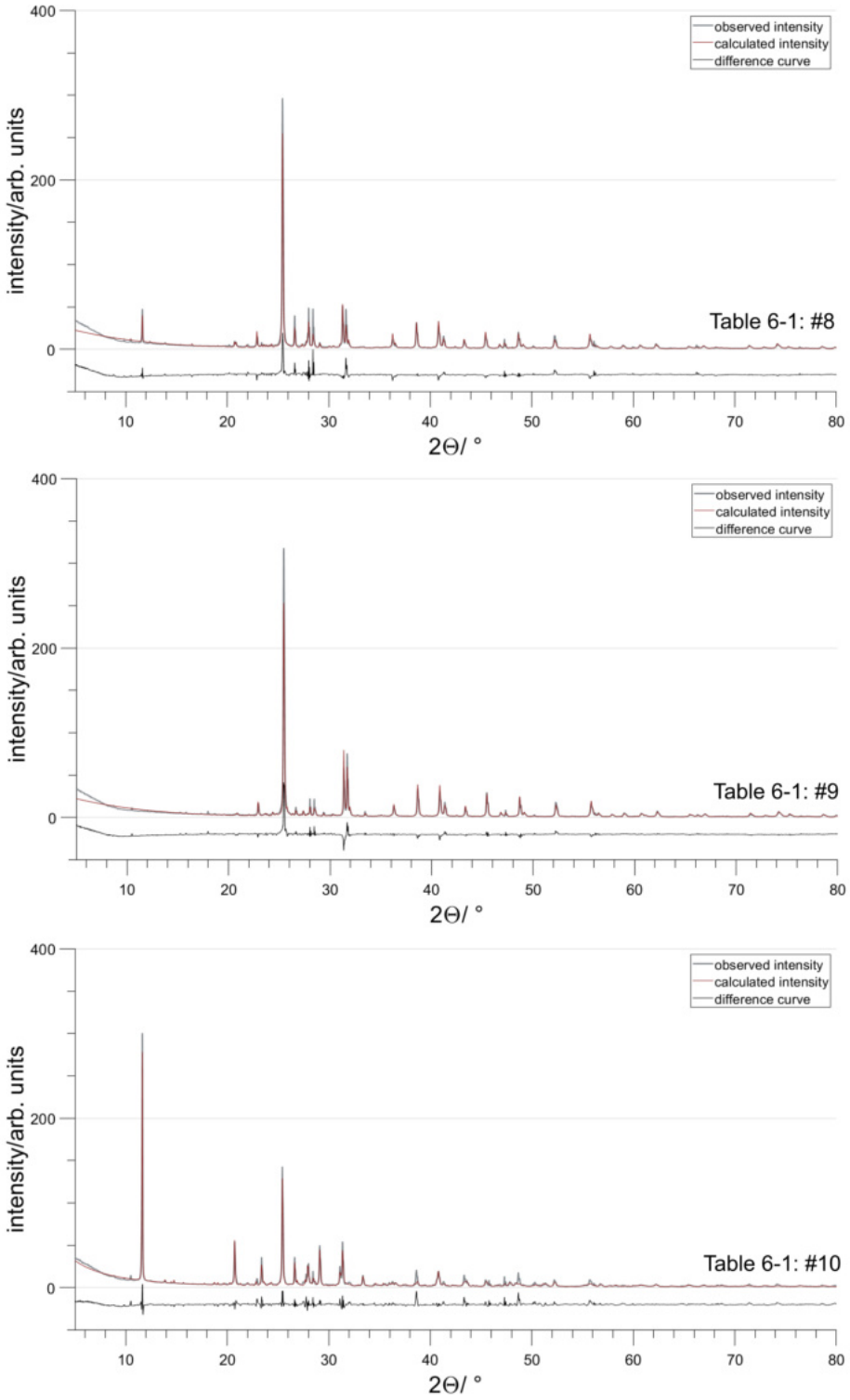


**Figure C-4:** Powder patterns of Atacama samples corresponding to Table 6-1 (III).

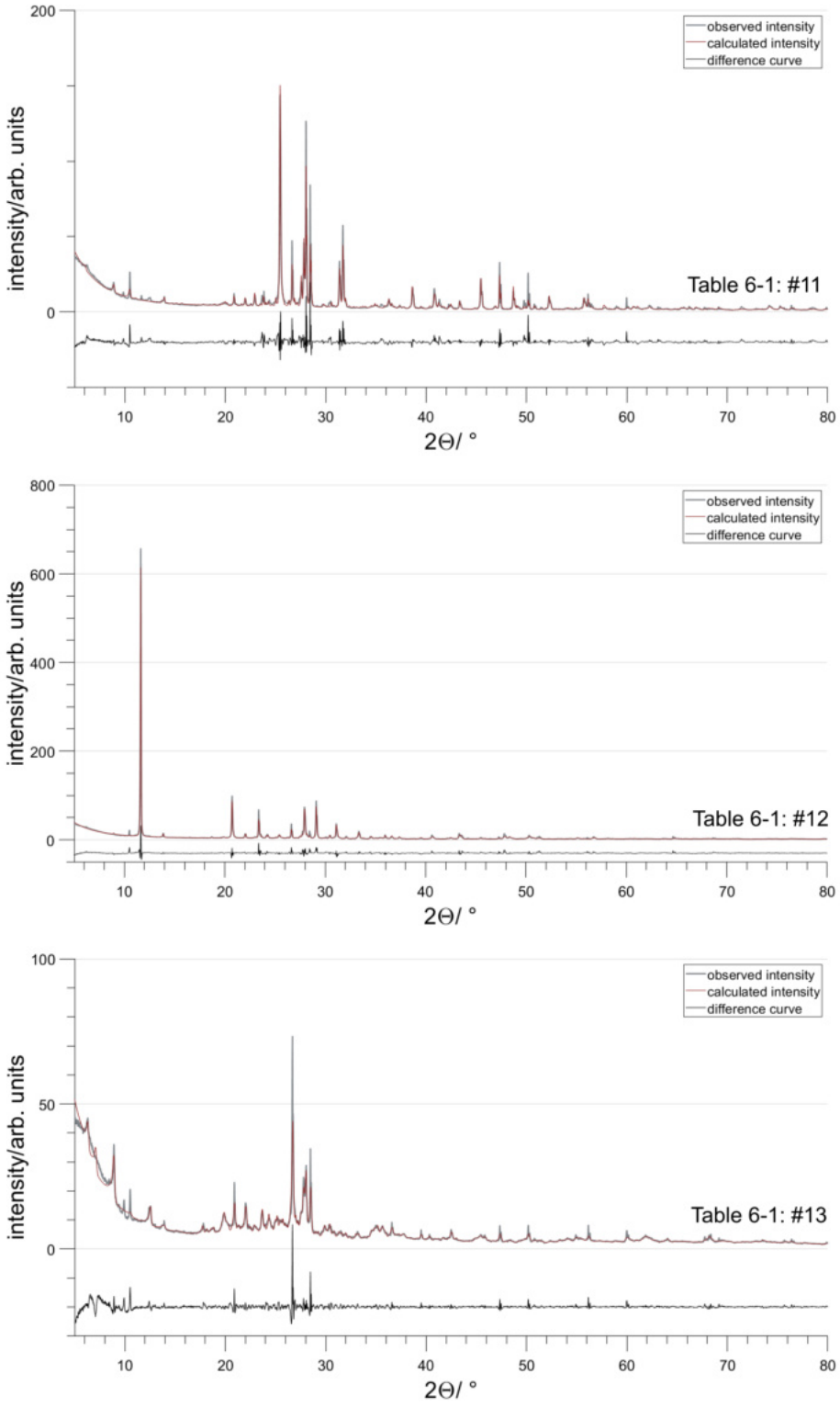


**Figure C-5:** Powder patterns of Atacama samples corresponding to Table 6-1 (IV).

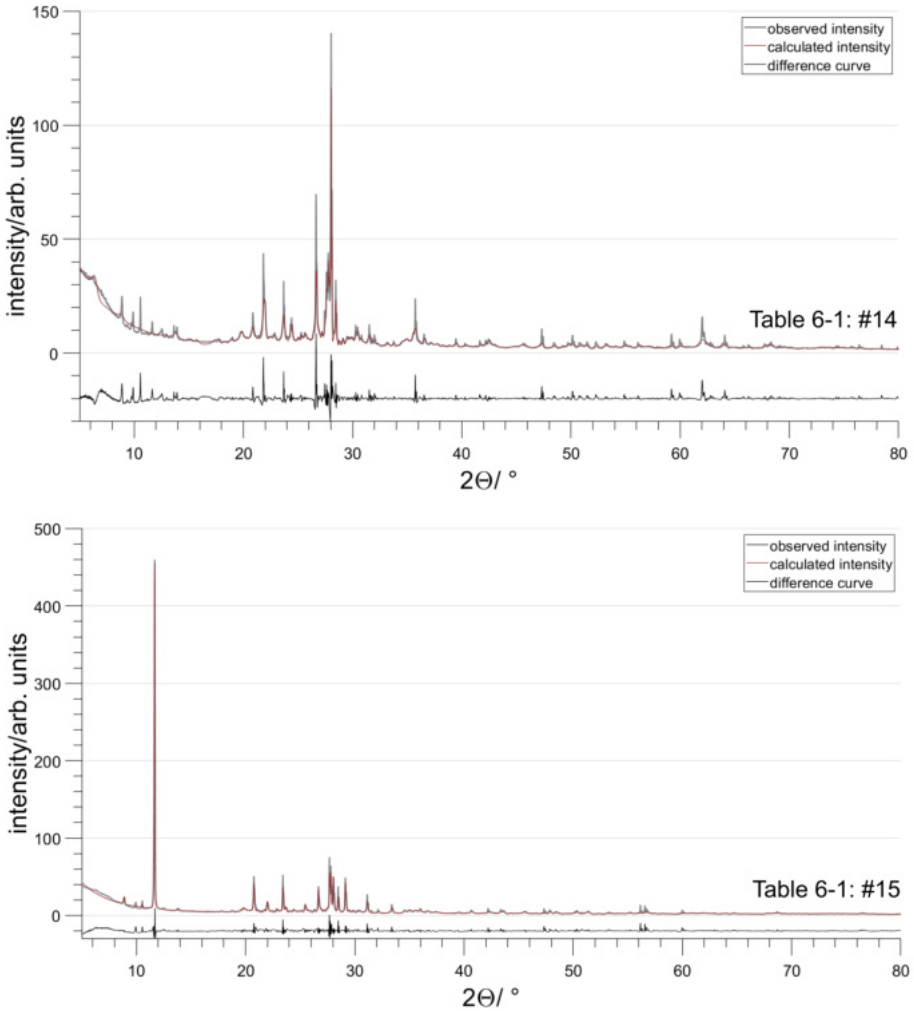


**Figure C-6:** Powder patterns of Atacama samples corresponding to Table 6-1 (V).

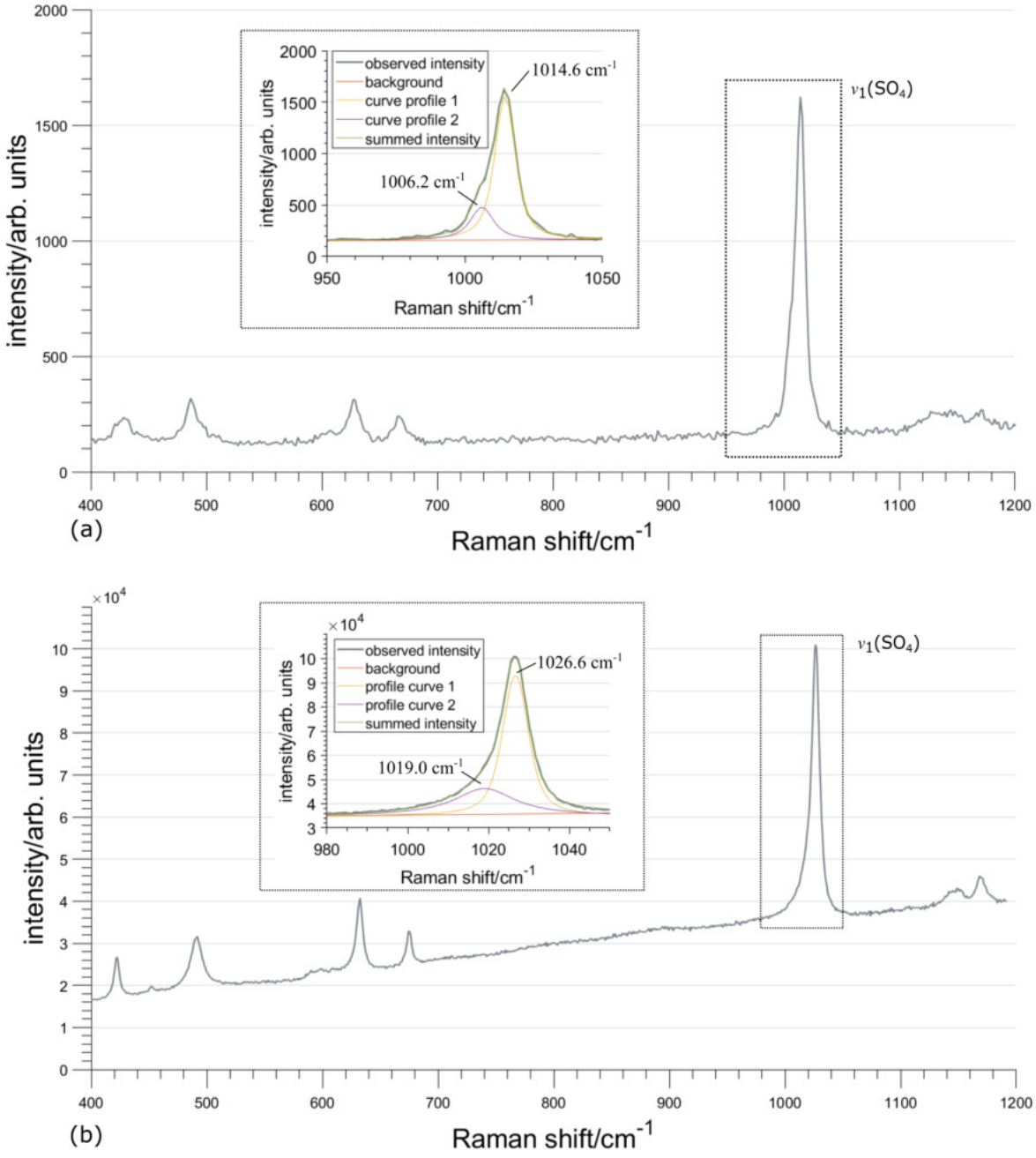


**Figure C-7:** Raman spectra of **(a)** hemihydrate rehydrated from $\gamma$-anhydrite and **b** $\gamma$-anhydrite obtained by gypsum heating at 150 °C for 72 h.

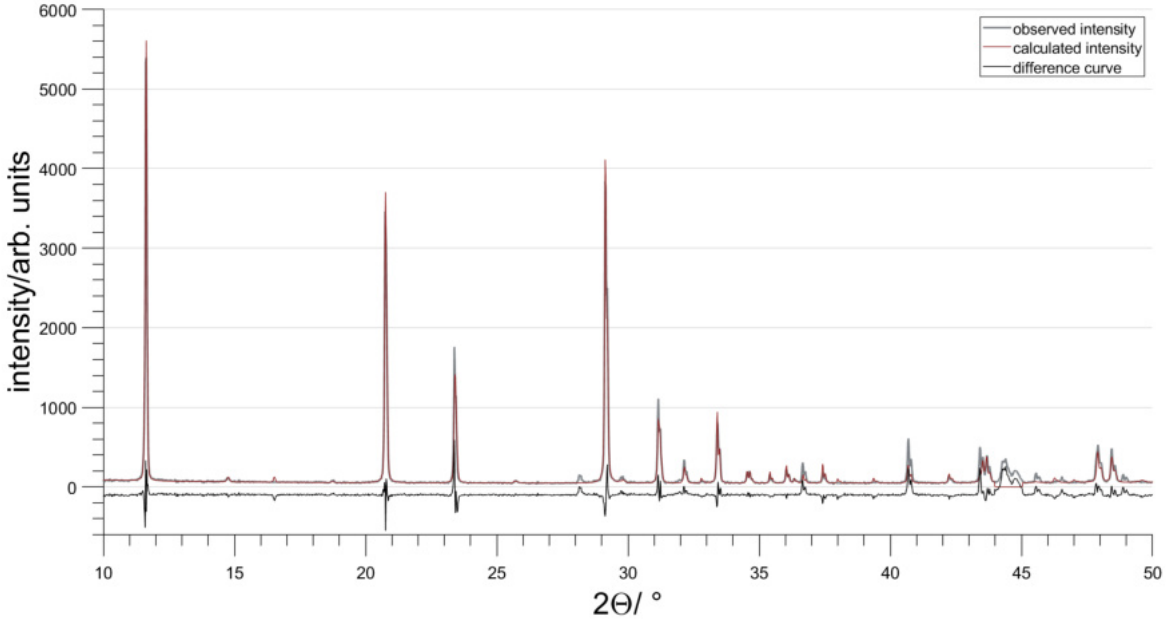


**Figure C-8:** Powder pattern of a gypsum sample after 10 days of treatment at 50 °C and 5% RH. The amount of hemihydrate is ≈ 1 wt.%.

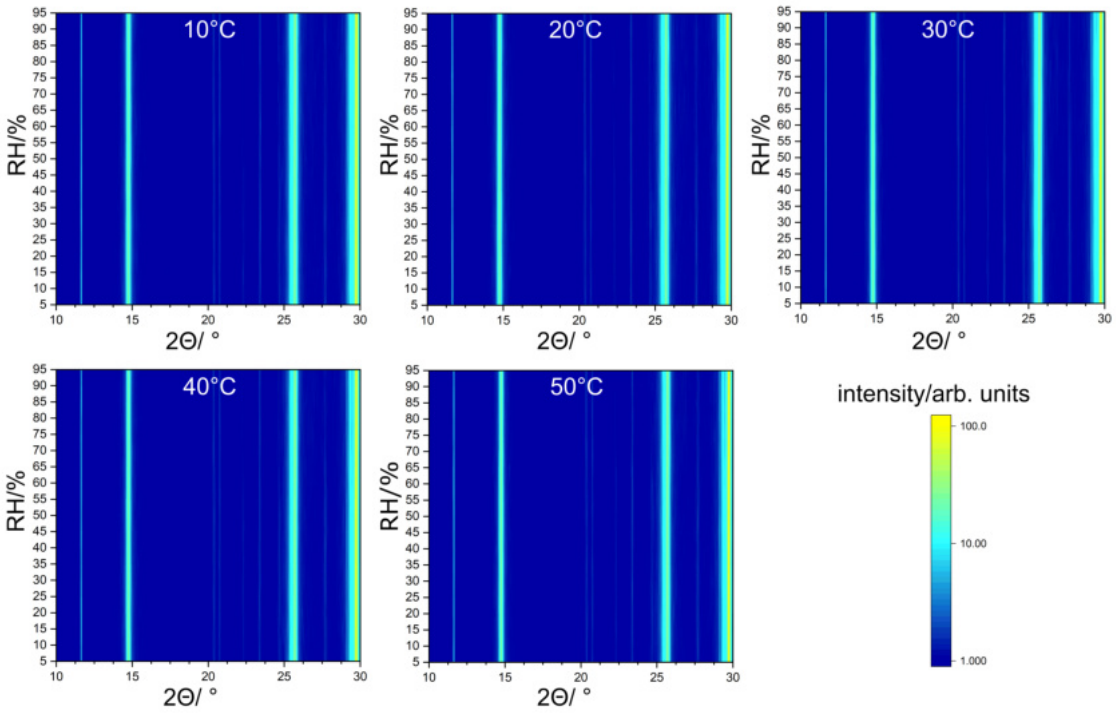


**Figure C-9:** Top views of powder XRD measurements of hemihydrate rehydration experiments. The samples were blended with 1% gypsum. Each humidity step was kept for 5 min.

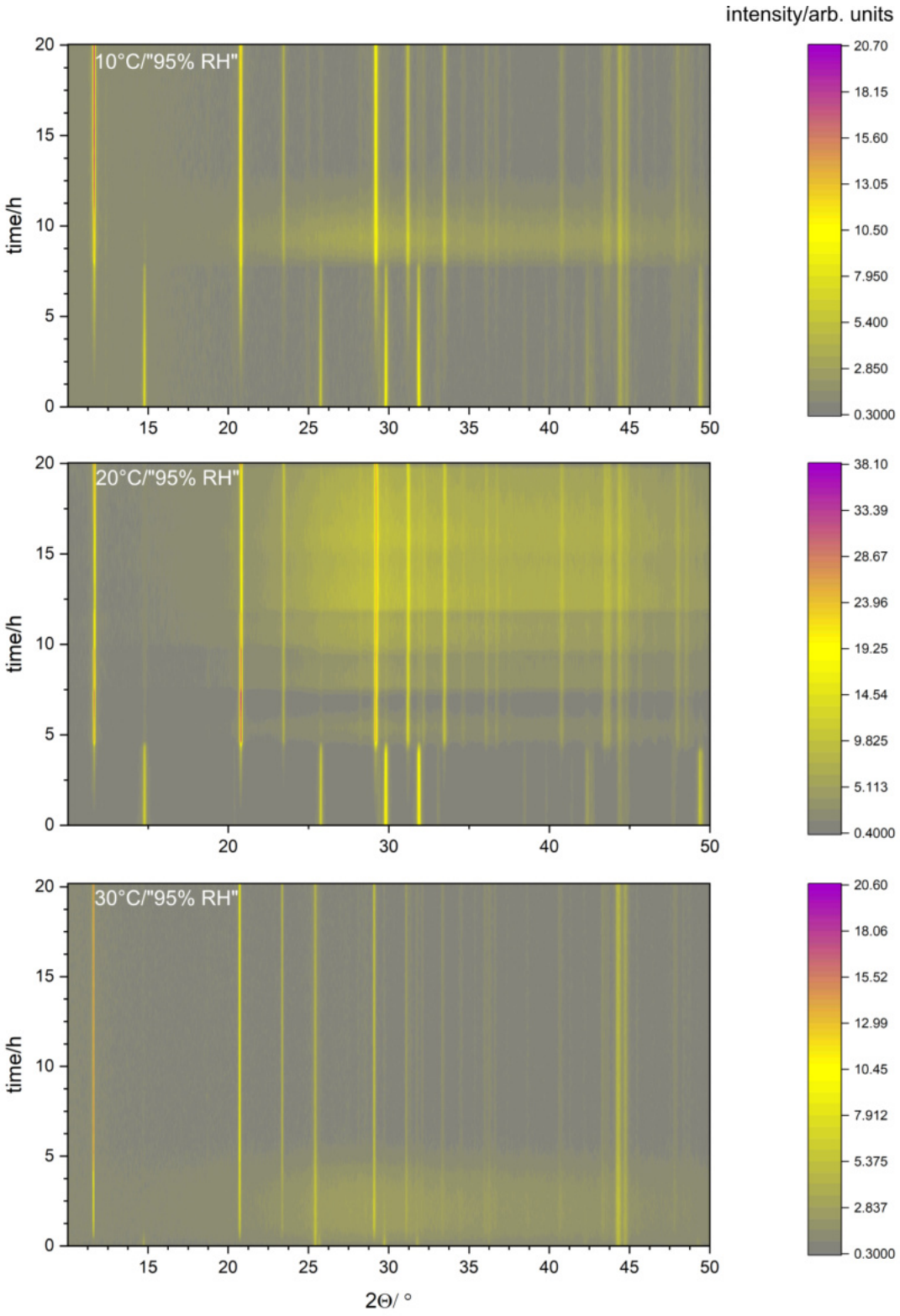


**Figure C-10:** Top views of powder XRD measurements of hemihydrate rehydration experiments at a constant nominal RH value of 95%. The measurements are impaired by humidity sensor failure.

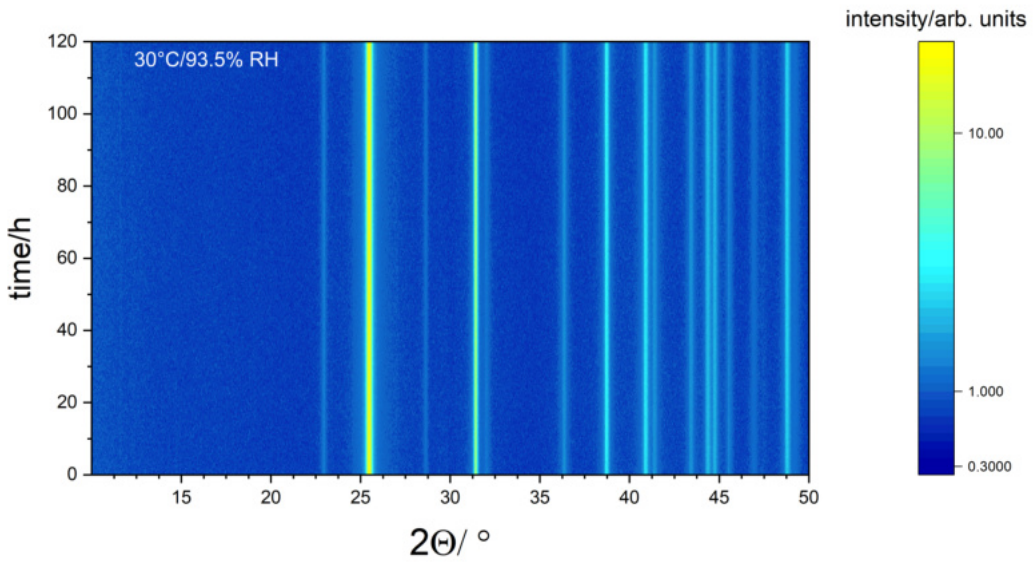


**Figure C-11:** Top view of powder XRD measurements of a $\beta$-anhydrite rehydration experiment.